MAGNETIC RESONANCE IMAGING OF HUMAN BRAIN ACTIVATION USING ENDOGENOUS SUSCEPTIBILITY CONTRAST

by

Peter Anthony Bandettini

A Dissertation Submitted to the Faculty of
the Graduate School of the
Medical College of Wisconsin in
Partial Fulfillment of the Requirements
for the Degree of Doctor of Philosophy

Milwaukee, Wisconsin
October, 1994

ABSTRACT

Local hemodynamic changes that accompany changes in brain activity cause local magnetic resonance imaging (MRI) signal changes. Functional MRI (fMRI) is the name used for the group of MRI techniques used to detect these changes to map human brain activation. In this dissertation, eight studies were carried out which included the dissection of activation–induced MRI signal change components and characterization of their correlation with the magnitude, timing, and extent of neuronal activation and subsequent hemodynamic events; post processing method development; and fMRI applications.

Study one involved the characterization of activation–induced signal change locations, dynamics, and magnitudes using echo–planar imaging (EPI) sequences with combinations of different hemodynamic sensitizations.

Study two involved the development and implementation of correlation and Fourier analysis for robust brain activation image creation.

Study three involved the development and use of a susceptibility contrast model that incorporated repeated smoothing function convolution and phase rotation to simulate spin diffusion in the presence of magnetic field perturbers. Simulated parameters included diffusion coefficient, vessel radii and orientation, blood volume, field strength, echo time, pulse sequence, and blood oxygenation.

Study four involved the assessment of relative susceptibility–related and non–susceptibility–related changes by the use of either separate or combined spin–echo and gradient–echo EPI sequences along with systematic echo–time incrementation.

Study five involved the measurement of the dependence of activation–induced transverse relaxation rate changes and functional contrast to noise ratios on field strength (0.5T, 1.5T, and 3T).

Study six involved characterization of the dependence of the magnitude of activation–induced MRI signal changes on changes in voxel volume, outer volume saturation, TR, and flip angle.

Study seven involved the measurement of the effects that respiratory stresses (hypoxia and hypercapnia) have on resting MRI signal and activation–induced MRI signal changes. A normalization method was also developed to enhance functional resolution and interpretability.

Study eight involved fMRI applications. Regions associated with simple, complex, and imagined complex finger tapping tasks were mapped in the entire human brain. Also, brain regions associated with hearing, reading, and generating words were mapped.

TABLE OF CONTENTS

LIST OF FIGURES

LIST OF TABLES

LIST OF ABBREVIATIONS

%HbO$_2$	percent hemoglobin saturation
ASE	assymetric spin echo
BOLD	blood oxygen level dependent
csf	cerebral spinal fluid
deoxy-Hb	deoxyhemoglobin
oxy-Hb	oxyhemoglobin
EPI	echo planar imaging
fMRI	functional magnetic resonance imaging
FOV	field of view
GE	gradient-echo
Hct	hematocrit
I	real component
IR	inversion recovery
MRI	magnetic resonance imaging
Q	imaginary component
RF	radiofrequency
ROI	region of interest
SE	spin-echo
SEGE	combined spin-echo and gradient-echo
TE	echo time
TR	repetition time
Y	fractional hemoglobin saturation

ACKNOWLEDGMENTS

During my second year of graduate school, the opportunity to help lay the groundwork of a new and potentially revolutionary human brain function imaging methodology presented itself to me. The fulfillment during the next three years of my graduate school career was absolutely overwhelming. I am very lucky, and have many people to thank.

The input and support of my co-advisors, Dr. James Hyde and Dr. Scott Hinks, is much appreciated. Dr. Hyde has established a rich environment at the Medical College of Wisconsin. His students are trained in the lost art of confident and aggressive scientific research. He has been a constant source of motivation, guidance, and insight. I also thank Dr. Hinks, from the Applied Science Lab at GE, for his willingness to be my co-advisor at a particularly critical time. His rigor and key suggestions have helped me tremendously.

I would like to also thank the other members of my committee. I could always count on Dr. Andrew Greene for a refreshing dose of rigor and healthy criticality regarding my work. His suggestions have proven to be right on target. I am fortunate to have heeded them. Dr. Victor Haughton's ongoing support, including a great trip to Norway, has greatly enhanced my graduate school experience. He has also shared with me his insightful clinical perspective of fMRI. Dr. Andrej Jesmanowicz's manic brilliance and pure enthusiasm have been inspiring. His post processing theory and code development has been incredibly helpful to almost all of the work in this dissertation. Also, no results would have come from the 3T scanner if it were not for his heroic efforts in EPI pulse sequence development. It was also an honor to have Dr. Seiji Ogawa, from AT & T Bell Labs, who coined the term "blood oxygenation level dependent" (BOLD) contrast, on my committee. His

seminal papers, which elegantly first described BOLD contrast, were the first that I turned to when starting my project. His work has taught me much. Dr. Ronald Tikofsky was the first neuroscientist to see my results, and was critical in jump-starting the fMRI effort at MCW. His enthusiasm for the noisy preliminary results helped convince Dr. Hyde that this fuzzy "using MRI to look at thoughts" stuff was worth pursuing as a dissertation project.

I was very fortunate to work, as an undergraduate, at MCW in the laboratory of Dr. Janis Eells, who gave me excellent guidance and a good sense of what research was all about.

During most of my graduate school career, I was financially supported by GE Medical Systems. For this I thank Dr. Richard Kinsinger, director of the Applied Science Lab, and Dr. Norbert Pelc, my first co-advisor. Although Dr. Pelc left for Stanford after a few months, he taught me much by his clear, creative, and rigorous example. My second co-advisor, prior to Dr. Hinks, was Dr. Carl Crawford, who helped galvanize my programming and writing skills. His prodding made me a better, more resilient scientist. In general, the experience at GE was highly valuable. I had access to the extensive facilities (roaming the halls many a night), and had the opportunity to interact closely with some of the best physicists, engineers, and programmers in the business.

I have been fortunate to have many excellent collaborators. Early fMRI research was a risk and an adventure for anyone doing it. The core of this early collaborative group consisted of Dr. Jeffrey Binder, Dr. Ted DeYoe, and Dr. Stephen Rao. These scientists spent a large portion of their time trying and succeeding at doing neuroscience research with fMRI in its most raw form. In the process, I have learned a tremendous amount from them. The collaborations continued to grow. This growing group of scientists included Dr. Elizabeth Aaron, Dr. Hubert Forster, Dr. Tom Hammeke, Dr. Wade

Mueller, Dr. Dr. Chip Morris, Dr. Joel Myklebust, Dr. Jay Neitz, Dr. Elliot Stein, Dr. Zerrin Yetkin, and Dr. Jeffrey Zigun. The enthusiasm, energy, and collegiality that permeates the fMRI effort at MCW is rare. I have enjoyed many hours of work and conversation with each of these researchers. Dr. Stein has been particularly helpful in the education that he has supplied to me via his vast library on cerebral metabolism and hemodynamics.

I am also grateful to Dr. Shi-Jiang Li, for introducing me to other types of functional magnetic resonance and for giving me my first opportunity to lecture on fMRI outside of MCW.

Although Dr. Robert Cox has only recently become part of the Biophysics Research Institute, his contribution has been tremendous. I have quickly learned that if I needed help on some sticky problem, I could turn to him to help get it solved in an impeccably rigorous and laser–like fashion.

The expert skills of many key people are also greatly appreciated. Lloyd Estkowski and Don Dickerson were masters of the stressful job of running the scanner and of countless other tasks that have become necessary with fMRI. Many times from midnight to sunrise, I was the volunteer while Lloyd or Don ran the scanner. Dick Johnson's skill with imaging hardware and Robert Prost's scanner expertise have not gone unnoticed. Dr. Chris Felix's careful administrative work and the work of Biophysics secretaries; Donna Walker, Margaret Wold, and Marian Klug, are appreciated. Also, the helpfulness of Nancy Nelson and Carol Rybeck in the graduate school office is appreciated.

Dr. Jerry Boxerman, Tim Davis, Dr. Ken Kwong, Dr. Bruce Rosen, and Dr. Greg Sorensen, from MGH, were also helpful in regard to the completion of the final copy of my dissertation. I am also very lucky to have met Dr. Kathleen Donahue. Her friendship, intelligence, and perspective, coupled with her incredibly open and giving nature has enhanced my life.

The camaraderie of the technologists, graduate students, and post–docs has also made my experience at MCW a fun and enriching one. I am honored to have been a part of this group. Most have also have volunteered multiple times for my experiments. I would specifically like to acknowledge a friend and pioneer fMRI volunteer, Wendy Graf. Early results obtained when she was a volunteer overwhelmingly convinced me that fMRI was real.

I have absolutely great friends outside of work. I have known Eric Gietzen, Rob Hartman, Mike Miller, and Peter Pembroke since high school cross country and track. I have also known Patrick Warczak since high school. The friendship of these guys has tremendously helped during my thesis writing. I value highly the rich experiences and conversations that I share with them.

Profound gratitude is felt towards my friend, colleague, and mentor; Dr. Eric Wong. Without Eric, fMRI would simply not exist at MCW. Countless times, he would casually present to me an elegant idea or a piece of pure creation, and then display incredible patience as he explained these ideas or creations to me usually more than once. These conversations are among my fondest memories of graduate school. During one conversation, he came up with the idea of using repeated convolution with a smoothing function instead of a Monte Carlo approach to simulate diffusion. I took this idea to heart and used it as the method for the simulations in chapter 6. He created the hardware and developed the pulse sequences and reconstruction methods for EPI at 0.5 and 1.5 Tesla. I have never met anyone more creative, more rigorous, more confident, more humble, more industrious, more focused, more brilliant, and more balanced than Eric. He is truly a great person, and I am truly fortunate and honored to have met and worked with him.

I would also like to thank my sister, Christine Peterson, her husband, David, and their son, Nicholas, for their unconditional support. Thanks also to my brother, Francis, for his support and help in my obtaining the computer for writing this dissertation. In addition, I thank my grand aunt, Julie Curto, for her constant cheer and enthusiasm for what I do.

Lastly, I thank my parents for their ongoing love and support. They have helped me in so many priceless ways. From the start, they have instilled in me a sense of fulfillment in doing my best.

CHAPTER 1

INTRODUCTION

The human brain is likely the most complex and least understood system known. The understanding of its workings is a naturally inspiring goal, and the development of new methods to further this understanding is fundamental to the pursuit of this goal.

New methods for understanding human brain function can be extensively applied. Clinically, these methods can allow for faster, cheaper, and more effective diagnoses and treatments of neurological, cognitive, or neurophysiologic pathologies. In neuroscience research these methods can complement and add to the vast current efforts on molecular to systems levels. Imaging of the human brain during learning, reasoning, visualization, language, and creative functions may give insights into the dynamic structures of these emergent processes, therefore helping to uncover principles of cognition.

The work presented in this dissertation involves the further advancement of several aspects regarding a new method by which human brain activation is noninvasively observed using magnetic resonance imaging (MRI) techniques, termed functional MRI (fMRI). First, relative locations and dynamics of activation–induced MR signal changes are characterized across several functional contrast weightings. Second, post–processing techniques tailored to the characteristics of fMRI time course data are developed and demonstrated. Third, a hypothetical biophysical model that helps to explain endogenous susceptibility–related activation–induced signal changes is constructed. Fourth, contrast mechanisms underlying fMRI

are explored by comparison of activation–induced transverse relaxation rate changes ($\Delta R2^*$ and $\Delta R2$) and observation of physiologic dependencies of the activation induced signal changes. These experiments are also compared with the biophysical model. Fifth, applications of fMRI are demonstrated. Lastly, potential future directions of fMRI research are described.

In this introduction, fundamental details of physiological events accompanying human brain activation, basics of magnetic susceptibility, a history of the development of fMRI, current research in fMRI, and an overview of what is presented in each chapter are described. Essentially, an attempt is made here to put into perspective the fMRI work that has been carried out worldwide, and to detail the work presented in this dissertation.

1.1 BRAIN ACTIVATION

Brain activation fundamentally consists of an increase in the rate at which action potentials are generated. The action potential, the unit of information in the brain, is a transient and cascading change in neuronal membrane polarity. At neuronal junctions, neurotransmitter synthesis, release, and uptake takes place, causing modulation of the action potential propagation (1-3). When a population of neurons experience these rapid changes in membrane polarity, measurable electrical and magnetic (1-7) changes in the brain are generated. Because of the energy requirements of membrane repolarization and neurotransmitter synthesis, brain activation is accompanied by measurable increases in metabolism (1-3, 8-13). These changes in brain activity cause, through several postulated mechanisms (1, 8-19), changes in blood flow (1-3, 8-25), blood volume (26-29), and blood oxygenation (28-32).

Brain activation takes place in specific regions, in specific "quantities," and at specific times, depending upon the mental task or tasks being performed (1-64). One major aspect of brain function research is in determining the relationships between the tasks and the corresponding activity locations, magnitudes, and dynamics. All techniques of imaging and assessing human brain function are based on localization and measurement of these electrical, magnetic, metabolic, and hemodynamic changes that are spatially and temporally associated with neuronal activation.

Methods that have been used, to date, other than fMRI, for determining human brain functional organization and regions of activation include lesion studies (2, 58), cytoarchitectural studies (1), electrical stimulation (50-52), optical imaging (53), near-infrared spectroscopy (NIRS) (28), thermoencephaloscopy (47, 48), electroencephalography (EEG) (1, 2, 6, 44-46, 49), event related potential mapping (ERP) (1, 2, 45, 46), magnetoencelography (MEG) (2, 39, 41-43), single photon emission tomography (SPECT) (1, 2, 8, 9, 39, 40, 59), xenon-washout computed tomography (Xe-CT) (1, 2, 8, 9, 19, 20, 59), positron emission tomography (PET) (1, 2, 8-10, 21-25, 29, 33-38, 40, 55, 58-62), and MR spectroscopy (MRS) (63, 64).

Limitations that set the boundaries of human brain functional imaging include spatial resolution, temporal resolution, sensitivity, registration with underlying anatomy, invasiveness, and correlation of measured changes with underlying neuronal activity. The particular types of brain function research that the above mentioned techniques can explore depend on these limitations. The described fMRI technique is free of several limitations imposed on other techniques, and therefore offers the potential to explore new dimensions in human brain function.

1.2 MAGNETIC SUSCEPTIBILITY CONTRAST

MRI emerged in the 1970's and 80's as a method by which high–resolution anatomical images of the human brain and other organs could be obtained non–invasively (65-69). The first types of image contrast used in MRI were proton density, spin–lattice relaxation (T1), and spin-spin relaxation (T2) contrast (70-74). The large number degrees of freedom in MR parameter space has allowed MR contrast types to expand from physical to physiological (75). The types of intrinsic MRI physiological contrast that have since been discovered and developed have included blood flow (75-78), diffusion (75, 79-83), perfusion (75, 81-90), and magnetization transfer (75, 91, 92). Chemical shift imaging has provided information about relative concentrations and distributions of several chemical species (75, 93, 94).

The effects of endogenous and exogenous paramagnetic materials and, more generally, of materials having different susceptibilities, has also been studied and applied in several significant manners. An understanding of susceptibility contrast is an essential prerequisite to the exploration of fMRI contrast mechanisms.

Magnetic susceptibility, χ, is the proportionality constant between the strength of the applied magnetic field and the resultant magnetization established within the material (95). In most biologic materials, the paired electron spins interact weakly with the externally applied magnetic field, resulting in a small induced magnetization, oriented opposite to the applied magnetic field, that causes a reduction of field strength inside the material. These materials are diamagnetic, and have a negative magnetic susceptibility.

In materials with unpaired spins, the electron magnetic dipoles tend to align parallel to the applied field. If the unpaired spins are in sufficient

concentration, this effect will dominate, causing the induced magnetization to be aligned parallel with the applied field, causing an increase in magnetic field strength inside the material. In a typical 70-kg human body, paramagnetic materials include iron (3-5 g), copper (70-120 mg), manganese (12 mg), nickel (10 mg), chromium (2 mg), cobalt (0.3 mg), vanadium (2 mg), molybdenum (13 mg), and tungsten (trace). Iron is approximately 30 times more abundant than all the other transition elements in a typical human body. Much of the iron is contained in red blood cells. In biological tissues, additional sources of paramagnetism include materials, which because of peculiarities in their chemical bonding, have unpaired spins. These include oxygen, O_2, and nitric oxide, NO (95).

The fMRI technique described in this dissertation is based on the understanding that blood has oxygenation–sensitive paramagnetic characteristics (95-98). Deoxyhemoglobin (deoxy-Hb) contains paramagnetic iron, while oxygemoglobin (oxy-Hb) contains diamagnetic oxygen-bound iron (95-98). The effects of oxygenation changes in whole blood on MR signal intensity have been generally established (97-108). The relationship between blood susceptibility and blood oxygenation, while understood for decades, has been recently characterized using an innovative MR–based technique, called MR susceptometry (108). Using this method, the susceptibility of completely oxygenated red blood cells was measured to be $-0.26 \pm 0.07 \times 10^{-6}$ (cgs units). With this technique, blood susceptibility was also shown to be linearly proportional to blood oxygenation (it decreases linearly as oxygenation increases). The susceptibility of completely deoxygenated red blood cells is $0.157 \pm 0.07 \times 10^{-6}$. The susceptibility difference between completely oxygenated and completely deoxygenated red blood cells is therefore 0.18×10^{-6}. The

effects of susceptibility and susceptibility changes on MR signal are described below.

Exogenous paramagnetic substances, which include Gd(DTPA) and Dy(DTPA) can give useful information regarding several aspects of organ function (109). In the brain, these agents can give information on blood volume and vascular patency (107-115). The effects of these agents on tissue T1, T2*, and T2, are highly dependent on chemical environment and compartmentalization, as has been observed (107-115) and modeled (109, 111-114, 116-129).

One mechanism of action for these compounds is dipolar interaction, having an effect on intrinsic T1 and T2 relaxation times (109, 111). This effect relies on interaction of water with unpaired spins. Homogeneous distributions of solutions containing paramagnetic ions display relaxivity changes that can be predicted by the classical Solomon–Bloembergen equations (111), but in the healthy brain, these agents, upon injection, remain compartmentalized within the intravascular space, which contains only about 5% of total brain water. The extent of agent–proton interaction is reduced by the limited rate at which diffusing or exchanging protons in the other 95% of brain water pass through the intravascular space, which is also less accessible due to the blood brain barrier. These combined effects greatly limit the agent–induced T1 effects, which rely on direct interaction of protons with the paramagnetic agents. In this case, T2* and T2 shortening effects, caused by contrast agent induced bulk susceptibility differences between intravascular and extravascular space (111-114, 116-125) dominate over classical dipolar relaxation effects.

Magnetic field inhomogeneities are created by the presence of materials having different susceptibilities. The effect on transverse relaxation by these inhomogeneities can be characterized by (107, 112-114, 116, 117):

$$1/T2^* = 1/T2 + 1/T2' . \qquad [1.1]$$

The relaxation rate, $1/T2^*$, also termed $R2^*$, is the rate of free-induction decay, and contributes to the signal intensity of gradient–echo sequences. The relaxation rate, $1/T2$, also termed $R2$, is the intrinsic tissue transverse relaxation rate, and contributes to the signal intensity of spin–echo sequences. The relaxation rate, $1/T2'$, also termed $R2'$, is the water resonance linewidth, which is a measure of frequency distribution within a voxel. The relative magnitude of $R2'$ is not only proportional to the susceptibility of the magnetic field perturber, but to the dimensions of the perturber relative to the local proton dynamics, as will be described later in the chapter.

To link the MR signal to the above expression, it is necessary to describe a simple model for MR signal when using gradient–echo or spin–echo sequences. The expressions that relate signal intensity to proton density, T1, T2 or T2*, and MR parameters are described below.

In a spin–echo sequence:

$$S(TE,TR) = S_O (1 - 2e^{-(TR-TE/2)/T1} +\ e^{-TR/T1})\ e^{-TE/T2}. \qquad [1.2]$$

The signal intensity, S(TE,TR), described as dependent on TE (the echo time) and TR (the repetition time) of the experiment. S_O is the proton density. At long TR values, the expression reduces to:

$$S(TE) = S_O \, e^{-TE/T2}. \qquad\qquad [1.3]$$

In a gradient–echo sequence:

$$S(\theta, TE, TR) = S_O \, e^{-TE/T2^*} \left[\left(\left(1 - e^{-TR/T1} \right) \sin\theta \right) \Big/ \right.$$
$$\left. \left(1 - e^{-TR/T1} \, e^{-TR/T2^*} - \left(e^{-TR/T1} - e^{-TR/T2^*} \right) \cos\theta \right) \right] \qquad [1.4]$$

The flip angle is θ. At $TR \gg T2^*$, this expression reduces to:

$$S(\theta, TE, TR) = S_O \, e^{-TE/T2^*} \left[\left(1 - e^{-TR/T1} \right) \sin\theta \right) \Big/$$
$$\left(1 - e^{-TR/T1} \cos\theta \right)]. \qquad\qquad [1.5]$$

At long TR values relative to T1, or as θ approaches $0°$, this expression reduces to:

$$S(TE) = S_O \, e^{-TE/T2^*}. \qquad\qquad [1.6]$$

If a flip angle of 90° is used with a long TR, similar transverse relaxation rate dependencies fall out for spin–echo and gradient–echo signal intensities. In the context of this thesis, which is based on the observation of signal changes over time that are hypothesized to be primarily due to changes in T2 and T2*, it is instructive to observe graphically the nature of these transverse relaxation rate changes by observing a) the TE dependence of the signal, b) the TE dependence of the signal differences between active and resting states (Sa - Sr), and c) percent signal change between active and resting states (Sa - Sr) / Sr) x 100, given a small variation in transverse relaxation rate

($\Delta R2^*$ or $\Delta R2$). In this example $R2^*$ and $\Delta R2^*$ are used, but these concepts also apply for $R2$ and $\Delta R2$.

Susceptiblity–related transverse relaxation rates are not necessarily described by single exponentials (116, 118), meaning that the measured relaxation rates or activation–induced relaxation rate changes may vary depending on what TE or combination of TE values is used in the measurements. Only "intrinsic" single exponential relaxation rate changes, by definition, are independent of TE. Nevertheless, as is described in chapter 7, most of the activation–induced signal changes behave, experimentally, as "intrinsic" $R2$ and $R2^*$ changes. Therefore, the below–demonstrated effects of intrinsic $R2$ and $R2^*$ changes are important to the understanding of the characteristics of the activation–induced signal changes as they will be discussed in this dissertation.

The first set of plots, shown in Figure 1.1, are of MR signal, assuming a $T2^*$ of 48 ms (resting state signal) and of 50 ms (active state signal). These values are typical for the $T2^*$ values in the brain and the difference in the relaxation rates is typical for activation–induced changes in $T2^*$. In these plots, S_O is equal to 1.
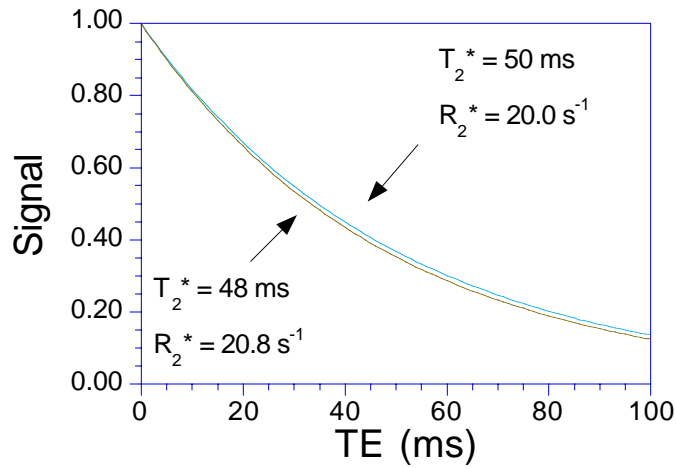
Figure 1.1. Plot of Signal vs. TE, using equation 1.6. S_O equals 1. The two curves represent typical values of R2* in the brain. The difference in relaxation rates represent typical differences between resting (20.8 s^{-1}) and activated (20.0 s^{-1}) R2* in the brain (-0.8 s^{-1}). These signals are referred to as Sr (resting signal) and Sa (active signal) in the discussion below. MR signal, in general, is S.

Considering that:

$$Ln(S) = TE/T2^* \qquad\qquad [1.7]$$

$$Ln(S)/TE = 1/T2^* = R2^*, \qquad\qquad [1.8]$$

R2* may be obtained by the slope of Ln(S) vs. TE, as shown in Figure 1.2.
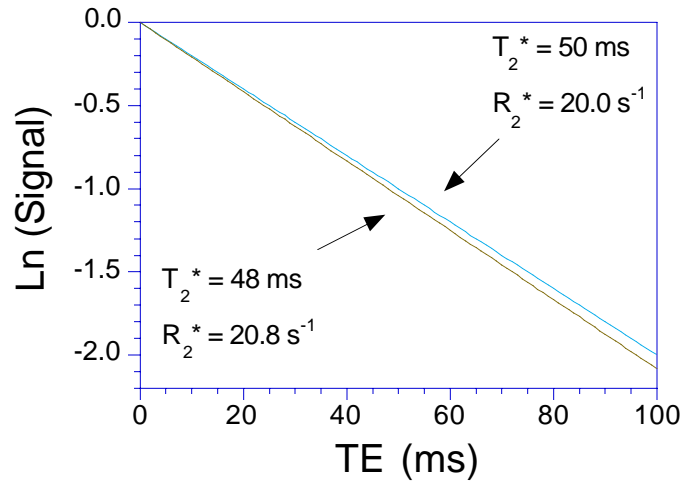
Figure 1.2 Ln(S) vs. TE. In chapters 7 and 8, transverse relaxation rates (R2 and R2*) are measured by applying a linear fit to curves such as these – which are generated using resting and activated signal intensity in the brain at multiple TE values. In the measurements where a single TE value is used, activation–induced changes in So are considered zero and single exponential decays are assumed.

Assuming that signal changes are affected by changes *only* in R2*, the change in relaxation rate, ΔR2*, may be estimated by measurement of Sr and Sa at single TE values and using the expression:

$$-Ln(Sa/Sr)/TE = \Delta R2*. \hspace{3cm} [1.9]$$

The expression relating percent change to ΔR2* is:

$$\text{percent signal change} = 100 \left(e^{-\Delta R2*\ TE} - 1 \right). \hspace{1.5cm} [1.10]$$

11

Figure 1.3 is a plot of the percent signal change vs. TE between the synthesized resting and activated curves. An approximately linear fractional signal increase with TE is demonstrated.
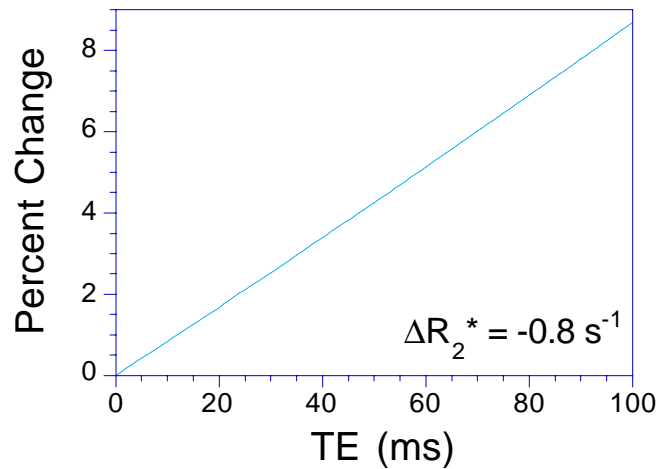
Figure 1.3 Percent change vs. TE from the same synthesized data set as shown above. Given a $\Delta R2^*$ value typically obtained (see chapter 7), a linear dependence of percent change on TE is observed in the TE range typically used.

If $\Delta R2^*$ is small relative to $R2^*$, the signal difference between the two curves will be maximized at TE $\approx$ T2* (gradient–echo) or T2 (spin–echo), as demonstrated below. Contrast between two signal intensities (Sa and Sr), having a difference in relaxation rate equal to $\Delta R2^*$, can be approximated by:

$$Sa - Sr = e^{-TE\,(\Delta R2^* + R2^*r)} - e^{-TE\,(R2^*r)} \qquad [1.11]$$

where R2*r is the relaxation rate associated with a measured Sr at a given TE value. The TE value at which Equation 1.11 is maximized is given by:

$$TE = Ln(\, (\, \Delta R2^* + R2^*r \,)/R2^*r \,)/\Delta R2^*. \qquad [1.12]$$

In the limit that $\Delta R2^*$ approaches 0, the TE value at which contrast is maximized approaches $1/R2^*r$ or $T2^*r$. A graphical demonstration of this contrast maximization is shown in Figure 1.4. Even though the percent change increases, as shown in Figure 1.3, the contrast or signal *difference* does not increase monotonically with TE.
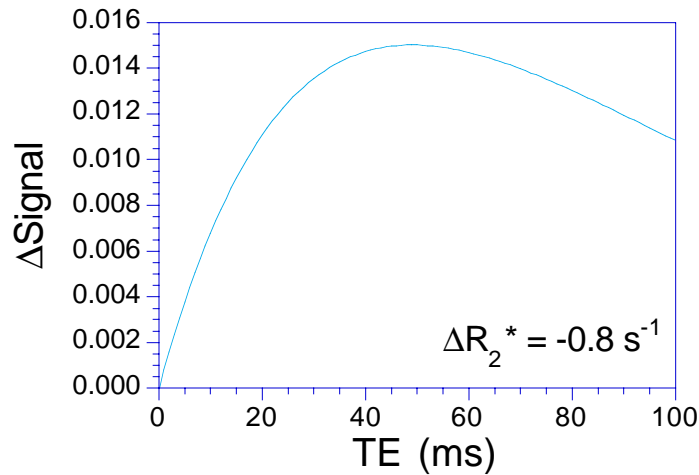
Figure 1.4 Plot of ΔS vs. TE from the same synthesized data sets as shown in the previous figures. A maximum is reached at TE $\approx$ T2*r ($\approx$ 48 ms).

In the presence of a magnetic field perturber, the relative R2 and R2* relaxation rates depend on: the diffusion coefficient (D) of spins in the vicinity of induced field inhomogeneities, the radius (R) of the field perturber (here simplified to a sphere), and the variation in the Larmor frequency at the

surface of the sphere (107, 112-114, 116-119). The expression for the proton correlation time, τ, is:

$$\tau = R^2/D. \qquad\qquad [1.13]$$

The variation in the Larmor frequency ($\delta\omega$), at the perturber surface is:

$$\delta\omega = \gamma(\Delta\chi)B_O , \qquad\qquad [1.14]$$

where γ is the gyromagnetic ratio, $\Delta\chi$ is the susceptibility difference, and B_O is the strength of the applied magnetic field. Depending on the relative values of these variables, intravoxel dephasing effects are commonly described by three regimes, termed the fast, intermediate, and slow exchange regimes (107, 112-114, 116-119). The exchange regimes are summarized in Table 1.1:

slow exchange	$\tau (\delta\omega) \gg 1$	$\Delta R2^* \gg \Delta R2$
		$\Delta R2' \approx \Delta R2^*$
intermediate exchange	$\tau (\delta\omega) \approx 1$	$\Delta R2^* > \Delta R2$
		$\Delta R2' < \Delta R2^*$
fast exchange	$\tau (\delta\omega) \ll 1$	$\Delta R2^* \approx \Delta R2$
		$\Delta R2' \approx 0$

Table 1.1: Summary of the exchange regimes commonly referred to when the effects of magnetic field perturbations on transverse relaxation rates are described.

In the fast exchange regime (116, 117, 119-125), the high diffusion rate causes all spins to experience a similar range of field inhomogeneities, therefore causing a similar net phase shift of all spins, and a minimal loss of phase coherence as well as a similar loss of phase coherence between gradient–echo and spin–echo sequences. The fast exchange regime is relevant in two particular cases.

In the human brain, the dephasing experienced in the presence of susceptibility–induced gradients in the vicinity of capillaries and red blood cells has been described as being in the fast exchange regime (107, 113, 117, 130).

The R_2 dependence on blood oxygenation was first observed by Thulborn et al. (97), and has since been confirmed by several other experimental studies (98-108). The T_2 ($1/R_2$) of blood increases as blood oxygenation decreases. As the inter–echo 180° spacing (during T_2 measurements) is increased, the change in T_2 is more pronounced, directly reflecting the diffusional mechanism within the vicinity of red blood cell-induced gradients, by which intravoxel dephasing occurs. When the maximum time between 180° pulses was used (48 ms), changes in blood T_2 from about 250 ms with a %HbO_2 (oxygen saturation of hemoglobin) of 100 to about 25 ms with a %HbO_2 of 30 were measured at 1.5 Tesla (105). In a study by Thulborn et al. (97) no change in the T_1 of whole blood was observed (at 182.4 MHz) upon a change in oxygenation. In that paper, it is suggested that the primary mechanism of relaxation change is related to diffusion or exchange of spins through susceptibility–induced gradients in the vicinity of the red blood cells and not to modulation of the proton–electron dipolar coupling.

It is also useful to note that, when the red blood cells are lysed, reducing the compartment size further, a greatly reduced sensitivity of blood T2 to blood oxygenation changes is observed (97), illustrating that, when field perturburtations (already in the fast exchange regime) are reduced further in size, less phase coherence is lost. Models developed in the literature, specifically describing effects on T2 by blood oxygenation changes have been confirmed by these observations (99, 100, 131). Oxygenation–dependent susceptibility effects have been used clinically in the detection of cerebral hemorrhage (102, 106).

Recent experiments by Hoppel et al. (107) helped to confirm, by comparing relative relaxation rates upon changes in oxygenation of whole blood, that these signal changes could be described as arising from within the fast exchange regime. These experiments show a $\Delta R2^*/\Delta R2$ ratio of about 1.5, demonstrating close agreement with the exchange regime model and simulations. In suspensions of various size microspheres containing Dy(DTPA), changes in relaxation rates also have shown agreement with the models (124, 126). The effects in this regime have been simulated (116, 117, 120, 121, 123, 124, 126-128, 131) and analytic expressions for the perturber induced changes in relaxation rates have also been derived (118, 119).

In the slow exchange regime, the magnetic field experienced by any spin can be approximated as a linear gradient or, in the extreme case, an off-resonance static field. This exchange regime would apply to situations where magnetic field gradients are created at large interfaces of tissues having susceptibility differences (e.g. bone, air, tissue), or in the space surrounding large vessels or trabecular structure. Because of the large spatial scale of the frequency offset, spin diffusion in an echo time would be a relatively insignificant factor.

The effects of off resonance effects near large interfaces of materials having different susceptibilities, have been characterized and imaged (129, 132-136). Dephasing effects created by susceptibility–induced gradients in the vicinity of bone trabecular structure and generalized structures have been modeled (137-142), and experimentally studied (143, 144). The R2* of bone was found to be proportional the trabecular density (143, 144). A decrease in R2* with age and with osteoporosis was also demonstrated (143). Given a change in trabecular density, the change in R2 was not perceptible, while the change in R2* was pronounced (144). The gradients induced in the vicinity of the trabecular structure, which contribute to a large R2' effect, are also likely to be the reason why bone is brighter in spin–echo images having similar parameters as gradient–echo images. All dephasing effects that occur are refocussed, when using a spin-echo sequence, by the 180° because no significant irreversible diffusion related dephasing occurs. These slow exchange regime effects have been also modeled in the context of susceptibility differences between lung tissue and air (145).

Ogawa et al. (146, 147) first observed and compared the relative oxygenation related changes in gradient–echo and spin–echo signal in the vicinity of large (radius > 50 μm) vessels. The gradient–echo signal changes were more pronounced and extensive than the spin–echo changes. The bulk susceptibility effects due to blood oxygenation changes *inside* of the large vessels are close to the fast exchange regime, as described above (because of the 2.5 μm radius red blood cells), but the susceptibility effects *outside* of the vessels are in the slow exchange regime, due to bulk susceptibility differences between intravascular whole blood and extravascular tissue creating magnetic field gradients that extend beyond the vessel wall.

Because the assumption is made, in the slow exchange regime, that spins either diffuse through linear gradients or experience a shifted resonance frequency, analytic expressions for these effects on decay rate have been derived (118, 140). The effects have also been simulated (116, 123, 124, 126-128, 141, 147). The dependence of relaxation rate change upon induced frequency shift has been found to be linear (140).

In the intermediate exchange regime, diffusing spins neither completely experience nor minutely sample the complicated gradients induced by the field perturbers. Analytic solutions are difficult to derive due to the large spatial heterogeneity of the induced field gradients. Therefore numerical simulation methods are required. These have included Monte Carlo techniques (111, 118, 119, 121, 122), and deterministic methods (128, 130).

The dephasing effects of spins in the vicinity of much of the human micro-vasculature, which has vessels ranging in radius from 2.5 μm in capillaries to 100 μm in pial vessels (19, 148), have been described as being within the intermediate exchange regime (107, 112-114, 116, 123, 124, 126-128, 130). Simulations have demonstrated that, given a change in the susceptibility–induced gradients within this regime, $\Delta R2$ is only slightly less than $\Delta R2^*$. In most studies performed in which relaxation rate changes were measured during alterations in blood oxygenation or bolus injections of paramagnetic contrast agents, ratios of $\Delta R2^*/\Delta R2$ in averaged regions of cortex have been within the range of about 3.7 to 4.1 for blood oxygenation changes and within the range of 3.6 to 3.8 for injections of paramagnetic contrast agents (107). These results have suggest that the dephasing effects caused by intravascular agents within the cerebral vasculature, can be described by intermediate exchange regime. It is likely that the most correct assumption is that the effects on spin dephasing, in a typical voxel in the

human cerebral vasculature, arise from all three regimes. The average effects of these regimes, as observed in the selected regions where the measurements were made, show an intermediate exchange regime effect. The magnetization dependence of the intermediate exchange effect is between linear and quadratic.

In general, the goals of understanding significant variables underlying these intrinsic signal changes include the desire for correlation, quantification, and artifact-removal, so that fMRI may become a more robust and useful tool so that more physiological information may be obtained more reliably.

The general models described above provide a starting point by which experimental results and simulations can be compared. In chapters 7, and 8, intrinsic changes in relative relaxation rates (R2 and R2*) that locally occur with brain activation are studied. These changes are compared with a model that is developed in chapter 6. The difficulty with this particular modeling problem is that the number of potentially significant unknowns is large. Details of predominant vascular scale, vessel geometry, oxygenation during rest and activation, hematocrit, proton dynamics, and hemodynamic control mechanisms are not known. Chapter 6 includes an analysis of these potentially significant variables that can contribute to activation–induced transverse relaxation rate changes.

1.3 HUMAN BRAIN ACTIVATION OBSERVED WITH MRI

Before the onset of MRI methods that entailed observation of intrinsic signal changes corresponding to brain activation–related hemodynamic changes, several MR techniques, using exogenous contrast were developed to

map several hemodynamic factors. The measurement of brain perfusion, in animals, has been made with diffusible contrast agents which include $CH^{19}F_3$ (149), D_2O (150), and $H_2^{17}O$ water (151, 152). The lack of sensitivity, high cost, and high toxicity of these techniques have prevented their use in humans.

Rosen et al. (112, 114) and Belliveau et al. (153) introduced a method to utilize susceptibility contrast produced by intravascular paramagnetic contrast agents and the high speed imaging capabilities of EPI to create maps of human cerebral blood volume (CBV). A bolus of paramagnetic contrast agent is injected and T_2 or T_2^* – weighted images are obtained at the rate of about one image per second. As the contrast agent passes through the microvasculature, susceptibility gradients (magnetic field distortions) are produced. These gradients cause an intravoxel dephasing of extravascular proton spins, resulting in a transient signal attenuation. The signal makes use of the T_2^* and T_2 shortening effect of intravascular paramagnetic contrast agents to create quantitative maps of human cerebral blood volume. Spin–echo sequences (T_2 - weighted) are generally used because of their exclusive sensitivity to smaller paramagnetic compartments such as capillaries, which are more homogeneously distributed than larger vessels, and therefore a more precise indicator of relative blood volumes between tissue types and between healthy and pathological tissue. The signal attenuation is linearly proportional to the concentration of the contrast agent (112, 114, 126, 153), which, in turn, is a function of blood volume. The extravascular amplification effect of the induced gradients, described above, is most readily demonstrated by the fact that, in tissue that has approximately 5% intravascular space, a 50% transient drop in signal is typically observed (27).

Ultrafast MRI techniques such as echo-planar imaging, (EPI) (68, 154, 155), and fast low angle shot, (FLASH) (156, 157), have allowed for the

observation of these transient signal intensity changes. Relative blood volume maps are calculated by a several step process that involves integrating the logarithm of the signal change during the first pass of contrast agent bolus (112, 114, 153). Clinical trials are underway in the testing of this technique for its utility in detecting regions of compromised blood flow due to stroke or tumors (158).

In 1991, an MRI method, using intravascular paramagnetic contrast agents, for imaging of human brain *activation* was introduced by Belliveau et al. (27, 158, 159). It was based on the understanding that, during neuronal activation, a localized increase in blood volume in the vicinity of the activated region is observed (26, 28, 29). The technique involves the creation of two cerebral blood volume maps by the above described method. Voxel-wise subtraction of a blood volume map created during a resting state (darkness) from a map created during an active state (photic stimulation) allowed for mapping of blood volume changes in the visual cortex caused by the task. During photic stimulation, localized increases in blood volume of 32 ± 10 % were detected in the visual cortex.

For the first time, hemodynamic changes accompanying brain activation were observed using MRI. Among the advantages of this technique are the high spatial resolution of MRI, the ability to register activation maps onto high resolution MR images obtained in the same session, the relative rapidity with which the maps are created, and the high sensitivity in detecting blood volume changes – allowing for single subject studies. The primary limitation of this technique is its invasiveness, which stems from the need for repeated injections of Gd(DTPA), which is has a that is limited by the federal drug administration.

The use MRI for the completely non–invasive assessment of brain activation was first demonstrated in August of 1991, at the 10'th Annual Society of Magnetic Resonance in Medicine meeting (160). In this plenary lecture, Dr. Brady stunned the audience, including myself, with a demonstration of a photic stimulation experiment initiated and carried out by Dr. Ken Kwong. An increase in MRI signal, using T2*-weighted gradient–echo EPI, occurred in activated visual cortex regions within seconds of photic stimulation onset. Similar results, using T1-weighted inversion recovery (IR) EPI at 1.5 Tesla (161), T2*-weighted gradient–echo EPI at 1.0 Tesla (162) and 1.5 Tesla (161, 163), and T2*-weighted FLASH at 4 Tesla (164) were subsequently reported in March of 1992 at the 10'th annual Society of Magnetic Resonance Imaging meeting in New York.

A working model constructed to explain these observations was that an increase in neuronal activity caused local vasodilatation which, in turn, caused and increase in blood flow (1, 3, 8-25). This increase in blood flow resulted in a local excess of oxygenated hemoglobin beyond the metabolic need, thus reducing the proportion of paramagnetic deoxyhemoglobin in the vasculature. This hemodynamic phenomenon was previously suggested by studies using other techniques (29-31), and only later came to the attention of MR investigators attempting to explain these localized activation–induced MR signal increases. A reduction in deoxyhemoglobin in the vasculature causes a reduction in susceptibility differences in the vicinity of veins, and red blood cells within veins, thereby causing an increase in spin coherence (increase in T2 and T2*), and therefore an increase in signal in T2* and T2 –weighted sequences. The model used to explain the signal changes observed with T1 weighted sequences was based on work of Detre et al. (85). The increase in flow causes an increase in apparent T1 of brain tissue by changing

the rate of longitudinal magnetization exchange between flowing with static spins, therefore causing an increase in signal with the use of T1-weighted sequences.

Figure 1.5 summarizes the working model that details the events that occur to cause activation–induced signal changes in flow-weighted and susceptibility-weighted sequences.
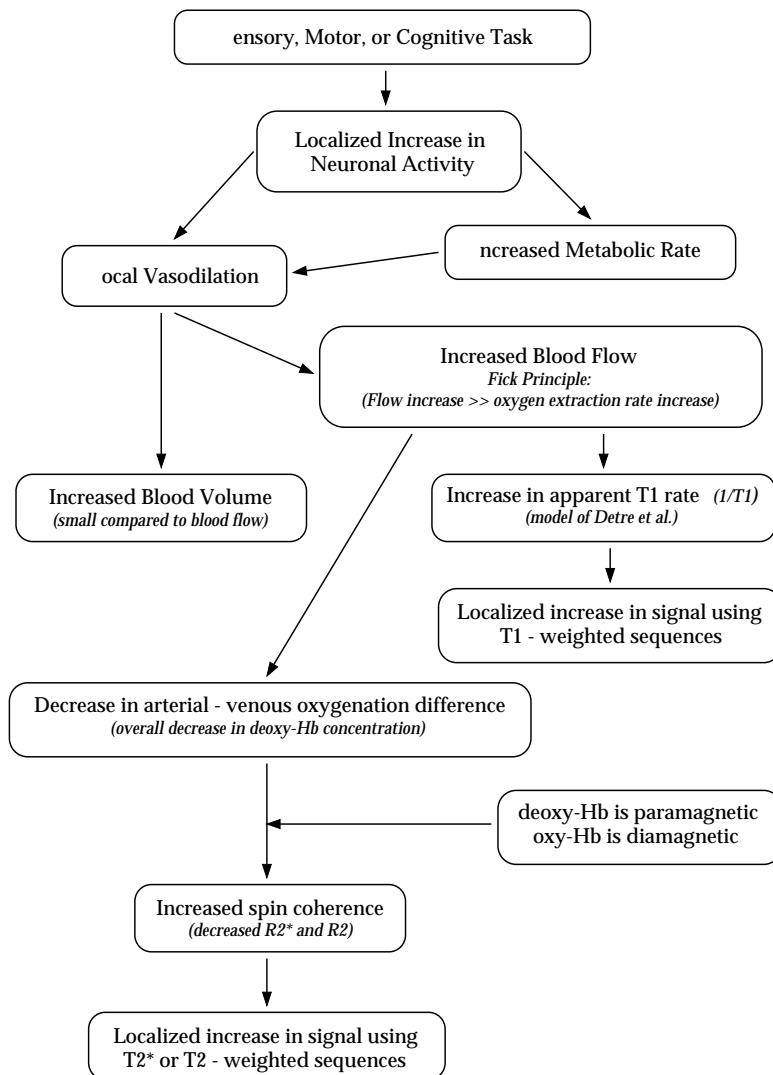
Figure 1.5: Flow chart of hemodynamic events that contribute to activation–induced MR signal changes.

At the same SMRI meeting as mentioned above, preliminary results were also presented which compared the relative R2 and R2' changes that occurred in human and rabbit brain upon oxygenation changes (165). Also, preliminary results were presented which described blood oxygenation effects in locally ischemic cat (166) and rat (167) brain.

At the time of the SMRI presentations, the previously mentioned dependence of blood T2 on oxygenation had been more completely established (97-107). Also, the nature of gradient–echo and spin–echo signal in the vicinity of large vessels on blood oxygenation had been since been published (146, 147). The dependence of gradient–echo signal on blood oxygenation in perfused tissue, where no vessels were discernible, had also been published by Ogawa et al. (168), Turner et al. (169), and Hoppel et al. (170). Also, Blood Oxygenation Level Dependent contrast had been previously coined BOLD contrast by Ogawa et al. (168) in 1990.

In July of 1992, the first papers were published which used MRI for the completely non–invasive detection of human brain activation (171-173). Regions in the primary visual cortex (171, 172) and motor cortex (171, 173), activated by visual stimulation and finger movement, respectively, were observed. Maps of brain activation were created in two manners. In the first manner, voxel-wise subtraction of an image or average of images obtained during the "resting" state from an image or average of images obtained during an "active" state was performed, therefore highlighting regions of signal change (171, 172). In the second manner, voxel-wise calculation of the temporal correlation between the time response of each voxel and an ideal, time shifted response to the activation timing was performed (173).

1.4 CURRENT FUNCTIONAL MRI RESEARCH

The most widely used fMRI technique for the non–invasive mapping of human brain activity is currently by gradient–echo sequences using BOLD contrast. The reasons for this are that gradient–echo EPI techniques have demonstrated higher functional contrast than spin–echo EPI techniques, and higher temporal resolution and functional contrast than inversion–recovery EPI techniques. Gradient–echo BOLD contrast is also most easily implemented by high speed multi–shot non–EPI techniques.

Since the initial breakthrough of fMRI, a substantial amount of research around the world has been devoted to its further development. This work can be divided into 3 overlapping and interdependent categories which include: 1) functional contrast mechanisms, 2) imaging platform development, which includes the development of new pulse-sequences and post–processing techniques, and 3) applications in neuroscience, psychiatry, pharmacology, physiology, and neurosurgery.

Contrast Mechanism Research

Research performed to characterize the details of the fMRI contrast mechanisms has been motivated by the desire to correlate the magnitude, spatial extent, and timing of the observed MR signal changes with the underlying magnitude, extent, and timing of neuronal activation. While it is generally accepted that MR signal changes are transduced through neuronally–induced hemodynamic changes, the following two relationships are not clear: a) the relationship between the degree, timing and extent of *neuronal activation* and the degree and extent of the induced *hemodynamic*

changes, and b) the relationship between the degree, timing and extent of *induced hemodynamic* changes and the degree, timing and extent of the MR *signal changes.*

The difficulty in activation–induced signal change contrast mechanism research is that the *actual* location, magnitude, and timing of neuronal activation is imprecisely known. In general, contrast mechanism studies have involved well controlled modulation of many potentially significant parameters. By parameter modulation and subsequent comparison with an ever–growing model which includes MR physics, cerebral physiology, and neurology, a large amount of convergent information about the relative contributions to MR signal change has been and continues to be obtained.

Research strategies that have led to a more complete understanding of fMRI contrast mechanisms have included: a) characterization of the dependence of the magnitude, timing, and spatial extent of activation - induced signal changes upon MR parameters such as TE (172, 174-181), TI (when using inversion–recovery sequences sensitive to flow) (89), flip angle (182), B_O (172, 178, 183-185), slice thickness and resolution (177, 186-188), outer volume saturation (189), and diffusion weighting (190-193) and pulse–sequence (spin–echo vs. gradient–echo) (174-176, 178-181) b) characterization of the resting signal, and activation - induced signal changes, during different degrees of hemodynamic stress (i.e. hypercapnia, hypoxia, ischemia, apnea, anoxia, hypercarbia) (146, 147, 168, 169, 194-199) or during different degrees of neuronal activity (visual flicker rate, finger tapping rate, syllable presentation rate) (171, 200-204). c) comparison of signal locations with macroscopic vessel maps (178, 186, 187, 205, 206) or neuronal activation maps (207-209) and d) modeling of activation - induced MR signal changes based upon knowledge of MR physics and human cerebral physiology (116-118, 124, 126-128, 210) .

While an introduction covering the details of all of the above mentioned experiments would be unnecessarily long, the salient details of a few will be discussed so that the context of the work presented in the thesis can be established. Important experiments that demonstrated that the observed MR signal changes (when using susceptibility–weighted sequences) were actually caused by changes in R2 and R2*, and not changes in other MR variables, such as proton density, diffusion, T1, or motion involved the characterization of the TE dependence of the signal change. A change in transverse relaxation rate (R2 or R2*) would cause an increase in fractional signal change with an increase in TE. This increase in fractional signal change with TE was demonstrated by several groups (172, 174-181).

To demonstrate that the R2* and R2 changes originate from changes in compartmentalized magnetic susceptibility, and not from intrinsic transverse relaxation rate changes related to other mechanisms, the fractional signal change at a given echo time and, more generally, the relaxation rate changes have been compared across pulse sequences and field strengths. As described in the above section on magnetic susceptibility, a change in the susceptibility difference between two materials has different effects upon spin–echo and gradient–echo sequences depending upon the size of the field perturber, the diffusion coefficient of spins in the vicinity of the perturber, and the variation in the Larmor frequency caused by the perturber. A change in intrinsic transverse relaxation rate would always cause equal changes in R2* and R2, but a change in transverse relaxation rate caused by a compartmentalized susceptibility mechanism causes *different* changes in R2* and R2 depending upon the variables mentioned above (perturber size, susceptibility, and diffusion coefficient). Most studies the made these comparisons have given results that show that the average ratio of R2*/R2 is in the range of 1.5 to 4.5

(174-176, 179, 180), but also shows much variation over space (176, 180), suggesting spatial variation in vessel architecture. The results of one study has demonstrated a much larger ratio of 9.3 (211). In general, several other studies have confirmed that gradient–echo sequences show a greater activation–induced signal change than spin–echo sequences (212, 213). Also, the maximum absolute difference in signal change has been observed to occur at the $T2^*$ and $T2$ of the tissue (174-176, 178-180). As previously mentioned, studies comparing relaxation rate changes caused by hemodynamic stresses in animals (107, 165), and bolus injection of contrast agents in animals (107) have observed similar relaxation rate ratios to those mentioned above.

With an increase in applied field strength, the induced differences in the Larmor frequency, created by $\Delta\chi$ between materials, increases, therefore increasing the rate of intravoxel dephasing. Given a constant activation–induced change in susceptibility, the percent signal change at a given TE and the relaxation rate change should increase as field strength increases. Comparisons of activation–induced fractional signal changes and relaxation rate changes made across field strengths, keeping all other variables constant, have demonstrated such an increase (183-185), providing further support of the hypothesized susceptibility–related mechanism of contrast. Studies which demonstrate the TE dependence of the signal changes and the relative $R2$ and $R2^*$ relaxation rate changes across field strengths are described in chapters 7 and 8.

The studies mentioned above have been fundamental in providing strong evidence that a primary mechanism of functional contrast, when using spin–echo or gradient–echo sequences, is by changes in susceptibility due to changes in the oxygen saturation of hemoglobin in the vasculature.

Recent investigations have suggested that combined contributions of both susceptibility and non–susceptibility related mechanism for activation–induced signal changes are present in most pulse-sequences (180, 182, 189, 214). Studies at low field strengths of 0.15 T have suggested that the *relative* contributions of susceptibility and non-susceptibility–related mechanisms are related to field strength (215) and additionally suggest that stimulus correlated motion may contribute to activation–induced signal changes (216).

The two types of non-susceptibility related activation–induced signal changes that have been described are "inflow" and "perfusion." The precise difference between what is known as "inflow" and "perfusion-related" signal changes is not entirely clear, but, in general, "perfusion-related" suggests exchange of inflowing and outflowing magnetization with static, in plane magnetization that generally occurs in capillaries, and "inflow-related" suggests time-of-flight effects from rapidly in-flowing, unsaturated spins generally in larger vessels entering the RF saturated plane without exchanging magnetization.

Work has been performed in separating inflow-related signal changes from susceptibility–related signal changes (182, 189, 214). Using FLASH sequences that incorporate short TR values and large flip angles, reduction in activation–induced signal changes has been observed to correspond with either reduction of the flip angle (182) or with application of outer volume saturation (189). Reduction in the inflow effect can also simply achieved by lengthening the TR. Differences in magnetization between inflowing spins and the steady state magnetization of the slice are reduced by these manipulations, therefore reducing activation–induced modulation of in-flow rate on signal changes. Among the work presented in chapter 9 is an analysis of the effects on the magnitude and distribution of activation–induced signal

changes by a) application of volume saturation and b) varying TR and flip angle.

In chapter 7, a study is presented which uses a combined spin–echo and gradient–echo, (SEGE-EPI), time course collection of images in which the TE values were systematically varied so that time courses of highly sampled $R2^*$ and $R2$ curves were obtained in a temporally and spatially registered manner (180). By linear interpolation of the $R2^*$ and $R2$ curves through the TE=0 intercept, non–susceptibility–related changes could be monitored simultaneously with the relative susceptibility–related changes. This study shows that the non-susceptibility related signal increase is minimal yet present during activation, demonstrating a small amount of flow-related contribution. Nevertheless, at a TR of 1 sec, susceptibility–related signal changes dominate in $T2^*$ or $T2$ - weighted sequences.

A technique introduced for quantifying microvascular blood flow, independent of oxygenation changes, has involved MR detection of inflowing labeled arterial water spins. With this technique, first demonstrated in animals (85, 217), blood water flowing to the brain is RF saturated outside the imaging plane (usually in the neck region). Because of the relatively long blood T1 times, saturated spins are able to maintain much of their magnetization state as they travel into the plane of interest and exchange, at the capillary level, longitudinal magnetization with bulk water in the brain. The resulting regional concentration of labeled spins in tissue is a function of regional tissue blood flow.

Methods have also been developed to observe flow changes independently of oxygenation changes. Kwong et al. (171) used an inversion recovery sequence to characterize activation–induced "perfusion" changes. A recently developed extension of a flow imaging technique that was first

demonstrated with animals (85, 217), named "echo-planar imaging with signal targeting and alternating RF" (EPISTAR) (89, 90), has been used to map both macrovascular and microvascular flow in humans. This technique is based on the idea of subtracting two image data sets that are identical except for differences in longitudinal magnetization arising from inflowing spins. One data set is acquired after a remote 180° pulse is applied to invert the inflowing arterial spins. The first set is subtracted from a second data set, acquired without the inversion pulse, thus giving a difference map which is a function of flow.

This technique can be made sensitive to different levels of flow velocity by varying the delay time between the inversion pulse and the image acquisition. Maps of arterial flow are created using a relatively short inversion pulse – acquisition delay time of 400 ms. Maps of microvascular flow and exchange processes are created using an inversion pulse - acquisition delay time of 1000 ms or more. After the 1000 ms waiting period, tagged magnetization is either within the capillary bed or in the extravascular space in the immediate vicinity of capillaries.

With the use of flow map subtraction, changes in blood flow corresponding to hemodynamic stress or brain activation can be mapped. The two maps can then be subtracted to reveal regions where changes in flow have occurred (89, 90).

In general, the issue of flow vs. oxygenation contrast entails understanding how much of the signal change (or what areas) are related primarily to oxygenation changes and how much is due to non-susceptibility related flow changes. It is essentially a question of localization, interpretation, and ultimately, quantification. In chapter 3, regions of activation–induced signal changes are compared, keeping all else constant, across 5 different pulse

sequences having weighting varied from flow to susceptibility of various sized compartments. These preliminary studies show that foci and distributions of activation–induced signal changes, while generally similar, do not completely overlap, suggesting that flow/oxygenation coupling and predominant susceptibility perturber sizes (e.g. vessel sizes) differ regionally.

Studies have also been performed attempting to characterize whether the activation–induced signal changes in susceptibility weighted sequences arise from predominantly intravascular or extravascular spins (190, 191, 193, 218). These studies, first performed by Song et al. (191) involved application of diffusion weighting or velocity nulling gradients and subsequent observation of the effects on the activation–induced signal changes (190, 191, 193). With the application of diffusion gradients, the activation–induced signal change are strongly damped, suggesting that the activation–induced signal change arises predominantly from rapidly moving blood in larger vessels, and/or diffusion coefficients in the vicinity of intermediate sized vessels is actually larger than expected.

In a more general case, the goal of separation of intravascular large vessel effects from extravascular effects has been pursued using other techniques that will be described more extensively in the fMRI platform development section of the introduction.

Studies have been performed to observe the activation–induced signal change dependence on other pulse sequence parameters. Activation–induced signal change magnitude and distribution dependencies on voxel volume have also been studied (177, 186, 188). The results of another study in chapter 9 show that, as voxel volume is decreased, the size of activated regions decreases and the average percent change in active regions is increased,

suggesting significant partial volume averaging of active with inactive regions at lower resolutions.

The response characteristics of the BOLD signal enhancement with neuronal activation have also been characterized. The latency of the activation–induced BOLD signal change in primary cortical regions can be reported in several manners. These include a) the time at which the signal first deviates from its steady state (off or on), b) the time at which the signal begins to reach a new steady state (off or on), or c) a fit of the increase or decrease to a function which approximates the response behavior.

DeYoe et al. (219) reported a time of about 2 sec. for the signal to deviate outside of 10% of its initial state (on or off). They also reported a shorter time to reach an "on" state than an "off" state. They reported a latency of approximately 5 to 8 seconds from stimulus onset to 90% maximum, and 5 to 9 seconds from stimulus cessation to 10% above baseline. Fitting the onset latency to a single exponential, Kwong et al. (171) have reported an onset rate constant of 4.4 ± 2.2 sec. using gradient–echo sequences weighting and a slightly higher rate constant of 8.9 ± 2.8 sec using inversion recovery sequences, supposedly sensitive to flow changes. Other initial fMRI studies have reported similar temporal characteristics (181, 203, 204, 220, 221). In chapter 4, fMRI signal change dynamics are characterized in detail.

Differences in latency over space have been studied. Latency differences (across active regions) on the order of a second have been observed in visual cortex regions (205, 206), and auditory cortex regions (204, 222). Differences in latencies have been observed to correlate with regions that also show coherent phase shifts (205, 206). Because of the generally random orientations of small blood vessels, oxygenation changes in microvessels (capillaries) would cause signal magnitude changes, but only minute net phase shifts, due

to the fact that heterogeneity of the gradient orientations from multiple vessels in each voxel would tend to cancel each other out. A large vessel, likely taking up most of the volume in a voxel and having a single orientation, would be much more likely to cause coherent phase shifts upon changes in blood oxygenation within the vessel (205, 223, 224). Because of these effects, it has been hypothesized that larger draining veins "downstream" from regions of activation–induced vasodilatation, and not delayed or networked neuronal activity, may be the predominant cause of these latency differences. It has been suggested that these phase shifts also cause subvoxel spatial shifts (especially for EPI) that can contribute to large positive or negative signal changes, especially in the presence of large signal intensity gradients over space (224). A comparison in latencies between different regions in the brain is presented in chapter 4.

It has been suggested (225) that some latency differences may, in fact, have a neuronal or cognitive origin. In one study, a region hypothesized to be involved with higher cognitive processing of auditory stimuli has shown a longer activation latency (225). This region did not correspond, anatomically, with "downstream" vessel flow.

The dependence of the signal change magnitude on the activation duration has also been studied (181, 203, 204, 220-222, 226, 227). During extended durations of activation, the signal enhancement has been observed to remain elevated (203, 204), but also has been observed to decrease (228). Reasons for the differences between studies may be due to differences in pulse sequence parameters and/or differences in the stimulation used. The stimulation that caused the signal to remain elevated may be a) causing less habituation or neuronal fatigue and/or b) selectively activating neurons that do not increase as much in oxidative metabolic rate. Also, activation

34

durations of 3 sec (181) to 0.5 (203, 204) and 0.3 (221) sec. caused, after a delay of 2 sec, signal enhancement that remained elevated until about 8 sec. following task cessation (203, 204). Generally, the longer the duration of activation, up to 5 seconds, the greater the magnitude of signal change. This study is also presented in chapter 4.

The dependence of the signal change magnitude on the rate at which the subject alternates from "active" to "resting" states ("on/off" switching rate) has also been studied (203, 204). In these studies, it was found that the relative induced signal in the motor cortex does not show a significant decrease until the "on/off" switching frequency is higher than 0.06 Hz. Above 0.13 Hz, the hemodynamic response does not follow the activation timing, and becomes saturated in the "on" state. The hemodynamic response appears to behave essentially like a low pass filter in the transduction of neuronal firing. The details of this study are also presented in chapter 4.

Occasional observations that are less understood include an undershoot in signal after activation (171, 229), and a decrease in the baseline value after the first activation period during cyclic activation (227). The origin of occasionally observed decreases(224, 230) in the signal during activation may be neuronal, hemodynamic, or incidental upon vessel architecture and image contrast.

Some studies, using functional spectroscopy (observation of the water peak) (231), have claimed to see a decrease in signal just prior to the normally observed signal increase (232). In addition, an imaging study at 4T has observed an initial decrease in signal just prior to the signal increase in a small proportion of voxels. A possible reason for this observation is that significant oxygen extraction, occurring immediately ($\approx$ 0.5 sec) after

activation, precedes the subsequent overabundance of oxygenation that is delivered (233).

Since the work of Turner et al. (169), and Ogawa et al. (146, 147, 168), and the preliminary work of Hoppel et al. (170), Kwong et al. (165), and De Crespigny et al. (166, 167), many studies have further explored the dependence of MR signal on physiological perturbations such as hypoxia, hypercapnia, apnea, hypercarbia, and anoxia to further characterize the mechanisms of endogenous susceptibility contrast, and to potentially apply these contrast mechanisms to assessment of vascular patency.

Only a few animal studies have demonstrated signal changes with stimulation (234-236), possibly due to non-optimal stimulation methods or effects of anesthetics. Many animal studies have been performed using chemically induced neuronal firing (195, 237, 238) or global hemodynamic stresses. The dependence of susceptibility-weighted signal on blood oxygenation in the rat brain has been further characterized by Ogawa et al. (195). In a recent rat study, acetazolamide and hypercarbia-induced changes in $R2^*$, but not diffusion coefficient or $R2$ were observed (239). Work has also been performed, on cats, by de Crespigny et al. (196, 197), demonstrating the ability to distinguish perfused from unperfused tissue using endogenous BOLD contrast. As mentioned, work by Hoppel et al. (107) in rabbits, and canines undergoing anoxia, hypercapnia, and contrast agent injections, has compared relative relaxation changes during these stresses.

In a recent study by Jezzard et al. (240) MR signal changes and blood oxygenation changes in the cat brain were simultaneously observed during periods of apnea, anoxia, and hypercapnia by the use of three independent methods: measurement of arterial blood oxygen saturation, measurement of venous blood oxygen saturation, and by the use of a method of

spectrophotometric reflectance directly from brain tissue (30). Not only were excellent correlations made between the measurements and the MR signal changes, but effects of blood volume changes on MR signal change were also characterized.

Work involving the use of non-susceptibility weighted sequences in the detection of global flow changes has been sparse. Hypercapnia-induced flow changes have been observed by Moseley et al. (241) using inversion-recovery fast spin echo (IR-FSE) techniques, sensitive to flow-induced T1 changes. With the use of EPISTAR (88), global signal changes corresponding to inhalation of CO_2 and injections of acetazolamide were observed as well.

In human studies involving hemodynamic stesses, gradient–echo MR signal changes have been observed during apnea (242, 243), hypoxia (198), and hypercapnia (198, 244). These studies are in general agreement with the animal studies. Regions of high signal change magnitude are observed to correspond to regions of high blood volume.

In one study (198), presented in chapter 10, the effects of hypoxia (inhalation of 12% O_2) and hypercapnia (inhalation of 5% CO_2) on resting and activation -induced signal changes were observed. This study had two purposes. The first was to help in deciphering the mechanisms by which activation–induced signal changes came about by the observation of competitive or synergistic effects of the hemodynamic stresses. The second was to compare on a pixel-wise basis, the signal changes in the motor cortex with finger tapping (with no stress) and during the stresses (with no finger tapping) to determine significant factors which contribute to signal change foci and distributions. Several findings were made. One was that hypercapnia (strong vasodilator) damped activation–induced signal changes while increasing overall signal. Hypoxia (weak vasodilator) caused minimal

damping of the activation–induced signal changes, while decreasing overall signal. The absolute magnitudes of signal changes during the stresses and those during finger tapping were well correlated on a voxel-wise basis, suggesting that regional differences in activation–induced change magnitude are primarily caused by spatial variations in vessel architecture, and not underlying neuronal activation. A method is outlined by which regional signal differences due to differences in vessel architecture are removed from neuro-functional MR images by normalization to a mask created by a global hypercapnic stress.

Studies have been performed which have observed modulation of MR signal by modulation of neuronal activation either by varying visual stimuli flicker frequency (171, 221), finger tapping rate (201, 203, 204), or syllable presentation rate (200, 245). The goal of these studies was to test if graded activation was able to elicit a graded MR signal changes. The hypothesis was that, if each presentation of a stimulus results in a similar set of neuronal events, then the integrated neuronal response, and possibly the resulting blood flow response, will be a function of the number of stimuli presented per unit time (225). Regional cerebral blood flow in the visual cortex was shown in a PET study to have a positive, linear dependence on the rate of stimulation up to approximately 8 Hz (23, 24), identical to that found using fMRI (171, 221). Effects of auditory word presentation rate have been demonstrated in some but not all active areas of the temporal lobe auditory cortex using PET (246).

Lastly, in the effort to further characterize the origin of activation–induced MR signal changes, several more sophisticated models describing activation–induced BOLD contrast have been put forward since the initial models of Ogawa et al. (127) and Weisskoff et al. (126). Most of these models

have addressed the question of BOLD contrast mechanisms from the MR perspective, using Monte Carlo techniques (124, 126, 127, 190, 192, 210), convolution of spin probability density function with magnetization maps (128, 130) and analytical approaches assuming the slow exchange regime (118) or fast exchange regime (119). In several of these models, considerations have been made of volume changes, flow-induced oxygenation changes, capillary recruitment, vessel radii changes, and oxygenation changes of blood in different sized vessels, and intravascular effects. The results have shown general qualitative agreement with experimental findings.

An attempt to explain the reason for the apparently paradoxical increase in oxygenation with activation has been put forth by Buxton et al. (247). This model suggests that an increase in blood oxygenation, happens so that, given an increase in oxidative metabolic rate and assuming that oxygen delivery to tissue is diffusion limited and capillary recruitment does not take place, oxygen supply at the most remote metabolocally active cell is maintained.

All of these models are likely to be naive from a physiological and MR viewpoint. Many significant variables are potentially left out. In chapter 6, a discussion is carried out on considerations made in the modeling methods, along with the deterministic diffusion modeling methodology and results(128, 130).

Platforms for fMRI

The first fMRI experiments were carried out using EPI at 1.0 Tesla (162), 1.5 Tesla (160, 161, 163, 171, 173, 183), 2.0 Tesla (181), 3.0 Tesla (184), and 4 Tesla (183), and fast multi-shot gradient-recalled imaging techniques at 1.5 Tesla

(208, 248-250), 2 Tesla (177, 227) and 4 Tesla (172). In general, fMRI platforms have varied considerably in terms of field strength, pulse–sequence, gradient and RF coil hardware, and post-processing methods. Development of fMRI platforms has been in the directions of 1) increased functional contrast to noise ratio, 2) improved post–processing techniques 3) increased temporal resolution, 4) increased spatial resolution, and 5) increased brain coverage. The optimal tradeoffs of these sometimes mutually exclusive directions have generally been determined by the goals and constraints of the specific applications. The fMRI hardware and pulse–sequence platform used for the work in this dissertation is described in chapter 2, and the post processing methods are described in chapter 5. A brief overview of fMRI platform development, covering each of the five categories listed above, is given.

Functional contrast to noise ratio

The functional contrast to noise ratio (fCNR) is a measure of the ability to detect of activation–induced signal changes in space (as opposed to non–activated regions) and time (as opposed resting state signal). The most fundamental of needs in fMRI is a high fCNR. When using gradient–echo sequences, maximal susceptibility contrast is achieved by using TE ≈ T2* (178, 179, 181). BOLD contrast also increases with field strength (116, 117, 124, 126, 127, 172, 178, 183-185, 251, 252). However, performance of BOLD contrast–weighted EPI is more difficult, but still possible, at higher field strengths (183-185, 233, 253), because of its sensitivity to off–resonance effects.

Functional contrast also benefits from an increase in the signal to noise ratio (SNR). Several simple strategies are commonly used in fMRI to increase SNR. The use a relatively long TR, 90° flip angle, and temporal averaging of several hundred images can be performed in an experimentally feasible

amount of time using EPI. Also, with EPI, the long data acquisition times that are typically used (40 to 80 ms) in order to achieve acceptable spatial resolution are approximately equal to the T2* of gray matter – optimal from the point of view of maximizing the SNR.

The SNR can also be increased by the use of region - selective RF coils. Optimally, the RF coil should couple only to the regions that are being studied - such as surface coils over the occipital pole in visual stimulation studies. However, it is becoming increasingly desirable for most functional imaging studies to observe the entire brain. For whole brain studies, whole head quadrature coils commonly used clinically for head and neck imaging are sub-optimal because they couple to other tissue that is not of interest, causing an unnecessary increase in noise. Recently, quadrature whole - brain transmit - receive coils that couple predominantly to the brain have been implemented for fMRI (254, 255).

To increase fCNR, it is also desirable to reduce the noise and artifacts. Many of the sources of signal contamination are not from system or thermal noise, but rather from cardiac and respiration–related pulsatile motion (256-263), subject movement (216), or possibly from susceptibility variations related to spontaneous changes in flow (264, 265), or from respiration - related changes in chest cavity size which has been suggested to cause changes in B_O as far away as the head region (266).

Several pulse sequences have demonstrated reduced sensitivity to pulsatile motion effects. The stability of EPI is due to the fact that physiologic motion is "frozen" during the 40 ms acquisition time of all Fourier space (k-apace), enabling stable line to line k-space registration that remains stable during each successive image. In standard multi-shot techniques, line to line k-space registration varies due to pulsatile motion during data acquisition

which takes on the order of seconds to minutes, thus causing non-repeatable low frequency ghosting variations across each image, and adding significantly to the noise (259, 261, 263).

In EPI, gross displacement generally manifests itself as misregistration at edges, and as some isolated signal propagation in the phase encode direction from rapidly flowing or moving spins (267). Asymmetric spin-echo EPI, with similar contrast weighting as gradient-echo EPI, has demonstrated a reduction of artifacts caused by rapidly flowing and pulsatile spins because the 180° pulse does not refocus rapidly flowing spins (268).

Of non-EPI techniques, multi–shot spiral-scan sequences (259, 261), sequences employing oblique motion compensation (269), and sequences employing navigator pulses (270), have all demonstrated more signal stability over time and less artifactual signal changes than standard 2D or 3D – FT multishot techniques.

Post-processing techniques

The challenge of accurately determining regions of significant activation from fMRI data is non–trivial and has yet to be solved. Some of the developments addressing this issue include: a) the development of accurate and robust motion correction (271, 272) and/or suppression methods, b) the determination of the noise distribution (257, 258, 273), c) the determination of the temporal (274) and spatial (275) correlation of activation-induced MR signal changes, and of baseline MR signal, d) the characterization or assessment of the temporal behavior or shape of activation-induced signal changes (200, 219, 222, 225, 273), and e) the characterization of how the above-mentioned factors vary in time, space (205, 206), across tasks (219, 225, 273,

276), and with different pulse sequence parameters (171, 176, 178, 188, 257, 258, 268).

The flexibility and rapid image sampling capabilities of EPI can aid in the reduction of various manifestations of motion artifacts, including pulsatile, sudden, gradual, and stimulus correlated motion. Because the rapid image sampling rate of EPI allows for critical sampling of many problematic noise frequencies, these frequencies can be rejected using simple band stop filters (121). With single–shot EPI, motion effects above the time scale of 40 ms to 100 ms are virtually eliminated. Slower motion that occurs between each shot (100 ms - 6 sec) cause primarily misregistration. These effects can be reduced by the use of currently available image registration algorithms (271, 272). In 2DFT techniques, motion on this time scale is manifested not only as misregistration but also as ghosting that is propagated throughout the image (259, 261). With EPI, very slow motion, manifested as a drift in the time course, is reduced simply by the ability to collect a larger number of on/off activation cycles (40 sec. per cycle) in a single time course whose duration is less than the time during which signal drift manifests itself (5 on/off cycles in under 4 minutes). Stimulus correlated motion also generally has a different signal change latency than activation–induced signal changes. This fact allows differentiation, using a sampling rate of at least 1 image every 2 sec, of stimulus correlated signal changes from activation-induced signal changes, based simply on the different temporal "shapes."

Many post processing techniques have been implemented to increase fCNR and to reliably obtain maps of significant activation–induced signal changes. The statistical methods include the use of z-scores (277), ANOVA (278), split - half t-test (259, 279), Kolmogrov-Smirnov (280), cluster analysis (281). and other non-parametric tests (282). Pre-statistical methods have

included cross-correlation analysis (220), auto-correlation analysis (283), phase-tagging (205, 206, 273, 284-286), principle component analysis (287), time-frequency analysis (288), and power-spectrum analysis (220, 257, 258, 289). As of yet, choice of a reference function for cross – correlation and related methods remains a user intensive task. Chapter 5 presents these cross-correlation functional image formation techniques which are also used throughout the rest of this dissertation.

Recently, a real–time updatable cross–correlation algorithm has been implemented (290). This algorithm allows images to be continually obtained until the quality of the functional correlation images (updated at a rate of one per second) is suitable. Rapid acquisition of echo-planar images can allow for rapid feedback in functional image quality and subsequently, a high degree of experimental tuning, and an increase in the rate of successful fMRI experiments per imaging session. Consider an investigation where 10 different stimuli are to be applied in 10 runs. If there is only a 5% chance that 1 run will be bad, then there is a $0.95^{10} = 60\%$ chance that all 10 will be good. If you need all 10 to be good, the experiment is thrown out 40% of the time. Immediate feedback can alleviate this problem.

One can also imagine performing experiments whose procedure depends on knowing results from just-completed runs. For clinical use, one can be sure, if using the real–time fMRI technique, that good results will be present before the patient leaves the scanner.

Currently, no one best post–processing technique exists or may ever exist because of the large number of changing variables which contribute to the activation–induced signal change, and underlying noise. The best types of post processing methods will likely be those that are adaptable to variations

(across scans, regions, tasks, and pulse-sequences) in signal and noise characteristics.

Temporal resolution

Because the fMRI signal change is based on hemodynamic changes, the practical upper limit on functional temporal resolution is determined by fCNR and by the variation of the hemodynamic response latency in space and in time (202, 203, 205, 206, 219, 222, 225). These variations may be due to differences in neuronal activation characteristics across tasks (219, 225) or to differences in vessel size (205, 206), or to other physiologic or anatomical differences. The upper functional temporal resolution is ultimately determined by the activation–induced signal change latencies and by the "spread" or variation in latencies, caused by hemodynamic factors, that may occur in time and in space.

Given the variations of the hemodynamic response, the upper limit of temporal resolution discrimination has been empirically determined to be on the order of one second (222), or less (291). With greater specificity for hemodynamic scale, higher fCNR, and innovative experimental design, this upper limit on temporal resolution may be increased even further.

Generally, high temporal resolution is not critical to fMRI, but it is useful to acquire images a reasonable amount of time for post processing purposes, and so that system drift or subject motion is kept at a minimum. It is also useful to sample rapidly for the observation of unique dynamic characteristics of the time course signal that may occur.

Other than FLASH and single–shot EPI, several pulse sequence strategies have been applied to perform fast fMRI in the presence of limitations on gradient slew rate and magnitude. High temporal resolution

fMRI techniques developed for use with conventional gradients include multi-shot FLASH (172, 177, 182, 186, 187, 189, 208, 214, 227, 248-250), turbo-FLASH (292), low resolution EPI (181, 293), multi-shot or interleaved EPI (294), echo-shifted flash (295, 296), reduced encoding imaging with generalized series reconstruction (RIGR) (297), spiral scan (206, 261), functional spectroscopy (231), keyhole imaging (298), TE-interlaced gradient–echo (299), fast spin–echo (300), and circular Fourier space BURST, (SUNBURST) (301). Several sequences, including EPI, interleaved EPI, and SUNBURST have been used to more rapidly create images having higher spatial resolutions using a localized gradient coil designed for rapid gradient switching in all three axis and having gradients of ≈ 2 G/cm in all three planes (302).

Spatial resolution

The upper limit on functional spatial resolution, similar to the limit of temporal resolution, is likely determined not by MRI resolution limits but by the hemodynamics through which neuronal activation is transduced. Evidence from *in vivo* high resolution optical imaging of the activation of ocular dominance columns (30-32) suggests that blood oxygenation changes occur on a spatial scale of less than 0.5 mm. Nevertheless, MR evidence exists which suggests that the blood oxygenation increases that occur upon brain activation may be more extensive than the actual activated regions (182, 186, 187, 205, 206, 212). In other words, it is possible that, while the local oxygenation may be regulated on a submillimeter scale, the subsequent changes in oxygenation may occur on a larger scale due to a "spill-over" effect.

To achieve the goal of high spatial resolution fMRI a high fCNR and reduced signal contribution from draining veins is necessary. Greater hemodynamic specificity, accomplished by proper pulse sequence choice,

innovative activation protocol design, or proper interpretation of signal change latency, may allow for greater functional spatial resolution. If the contribution to activation–induced signal changes from larger collecting veins or arteries can be easily identified and/or eliminated, then, not only will the confidence in brain activation localization increase, but also the upper limits of spatial resolution will be determined by scanner resolution and fCNR rather than variations in vessel architecture.

Currently, voxel volumes as low as 1.2 microliters have been obtained by functional FLASH techniques at 4T (251), and experiments specifically devoted to probing the upper limits of functional spatial resolution, using spiral scan techniques, have shown that fMRI can reveal activity localized to patches of cortex having a size of about 1.35 mm (284). These studies and others, carried out using EPI (273, 285, 286) and multi-shot spiral scanning (284, 303), have observed a close tracking of MR signal change as the location of visual stimuli was varied.

To complement the studies probing the upper spatial resolution limits, several studies have been performed comparing fMRI foci of activation with those of other brain imaging methods, including MEG (207, 226), PET (304). EEG (226), and presurgical electrical stimulation (209, 305). Generally, a high degree of spatial correlation has been observed. Recently, a promising method by which patient's EEG readings may be recorded during a fMRI session has been developed (306), potentially allowing MR constraint of the inverse problem, therefore enabling the combination high functional spatial resolution of fMRI with high temporal resolution of EEG (226).

Techniques used to characterize functional contrast mechanisms of fMRI have also been directly implemented to improve the reliability and interpretability of fMRI data sets by enabling identification and/or

elimination of artifactual signal changes arising from larger "downstream" vessels. High resolution T2*-weighted imaging at high fields allows identification of veins as dark lines or spots (178) caused by the originally observed BOLD effect in the vicinity of large vessels in rats (146). Incidentally, these regions typically appear as regions having the highest activation–induced signal changes. Also, these regions have a higher signal variance over time.

In addition, high resolution angiography (186, 187) or flow weighted images (214) in combination with high resolution fMRI has also allowed identification of signal changes originating from larger vessels.

As discussed above, spin–echo techniques are less sensitive to extravascular large vessel effects of oxygenation changes because macroscopic ΔB_O are refocussed and diffusing spins sample only a small ΔB_O created by the relatively shallow extravascular gradients. Instead, spin–echo sequences are sensitive to changes in B_O on a smaller scale such as a red blood cell or a capillary. Functional images have been created using spin–echo sequences (174-176, 179, 180, 184, 212, 213). These images contain supposedly less extravascular macrovascular contributions (but do contain intravascular red blood cell effects). Therefore regions showing enhancement either have voxels which contain capillaries or voxels which contain very large vessels in which the intravascular red blood cell effect contributes.

As discussed, in FLASH techniques that use a relatively short TR, inflow related artifactual (large vessel) signal changes have been reduced by reduction of the excitation flip angle (182), outer volume saturation (189), and centric reordering of phase-encoding steps (178, 214). Outer volume saturation not only reduces signal changes related to non-BOLD-related inflow effects, but also to intravascular BOLD-related signal changes arising from spins

within the inflowing veins. Outer volume saturation does not reduce extravascular BOLD effects from the nulled out inflowing spins. The effects of outer volume spin saturation on activation–induced signal changes obtained with gradient–echo EPI at longer TR values are studied in chapter 9.

Application of bi-polar gradients can selectively null signal based upon spin velocity. Preliminary data suggests that intravascular BOLD effects from vessels containing rapidly flowing spins are removed with the use of bipolar gradients (190, 191, 193, 218).

One of the studies in chapter 10, which is a characterization of the effects of hypercapnia and hypoxia on resting and activated MR signal, shows that the relative variations in activation–induced signal changes are predominantly caused by spatial differences in vessel architecture, which includes pixel-wise variations in blood volume, vessel orientation, and resting oxygenation (198). Images created during activation are normalized by images created during a global hypercapnic stress. The assumption is made that hypercapnia and neuronal activation cause similar hemodynamic events; one global and the other local. Division of a "percent change during brain activation" image by a "percent change during hypercapnia" image gives a ratio map that is normalized to the signal change accompanying global vasodilatation.

Using the hypothesis that "down stream" oxygenation changes in collecting veins occur up to a second after the oxygenation changes in microvessels in the immediate vicinity of the brain parenchyma, large draining vein effects have been identified by latency differences in signal changes (205, 206). Also, coherent phase (224) shifts, upon task-activation have also been used to identify draining vein effects. Longer signal change

latencies have been observed to correlate spatially with coherent phase shifts (205).

Also, the EPISTAR technique has demonstrated the ability to selectively image activation–induced parenchymal flow changes (88) by judicious choice of TI time and inversion pulse location.

Spatial correlation of functional images with underlying anatomy is also a unique and powerful aspect of fMRI. In general, functional images are directly registered with the images used to create them, but if higher quality underlying anatomical images are desired, registration issues need to be addressed. Methods have been developed to unwarp echo-planar images (307). In addition, a method that uses spatial cross-correlation has been developed to register functional images onto high resolution data sets if necessary (248).

Brain coverage

Coverage of the entire brain is essential for many neuroscience applications which need to observe distributed networks and regions in the base of the brain. Several sequences can be used for time efficient whole brain imaging. These include multi-echo 2D FLASH (308), 3D echo-shifted flash(309), EPI (230), and SUNBURST (255). Quadrature transmit and receive coils have also been designed for high sensitivity whole brain imaging at 0.5 Tesla (185), 1.5 Tesla (254), and 3.0 Tesla (185, 255).

The base of the brain is one area that has proven problematic in fMRI. One difficulty that arises is that gradient–echo images, due to their sensitivity to macroscopic off-resonance effects, have large regions of signal dropout at the base of the brain, due to of susceptibility-induced gradients at interfaces of bone, tissue, and air. The effect of macroscopic susceptibility-induced

50

gradients on MR images has been characterized (129, 132-136). EPI techniques are more sensitive to these effects because of the generally larger voxel volumes used and the low sampling rate in the phase-encode direction. Possible solutions to this difficulty include the use of smaller voxel sizes, spin–echo sequences, and/or flow-only-sensitive inversion recovery spin–echo sequences. Focused shimming on the specific region may be a viable alternative as well.

Applications of fMRI

Several unique advantages of fMRI make it an immediately useful technique. Because the physiological contrast is endogenous, the technique is completely noninvasive, thereby lending itself to extended or repeated use in single subjects. This permits the study of long term changes such as learning or habituation, and permits many experimental manipulations to be used. In addition, the BOLD contrast to noise ratio is high enough so that significant activation–induced signal changes may be observed in a single data set in 20 seconds.

Another advantage of fMRI is the ease of registration of brain activation images with high resolution anatomical MR images. As mentioned, all brain activation images are directly registered with the images from the data set used to create them. In the same scanning session in which functional MR time course series are obtained, other pulse sequences can be used to collect high resolution, high contrast anatomical images on which the activation images can be directly overlaid after possibly some unwarping. Three dimensional brain activation data sets may also be obtained and fused directly with similar sets of high resolution anatomical images obtained

during the same session. This information can then be transformed into a common coordinate system to aid the specification of the positions of activity foci within the brain. This transformation can be helpful for intrasubject averaging, but is also helpful for combining functional *and* anatomical MR data with information from other functional imaging techniques (226).

Owing to these advantages, ease of use and accessibility of fMRI, many areas of the brain and many different tasks have already been studied. Most studies involving the development of fMRI from a contrast mechanism, pulse - sequence, and post - processing standpoint have used primary motor and visual cortex activation due to the easily elicited signal changes. Listed below are some of the applications of fMRI that have gone beyond simple finger tapping or visual stimulation. The primary auditory cortex (310-316) the cerebellum (317-319), and the primary somatosensory cortex (320, 321) have been studied using fMRI. Detailed mapping of regions activated in the primary motor cortex (214, 322-324) and visual cortex (273, 279, 284-286, 303, 325-330) has been performed. Tootell et al. have mapped area MT (285), and observed transient activation in MT/V5 illicited by a the illusion of motion following stimulation by radially moving concentric rings (329).

Subcortical activity has also been observed during visual stimulation (283) and finger movement (230). Activity elicited in the gustatory cortex has also been mapped (331). Other studies using fMRI have observed organizational differences related to handedness (332). Activation changes during motor task learning have been observed in the primary motor cortex (333) and cerebellum (334, 335).

Cognitive studies in normal subjects have included word generation (336-338), mental imagery (339, 340), mental rehearsal of motor tasks and complex motor control (230, 341, 342), speech perception (310, 312, 313, 343,

344), single word semantic processing (312, 313, 343, 344), working memory (345, 346), spatial memory (347), and visual recall (348). Studies have also observed modulation of activity by attention modulation (273).

Studies have also been performed involving specific pathologies. Abnormal connectivity of the visual pathways in human albinos has been demonstrated (349). Changes in organization in the sensorimotor area after brain injury has been observed (350). One study has demonstrated larger fMRI signal changes, on the average, in schizophrenic patients (351). The ability to localize seizure activity has also been demonstrated by fMRI (352). In addition, preliminary data demonstrating the effects of drugs on brain activation have been presented (353). Activity associated with obsessive–compulsive behavior has also been observed (354, 355)

The immediate potential for clinical application is currently being explored. "Essential" areas of the sensory and motor cortex as well as language centers have been mapped using both fMRI and electrical stimulation techniques (209, 305). Activity foci observed across the two methods have shown a high spatial correlation, demonstrating the potential for fMRI to compliment or replace the invasive technique in the identification of cortical regions which should be avoided during surgery. Along, this avenue of research, fMRI has developed the ability to reliably identify the hemisphere where language functions reside, potentially complimenting or replacing the Wada test (hemisphere specific application of an anesthetic amobarbital) for language localization that is also currently used prior to surgery (356).

Several review articles and chapters on fMRI techniques and applications are currently available (202, 275, 311, 357-365). In general, the fMRI research avenues: contrast mechanism research, functional imaging platform development, and applications are progressing in a manner that is

both complimentary and synergistic. Because of the rigor and creativity of the investigators in this newly created and interdisciplinary field and, in part, because of the robustness of EPI as a functional imaging tool, fMRI is progressing at an accelerating pace.

1.5 OVERVIEW OF THE WORK TO BE PRESENTED

The work in this dissertation involves three general aspects of fMRI. The first aspect is directed towards the further uncovering of the connections between neuronal activation, hemodynamic changes, and NMR signal changes, summarized in Figure 1.6. This involves: a) (left side of figure) modulation of locations, dynamics, and task intensities and observing the behavior of the MR signal, and b) (right side of figure) modulation of MR contrast weightings and observation of relative locations, timings, and magnitudes of the MR signal changes. Also, a biophysical model is created and compared with measured components ($\Delta R2^*$ and $\Delta R2$) of the activation–induced MR signal across field strengths and across different regions in the brain. Modulation of cerebral hemodynamics by physiological stresses is also performed.
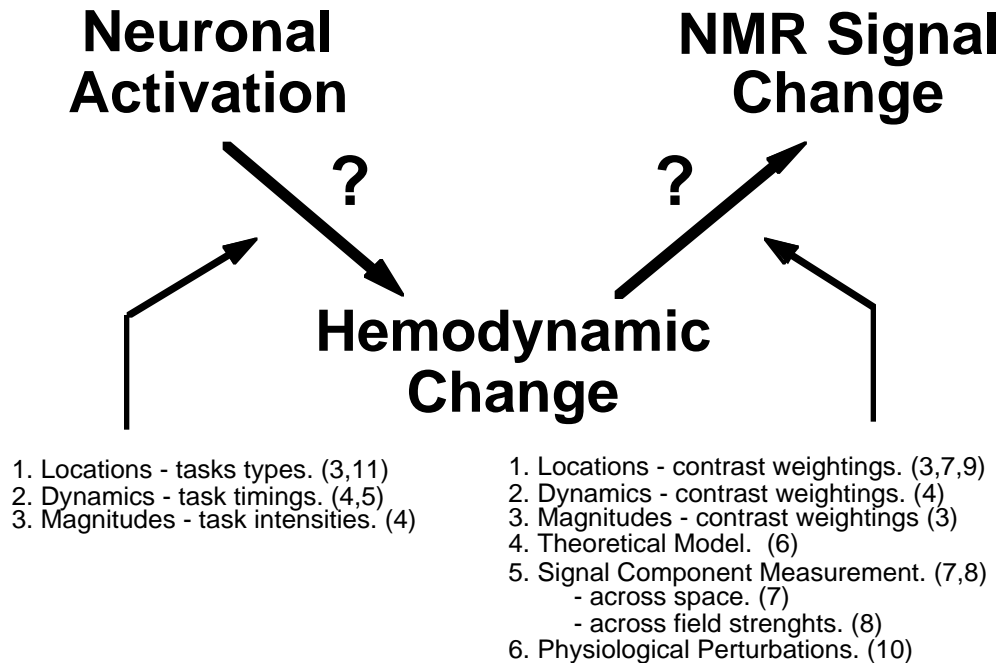
Neuronal Activation

NMR Signal Change

? ?

Hemodynamic Change

1. Locations - tasks types. (3,11)
2. Dynamics - task timings. (4,5)
3. Magnitudes - task intensities. (4)

1. Locations - contrast weightings. (3,7,9)
2. Dynamics - contrast weightings. (4)
3. Magnitudes - contrast weightings (3)
4. Theoretical Model. (6)
5. Signal Component Measurement. (7,8)
   - across space. (7)
   - across field strenghts. (8)
6. Physiological Perturbations. (10)

Figure 1.6: Schematic illustration of the two primary relationships in fMRI that are incompletely understood and the work presented in this dissertation (chapters are in parenthesis).

The second aspect of this dissertation involved the development and testing of post processing methods tailored to fMRI signal changes. The third aspect of this dissertation involved the presentation of applications of the developed techniques. Below is a summary of the chapters.

Chapter 2 consists of two methods sections. The first is a description of the hardware and pulse sequences used. The second is a description of strategies to uncover fundamentals of fMRI signal dynamics and contrast mechanisms.

Chapter 3 consists of an analysis of the locations of activation–induced signal changes across different MR contrast weightings.

Chapter 4 consists of an analysis of the dynamics of the activation–induced signal changes across different MR contrast weightings. The signal change latency is compared between proximate regions and between activation types. In addition, MR signal behavior is observed over different activation timings and intensities.

Chapter 5 consists of the development and description of post–processing methods that are applied to fMRI time course data sets to obtain images highlighting regions of temporally correlated signal changes.

Chapter 6 consists of a description and development of a mathematical model describing BOLD contrast. Using a method that incorporates repeated convolution with a smoothing function and phase rotation to simulate spin diffusion in the presence of magnetic field perturbers, the dependencies of the absolute and relative changes in transverse relaxation rates ($\Delta R2^*$ and $\Delta R2$) on biophysical and physiologic parameters are explored.

Chapter 7 consists of a comparison of activation induced relaxation rate changes and longitudinal magnetization changes. Several aspects of gradient–echo and spin–echo sequences are compared with each other, and the results are compared with the model presented in chapter 6.

Chapter 8 consists of a comparison of $\Delta R2^*$, $\Delta R2$ and functional contrast to noise at 0.5 Tesla, 1.5 Tesla, and 3.0 Tesla. Results are compared with the model in chapter 6.

Chapter 9 consists of an analysis of the dependence of several aspects of activation–induced signal changes on several MR parameters. The dependence of activated volume and functional contrast to noise on voxel volume is observed. The dependence of activation location and magnitude

on outer volume saturation is observed. The dependence of signal change magnitude and noise upon TR and flip angle is also observed.

Chapter 10 consists of observations of the effects of hypercapnia and hypoxia on resting MR signal and activation–induced MR signal changes. Also, a method for removal of differences in signal caused by spatial variation of vessel architecture is presented.

Chapter 11 consists of specific applications of fMRI to neuroscience research. Activation elicited during tasks which include reading words listening to spoken words, and silently generating words is demonstrated. Also, whole brain and extended time course studies are performed during simple, complex, and mental rehearsal of complex finger movements.

Chapter 12 consists of a summary and discussion regarding the future development of fMRI.

CHAPTER 2

METHODS

In this chapter, an overview is presented of the hardware, software, analysis procedures, and basic experimental procedures in this dissertation. All studies were performed on healthy human volunteers.

2.1 HARDWARE

Three MR scanners were used. A GE Signa 1.5 Tesla (63.87 MHz) 100 cm bore scanner was used for most of the experiments presented. Also, a GE Signa 0.5 Tesla (21.29 MHz) 100 cm bore scanner and a Bruker Medspec 3T/60 3.0 Tesla (127.74 MHz) 60 cm bore scanner were used in the study presented in chapter 10, which describes the characterization of the dependency of activation–induced MR signal changes on B_O.

Single–shot echo–planar imaging (EPI), the ultrafast imaging technique used in all the studies, requires strong and rapidly switched gradients. These requirements in gradient strength and switching speed were satisfied using a three–axis, balanced torque head gradient–coil.

Figure 2.1: Three–axis balanced torque gradient coil used in all studies. The low inductance coil, designed to create strong and rapidly switched gradients, allows echo–planar imaging without the requirement of additional gradient amplifiers.

The gradient coil, shown in Figure 2.1, was designed and constructed by E. C. Wong (302). The method of design was conjugate gradient descent (366). It has an inner diameter of 30 cm and a length of 37 cm. The gradient fields were optimized for a region that covered the human brain (cylinder of diameter 18.75 cm and length 16.5 cm.) The maximum gradient strengths (G/cm@100 Amps) are 2.272 for X, 2.336 for Y, and 2.487 for Z. As a result of the extremely low coil inductance (0.149 mH for X, 0.174 mH for Y, and 0.076 mH for Z), the minimum rise time from zero amplitude to full scale is approximately 50 μs.

In all the studies performed, high–sensitivity transmit–receive quadrature endcapped birdcage radio–frequency (RF) coils, shown in Figure 2.2 and 2.3, were used in order to maximize the filling factor in the limited

space of the gradient coil. A copper RF shield was used to isolate the RF fields from the gradient coil. Also, all coils also have a circular endcap that fits snugly within the RF shield on the inner surface of the gradient coil. The endcap is cut into wedges that are bridged by capacitors to block gradient eddy currents while providing an RF current path. The endring is also similarly bridged by a capacitor. Also, for the 3.0 Tesla and 1.5 Tesla coils, $\lambda/2$ cables are connected from the outer rods carrying the matching capacitors to the opposite rods to distribute the loading more symmetrically. All coils are driven symmetrically through a 90° hybrid combiner.
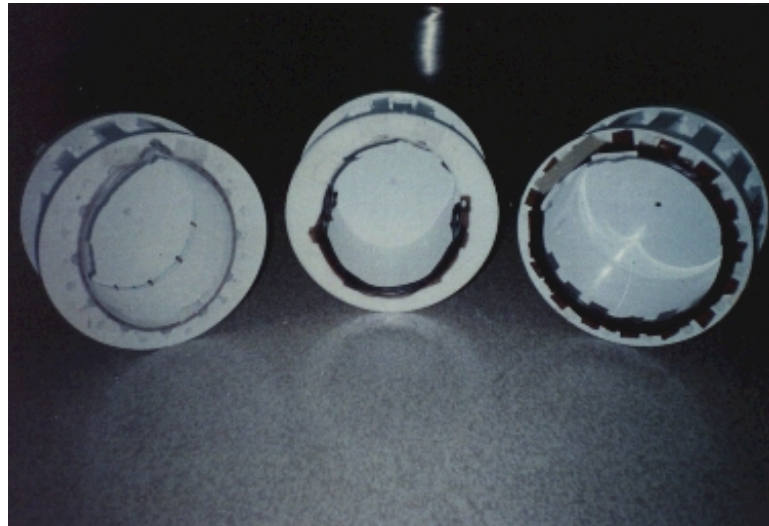
Figure 2.2: Front view of transmit–receive quadrature endcapped birdcage radio–frequency (RF) coils used in all studies. Left: Coil used at 0.5 Tesla. Middle: Coil used at 1.5 Tesla. Right: Coil used at 3.0 Tesla.
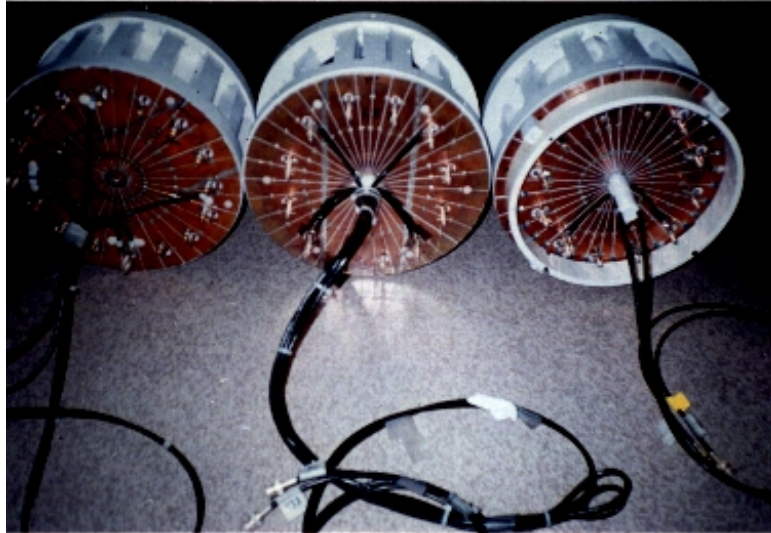
Figure 2.3: Rear view of the RF coils used. Left: Coil used at 3.0 Tesla. Middle: Coil used at 1.5 Tesla. Right: Coil used at 0.5 Tesla.

The RF coil used at 1.5 Tesla (254), is a lowpass elliptical 12 element coil having a length of 16 cm. Major and minor axis lengths are 23.0 cm and 19.0 cm respectively. The S/N improvement over a standard GE birdcage coil has been measured to be approximately 1.5 (254).

The RF coil used at 3.0 Tesla (255), is a bandpass circular and has 16 elements. It has a length of 16.5 cm. and a diameter of 23 cm.

The RF coil used at 0.5 Tesla, is a lowpass elliptical, 12 element coil having a length of 16 cm. Major and minor axis lengths are 24.0 cm and 20.0 cm respectively. One difference in this coil is that it has a notch for a subject's nose to allow more freedom of movement. When the notch is included, the major axis is 25 cm.

An apparatus, developed by E. DeYoe and J. Neitz, that presented visual stimulation triggered by a scanner–output sync pulse (219, 273, 325, 330, 362) was used for several experiments in chapter 4 that required precise

stimulus timing. Using this device, dynamic, computer graphics–based visual images were directly projected onto the subjects' retinae. The image generator was a modified Sharp XG2000U video projector driven by Cambridge Instruments VSG video graphics board installed in a personal computer. The image plane was then viewed through a custom optical system that included a wide field, magnifying eyepiece, a 45° prism, and additional objective lenses for adjusting magnification and minimizing chromatic aberration. Two sets of imaging optics were combined to provide full binocular viewing. In one study (219), monocular visual stimulation was presented.

All image reconstruction and time–course image analysis was performed on Tektronics XD88, Sun Sparcstation 10, or a Sun Sparcstation 1+ workstations. Further processing of time course data and images was performed on Macintosh Quadra 660 AV, Quadra 840 AV, or Centris 650 computers.

2.2 PULSE SEQUENCES

The general imaging procedure in all studies involved first locating the imaging plane(s) of interest with the use of conventional imaging techniques. These conventional images were generally $T2^*$–weighted gradient–recalled at steady state (GRASS) images. The motive, at this stage, was to obtain, as rapidly as possible, high resolution (256 x 256 matrix) images having sufficient contrast for differentiation of gray matter from white matter. The option then was also available to superimpose functional images, obtained using EPI during the same session, onto the higher resolution and contrast GRASS images.

In all studies, single–shot EPI was used. The EPI sequences used at 1.5 T and 0.5 T were developed by E. C. Wong, and those used at 3 T were developed by A. Jesmanowicz. All the sequences are shown at 8 x 8 resolution for illustrative clarity.

For all EPI sequences, chemical shift saturation, shown in Figure 2.4, was employed before the excitation pulse. The saturation pulse selectively excites the spins at the fat resonance frequency then the gradient in the y–plane dephases all transverse magnetization. It is important to employ fat saturation when using EPI due to its increased sensitivity to off–resonance effects. If this pulse were not used, the fat signal would appear shifted several pixels in the phase–encode direction. Also, phase correction procedure would be less effective.
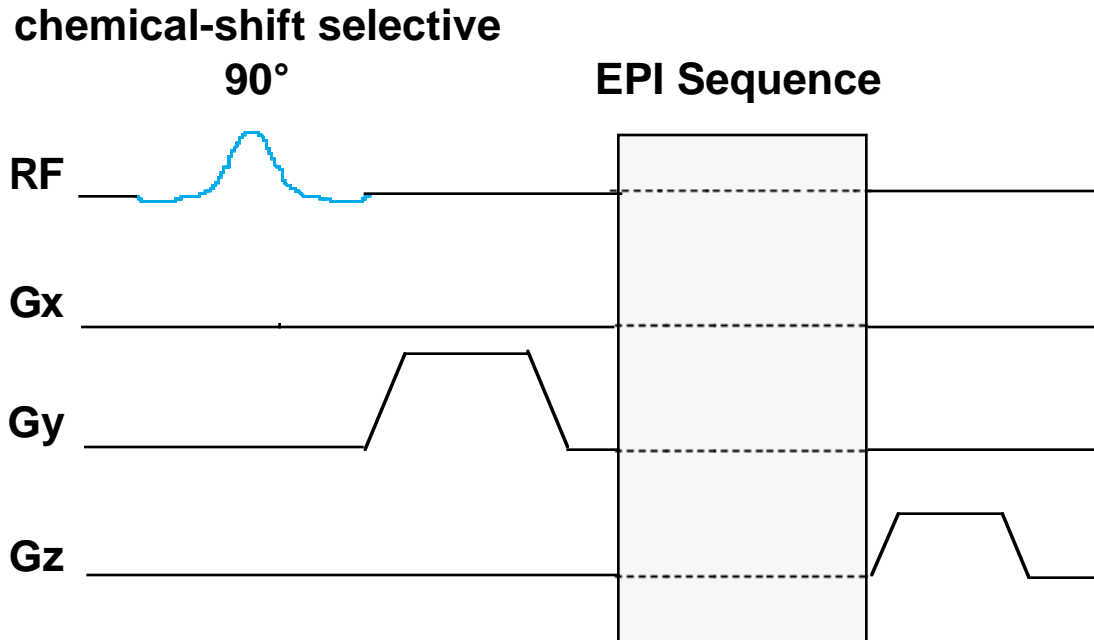
Figure 2.4: The chemical shift–saturation section of the pulse–sequence. This method is used to remove the fat signal prior to acquisition.

Data were collected at a rate of 125 kHz or 8 μs per IQ pair. For all echo–planar images, phase correction was carried out using a two–line internal reference (during which the y–gradients were turned off) for each image (367, 368).

The minimum obtainable voxel volume, given the above parameters, single–shot EPI, and full–k space reconstruction, is about 1.5 x 1.6 x 1.6 mm^3, (FOV = 16 cm, matrix size = 96 x 96), requiring a readout window length of 80 ms. Points obtained on the ramps of the oscillating gradient were not used in image formation.

In most studies presented, the matrix size is 64 x 64, the slice thickness ranges from 5 to 10 mm, and the FOV is 24 cm. This gives an in–plane voxel dimension of 3.75 x 3.75 mm^2. The readout window duration of 40 ms.

Considering that the relationship between oscillating gradient strength, Gx, field of view, FOV, and sampling time, t_S, is:

$$Gx = 1 / ((\gamma/2\pi) \text{ FOV } t_S). \qquad [2.1]$$

The maximum gradient necessary for a typical FOV of 24 cm is 1.22 G/cm. Assuming an oscillating gradient rise time from 0 to 1.22 G/cm of 56 μs, the slew rate at a distance from isocenter, or radius, r, of 9 cm (estimated radius of a human head), is given by:

$$\text{Slew rate} = (Gx_{max} \text{ r }) / \text{ rise time}_{0 \text{ to max.}} \qquad [2.2]$$

The slew rate, given these parameters, is 19.6 T/sec., which is within the FDA limits of 20 T/sec. Of course, the slew rate increases linearly with the distance from the gradient iso–center.

The EPI pulse sequences used in this dissertation include:

a) Gradient–echo EPI (GE–EPI). Shown in Figure 2.5. The readout window occurs during the free–induction decay after the initial 90° flip angle. At shorter TR values, smaller flip angles, θ, are used to optimize S/N. The optimal θ to use is given by the Ernst angle relationship:

$$\cos (\theta) = e^{-TR/T1}. \qquad [2.3]$$

At the TR values commonly used, the flip angle for brain imaging (gray matter T1 ≈ 600 ms), is very close to 90°. The effective TE occurs at the center of the readout window $k(x,y) = (0,0)$. Variation of TE causes variation in T2*–weighting. The TE generally used in most time course series, for

maximal T2*–weighting, is 40 ms (TE ≈ T2* of gray matter). T2*–weighting gives maximal intrinsic activation–induced contrast to noise values. This sequence is therefore used in post–processing development, dynamics studies, contrast mechanism studies, and applications in chapters 3 to 11.
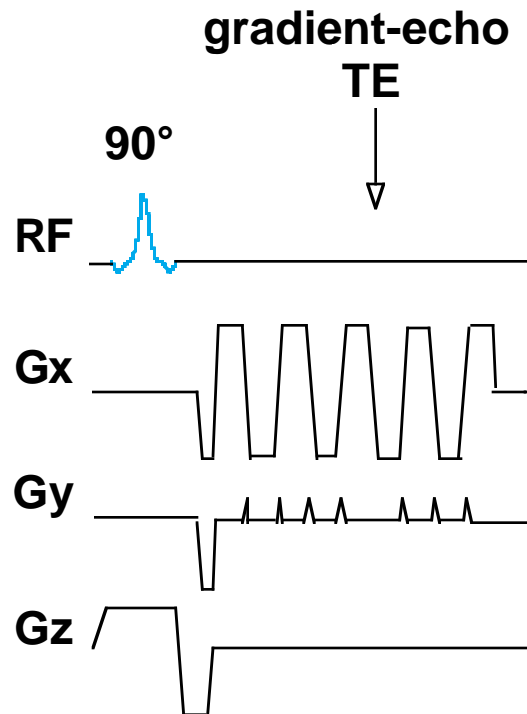

Figure 2.5 : Gradient–echo EPI.

b) Spin–echo EPI (SE–EPI). Shown in Figure 2.6. The center of the readout window and where $k(x,y) = (0,0)$ occurs at the spin–echo. Variation of TE causes variation in T2 weighting. The TE used in most time course series that maximizes T2–contrast is 110 ms (TE ≈ T2 of gray matter). This sequence was used in chapters 6, 7 and 8. The purpose was to compare activation induced signal changes with those obtained using gradient–echo sequences.
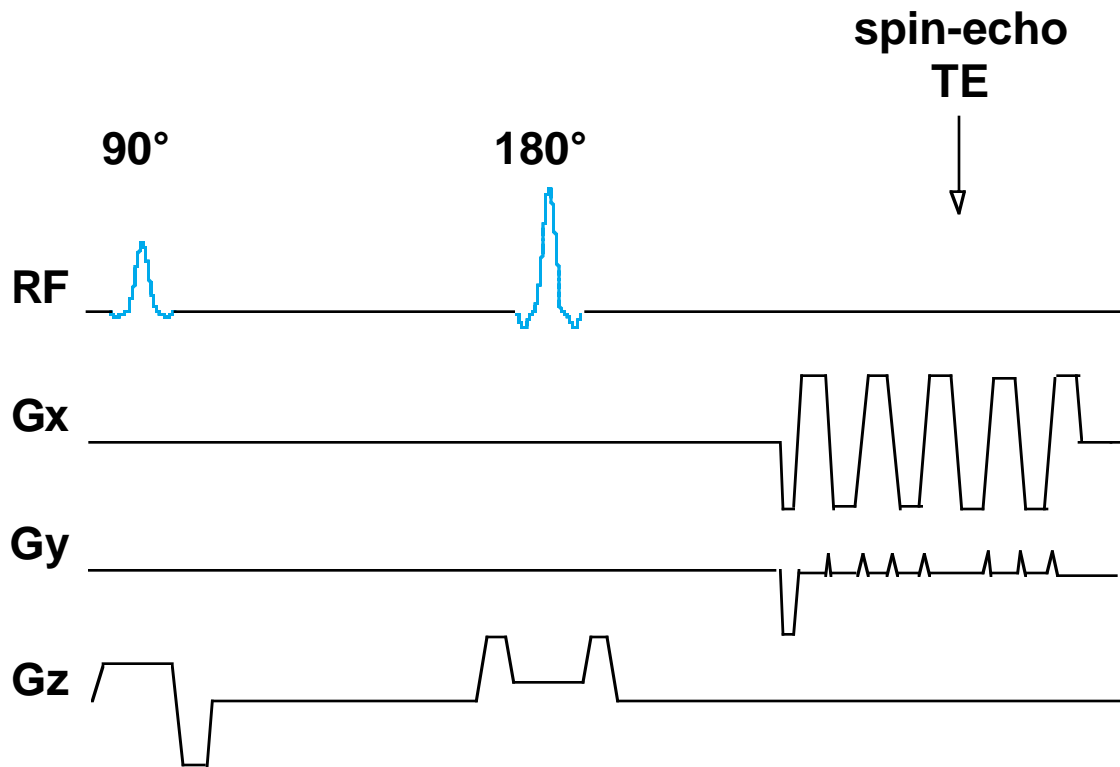
Figure 2.6 : Spin–echo EPI.

     c) Combined spin–echo and gradient–echo EPI (SEGE–EPI). Shown in Figure 2.7. Spin–echo and gradient–echo image pairs are collected in two sequential readout windows occurring during the FID and the spin–echo. This sequence was used in chapter 7 to obtain time courses of spatially and temporally registered GE and SE image pairs. Systematic incrementation of the two TE values in each sequential time course image also allowed for the simultaneous mapping of relative transverse relaxation rates (R2*, R2, and R2') and steady state magnetizations.
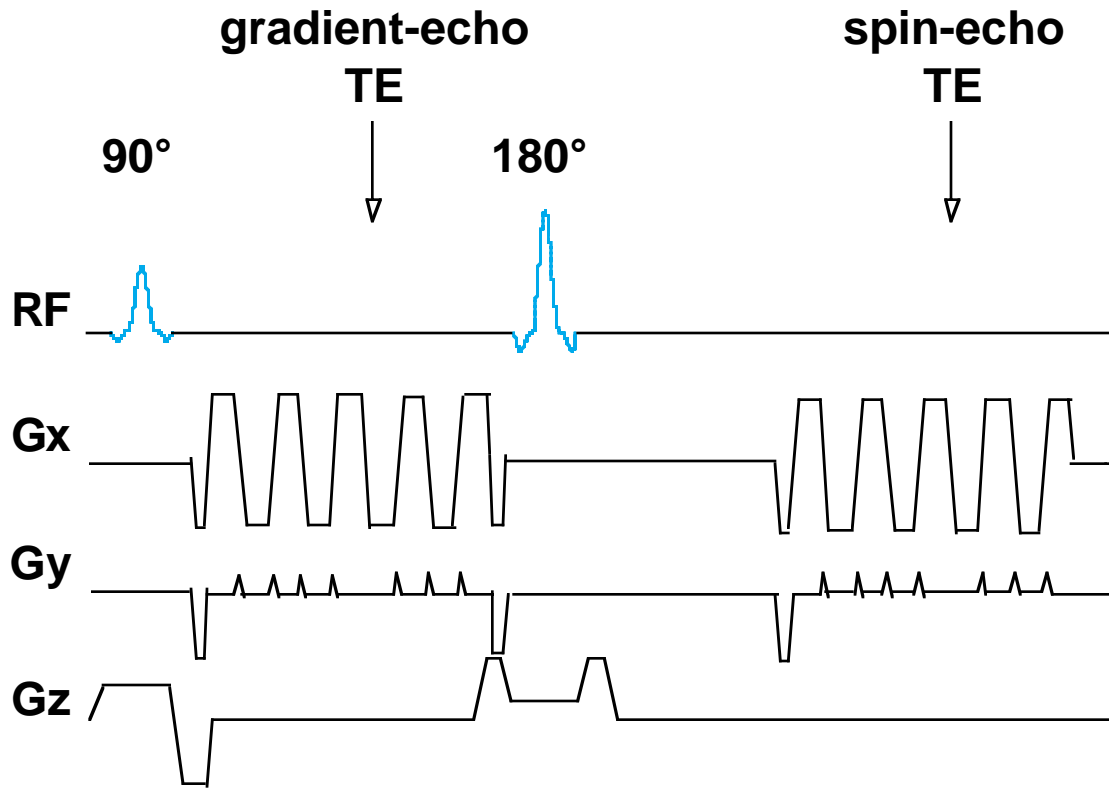
Figure 2.7 : Combined spin–echo and gradient–echo EPI.

d) Asymmetric spin–echo EPI (ASE–EPI). Shown in Figure 2.8. The center of the readout window and k(x,y) = (0,0) are shifted relative to the center of the spin–echo. The 180° pulse timing is shifted while the readout window and oscillating gradient timing are kept constant. A readout gradient offset time of τ, is created by a 180° shift of τ/2. In this manner, T2*–weighting is introduced into the images. The readout window offset time, τ, contributes the equivalent T2'–weighting as a gradient–echo image having TE = τ.
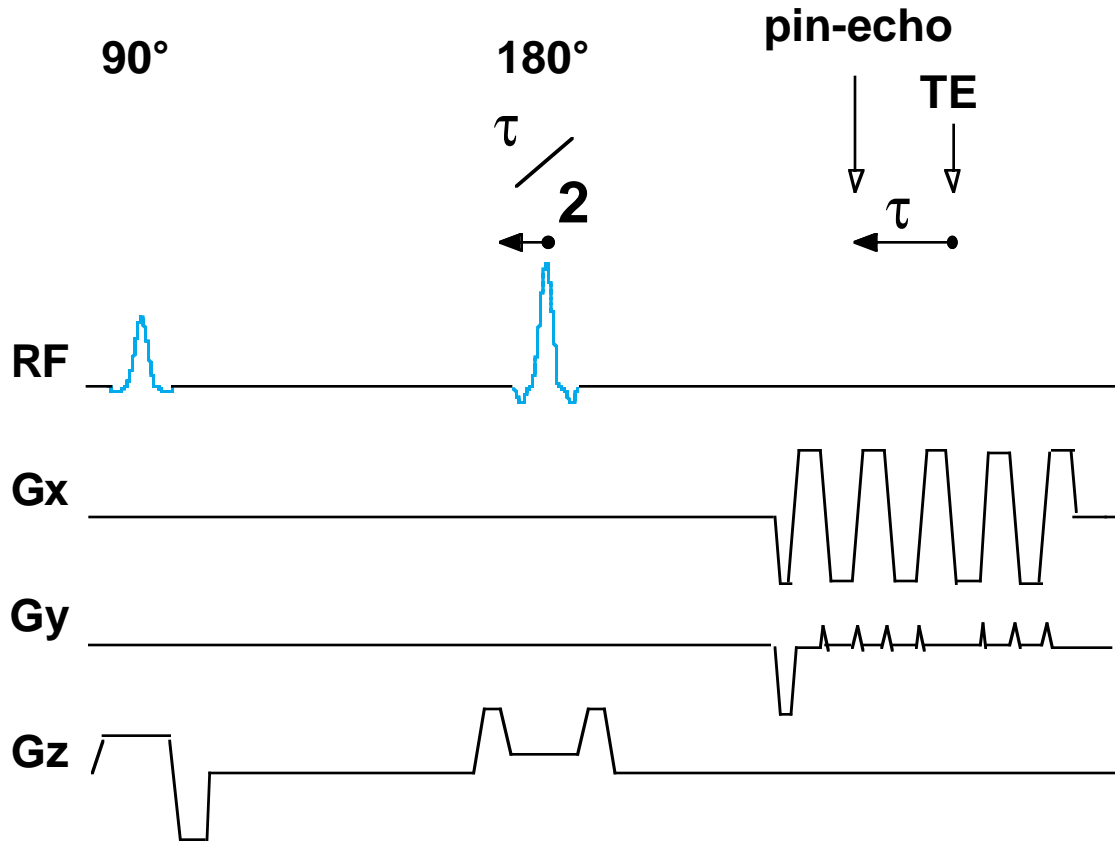
Figure 2.8 : Asymmetric spin–echo EPI.

e) Inversion recovery EPI (IR–EPI). An inversion pulse is placed prior to a spin–echo EPI sequence, therefore introducing T1–weighting into the images. The TI used in most time course series was 1200 ms. The T1–sensitivity makes this sequence more sensitive to BOLD–independent flow changes.

f) Asymmetric spin–echo inversion recovery EPI (ASE–IR–EPI). An inversion pulse is placed prior to an asymmetric spin–echo EPI pulse sequence so that T1 and T2* weighting may be simultaneously obtained in the same image.

The basic inversion–recovery sequence is shown in Figure 2.9.
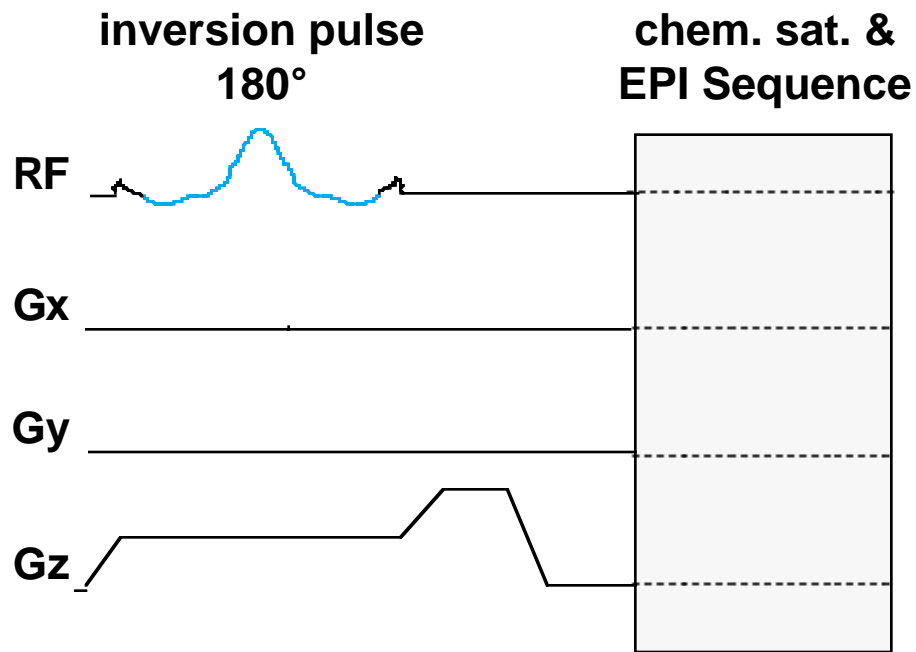
Figure 2.9 : Inversion–recovery EPI. Inversion time, TI, is the time between the inversion pulse and the 90° excitation pulse of the EPI sequence.

Sequences d, e, and f were used only in chapters 3 and 4 for a comparison of the locations and timings of activation–induced signal changes across different contrast weightings.

2.3 ANALYSIS PROCEDURES

Time course series consisting of as many as 1024 sequential single–shot echo–planar images were collected in all the studies performed. The inter–image time or TR was between 200 and 6000 ms. For most studies the TR was 1000 ms. The most controllable, repeatable, and easily localized brain activation paradigm was found to be repetitive sequential tapping of fingers

to thumb. In chapters 3 and 11 visual stimulation was also performed. In chapter 11, cognitive tasks were carried out as well. During the time course collection of images, brain activation timing was generally carried out in a repetitive "on/off" manner, allowing adequate time for the hemodynamic response to reach a steady state. Also, in chapter 10, hemodynamic stresses were applied during the time course, during which the subject either rested or performed repetitive finger tapping.

The time courses of images were always first inspected using an analysis tool, developed by E. C. Wong and A. Jesmanowicz, which displays any one image of the time course series and a matrix of signal vs. time plots corresponding to a specified square region of interest that may be moved in the image or varied in size. The next step generally involved a process by which an "ideal response," "reference waveform," or "reference vector" representing the expected signal change was chosen or synthesized. This waveform was then used in cross–correlation calculation with the "signal vs. time" response of every pixel. These post processing methods are discussed in detail in chapter 5.

The formation of images that highlighted regions demonstrating temporally correlated signal changes was a first step in subsequent analysis procedures that were carried out. All data was obtained from signal vs. time plots or from functional images.

Signal vs. Time Plots
a) Signal vs. time plot from one pixel in an activated region.
b) Signal vs. time plot from the average signal of several pixels chosen automatically from a threshold image or manually.

From this information of signal vs. time, signal difference, percent change, and relaxation rate change ($\Delta R2^{(*)}$ = -Ln(Sa/Sr)/TE), was estimated from the average, in time, of the signal during the on and off periods respectively. This type of analysis was carried out in all the studies on the Macintosh computers mentioned using Microsoft Excel, Cricket Graph, and Kalidagraph programs.

Functional Images
a) Image that displays the correlation of a chosen or synthesized reference waveform (normalized) with the time response of every voxel in the image.
b) Image that displays the correlation coefficient (scalar product of the normalized reference waveform with normalized time course signal in each voxel) in the image.

Voxels having time courses that did not have a temporal correlation coefficient above a chosen threshold were removed. Scalar product calculation was then carried out on the un–normalized remaining voxels. These scalar product maps were then superimposed upon either the first echo planar images in the time course series or upon a high resolution image obtained with a conventional pulse sequence during the scanning session. The superimposition of images as well as all "high–end" image manipulation was carried out using NIH Image, Adobe Photoshop, and Power–Point programs on a Macintosh.

Maps created without the application of a correlation–coefficient threshold were helpful in giving qualitative information regarding artifactual signal changes or contrast to noise values.

Other types of maps were created as well. Percent change maps were created in chapters 7, and 10. Relaxation rate and steady state magnetization maps were also created in chapter 7. These maps were either created of all pixels in the image or only of those pixels that have demonstrated a correlation coefficient above a chosen threshold in a previous time course series.

2.4 EXPERIMENTAL PROCEDURES

Contrast mechanism research in this thesis can be thought of as based on selective modulation of variables hypothesized to be involved with the connection between activation and MR signal change. The question marks indicate the "unknowns." A "bottom up" approach is taken by modulation of physiologic parameters, and a "top down" approach is taken by modulation of MR parameters. An inclusive flow chart, shown in Figure 2.10 outlines this modulation procedure. Several modulations shown in this chart, including those of pharmacologic agents and exogenous contrast agents, were not performed in the studies presented. Also, many types of experiments in the three modulation categories were not performed. The modulation process is iterative in that the types of experimental modulations performed in the future will become more sophisticated as more is understood.
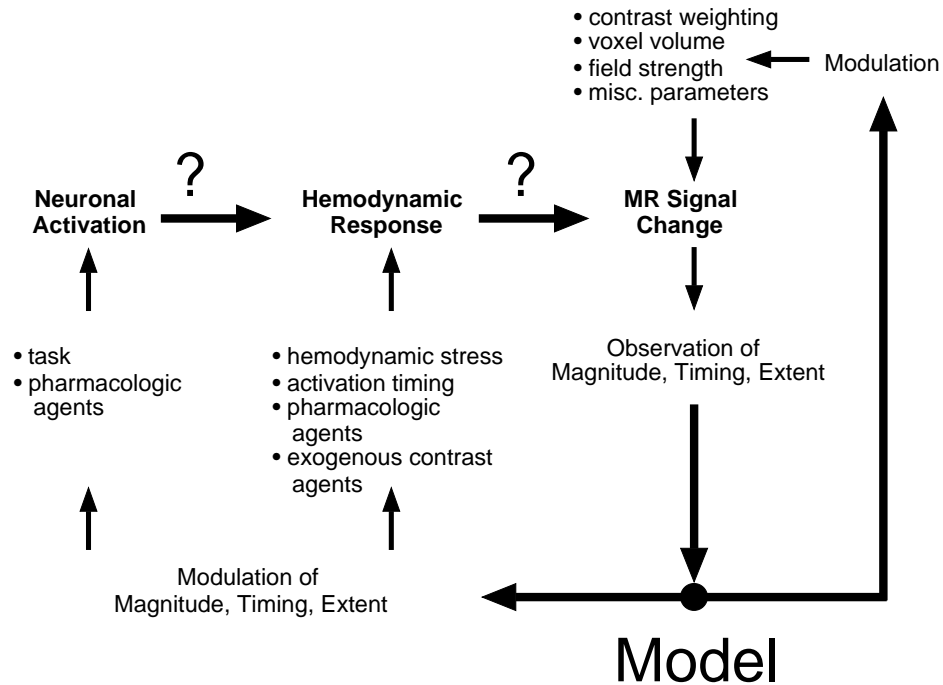
FMRI Contrast Mechanism Research

Figure 2.10: Flow chart summarizing research strategies involved with uncovering the relationship between neuronal activation and MR signal changes.

In chapter 4, the activation timing and intensity is modulated. In chapter 10, the hemodynamic response is modulated by hypoxic and hypercapnic stresses. In chapters 3, 7 , 8 , and 9, MR parameters, including field strength, pulse–sequence, and pulse–sequence timing are modulated. In chapter 6, a model outlining the effects of potentially significant hemodynamic variables in BOLD contrast is constructed.

When these modulations are performed throughout the dissertation, several characteristics of the MRI signal change are observed, including the signal change magnitudes, dynamics, and locations. These observations are

then compared qualitatively and quantitatively with a model that takes a theoretical approach to the explanation of the MR signal changes. The model, constructed and demonstrated in chapter 6, serves as a means of outlining the potentially significant susceptibility contrast–related variables and their relative effects on the MR signal. In particular, the model is constructed to be compared primarily with the experimental results.

Overall, a combined "bottom–up," "top–down," and theoretical methodology is carried out in the following chapters so that a further understanding of the spatial, temporal, and potentially quantitative connection between brain activation and MR signal change may be obtained.

CHAPTER 3

SIGNAL CHANGE LOCATIONS

3.1 INTRODUCTION

In this chapter, the activation–induced signal change locations are compared across several EPI pulse sequences. This analysis complements the studies in chapter 4, in which activation–induced signal change dynamics are characterized. This chapter also serves as an introduction to the susceptibility contrast mechanism analysis presented in chapters 6, 7, 8, and 10.

As described in chapter 1, the evidence strongly suggests that activation–induced MR signal changes are fundamentally related to neuronally–triggered hemodynamic changes (1-3, 8-32). The cerebral hemodynamic response can be thought of as a temporal and spatial transform function in the detection of increased neuronal activity. A primary goal in fMRI is the spatial correlation of activation–induced MR signal changes with underlying neuronal activation which requires precise characterization of the hemodynamic transform function. Ideally, it would be best to first locate neuronal activation foci, and then to compare the focal region with the regions of signal enhancement obtained with fMRI. Unfortunately, this strategy is not possible due to the limitation that regions of neuronal activation cannot currently be non–invasively localized in healthy humans. It is therefore necessary to apply other strategies to assess the spatial correlation between fMRI signal enhancement location and underlying neuronal activation.

A direct first step in the linkage between neuronal activation foci and MR signal enhancement is to test whether foci of MR activation differ across pulse sequence weightings. It is understood that the pulse sequence parameter choice directly affects image contrast weighting and, most importantly, weighting for the specific types of activation–induced hemodynamic changes.

In general, the activation–induced signal changes in spin–echo sequences are thought to arise primarily from blood oxygenation changes in red blood cells and capillaries. The changes in gradient–echo sequences are thought to arise from blood oxygenation changes in red blood cells, capillaries, and larger vessels as well. The changes in inversion–recovery sequences are thought to arise from microvascular perfusion changes.

In the first section of this chapter, a combined spin–echo and gradient–echo EPI sequence (SEGE–EPI), shown in Figure 2.7, was used to obtain spin–echo and gradient–echo time course series simultaneously during finger movement and visual cortex stimulation. Simultaneous image acquisition substantially reduces the small amount of systematic error that occurs across separate trials. Functional correlation images are then created and compared.

In the second section, a comparison of activation–induced signal change locations is made using separate gradient–echo (Figure 2.5), spin–echo (Figure 2.6), asymmetric spin–echo (Figure 2.8), inversion–recovery (Figure 2.9), and asymmetric spin–echo inversion–recovery sequences.

3.2 COMBINED SPIN–ECHO AND GRADIENT–ECHO STUDY

A time course series of 200 sequential spin–echo and gradient–echo image pairs were obtained using SEGE–EPI. Gradient–echo TE = 30 ms and spin–echo TE = 110 ms. TR = 1 sec. Voxel volume = 3.75 x 3.75 x 5 mm. Typical

results are shown. A high–resolution anatomical image of the chosen slice for the motor cortex study is shown in Figure 3.1. The first images in the time course series are shown in Figure 3.2.
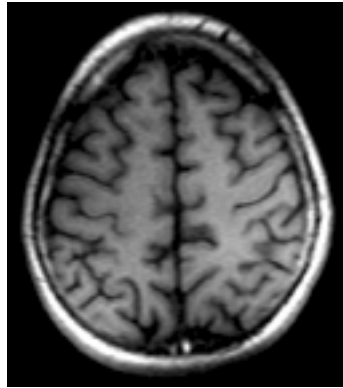

Figure 3.1: High resolution anatomical image of the chosen slice for the combined spin–echo and gradient–echo EPI (SEGE–EPI) motor cortex study.
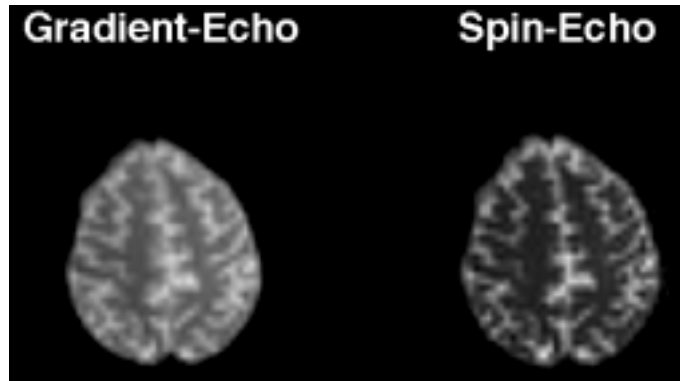

Figure 3.2: First image pairs from SEGE–EPI time course series. TR = ∞. GE TE = 30 ms. SE TE = 110 ms.

During the time course series, the subject cyclically alternated 20 sec. rest with 20 sec. self–paced sequential tapping of fingers to thumb. The reference vector used in the creation of correlation images was created from a

spatial (over the activated voxels) and temporal (over each of the 5 activation–rest cycles) averaging. The correlation images are shown in Figure 3.3. No threshold was used.
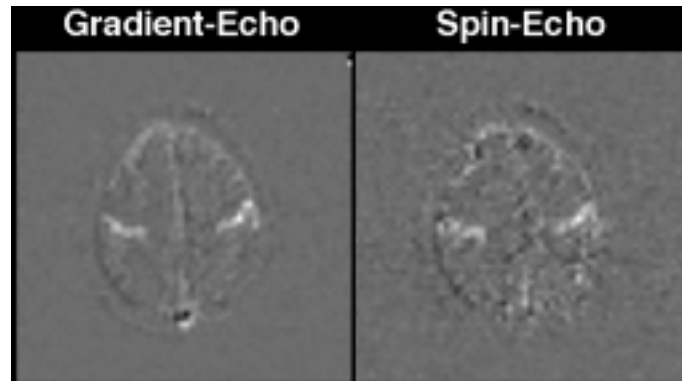
Figure 3.3: Simultaneously obtained correlation images. Regions activated in motor cortex by bilateral finger tapping are apparent. These images were created by scalar product calculation of a normalized reference vector representing the expected time course response with the un–normalized time course signal of every voxel. (For more detail on post processing methods please refer to chapters 2 and 5.)

The functional contrast to noise is generally higher in the gradient–echo correlation images. The smaller contrast in spin–echo correlation images are due to a) a smaller change in transverse relaxation rate and/or b) less overall signal due to the longer TE. In chapter 7, a more complete analysis of transverse relaxation rate changes is performed, demonstrating that the smaller contrast to noise is primarily due to a smaller (by a factor of 3 to 4) activation–induced change in transverse relaxation rate (i.e.: $R2^*/\ R2 \approx 3$ to 4).

A high correlation (as opposed to correlation coefficient) is observed in the sagittal sinus in the GE time course series. These changes in gradient–

echo time course series are common and may arise as a result of the large pulsatile inflow–related (unsaturated spins entering the saturated plane causing signal enhancement) or flow velocity related (velocity variations causing a net phase shift results in a slight displacement or signal void) signal changes in the motor cortex. A very large signal change (large magnitude) that has a small correlation coefficient with the reference vector would nevertheless likely have a large correlation (or dot product), as shown here. It should be noted that these large artifactual dot product values may be positive or negative (since they result from a noise–like process), and likely come from pulsatile csf or blood flow.

The pulsatile changes are observed less frequently in the spin–echo functional image. The reason for this is most likely that the slice–selective 180° pulse 55 ms after the initial 90° pulse does not refocus rapidly flowing spins, therefore creating a signal void where the artifactual signal changes would occur with the use of gradient–echo sequences.

For a more detailed comparison of the activated regions, magnified images of the active regions in motor cortex are shown in Figure 3.4.
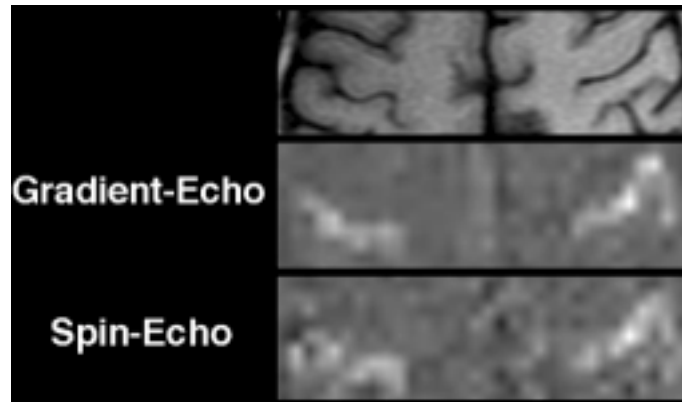
Figure 3.4: Magnification of functional correlation images shown in Figure 3.3, with anatomical image of same region displayed for reference.

The basic comparisons made are in activation foci and distribution. The activation–induced signal change locations appear to overlap significantly, especially in several sulcal regions. Nevertheless, several voxels show activation exclusive to each sequence.

The reasons for these differences and similarities are not entirely clear, but may reflect different hemodynamic events or similar hemodynamic events happening on different spatial scales (i.e.: Large vessels in sulci with gradient–echo sequences as opposed to small vessels in cortex with spin–echo sequences.). The shape of the activation pattern obtained using the spin–echo sequences appears more amorphous and fragmented. It is also less extensive. The hypothesis is that spin–echo sequences may show changes proximate to activated brain parenchyma (capillaries), but may also show changes from within large vessels (red blood cells), whereas signal changes in gradient–echo sequences show maximal changes in voxels containing large vessels, and show a larger extravascular effect. In chapters 6 and 10, it will be demonstrated

that relative blood volume (in each voxel) heavily weights the magnitude of the activation–induced signal changes.

Figure 3.5 is a depiction of magnified functional images of the visual cortex. These images were created in a similar manner as those in Figure 3.5. The stimulus was an 8 Hz flashing checkerboard.
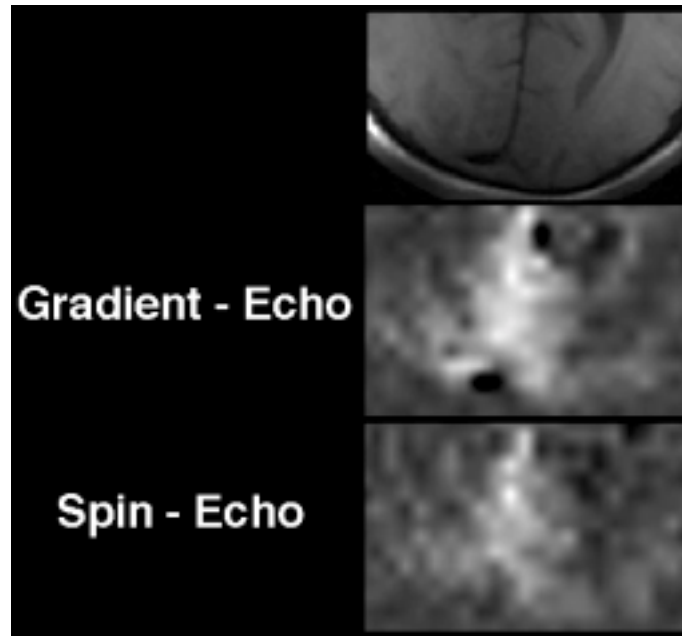

Figure 3.5: Magnification functional images obtained simultaneously of the visual cortex during 8 Hz flashing checkerboard stimulus. An anatomical image of same region is displayed for reference.

In functional images from the visual cortex, a very high intensity region is observed in the sagittal sinus that is not observed in the functional image obtained using the spin–echo sequence. As discussed, this area of high signal intensity is possibly due to one or a combination of: a) random pulsatile flow effects, b) blood oxygenation changes within large vessels, c) changes in blood flow velocity, and d) blood oxygenation–related frequency

shifts that cause shifts in signal from one voxel (one voxel ≈ 20 Hz) to the next, causing signal changes related to relative image signal intensity.

From this study, it is clear that regions of activation do not overlap completely. The model for these relative effects is constructed in chapter 6 and the components of the signal changes are studied in more detail in chapters 7, 8, and 10.

3.3 COMPARISON OF CONTRAST WEIGHTINGS

In this section, the relative signal change locations, magnitudes, and functional contrasts were compared, keeping all other variables constant, using time course series of six different pulse sequence weightings. Each time course series consisted of 240 sequential images each. TR = 2 sec, and voxel dimensions = 3.75 x 3.75 x 5 mm^3. Total time course length was 480 sec. During each time course series, sequential, bilateral finger tapping was performed in alternating 20 sec rest and 20 sec activation cycles. Reference vectors and correlation images were also created in a similar manner as the above study. A reference vector was created from each individual time course series. The six contrast weightings performed are shown in Table 3.1.

sequence	parameters	contrast weighting	Flow	Oxygenation BOLD (>20μm)	Oxygenation BOLD (<20μm)
inversion recovery (IR)	TI = 1200 TR = 2000 TE = 60	high T1 slight T2	**X**		x
asymmetric spin-echo inversion recovery (ASE-IR)	TI = 1200 TR = 2000 TE = 60 tau = 40	high T1 high T2* slight T2	**X**	**X**	**X**
asymmetric spin-echo (ASE)	TR = 2000 TE = 60 tau = 40	high T2* slight T2		**X**	**X**
spin-echo (SE)	TR = 2000 TE = 60,100	slight T2, high T2			x,**X**
gradient - echo (GE)	TR = 2000 TE = 40	high T2*		**X**	**X**

Table 3.1: Pulse sequences, parameters, and the corresponding contrast weightings. The size of the x's roughly corresponds to the relative degree of sensitivity, according to the current models, to flow or to changes in blood oxygenation in large (greater than 20 μm) compartments and small (less than 20 μm) compartments. The sequences are illustrated in chapter 2.

The above contrast weightings are used in the following functional and anatomical images. In Figures 3.6 to 3.11 the letter and corresponding contrast weighting are:

A = Inversion Recovery, TI = 1200 ms, TR = 2000 ms, TE = 60 ms.

B = Asymmetric Spin–echo Inversion Recovery, TI = 1200, TR = 2000, TE = 60 ms, $\tau = 40$ ms.

C = Asymmetric Spin–echo, TR = 2000 ms, TE = 60 ms, $\tau = 40$ ms.

D = Spin–echo, TR = 2000, TE = 60 ms.

E = Spin–echo, TR = 2000, TE = 100 ms.

F = Gradient – Echo, TR = 2000 ms, TE = 40 ms.

Figure 3.6 displays the first image in each of the time course series used. Figure 3.7 displays the corresponding functional images. Figure 3.8 displays the corresponding functional images after the correlation coefficient threshold was applied. Figures 3.9 through 3.11 display magnifications of the corresponding images.
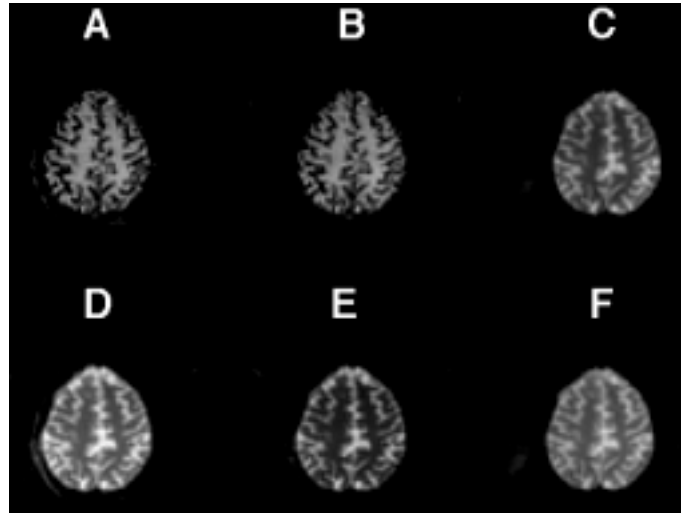

Figure 3.6: First image from each of the six time course series corresponding to the pulse sequences mentioned above.
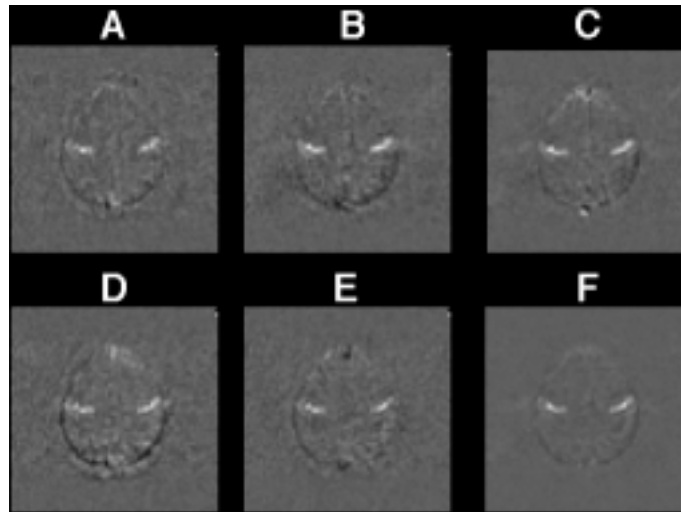
Figure 3.7: Correlation images created from the corresponding time course series. Note the differences in contrast to noise and artifact.
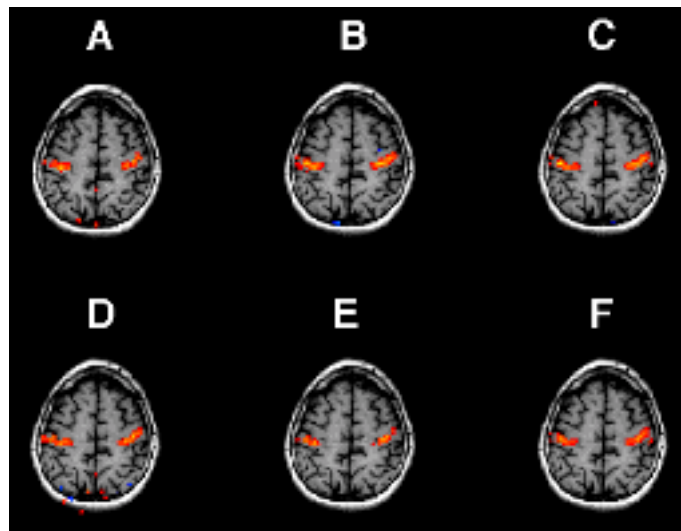
Figure 3.8: Correlation images after application of a threshold. Yellow = highest correlation.
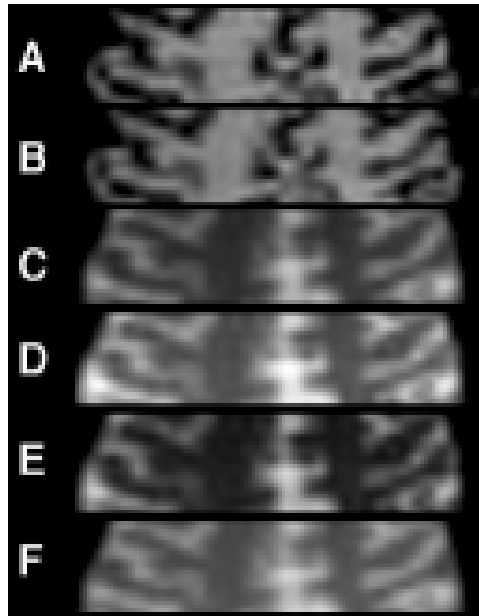
Figure 3.9: Magnification. First image from each of the six time course series.
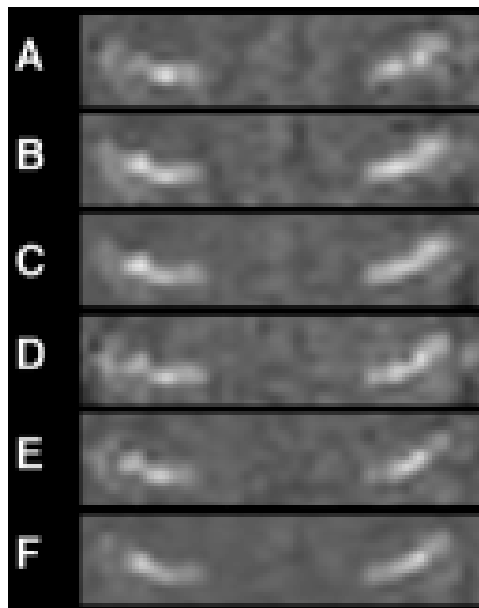

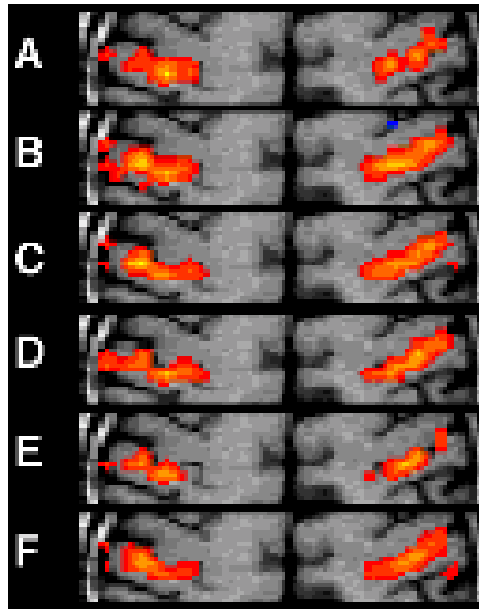**Figure 3.10:** Magnification. Corresponding correlation images.

Figure 3.11: Magnification. Corresponding correlation images after application of a threshold.

Since the functional images were not obtained simultaneously, more variability is present across the time course series. Such variability especially makes comparison of artifactual signal changes difficult.

One key observation is the systematic contrast–weighting–related shift in activation foci that is especially apparent upon study of Figures 3.10 and 3.11. Note that in the T2*–weighted images, the "hot spot" or focal points of activation appear more lateral on both sides. In the T1–weighted and the T2–weighted images, the focal points are located several millimeters more central. In the correlation image that was obtained using the asymmetric spin–echo inversion–recovery sequence, which is both T2* *and* T1–weighted, *two distinct* foci appear (most clearly on the left side of the image: left motor

cortex), that match the corresponding individual foci obtained using the other sequences.

It is difficult to make further statements about these relative locations without a means for identification of the predominant vessel size in each voxel. Nevertheless, some tentative statements can be made. Large pial veins tend to drain laterally (148). The T2*–weighted foci appear to correspond to the lateral locations. The capillary bed, located in parenchymal tissue, is more likely to be more central within this slice location. The more central activation locations correspond to the T1–weighted and T2–weighted foci in this and the above study.

From signal vs. time plots averaged from the activated regions of interest in Figure 3.8 and 3.11, a comparison of percent signal change and contrast to noise was made. Figure 3.12 displays the percent signal change and Figure 3.13 displays the measured signal changes divided by the standard deviation, in time, of the averaged signal in signal in resting cortex.
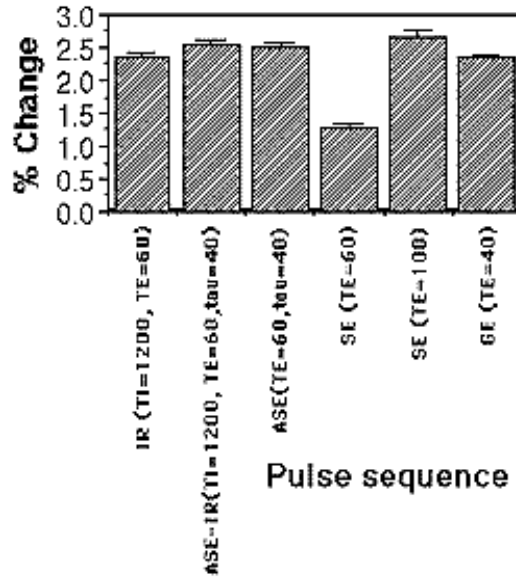
Figure 3.12: Average percent signal change values obtained from the activated regions in Figure 3.8 and 3.11.
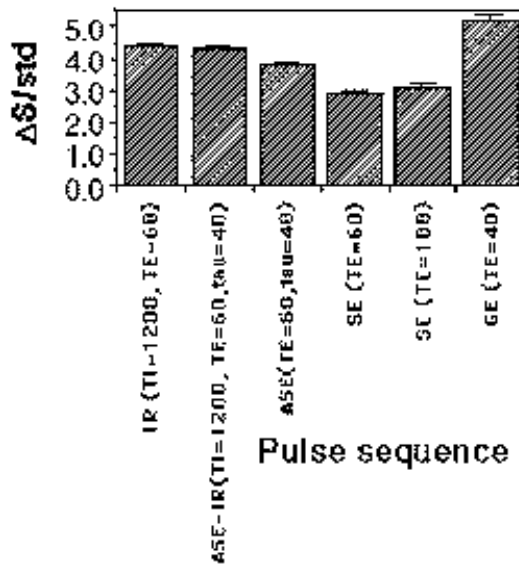

Figure 3.13: Average functional contrast to noise values obtained from the activted regions in Figure 3.8 and 3.11.

As expected, fractional signal change increases with TE, (spin–echo sequences), suggesting a transverse relaxation–rate change mechanism. More detailed studies of the TE dependence of the fractional signal changes are carried out in chapters 6 through 8.

While the fractional signal change is highest in the spin–echo TE = 100 ms sequence, the highest functional contrast to noise is apparent in the gradient–echo sequence at shorter TE values, in agreement with the hypothesis that the signal change arises from a compartmentalized susceptibility relaxation rate change ($\Delta R2^* > \Delta R2$, and $T2^* < T2$).

It is interesting to note, at the risk of over–interpretation of these single–study results, that the percent signal change in the asymmetric spin–echo inversion recovery sequence is not equal to the asymmetric spin–echo sequence percent change plus the inversion–recovery percent change. This apparent lack of an additive effect may suggest that the $T2^*$–related signal changes and the T1–related signal changes are coming from slightly different foci. If the signal changes originated from the same area, then they should have added in the sequence that included both contrasts.

3.4 DISCUSSION

These studies indicate that different image contrast weightings give different information regarding the activation–induced hemodynamic changes. Testing the hypothesis put forward in this section is difficult. Since it is currently not possible to observe activation–induced neuronal changes directly in humans, these signal changes must be biophysically and physiologically modeled and compared with carefully planned and controlled experiments.

CHAPTER 4

SIGNAL CHANGE DYNAMICS

4.1 INTRODUCTION

In this chapter, activation–induced MR signal change dynamics are studied. The purpose is two–fold. First, a more complete and precise dynamic model of the hemodynamic response may allow for more robust extraction of meaningful time–course information from noise and artifactual signal changes. Second, information about the response characteristics, as they are observed with MR, can be compared with response characteristic information obtained using other techniques, such as intrinsic optical imaging (30-32, 240), so that the mechanisms of MR contrast may be better understood. This incompletely understood "hemodynamic transfer function" can be modeled on several levels. Superficially, it can be considered a black box that gives an output in response to an input. Ultimately, the goal is to fully understand it on a physiological and biophysical level. Exploration of the dynamics initially allows modeling on the "black box" level, but also is an important avenue by which a deeper understanding of the underlying physiological and biophysical process may be obtained.

First, the MR signal change latency is characterized. The variations in signal latency are studied across MR contrast weightings used, across different active regions in the brain, and across different brain activation tasks. Second, characteristics of the hemodynamic transfer function, using gradient–echo EPI, are determined by variation in activation duration and periodicity.

Primary brain activation (finger tapping) is used to supply a reliable input because the activation timing is easily controlled and activated regions are easily localized.

4.2 LATENCY COMPARISONS ACROSS MR CONTRAST WEIGHTINGS

This section is a comparison of activation–induced MR signal change latency across MR contrast weightings. From these comparisons, differences in the time course of hemodynamic events, (i.e. flow changes vs. oxygenation changes, and large vessel oxygenation changes vs. small vessel oxygenation changes), are hypothesized.

A time course of 500 SEGE-EPI (see Figure 2.7) gradient–echo (TE = 30 ms) and spin–echo (TE = 110 ms) image pairs (voxel volume = 3.75 x 3.75 x 5 mm$^{3)}$ was collected of an axial slice containing the motor cortex (TR = 1 sec.). During sequential image collection, the subject alternated 20 sec. rest with 20 sec. sequential finger tapping. A total of 12 on–off cycles were performed. Figure 4.1 shows a high resolution image of the chosen plane, the respective gradient–echo and spin–echo anatomical and correlation images before and after a threshold correlation coefficient of 0.45 was used. Voxels that had a correlation coefficient greater than 0.45 in *both* the spin–echo and gradient–echo sequences, shown in Figure 4.2, were spatially averaged and plotted over time. The time course plot is shown in Figure 4.3.
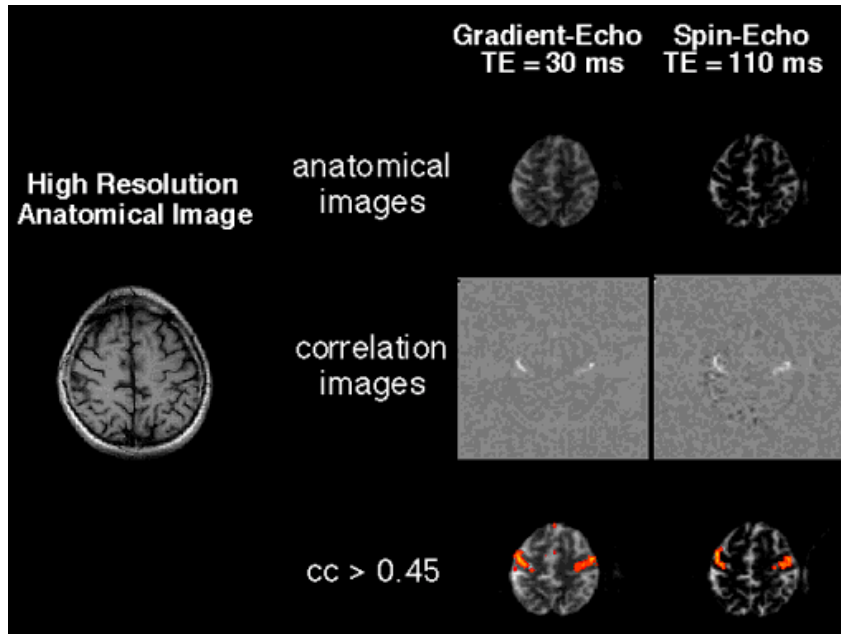
Figure 4.1: High resolution anatomical image and corresponding images obtained by time–course collection of SEGE-EPI pairs. Top: first anatomical images in time course. Middle: correlation images before a threshold was applied. Bottom: correlation images after a threshold (cc > 0.45) was applied.
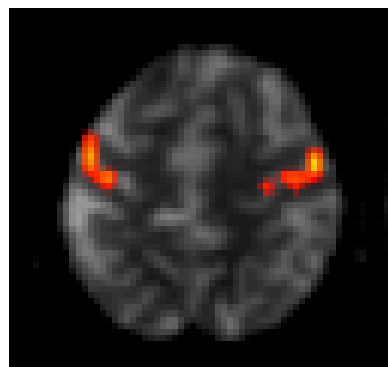

Figure 4.2: Correlation image, superimposed on the high–resolution anatomical image, showing voxels having a correlation coefficient > 0.45 in both the spin–echo and gradient–echo time course series.
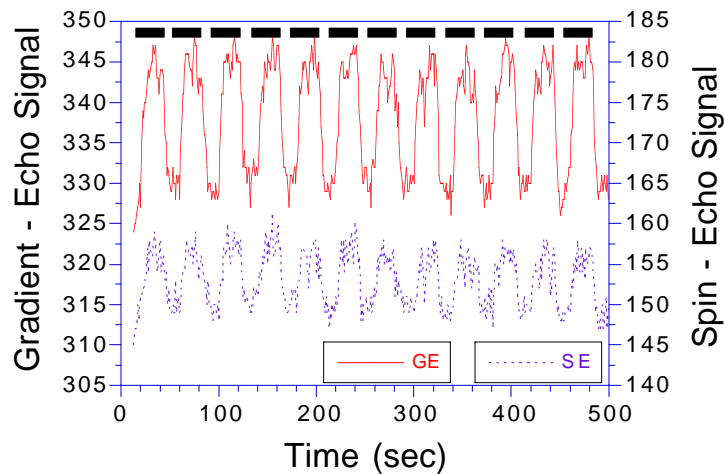
Figure 4.3: Spin–echo and gradient–echo signal intensity vs. time obtained from the motor cortex region in Figure 4.2. Vertical scales have the same range. Horizontal bars indicate when bilateral finger tapping was performed.

The signal, shown in Figure 4.3, remains stable over the entire time–course. Many time course series tend to show either a consistent undershoot after the initial cycle or a downward drift (171, 177, 227, 229). Common artifacts include motion related drift, respiration related signal change, and pulsatile signal changes. In this time course series, the on–off response appears to maintain a similar shape and magnitude throughout. This plot also illustrates the relative functional contrast typically obtained with spin–echo and gradient–echo sequences since the vertical scales have the same ranges. To characterize the average latencies, each on–off cycle was normalized and averaged in time. The cycle–averaged plot for the spin–echo and gradient–echo time course is shown in Figure 4.4.
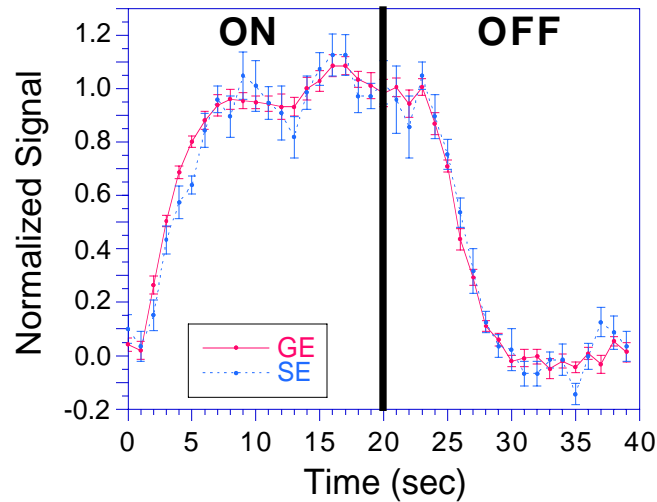
Figure 4.4: Spin–echo and gradient–echo time course created by averaging all of the 12 on–off cycles in Figure 4.3.

To describe the onset latencies, Kwong et al. (171) used a fit to a single exponential approach to equilibrium, shown in equation 4.1.

$$y = 1-e^{-(t/k)} \qquad [4.1]$$

The value, k, is the rate constant and t is time from stimulation onset, in seconds. The rate constant in the visual cortex, using a gradient–echo sequence, was reported to be 4.4 ± 2.2 sec., and using an inversion–recovery sequence, was reported to be 8.9 ± 2.8 sec. (171). The consistency of these time constants and the reasons for the difference have not been determined.

A monoexponential model of the signal change onset is an oversimplification of the behavior of the MR signal change on activation, but for comparison purposes with the literature values, we performed similar fits using Kalidagraph™ graphing and fitting program. From Figure 4.4, we

found the onset time constants to be 3.67 ± 0.30 for the gradient–echo sequence and 4.19 ± 0.46 for the spin–echo sequence. These time constants are within the range reported in the literature.

Figure 4.5 shows a comparison of cycle–averaged time courses obtained from activated motor cortex regions in inversion recovery (TI = 1200 ms, TE = 60 ms) and gradient–echo (TE = 40 ms) time course series. TR = 3 sec.
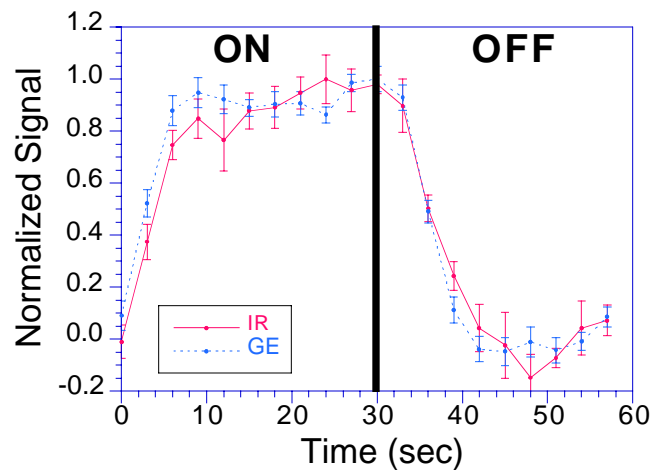

Figure 4.5: Cycle–averaged inversion–recovery and gradient–echo time course series.

The measured signal onset time constants from Figure 4.5 were: 3.65 ± 0.52 sec. for the gradient–echo sequence and 5.81 ± 0.49 sec. for the inversion–recovery sequence. The inversion–recovery time constant was larger than the gradient–echo time constant, but was smaller than the time constant reported in the literature (171).

A comparison of activation–induced signal change latency across the same six contrast weightings as shown in section 3.2, excluding the spin–echo

sequence at TE = 60 (because SE TE = 100 was also T2 –weighted), was also performed. The signals from the activated regions in Figure 3.8 and 3.11 were cyclically averaged across the five on–off cycles. TR = 2 sec. Figure 4.6 displays the cycle–averaged signal vs. time.
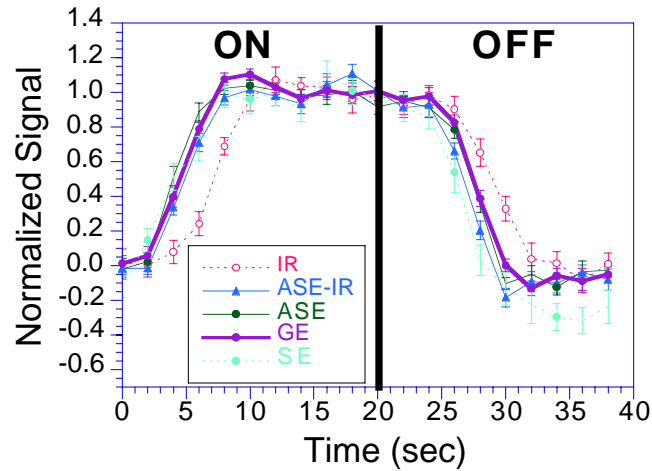

Figure 4.6: Cycle–averaged signal vs. time from the inversion recovery (IR), asymmetric spin–echo inversion–recovery (ASE–IR), asymmetric spin–echo (ASE), gradient–echo (GE), and spin–echo of TE = 100 ms (SE) time course series used in section 3.2.

The onset time constants were as follows: IR = 7.28 ± 1.68 sec., ASE–IR = 5.14 ± 1.05 sec., ASE = 4.23 ± 0.84 sec., GE = 4.42 ± 0.94 sec., and SE = 4.64 ± 0.70 sec. Once again, the inversion recovery sequence time constant is largest. It is interesting to note that the asymmetric spin–echo inversion recovery sequence, having both BOLD and perfusion (apparent T1 change) contrast weighting, shows a time constant that is between the pure BOLD contrast weighted sequence and perfusion contrast–weighted sequences. The spin–

echo time constants were also consistently longer, by a relatively small amount, than the gradient–echo time constants.

4.3 LATENCY COMPARISON ACROSS SPACE

Using the same data set as presented in Figures 4.1 through 4.4, a comparison of the signal change latency was made over space. Signal change latency differences may exist in space because of changes in blood oxygenation that may occur at a rate that is limited by the circulation and blood mixing rate in the cerebral vasculature. Spatial latencies in networked neural processes happen on a time scale ($\approx$ 100 ms) that appears to be currently unresolvable by fMRI. Methods have been put forth which claim to be able to identify draining veins by spatial latency comparisons (205, 206). It can be imagined that large draining veins downstream from activated cortex may change in oxygenation slightly later than the blood in the capillary bed that is immediately adjacent to the source of vasodilatation.

From the study in section 3.2, it appears that the largest signal changes in the T2*–weighted sequences, known to be weighted by voxels having large blood volume (in large vessels), are at the lateral periphery and in the sulci. The largest signal changes in the IR sequences, thought to be sensitive to flow changes in the microvasculature, are shifted more centrally. For this reason, two voxels located laterally and centrally (hypothesized to be locations of predominant vessels and capillaries respectively) were chosen for comparison. These voxel locations are illustrated in Figure 4.7. Figure 4.8 shows the cycle–averaged plot of the voxels chosen.
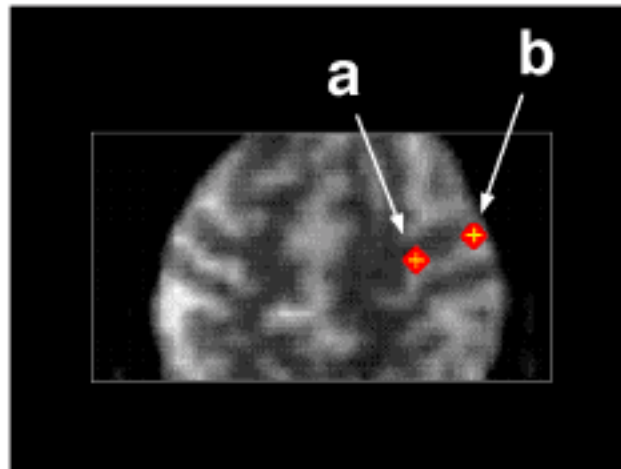
Figure 4.7: Voxels a and b chosen for the onset latency comparison.
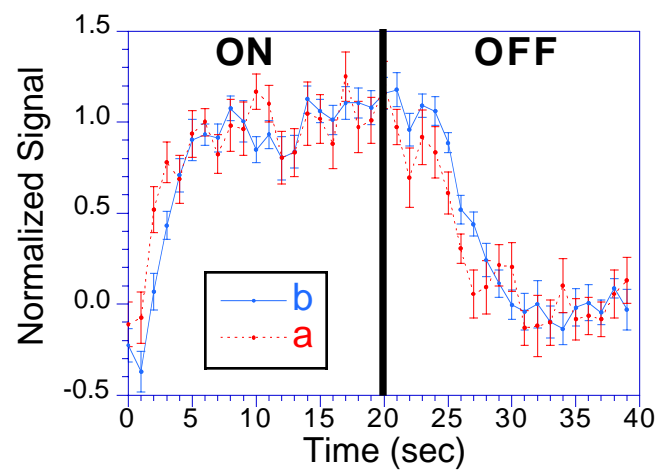

Figure 4.8: Cycle–averaged plots of voxels a and b from Figure 4.7.

The onset time constants measured from plots a and b are 3.98 ± 0.79 sec. and 2.83 ± 0.50 sec. respectively. While this is only a comparison of the time course of two voxels, the data nevertheless demonstrates latency differences in space that supports the hypothesized large vessel location and

proposed delayed oxygenation change. Such a "spread" in latency may set the upper limit on the temporal resolution of fMRI.

4.4 LATENCY COMPARISON BETWEEN TASKS

Other studies have observed large difference in latencies in activated regions that are apparently not within the same vascular region (i.e. downstream) and that correspond to functionally different regions of the brain. A significant difference was reported, during a semantic decision making task, between the primary auditory cortex and the left frontal region of the brain (225). Such latencies may reflect additional integrated cognitive neuronal mechanisms becoming activated during cognitive tasks.

Differences in latency between primary brain activation tasks have also been observed (219). This study details the findings. In this study, 12 series of 75 sequential images of the same plane in the brain were obtained using a TR of 1 sec. TE=40 ms. Voxel volume = 3.75 x 3.75 x 15 mm^3. Sync pulses generated by the scanner at the 25'th and 50'th scans were used to trigger onset and cessation of a 32° red–black checkerboard flickering at 8 Hz. Only one eye (right eye) was stimulated. Alternate time course series were delayed 0 or 0.5 sec. relative to the sync pulses so that an effective, averaged, sampling time of 0.5 sec. could be obtained with a TR of 1 sec. Separate time course series were obtained of an plane in the motor and visual cortex (12 time course series each). The subject sequentially tapped fingers to thumb in a self–paced manner only when the visual stimulus was observed.

Figure 4.9 shows the normalized signal changes. The rise time from stimulus onset to 90% of maximum was 5 sec. for motor cortex and 8 sec. for visual cortex. The time for the signal to decrease from the activated state to

within 10% of baseline was 9 sec. for both visual and motor cortex. The delay from the stimulus onset to the time at which the signal first departed from baseline was approximately 2 to 3 sec. for both cortical areas. The delay from stimulus cessation to the beginning of a fall in signal intensity was 3 to 4 sec. The onset time constants were measured to be 4.4 ± 0.40 sec. for the visual cortex and 2.8 ± 0.37 for the motor cortex.
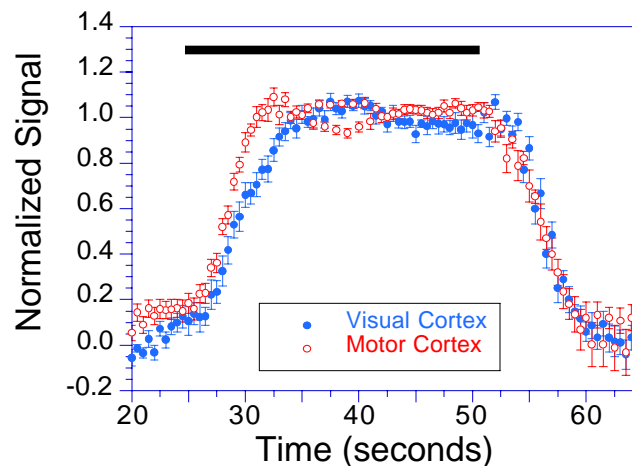

Figure 4.9: Normalized signal change from visual and motor cortex.

The reasons for the differences in the latencies between the visual and motor cortex are unclear. Possible reasons may be that the visual cortex ROI may have been over a large vessel, thus giving a more latent response, or that "stronger" activation of motor cortex, (i.e. active finger movement vs. passive viewing), may have driven the flow and oxygenation changes more strongly.

One study (232) using functional spectroscopy has claimed to observe a transient signal *decrease* of approximately 0.25% *before* the typically observed signal increase. In an effort to observe these changes, 14 time course series,

from the same volunteer, same session, and same ROI of the visual cortex were obtained. Total number of images = 200. TR = 200 ms. TE = 40 ms. Voxel volume = 3.75 x 3.75 x 5 mm^3. A binocular visual stimulation device, described in chapter 2, that was similarly driven, as above, by an output scanner sync pulse for precise stimulus timing, was used. Data acquisition for the 200 sequentially obtained images was not started until steady state magnetization was achieved (15 sec. of RF excitation). Each time course series consisted of 20 sec. rest, then 20 sec. stimulation. The signal intensity from the ROI vs. time for each of the 14 trials, is shown in Figure 4.10.

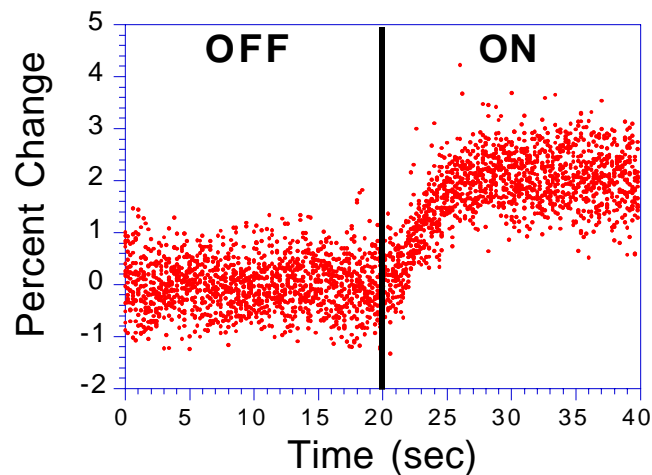**Figure 4.10:** Scatter plot of percent change vs. time from visual cortex. Included are 14 trials.

Figure 4.11 shows percent signal change, averaged from the 14 time course series shown above. The signal for each time point as it was averaged across the 14 trials. The measured onset time constant for this study was 3.33 ± .15 sec. Even though a 0.25% signal change would seemingly be observable

here, no significant decrease in signal was observed immediately prior to the observed signal increase. This study does not rule out the possibility that the spatially averaged signal may have included voxels that demonstrated the mentioned signal decrease.
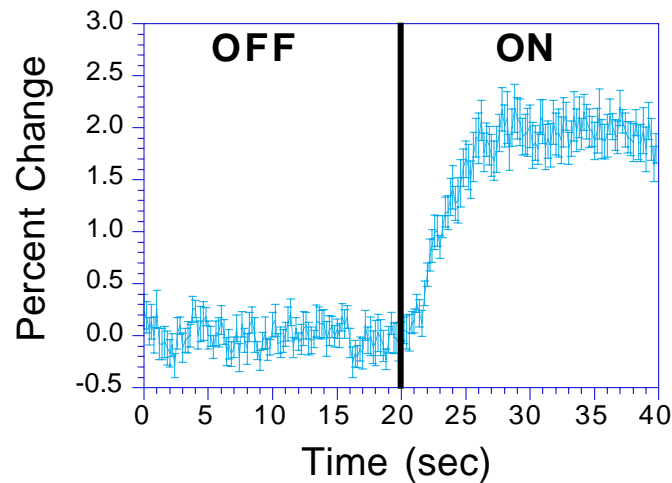

Figure 4.11: Plot of average percent signal change vs. time from visual cortex. Included are 14 trails.

The lack of an observed decrease may be simply due to the fact that most voxels, or those voxels giving the strongest response may not exhibit a signal decrease prior to the signal change onset. More detailed study of individual voxels during repeated trials is necessary. Also, the signal decrease observed in the previously mentioned study (232) was observed using significantly different stimuli, stimuli timing, pulse sequences, contrast weighting, and signal acquisition timing.

To observe the reported signal decrease at 1.5 Tesla, several additional experimental considerations may be necessary. These include a) higher

resolution, b) a breath–hold during the data acquisition, c) gating the beginning of the acquisition to the heart–rate (or gating of the beginning of the stimuli to the heart–rate), d) a bite – bar for additional subject restraint, e) additional time–course averaging, and/or f) higher signal to noise ratio.

Overall, the observations in this section demonstrated highly repeatable signal change magnitudes and latencies that were somewhat task–dependent. Variation in time constants was observed across tasks and trials. Internal comparisons of time constants reduced some of the systematic variations. The reasons for these variations may be many. The onset time constant using BOLD contrast is similar to that reported by Grinvald et al. (31) using optical imaging of intrinsic, oxygenation–dependent signals in awake monkeys.

4.5 ACTIVATION DURATION DEPENDENCY

To observe the effects of both short term and long term activation of the primary motor cortex, subjects were instructed to tap their fingers to thumb in a self paced, consistent, and repetitive manner for durations ranging from 0.5 sec. to 6 minutes. The impulse response and steady state characteristics of the induced vascular response were thereby obtained. Time course collection of gradient–echo T2*–weighted echo–planar images was used. TR = 1 sec. for most studies, and 6 sec. in one study. Voxel volume = 3.75 x 3.75 x 10 mm^3. First, activated regions were identified from periodic stimulation paradigms. Then, the signal in these regions was observed during the time–course collection of images during which finger tapping duration was varied from 0.5 sec. to 6 minutes.

For the long–duration, or tonic, activation study, the finger tapping (self paced sequential) timing was: 0–1:00 rest, 1:00–7:00 right fingers, 7:00–8:00 rest, 8:00–14:00 left fingers, 14:00–16:40 rest. A total of 1000 images was collected. Figure 4.12 shows the signal intensity vs. time from a voxel in the left and right motor cortex respectively. The signal enhancement remained stable for the entire 6 minute duration. In addition the study was repeated with a TR of 6 seconds to allow complete magnetization recovery between sequential images, thus eliminating any T1 or inflow sensitization. The results again showed a consistent elevation of signal during the entire duration of activation, giving evidence that oxygenation, and not just flow, remains in an elevated state for the entire 6 minutes of activation.
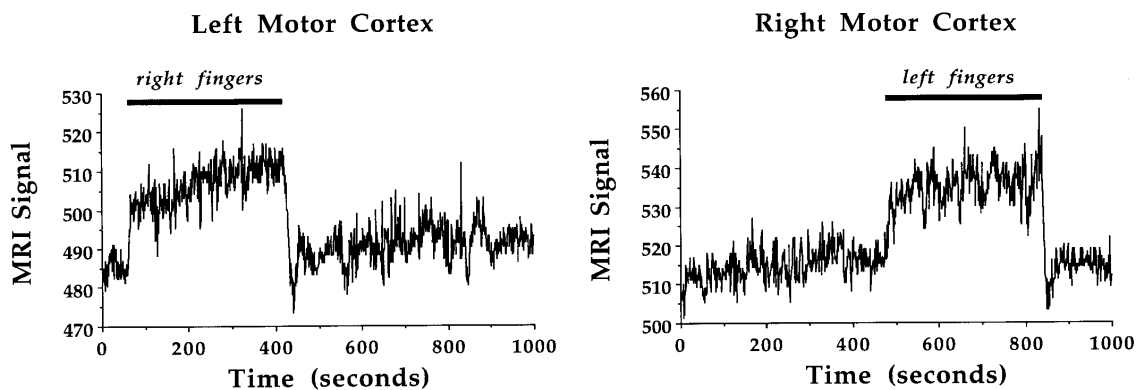
Figure 4.12: Signal vs. time plots from a voxel in the left and right motor cortex during 6 minutes of self–paced sequential finger tapping on each hand.

For the short–duration or pulsed activation study, the subject was cued twice during the time course to perform bilateral finger tapping of the forefinger to thumb, at maximal tapping frequency ($\approx$ 6 Hz), for periods of durations ranging from 0.5 sec. to 5 sec. TR = 1 sec. The results are shown in Figure 4.12.

For the 0.5 sec. activation duration signal enhancement began 2 to 3 sec. after the onset of activation, 1.5 to 2.5 sec. after the cessation of movement, and continued for another 3 to 5 seconds before returning to baseline. For all activation durations, the signal returned to baseline approximately 8 seconds after the cessation of movement. The percent signal change also showed an increase with the length of the activation duration.

For the shortest term duration, the signal change can be considered the hemodynamic impulse response. Convolution of this function with neural input functions (typically boxcar functions), likely would give the typically observed signal change shapes. It is interesting to note that the 0.5 sec. temporal response resembles the deconvolved response function reported by Friston et al. (274).

Overall, this study has demonstrated that long term duration activation creates a stable elevated MR signal. It is also apparent that brief intense spikes of activation are detectable as well.
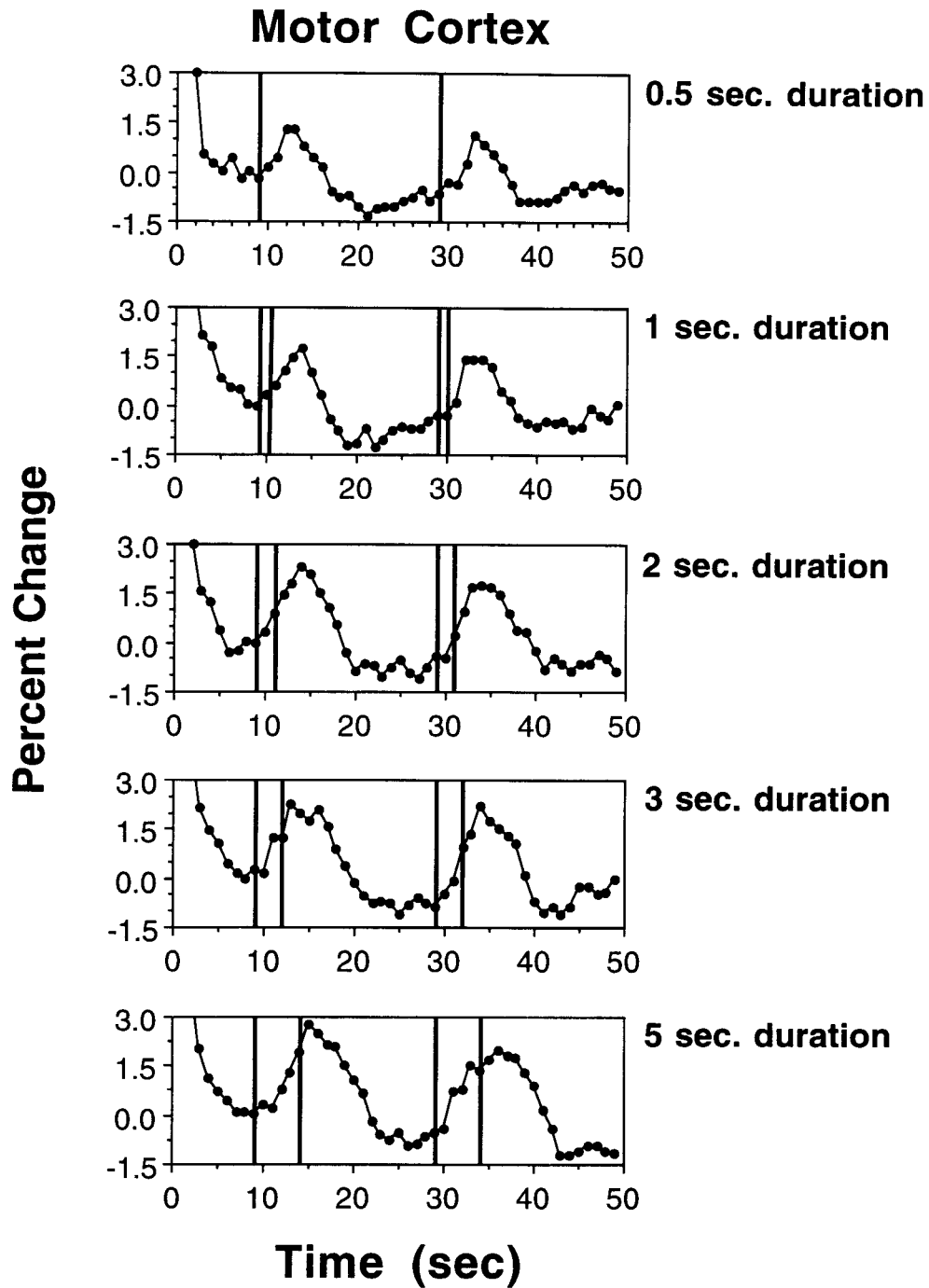
Figure 4.13: Percent change vs. time plots from the motor cortex. Two episodes of finger tapping ($\approx$ 6 Hz) were performed for durations ranging from 0.5 to 5 sec.

4.6 ON–OFF SWITCHING RATE DEPENDENCY

The following on/off (i.e.: active/resting) switching rate study was motivated, in part, by the desire to arrive at an on/off activation rate that maximized both the induced signal amplitude and the number of activation cycles in a time course. These goals are important for creation of high quality brain activation images by cross–correlation or Fourier analysis, and for extraction of relative spatially–distributed latency information. Generally, the on/off rate–dependent damping of the activation induced signal enhancement by the intrinsic hemodynamic response time is characterized by this study.

To test the dependence of signal amplitude on the on/off switching frequency, subjects tapped their fingers to thumb, bilaterally, in a self–paced, consistent, and repetitive manner for on/off cycles ranging from 0.02 Hz (25 sec. "on" and 25 sec. "off") to 0.5 Hz (1 sec. "on" and 1 sec. "off"). TR = 1 sec. Figure 4.14 shows the percent signal from the same pixel for on/off finger activation frequencies ranging from 0.02 Hz to 0.5 Hz. Figure 4.15, showing relative amplitude versus on/off activation rate, summarizes the results.
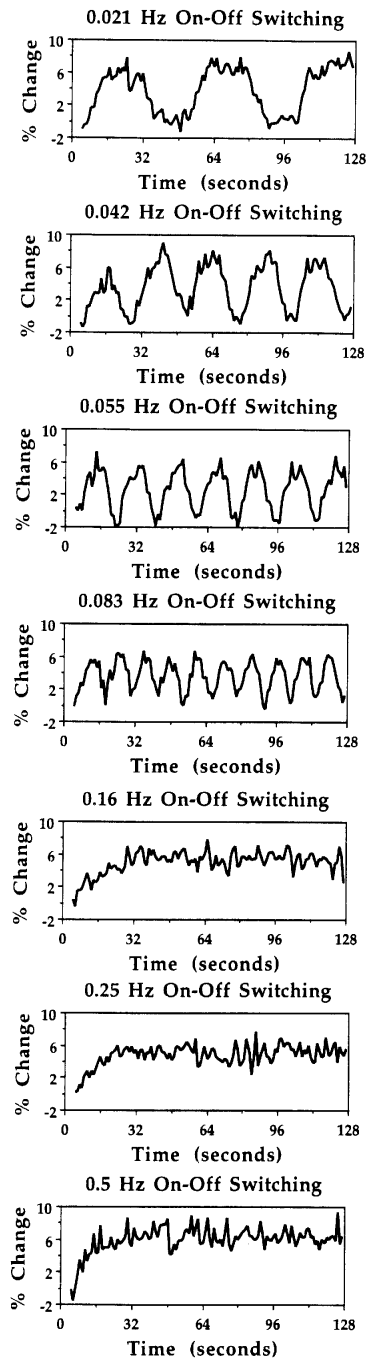
Figure 4.14: Signal from the same pixel in the motor cortex obtained during cyclic on/off finger movement. As the on/off frequency is increased from 0.024 Hz to 0.5 Hz, the activation–induced amplitude becomes decreased and the signal becomes saturated in the "on" state.
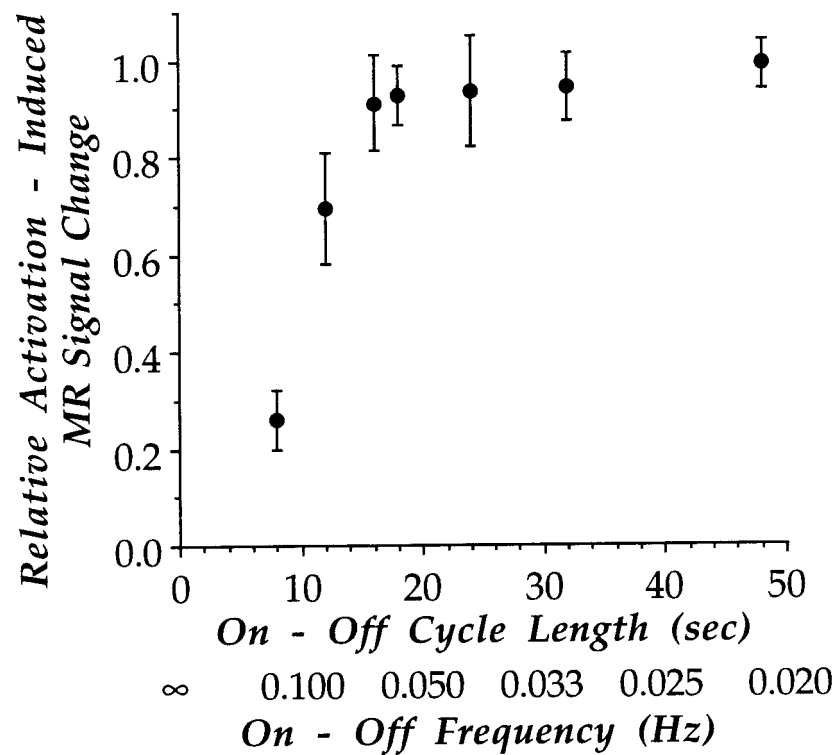
Figure 4.15: Summary of the dependence of the relative amplitudes of the activation–induced signal on switching frequency. The activation–induced signal begins to become reduced at on/off rates above 0.06 Hz.

Because the time to reach a baseline after cessation of activity is slightly longer than the time to plateau in an "on" state, the signal becomes saturated in the "on" state with the faster on/off frequencies. The relative activation–induced signal amplitude in the motor cortex does not show a significant decrease until the switching frequency is higher than 0.06 Hz, (8 sec. "on" and 8 sec. "off"), and does not follow the activation timing above 0.13 Hz. Also, the time to reach the saturated "on" state decreases as the on–off rate increases.

In addition to temporal characteristics of the activation–induced signal change, the magnitude of the event–related signal changes observed using BOLD contrast may depend upon characteristics of the stimulus input. Like PET, the observed BOLD signal changes presumably reflect, indirectly, rate of neuronal firing integrated over time within a large neuronal pool. If each presentation of a stimulus results in a similar set of neuronal events, then the integrated neuronal response, and possibly the resulting blood flow response, will be a function of the number of stimuli presented per unit time. Regional cerebral blood flow in the visual cortex was shown in one PET study to have a positive, linear dependence on the rate of stimulation up to approximately 8 Hz (23, 24). An identical rate–response function has been demonstrated in the visual cortex using neuro–functional MRI techniques (27, 171, 221). Effects of auditory word presentation rate have been demonstrated in some but not all active areas of the temporal lobe auditory cortex using PET (200, 245).

In the following studies, time course series of images were collected during which the rate of forefinger to thumb finger tapping was varied from 1 Hz to 5 Hz. Subjects were instructed to tap their fingers on pace with a metronome. Relative fractional signal changes in primary motor cortex, were then measured.

Figure 4.16 is a plot of signal vs. time from a pixel in the primary motor cortex. The tapping frequency was varied every 20 sec. from 5 Hz down to 1 Hz, and back up to 5 Hz.
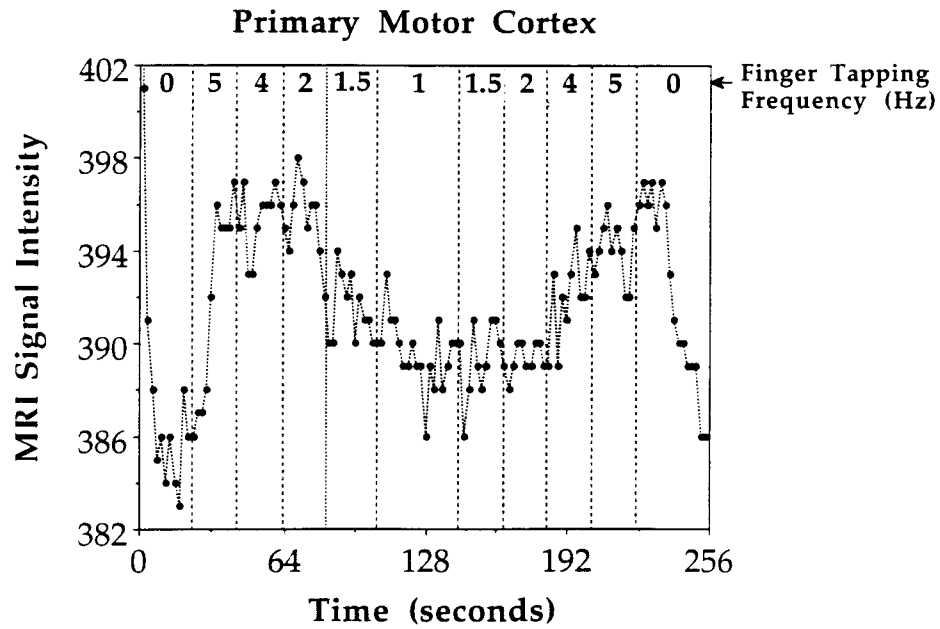
Figure 4.16: Signal vs. time plot from primary motor cortex, during which the subject varied tapping frequency from 1 Hz to 5 Hz.

In a similar study, the subject alternated rest with finger tapping at a single frequency in separate time course trials. In a region in the motor cortex, the percent signal change from baseline was measured. Figure 4.17 shows the relationship, in this study, between percent signal change and tapping frequency. A linear relationship, above 2 Hz, is observed.

Primary Motor Cortex
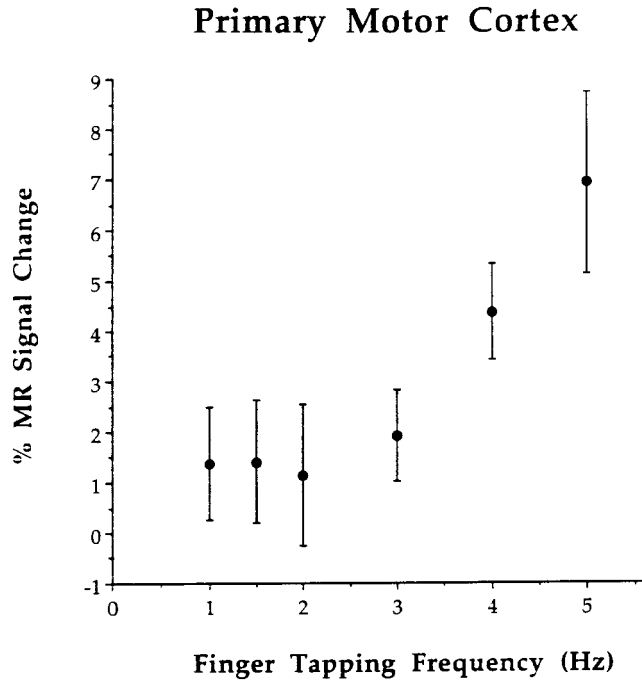
Figure 4.17: Fractional signal change vs. finger tapping frequency from a region in primary motor cortex.

On the vascular level, the implication is that, with an increase in tapping frequency, the excess in oxygen delivery increases. The neuronal and vascular mechanism by which this occurs is not well understood. Nevertheless, this study implies that MRI is able to detect graded responses that occur on the neuronal and/or hemodynamic level.

4.8 DYNAMICS OF PHYSIOLOGICAL FLUCTUATIONS

To complement the study of the activation–induced signal change dynamics, it is also important to characterize the nature of the noise. Many physiological factors effect the MR signal in space and in time. The signal

114

change that is elicited during brain activation likely originates from perfusion or oxygenation changes. MR sequences are, in general, sensitive to gross motion and flow. A resting brain moves at respiration and cardiac frequencies. Blood and csf in the brain also change flow velocities during the cardiac cycle. These effects on echo – planar images have been characterized (267). The preliminary study described below maps the predominant noise source.

In this study, a time course of images was rapidly collected during rest. After reaching steady state magnetization, 125 images were collected in 25 sec. Voxel volume = 3.75 x 3.75 x 10 mm^3. Flip angle = 60°. TR = 200 ms. Signal intensity was measured from a voxel in the sagittal sinus. Figure 4.18 shows a plot of signal vs. time and the Fourier transform of that signal. The peak at about 45 beats per minute corresponds to the volunteer's heart rate. An anatomical image of the axial slice observed and the spectral density image at that frequency is shown in Figure 4.19. High signal intensity regions in this image correspond to regions of csf and large vessels. The reason for these signal changes is likely periodic time–of–flight inflow effects of unsaturated magnetization.
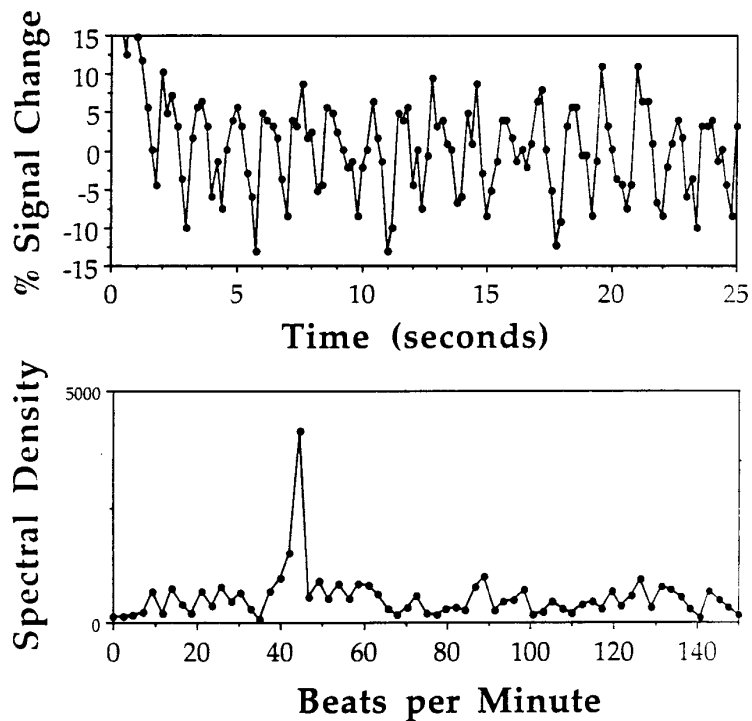
Figure 4.18: Signal change vs. time from a voxel in the sagittal sinus, and, below, the Fourier transform of the signal change, showing a peak at the heart–rate.
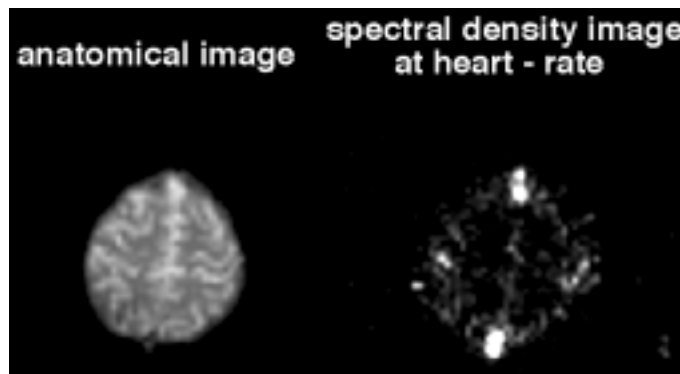

Figure 4.19: Anatomical image and spectral density image at the heart–rate frequency peak, revealing regions of pulsating signal changes in the brain.

116

This cardiac cycle source of noise, as well as that due to respiration–induced changes, have been found to be the predominant source of noise in fMRI (257, 258). Elimination of this noise by band–stop filters (260) or other techniques would a) allow parametric statistics to be applied to the data, by removing all noise that does not have a normal distribution, and b) increase the overall contrast to noise in fMRI studies, allowing for more subtle signal changes and signal change differences to be discerned.

4.9 DISCUSSION

These preliminary studies are an initial attempt to characterize the general response characteristics of the activation–induced MR signal changes. It is necessary not only to determine the average response characteristics, but also the variations across pulse sequence, space, and task, so that more *a priori* information may be applied to post processing strategies and so that underlying mechanisms of contrast may be extracted by comparison to physiological models already constructed using other techniques.

It was found that the latency varies slightly with pulse sequence, over space, and possibly with the task performed. It was also found that the time for the signal to return to baseline after the cessation of the task is slightly longer than the initial signal increase time. Furthermore, it was also found that the hemodynamic transfer function is essentially a low pass filter in the detection of neuronal firing, but the hemodynamic response system has a very high gain, such that brief episodes of brain activation still elicit a signal change. The system also exhibits a graded response with intensity of task, as shown by the dependence of the signal change on finger tapping rate. It is shown that in many regions of the brain in the vicinity of pulsatile csf and

blood, the noise is not normally distributed, and has most power at the heart rate frequency.

In general, to correlate signal changes with neuronal activity quantitatively, more needs to be understood regarding a) the relationship between neuronal firing (number of neurons and their firing rate) and the intensity of a task, stimulus, or "cognitive load," b) the coupling mechanism between neuronal firing an vasodilatation, and c) the exact relationship between the MRI signal enhancement and all the relatively unknown details concerning the pixel by pixel distribution of blood oxygenation and volume, as well as vessel geometry. These unknowns are addressed in several manners in the following chapters.

CHAPTER 5

POST PROCESSING STRATEGIES

5.1 INTRODUCTION

Brain activation is accompanied by localized hemodynamic events that cause MR signal changes. These changes are typically detected, in time, by sequential collection of susceptibility-weighted and/or flow-weighted images.

A goal in post-processing of fMRI time-course data sets is to extract and map as much "interesting" information as possible as robustly and efficiently as possible. In this course, an overview of the strategies, issues, and challenges involved with achieving this goal are presented.

Generally, the better methods use as much *a priori* information as possible concerning a) the expected activation - induced signal change (the neuronal response and hemodynamic transfer function) and b) the noise, artifacts, and physiologic fluctuations, so that the two may be reliably separated. However, if too much is assumed, "interesting" information may be overlooked or not optimally extracted. It is important, given imprecise knowledge of the variations in the types of neuronal and hemodynamic responses, to balance extraction power with a healthy amount of criticality.

In this chapter, image processing strategies for functional magnetic resonance imaging (fMRI) data sets are considered. The analysis is carried out using the mathematics of vector spaces. Data sets consisting of *N* sequential images of the same slice of brain tissue are analyzed in the time-domain and also, after Fourier transformation, in the frequency domain. A technique for

thresholding is introduced that uses the shape of the response in a pixel compared with the shape of a reference waveform as the decision criterion. A method is presented to eliminate drifts in data that arise from subject movement. The methods are applied to experimental fMRI data from the motor-cortex and compared with more conventional image-subtraction methods. Several finger motion paradigms are considered in the context of the various image processing strategies. The most effective method for image processing involves thresholding by shape as characterized by the correlation coefficient of the data with respect to a reference waveform followed by formation of a cross-correlation image. Emphasis is placed not only on image formation, but also on the use of signal processing techniques to characterize the temporal response of the brain to the paradigm.

The activation-induced signal change has a magnitude and time delay determined by an imperfectly understood transfer function of the brain. This transfer function may be characterized by variables independent of brain activity and variables dependent on brain activity. Activity-independent variables that are likely to be relevant include the baseline values of blood pressure, hematocrit, blood volume, blood pO_2, perfusion rate, vascular tone, and neuronal metabolic rate. Activity-dependent variables include vasodilatation magnitude, location, and activated changes in the values of blood volume, blood oxygenation, blood perfusion, and neuronal metabolic rate, all of which may be affected by the number and firing rate of individual neurons.

Images depicting activation induced brain function are generally created by subtraction of magnitude images obtained during a resting state from magnitude images of the same tissue obtained during activation (171, 172, 177, 181, 227). As the number of images used for averaging increases, the

time of imaging increases, allowing other physiological processes (i.e., gross motion, pulsatile blood and CSF flow, and pulsatile brain motion) to contribute to artifactual signal changes unrelated to induced neuronal activity. These artifactual signal changes, if not removed, contaminate the images. Simple image subtraction neglects useful information contained in the time response of the activation-induced signal change, and is, therefore, an ineffective means to differentiate artifactual from activation-induced signal enhancement. Use of a time course of single-shot echo-planar images in combination with control of the brain-activation timing results in data that can be processed in ways that permit differentiation of activation from artifact. Several methods to obtain high contrast-to-noise brain function images that are artifact-free are described here. It should be mentioned that the mathematical development and the writing of the post processing code was carried out primarily by Andrej Jesmanowicz.

The brain-function image formation strategies introduced in this paper make use of a time-course of sequentially-obtained single-shot echo-planar images of the same plane. The data set is a block of two spatial dimensions and one temporal dimension. A thresholding technique that uses the *shape* of the time-course signal for the decision criterion is introduced and described. Data are examined both in the time domain and, through Fourier transformation of the time-course data in each pixel of the data set, in the frequency domain. A motor cortex activation paradigm is used to compare the post-processing strategies of simple image subtraction, temporal cross-correlation, and Fourier analysis, and to illustrate the effectiveness of the thresholding technique. The number of cycles of the finger tapping activation paradigm was also varied to illustrate characteristics of the Fourier analysis. Lastly, fMRI display methods are discussed.

A data set consisting of *N* images acquired from the same slice of tissue at equally spaced intervals of time is considered. Combining and processing of multiple data sets from a particular individual or from a number of individuals is explicitly not considered. The mathematical development is carried out using the vocabulary of vector spaces (369).

Functional response to a typical motor cortex activation paradigm serves to illustrate the nature of the data more specifically. Figure 5.1 displays the first image in the time course. Regions A and B cover the right and left motor cortices, respectively. Region C covers the sagittal sinus. The time course consisted of 128 images and lasted 4 min. 16 sec. The activation paradigm was self-paced sequential tapping of fingers to the thumb. Starting with image #5, the subject was instructed to tap the right fingers for eight images (16 sec), then immediately to tap the left fingers for eight images and so on, until the end of the time course. Figures 5.2 a b and c are 7 x 7 pixel time-course displays corresponding to the boxed regions of Figure 5.1. The combination of spatial and temporal information in Figs. 5.1 and 5.2 allows easy identification of temporally correlated signals in active brain regions.
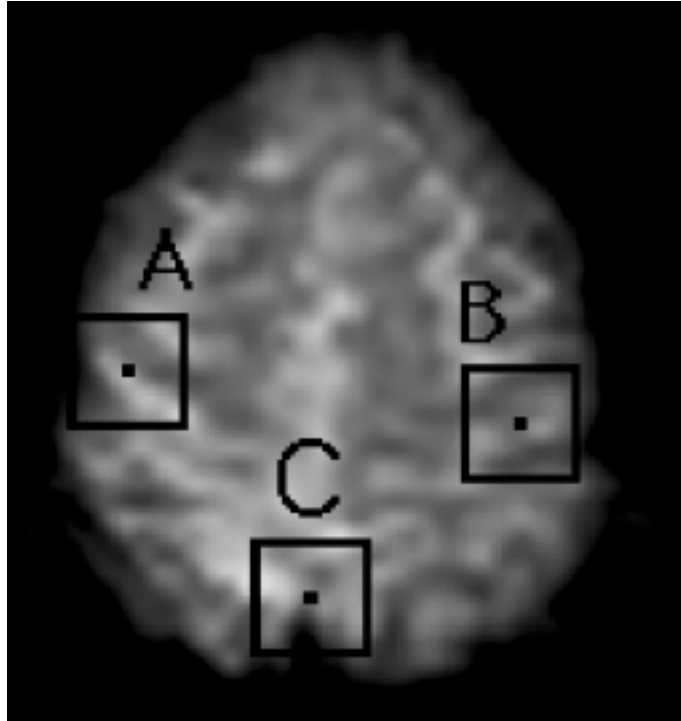
Figure 5.1: Axial image containing the motor cortices. Voxel dimensions are 3.75 x 3.75 x 10 mm. TR/TE = ∞/40. This is the first image from the echo-planar time-course series and is used as an anatomical reference. The high signal intensity from CSF highlights contours of the sulci. Boxes A and B are 7 x 7 pixel regions presumably covering the right and left motor cortices, respectively. The spectral-spatial and temporal-spatial plots, shown in Figs. 5.2 and 5.3, are from the boxed regions. The time-course and spectral plots shown in Figs. 5.5, 5.8 and 5.10 are from the center pixel in each box.

In the display of Figure 5.2, the lowest value of the N data points in each pixel has been set to zero. Thus, the signal intensity offsets of the data in the various pixels of Figure 5.2 with respect to true zero are, in general, different. Data corresponding to the first several images in the time course are

acquired before magnetization has reached equilibrium. These points are present in the display of Figure 5.2, but are usually deleted manually during image processing. Figure 5.2 is called a "temporal-spatial" display since the data are in the time domain. All data are positive and displayed to the same scale.

It may be desirable to create an alternative display for visual inspection by forming the magnitude of the Fourier transform of the data in each pixel of Figure 5.2. The cyclic and interleaved time response induced by the interleaved hand modulation of the finger-tapping task is appropriate for Fourier analysis (220, 289).
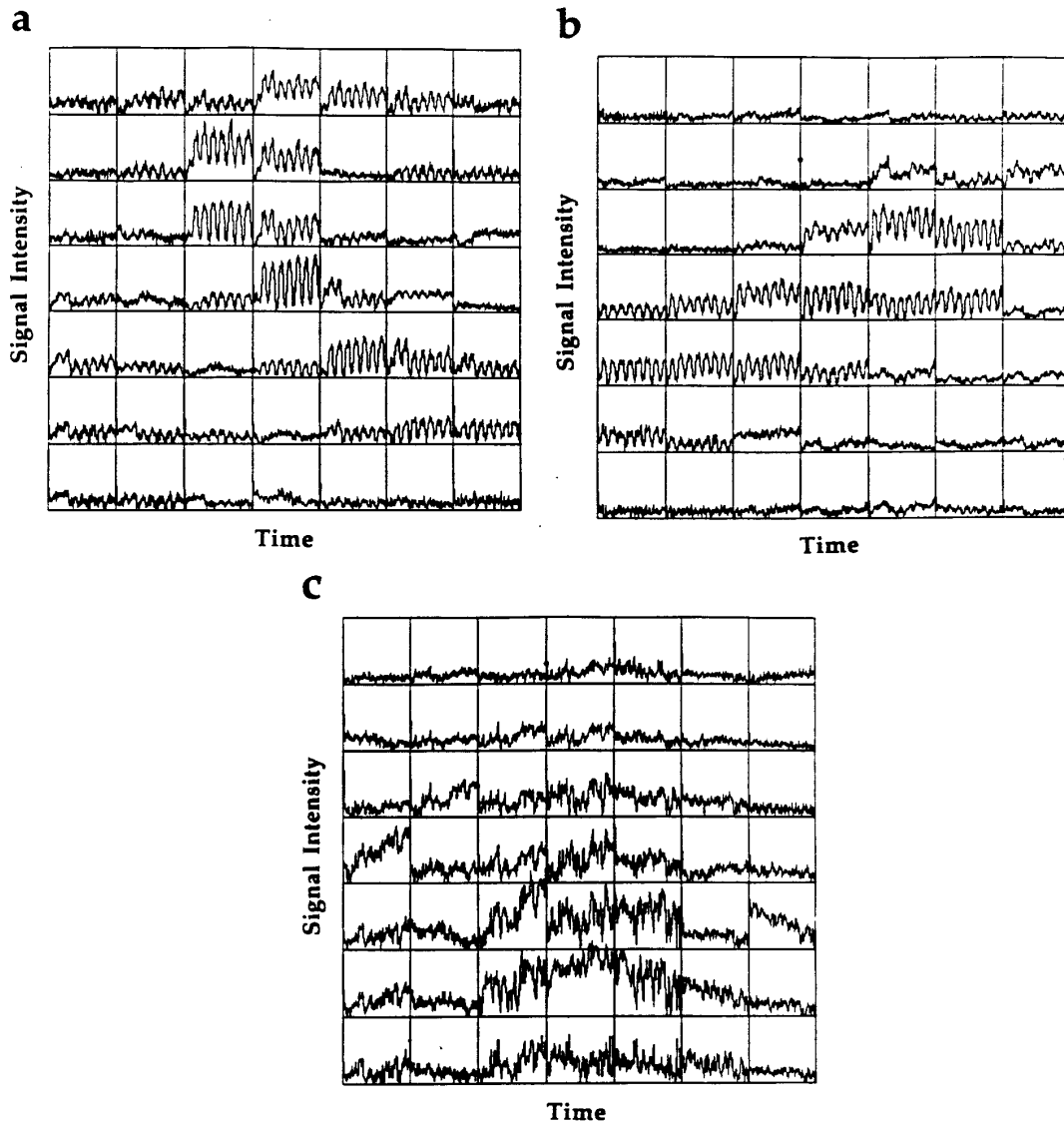
Figure 5.2: Temporal-spatial plots from the 7 x 7 pixel boxes in Figure 5.1. The active regions, revealed by the signal changes temporally correlated to the activation time course, are sharply outlined. a) Plot from box A, covering the right motor cortex. b) Plot from box B, covering the left motor cortex. c) Plot from box C, covering the sagittal sinus.

In order to produce such a display, the first few data points in a given pixel are deleted as determined by inspection of the data: five such points is

typical. The vertical axis is then redefined such that zero corresponds to the average value of the remaining data. The data are then shifted to the left and zeros added as required to arrive at a number of points that is equal to a power of two, usually 128. The FT is calculated assuming the signal is real.

Figures 5.3 a, b, and c show the magnitude of the Fourier transform of the time response in Figs. 5.2 a, b, and c. In the process of forming the magnitude, phase information is lost, and, therefore, Figure 5.3 intrinsically contains less information than Figure 5.2. The display of Figure 5.3 is called a "spectral-spatial," display since the data are in the frequency domain.
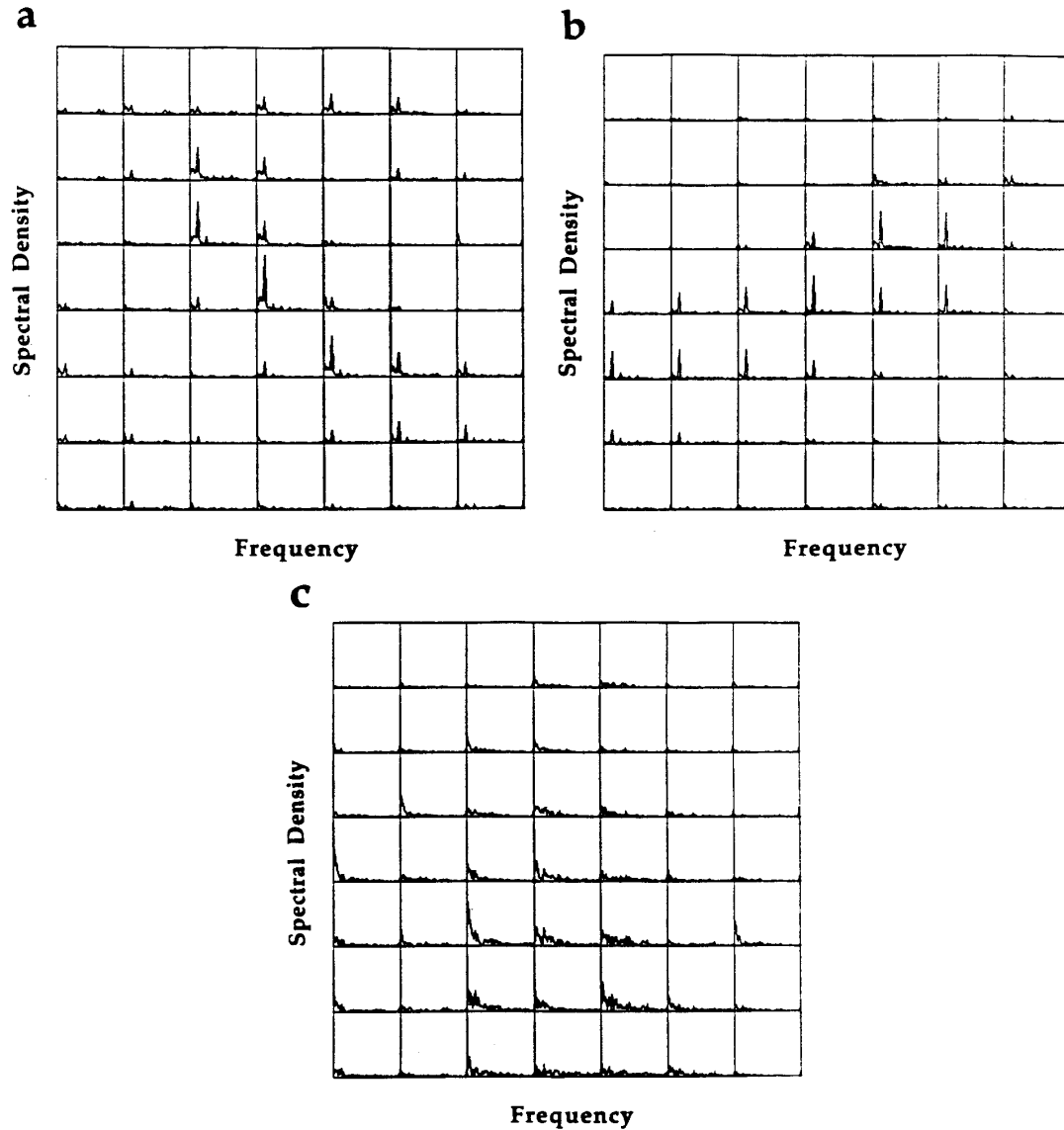
Figure 5.3: Spectral-spatial plots from the 7 x 7 pixel boxes in Figure 5.1. Application of the Fourier transform to each pixel in the time-course data set gives a sharp peak at the activation frequency. a) Plot from box A, covering the right motor cortex. b) Plot from box B, covering the left motor cortex. c) Plot from box C, covering the sagittal sinus.

127

Signal processing begins with the data in either a temporal-spatial or spectral-spatial display. There are two objectives of signal processing in functional magnetic resonance imaging: mapping of the response onto an anatomical image, and characterizing the temporal response. The time-domain data of Figure 5.2 as well as the frequency-domain data of Figure 5.3 can be of value in achieving each of these objectives.

Key to our approach is formation of the correlation coefficient, *cc*, for each pixel.

$$cc = \frac{\sum_{n=1}^{N} (f_i - \mu_f)(r_i - \mu_r)}{\left[\sum_{n=1}^{N} (f_i - \mu_f)^2\right]^{1/2} \left[\sum_{n=1}^{N} (r_i - \mu_r)^2\right]^{1/2}}$$

[5.1]

Here f_i ($i = 1...N$) is the time-course function in a given pixel. It can be considered to be an N dimensional vector. There is no requirement that N be a power of 2 for temporal data in calculating the correlation coefficient. A reference waveform or vector is denoted by r_i. This reference may be an experimental time-course function **f** in some particular pixel or an average of several experimental **f**'s, which is then correlated with the **f**'s in other pixels. Alternatively, it could be synthesized (173). Terms μ_f and μ_r are the average values of vectors **f** and **r**, respectively.

It is instructive to carry through an analysis of Eq. 1 in vector-space vocabulary. Define in N dimensional vector space a diagonal vector **d** of unit length (i.e., all coefficients equal to $N^{-1/2}$). See Figure 5.4a. Then the average value μ_f of the function **f** can be written:

128

$$\mu_f = \frac{1}{N} \sum_{i=1}^{N} f_i = \frac{1}{N^{1/2}} \mathbf{d} \cdot \mathbf{f}.$$

[5.2]

A vector $\boldsymbol{\mu}_f$, is defined, which has values of μ_f along every axis and is therefore along $\mathbf{d}$ and of magnitude $N^{1/2} \mu_f$. Vector $\boldsymbol{\mu}_f$ represents the average value of $\mathbf{f}$. A similar definition is made for vector $\boldsymbol{\mu}_r$. New vectors are defined

$$\boldsymbol{\sigma}_f = \mathbf{f} - \boldsymbol{\mu}_f \quad \text{and} \quad \boldsymbol{\sigma}_r = \mathbf{r} - \boldsymbol{\mu}_r.$$

[5.3]

In classical statistics, the standard deviation of function f, $(SD)_f$, is given by

$$(SD)_f = \left[\frac{1}{N-1} \sum_{n=1}^{\infty} (f_i - \mu_f)^2 \right]^{1/2}$$

[5.4]

and similarly for reference function r. It is noted that the magnitudes of vectors $\boldsymbol{\sigma}_f$ and $\boldsymbol{\sigma}_r$, denoted σ_f, σ_r, are proportional to the corresponding standard deviations.

$$(SD)_{f,r} = \frac{N-1}{N^{1/2}} \sigma_{f,r}$$

[5.5]

Vectors σ_f and σ_r are orthogonal to **d**, (shown in Figure 5.4a), which means only that the averages of the values of their components are zero.

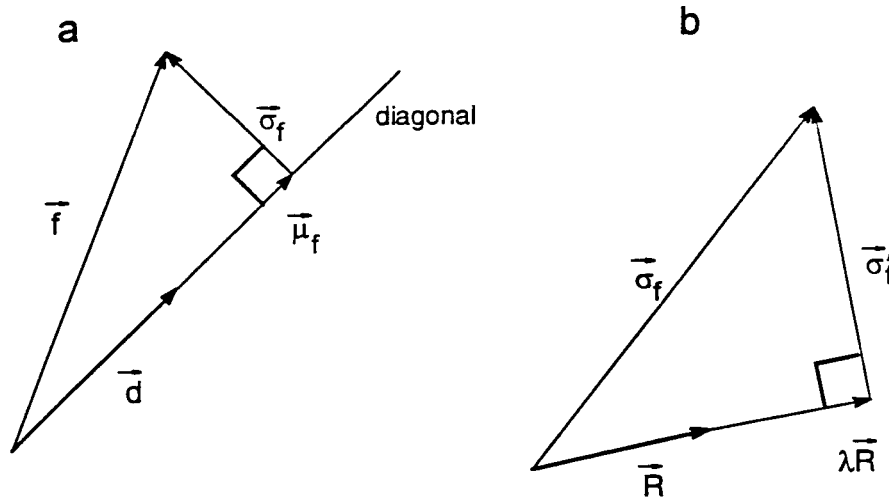**Figure 5.4:** Vector space diagrams. a) Projection of the time-course data **f** onto the diagonal vector **d** provides a definition of vectors μ_f and σ_f. The average value of **f** is given by $|\mu|_f N^{-1/2}$. The standard deviation vector σ_f contains functional information. b) Orthogonalization of σ_f with respect to drift vector **R** in order to arrive at σ'_f, a vector that no longer contains the drift artifact.

This is the simplest and nearly trivial example of orthogonalization of vectors according to the Gram-Schmidt process (369), and is equivalent to shifting the zero of the original data in a pixel such that the average is zero. Vector σ_f contains the functional magnetic resonance information and vector

σ_r is the corresponding reference vector. In vector-space notation, Eq. 5.1 can be written:

$$cc = \frac{\boldsymbol{\sigma}_f \cdot \boldsymbol{\sigma}_r}{\sigma_f \, \sigma_r}.$$

[5.6]

For the purpose of producing functional magnetic resonance images, a "thresholding" technique has been developed. Thresholding suppresses not only noise, but also eliminates spurious correlation in pixels with very large signal changes arising from pulsatile blood and cerebral spinal fluid (CSF) flow (267). A map of zeros and ones of dimensionality the same as the image's is produced. "Ones" are assigned to pixels that have time-course shapes that are similar to that of σ_r and "zeros" to the other pixels. The data set is multiplied by the map. Data that survive are subject to further processing.

The value of *cc* always varies between +1 and -1. A threshold value *TH* between 0 and +1 is selected; and data in each pixel where

$$|cc| < TH$$

[5.7]

are rejected (i.e., set to zero). The correlation coefficient is a measure of the correspondence of the shapes of the reference waveform and the functional waveform.

This thresholding process can be viewed more intuitively using the vocabulary of vector space. The angle a between the vectors σ_f and σ_r is

$$\alpha = \cos^{-1} \left| \left[\frac{\boldsymbol{\sigma}_f \cdot \boldsymbol{\sigma}_r}{\sigma_f \, \sigma_r} \right] \right| .$$

[5.8]

A threshold value *TH* implies acceptance of data when

$$\alpha < \cos^{-1}(TH).$$

[5.9]

A value for *TH* of 0.7 (Eq. 5.7) corresponding to an angle a of 45˚ is a typical and useful threshold. The smaller the angle α, the more closely the shapes resemble each other. Thresholding, as described here, can be carried out using either the time-domain data or the frequency-domain data.

A common artifact in functional magnetic resonance imaging is a linear drift of the signal with respect to time, which seems to arise from slight patient motion during the approximately two minutes over which the data set is acquired and also to be associated with large gradients of image intensity. It is more frequently observed in neurologic patients and less frequently in well-motivated volunteers. In these cases, functional waveforms in the temporal-spatial display are readily recognized by eye, superimposed on a linear ramp. However, correlations with respect to the reference waveform can be very greatly reduced. This type of artifact is readily eliminated from the data by orthogonalization of vectors according to the Gram-Schmidt process (369). The drift is described by a vector, and the component of σ_f that is orthogonal to the drift vector is determined.

The linear drift in the data σ_f is described as the artifactual addition to the true data σ'_f of a signal that varies linearly in index i (i.e., time) and has average value 0. One can write, in vector notation,

$$\boldsymbol{\sigma}_f = \boldsymbol{\sigma}'_f + \lambda \mathbf{R}.$$

[5.10]

Vector, $\mathbf{R}$, describes the linear drift or Ramp, and is normalized. See Figure 5.4b where the relevant geometry is illustrated. The Gram-Schmidt process is designed to find vector σ'_f, which will be orthogonal to $\mathbf{R}$ and, therefore, no longer contain the drift.

Vector $\mathbf{R}$ is known and the problem is to find λ. In addition to Eq. 5.10, one can write

$$\mathbf{R} \cdot (\boldsymbol{\sigma}_f - \lambda \mathbf{R}) = 0$$

[5.11]

or

$$\boldsymbol{\sigma}'_f = \boldsymbol{\sigma}_f - (\mathbf{R} \cdot \boldsymbol{\sigma}_f)\mathbf{R}.$$

[5.12]

Equations 5.10-5.12 describe the elimination of constants and ramps from the original data using Gram-Schmidt orthogonalization. The orthogonalization procedure can readily be generalized to eliminate any function from the original data. It is remarked that drift might also be related to brain activity in some situations. It would be possible to produce an image from the values of λ.

Functional MR images can be produced in a variety of ways. The most powerful for high quality images is the use of Eq. 5.6 to form *cc* on the data of each pixel that has passed the thresholding mask. The correlation coefficient suppresses relative amplitude information. The value *cc* characterizes the shape; identical shapes, but different amplitudes would have the same correlation coefficients. One can produce an image from *cc*, but if relative amplitude information is displayed, the data in each pixel must be multiplied by σ_f / σ_r. Such an image is called a "cross-correlation image." This is a preferred display. In this laboratory, the correlation coefficient images are sometimes referred to a as "normalized" and the cross-correlation images are referred to as "un-normalized." If linear drifts have been removed, σ'_f and σ'_r should be used rather than σ_f and σ_r both for thresholding and for formation of the cross-correlation image. The reference function can also be shifted systematically in small increments of time, which may prove useful in comparing the temporal responses of various brain regions.

As an alternative approach, cross-correlation images following Eq. 5.1 can be formed using the frequency-domain data. Thresholding as described here can be combined with the conventional image display techniques of subtraction of any two images in the original data set, or averaging any two groups of images in the original data set and subtracting them.

If the heart rate is constant during the time of acquisition, artifactual periodic signals can occur that appear in the frequency domain display as a spurious peak unrelated to the stimulation paradigm but dependent on the choice of TR. One can, in fact, produce an image using the amplitude of the signal at this frequency in each pixel in the spectral display, which highlights major arteries and regions of CSF. The peak that appears close to zero frequency in some pixels of Figure 5.3 may be such an artifact. Gram-Schmidt orthogonalization could be used to eliminate periodic signals that are present in the data in situations where the reference function is formed from data in a pixel or group of pixels. However, if the periodic signal is absent in the reference function, it will be automatically suppressed in the correlation image.

5.2 APPLICATIONS

Activation Paradigm

The response to the activation paradigm used above is considered in more detail. Figure 5.5 displays the time course of the center pixels in boxed regions A and B of Figure 5.1 along with the timing of the activation paradigm and the corresponding Fourier transforms. Although a delay is present between stimulus and activation, the relative phase of the signal enhancement between hands and the magnitude of the signal enhancement remains relatively constant. The boxed regions A and B cover, presumably, the right and left motor cortices, respectively. The signal enhancement from each box follows the activation timing from the contralateral hand.
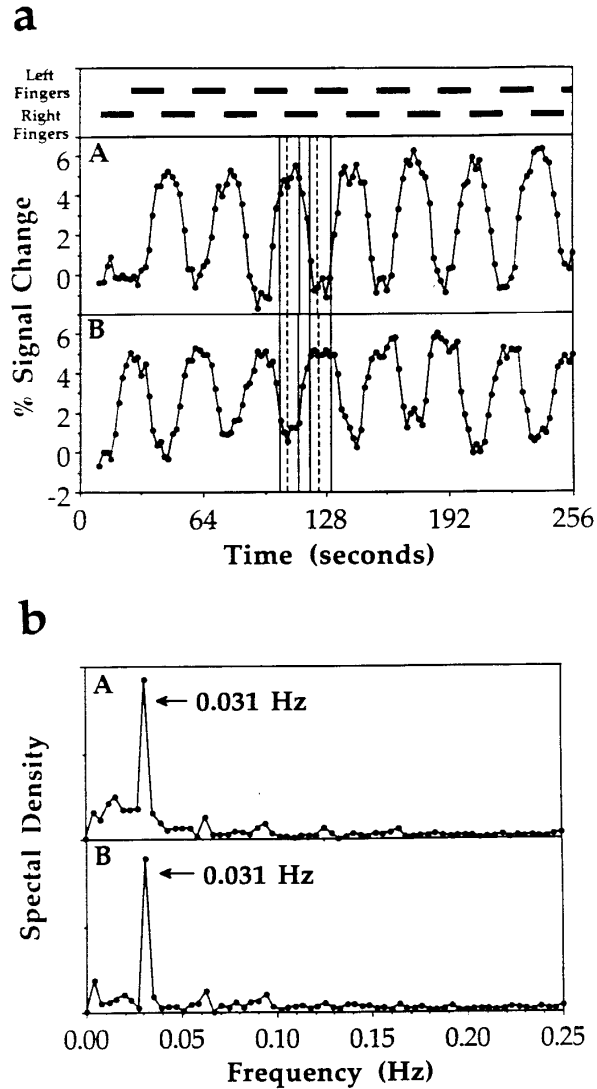
Figure 5.5: Plots from the center pixels in boxed regions A and B of Figure 5.1. The activation paradigm of interleaved alternating hand finger movement is shown at the top. The on/off cycle rate is 0.031 Hz. a) Plots from the center pixels in boxes A and B show close correspondence to the left and right finger movements, respectively. b) Plots of the spectral density vs. frequency from the center pixels in boxes A and B reveal sharp peaks at the same frequency, 0.031 Hz. The maximum oscillation frequency detectable, 0.25 Hz, is the Nyquist frequency (NF), and is determined by $NF = 1/(2 \times TR)$.

Subtraction

Images 54 and 62, illustrated by the dotted lines in Figure 5.5a, were obtained during periods of peak signal enhancement for the right and left motor cortices, respectively. The image obtained by subtracting Image 54 from Image 62 (shown in Figure 5.6a) reveals the expected positive signal enhancement in the left motor cortex and negative signal enhancement in the right motor cortex. Note the artifactual signal enhancement in the sagittal sinus region, which is likely to arise from time-of-flight flow effects of CSF or blood (267).
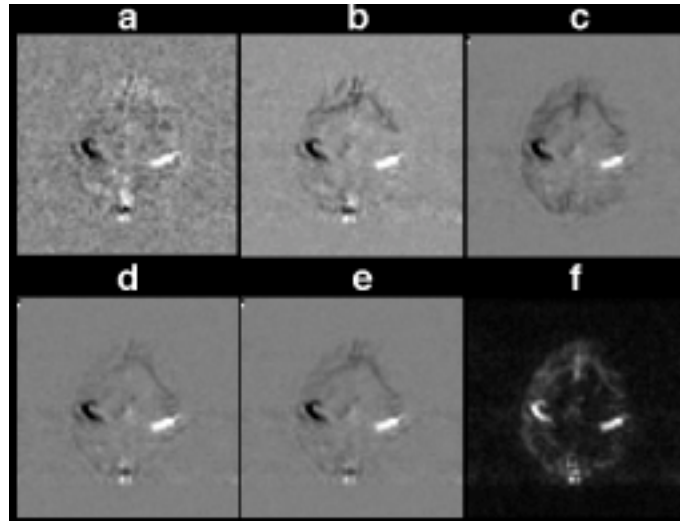
Figure 5.6: Functional images from identical time-course series obtained by six different methods. a) Single image subtraction of Image 54, obtained during peak right motor cortex activation from Image 62 obtained during peak left motor cortex activation (illustrated in Figure 5 by dotted lines). b) The average of Images 52-57 subtracted from the averaged Images 60-65 (illustrated by solid lines in Figure 5). c) Cross-correlation image obtained by taking the dot product of each time-course vector with a synthesized box-car vector (displayed in Figure 7a). d) Cross-correlation image obtained by taking the dot product of each time-course vector with vector Figure 5.5a from the center of box B. e) Cross-correlation image obtained by taking the dot product of each time-course vector with the synthesized time-averaged vector of Figure 5.7b (see text). f) Spectral density image. Note that the phase information is lost.

<u>Averaging with Subtraction</u>

The ranges of averaged images are shown in Figure 5.5a as solid lines on each side of each dotted line. The average of Images 52 to 57 was subtracted from the average of Images 60 to 65 and displayed in Figure 5.6 b. Although, the image quality is improved somewhat, the artifactual signal enhancement in the sagittal sinus region is still present.

<u>Cross Correlation</u>

Box-car "ideal" vector. Figure 5.7a illustrates a first approximation of the activation-induced signal enhancement time course. The box-car waveform can be considered as a 128 dimensional vector. The delay between the induced signal enhancement and neuronal activation is taken into consideration by adjustment of the phase of the box-car waveform. The dot product (i.e., scalar product) of this reference vector with each vector formed by the time-course signal evolution in each pixel is displayed in Figure 5.6c. This is a cross-correlation image using a synthesized reference as discussed in the Theory section. The dot product of a box-car waveform and a time-course series is essentially the same as averaging all images during the interleaved "on" periods and subtracting the average of all images during the interleaved "off" periods. Because all 128 images in the time course were used, the contrast-to-noise increases, even though the actual pixel responses do not represent box-car waveforms. In fact, the use of a box - car waveform may filter spurious correlations contained in the data that are related to respiration and heart rate.
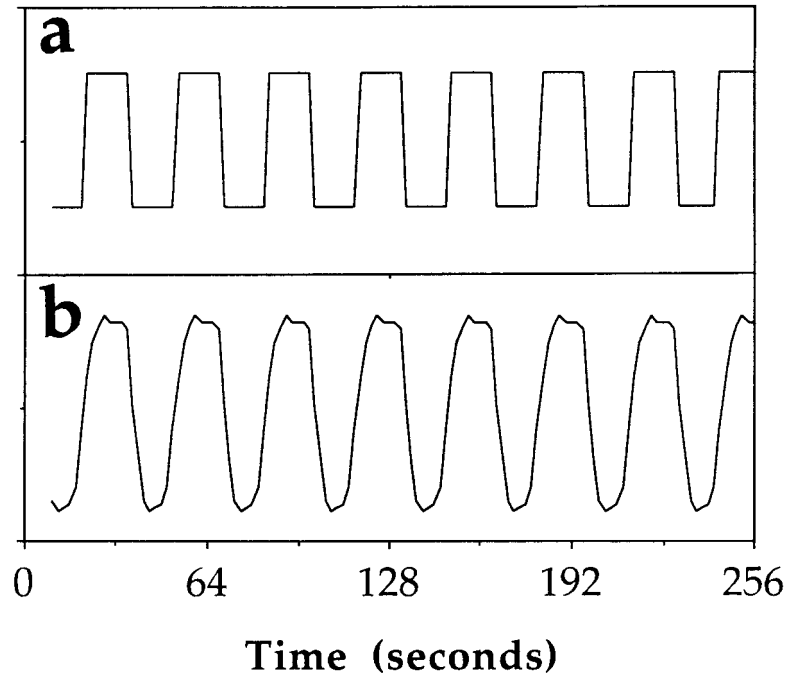
Figure 5.7: Synthesized vectors used to create functional images. Both vectors correspond with expected signal enhancement in the left motor cortex (box B, Figure 5.1). a) Box-car waveform used in creation of the cross-correlation image in Figure 5.6c. b) Time-averaged waveform used in creation of the cross-correlation image in Figure 5.6e. (See text.)

Actual pixel vector. The temporal response of the MR signal to functional brain activity is an incompletely understood process in which information is transduced from neuronal activity through vascular changes, blood chemistry changes, and field inhomogeneities to changes in the MR signal. Therefore, until an accurate and well parameterized model for functionality induced MR signal changes is established, the use of ideal response vectors as the basis for correlation is necessarily over simplistic. As an alternative, it is useful empirically to select the response of one or more

140

pixels in the actual data set for use as the reference vector. The correlation image using this reference vector is displayed in Figure 5.6d. The image quality is improved compared with Figure 5.6c (because the reference vector more closely approximates the actual response vectors and the dot products are higher). A problem with using this strategy for creating a reference vector is that any artifactual signal enhancement related to, among other artifacts, gross motion, pulsatility, or flow, may also be present in the reference vector; artifactual signal changes that may occur at various times in the time course will appear correlated to the reference vector. In addition, the noise that is present in the reference vector will correlate with itself, creating an artificially elevated magnitude of correlation in that pixel.

Time-averaged response vector. In this section, a reference time-course vector is considered that is formed by averaging across cycles in time. A time-averaged response vector was produced by averaging each 16-image (32 sec) cycle of vector B in Figure 5.5a, and replicating this time-averaged cycle throughout the time-course vector. The time-averaged-response vector is illustrated in Figure 5.7b. The corresponding cross-correlation image using this reference vector is displayed in Figure 5.6e. The image quality is improved slightly, although signal enhancement is still present in the artifactual region near the sagittal sinus. The artifactual signal enhancement was not as evident in the image that was created using the box-car reference vector. This may suggest some slight correlation of the signals from the sagittal sinus with a specific aspect of the reference vector. Very high signal-intensity variations with only slight correlation will cause artifacts in a functional image created in this manner. The thresholding method addresses this issue, as will be shown.

Fourier Transform

Figure 5.5b shows the magnitude of Fourier transforms of the time responses in Figure 5.5a. A peak is apparent at 0.031 Hz. The spectral-density image at 0.031 Hz is shown in Figure 6f. Both motor cortices are switching at identical rates, although, exactly out-of-phase. The activation pattern is the same as that revealed by the cross-correlation techniques. The signal enhancement at the sagittal sinus appears once again and is due to the broad-band effect that occurs with sampling of time-of-flight signal changes that occur throughout the cardiac cycle.

Faster switching paradigm. The paradigm was changed so that the subject doubled the switching rate of Figure 5.5a. The time courses of the same pixels in the center boxes A and B are displayed in Figure 5.8a along with the Fourier transforms of the corresponding time plots, Figure 5.8b. As expected, the peak is shifted to 0.062 Hz. The spectral-density image at this peak (Figure 5.9a) reveals the same activation pattern with less artifactual signal enhancement. The cleaner image arises from reduced spurious harmonic content at 0.062 Hz in the original time-course data relative to 0.031 Hz, but the physiological basis for this observation is not well understood.
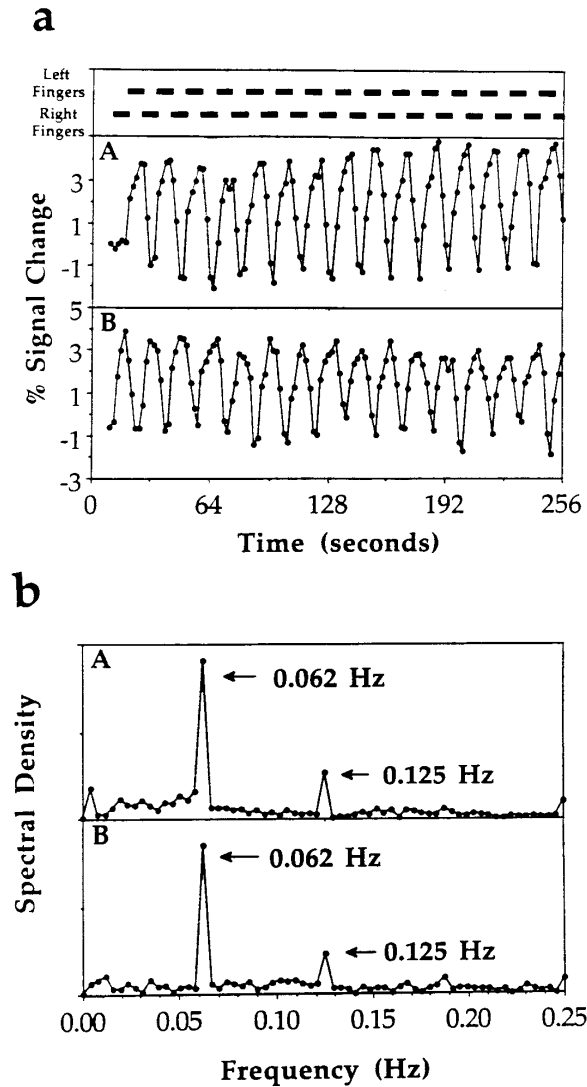
a

b

Figure 5.8: Plots from the center pixels in boxed regions A and B of Figure 5.1. The activation paradigm of interleaved, alternating hand finger movement is shown at the top. The on/off cycle rate is 0.062 Hz. a) Plots from the center pixels in boxes A and B show close correspondence with the left and right finger movements, respectively. b) Plots of the spectral density vs. frequency from the center pixels in boxes A and B reveal sharp peaks at the same frequency, 0.062 Hz. Also evident is response at the second harmonic, 0.125 Hz, indicative of the asymmetric nature of the time course.
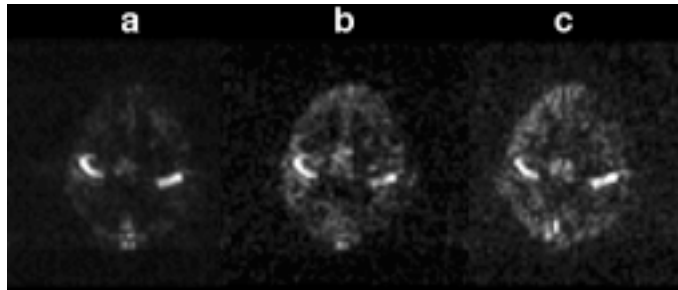
143

Figure 5.9: Functional images obtained by Fourier transform of the time-course data set. a) Fundamental frequency image at the spectral peak of 0.062 Hz (see Figure 5.8b). b) Second harmonic image at the 0.125 Hz peak. The second harmonic image gives spatial information related to regions that have asymmetric time courses. c) Fundamental frequency image at the spectral peak of 0.125 Hz (see Figure 5.10b), demonstrating that 8 sec on/off cycle rates may be used in creation of functional images.

Higher harmonics are observed in the spectral displays as well. The second harmonic image at the 0.125 Hz peak, indicative of the asymmetric nature (i.e., lack of symmetry about the peak center) of the time response, is shown in Figure 9 b. The activation pattern varies somewhat. The premotor, sensory and supplementary motor regions appear enhanced.

Fastest switching paradigm. The switching rate was redoubled to 0.125 Hz. The time courses (Figure 5.10a) involve the same pixels used previously. They show an increase in the steady-state baseline because the hemodynamic response is insufficiently rapid to follow the paradigm. Nevertheless, the vascular response is incompletely damped, and form the Fourier transform of the response exhibits a peak at 0.125 Hz (Figure 5.10b). The spectral-density image at 0.125 Hz (Figure 5.9c) reveals, once again, the same activation pattern

as Figure 5.9a, but with increased artifactual signal enhancement. This is likely to arise from a decrease in relative amplitude of the spectral-density peak because of a decrease in the average amplitude change in the time course.
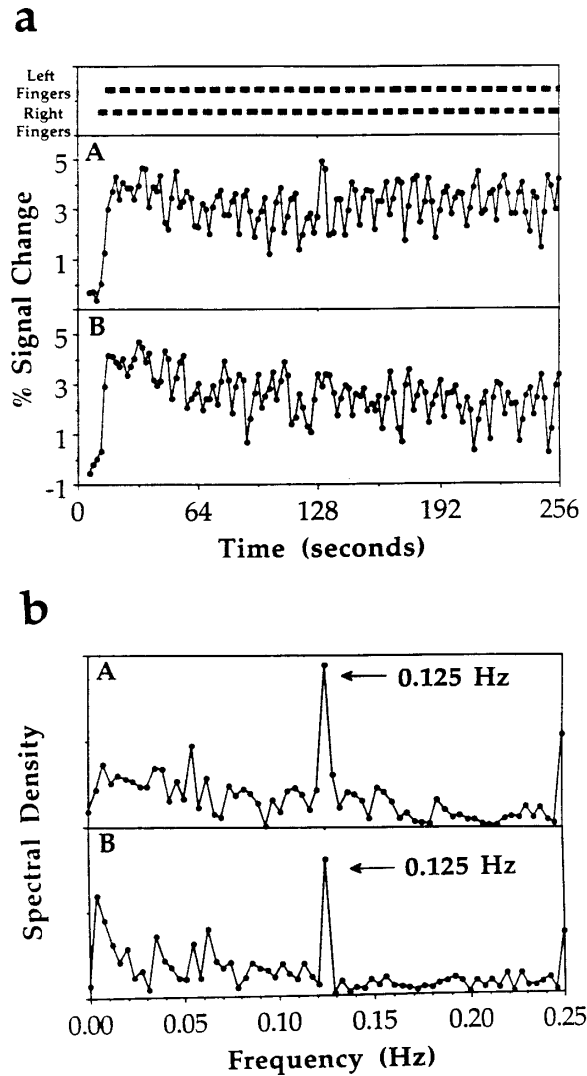
Figure 5.10: Plots from the center pixels in boxed regions A and B of Figure 5.1. The on/off cycle is 0.125 Hz. a) Plots from the center pixels in boxes A and B correspond with the left and right finger movements, respectively. Because of the high oscillation rate, the baseline value is at a higher steady-state level and the oscillation amplitude is reduced; however, the on/off cycle is clear. b) Plots of the spectral density vs. frequency from the center pixels in boxes A and B reveal sharp peaks at 0.125 Hz. A second harmonic peak is apparent.

Multiplexed frequency switching paradigm. In using the Fourier transform technique, only the frequency of the activation needs to be known to create a brain function image. An advantage of this analysis technique is that multiple stimuli can be multiplexed into a single time course to reveal activated brain regions in spectral density images that correspond with each activation frequency.

To demonstrate this advantage, a subject was cued to moved the fingers of the right hand at an on/off switching rate of 0.08 Hz, and the fingers of the left hand at a 0.05 Hz. The time course consisted of 94 sequentially obtained images. The first image in the time course is shown as a reference in Figure 5.11. Figures 5.12a and b are 5 x 5 pixel matrices of time courses from the regions corresponding to boxes A and B in Figure 5.11. Figure 5.13a shows the activation timing for each hand and the signal response from the center pixel in each region. It is observed that the time course of box A (over the right motor cortex) and box B (over the left motor cortex) follow the activation frequencies of the left and right hands, respectively. The Fourier transform of the data set (Figure 5.13b) reveals peaks at 0.08 Hz and 0.05 Hz. Spectral density images at each peak (Figs. 5.14a and b) reveal enhancement in the right and left motor cortices, respectively, as well as broad-band artifact in the sagittal sinus.

It is interesting to note that, while a detailed comparison between correlation methods and Fourier methods is outside the scope of this chapter, a few subtle differences exist between the techniques.

First, consider the case of only one paradigm timing that is used in a series of images. As shown above, the Fourier transform from an activated region consists of a fundamental and possibly several harmonics since the signal behavior over time does not represent a perfect sinusoid. Calculation

of the correlation of the time course of images with a more precisely matched waveform (such as that in Figure 5.7b) would increase the signal to noise ratio of the functional image over that of observation of the spectral density at the fundamental, since much of the spectral power is spread over the harmonics. Nevertheless, to use the correlation method optimally, the shape of the waveform needs to be known. The shape of the waveform is never perfectly known, but some approximations can be made. For paradigms that have extended on or off times (i.e.: those that approach the appearance of box-car functions), calculation of the correlation with a box car reference waveform would likely give a higher quality functional image than the calculation of the Fourier transform and subsequent inspection of the spectral density images. As the on / off period becomes shorter, the response begins to represent a sinusoid, therefore, the calculation of the Fourier transform may be preferred. Regardless, it is always optimal to use, as the reference waveform, the function most precisely representing what is expected from the response.

A second subtlety that applies generally is that, not only it is ideal to use the reference waveform most precisely representing what is expected from the response, but it is also ideal to use a task timing that is furthest away from the predominant physiologic noise frequencies. This is likely to occur somewhere between very slow on - off cycles and very fast on - off cycles. Low frequency physiologic fluctuations include those related to gross motion and changes in respiration and/or cardiac cycle rate. High frequency physiologic fluctuations include those related to heart rate, beat frequencies of the heart rate, and respiration rate.

A third subtlety arises when one considers the case of multiplexing two on / off activation timings into one time course. The frequencies chosen for

demonstration of multiplexing were not multiples the same number because the fundamental frequency of one may have overlapped with the harmonic of the other. Even if the timings were orthogonal, some sharing of spectral power of the responses may have occurred, causing imperfect differentiation of distinct functional regions. For the case of correlation with reference waveforms that more closely matched the signal response functions, this problem (sharing of harmonics with fundamentals or harmonics with harmonics) would be reduced, since the expected responses are closer approximations of the actual responses.

It is important to note that, in the limit were the response is exactly a sinusoid, the two techniques (correlation and Fourier transformation) are identical. Direct correlation analysis becomes more powerful as the response shape and periodicity degrade. In the demonstration, the latency insensitivity Fourier transform analysis was demonstrated as an advantage, but this latency insensitivity can also be achieved using correlation analysis as well.
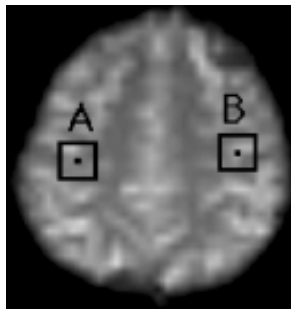

Figure 5.11: Axial image in which the voxel dimensions are 3.75 x 3.75 x10 mm^3, and TR/TE = ∞/40. Boxes A and B are 5 x 5 pixel regions that presumably cover the right and left motor cortices, respectively. The temporal-spatial plots, shown in Figure 5.12, are from the boxed regions. The time-course and spectral plots, shown in Figure 5.13, are from the central pixel in each box.
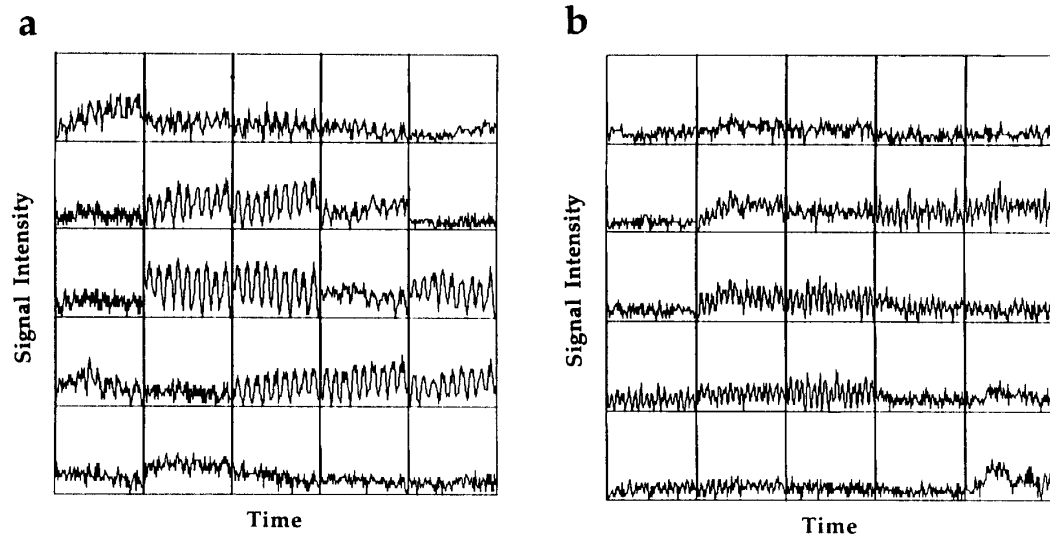
Figure 5.12: Temporal-spatial plots from the 5 x 5 pixel boxes in Figure 5.11. The active regions, which are revealed by the signal changes that are temporally correlated with the activation time course, are again sharply outlined and have distinct frequencies that correspond to the different on/off finger movement cycles of each hand. a) Plot from box A (right motor cortex). b) Plot from box B (left motor cortex).
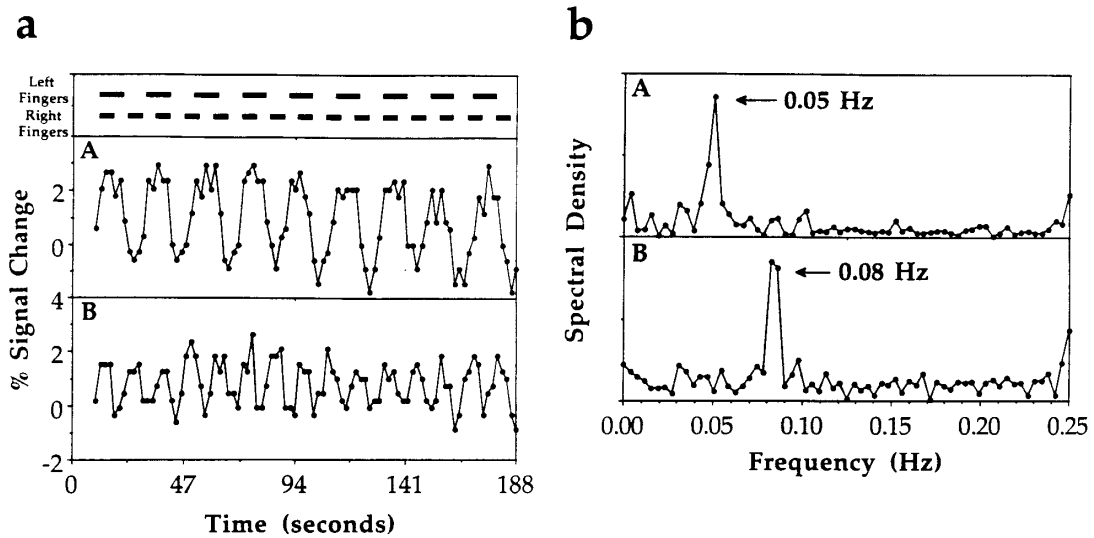
Figure 5.13: Plots from the center pixels in boxed regions A and B of Figure 5.11. At the top is the activation paradigm that involves on/off frequencies of 0.05 Hz for finger movement of the left hand and of 0.08 Hz for finger movement of the right hand. a) Plots from the center pixels in boxes A and B correspond closely with left and right finger movements, respectively. b) Plots of the spectral density vs. frequency from the center pixels in boxes A and B, which reveal peaks at the activation frequencies that correspond again to the left and right hand activation frequencies, respectively. There were no peaks at frequencies that correspond to sums and differences (i.e., the brain did not function as a "mixer" in this experiment). Note that since the activation frequency for either hand did not occur on a multiple of 0.25/128 spectral points, the actual peak is between two points. This misregistration of the peaks results in slightly noisier functional images.
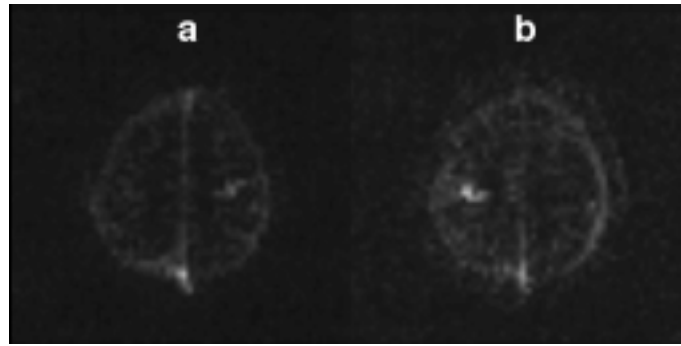
Figure 5.14: Functional images obtained from the Fourier transform data set in which finger movement of the left and right hands was at on/off frequencies of 0.05 Hz and 0.08 Hz, respectively. a) Spectral density image at 0.08 Hz reveals high signal intensity in the left motor cortex. b) Spectral density image at 0.05 Hz reveals high signal intensity in the right motor cortex.

<u>Image Formation with Thresholding</u>

Time domain. A common artifact in time-course data sets occurs near the sagittal sinus or larger vessels. Very intense, seemingly noise-like, fluctuations are seen that are presumably associated with pulsatile flow effects. Cross-correlation with a reference vector can result in apparent response in these regions in the absence of induced brain activation. Figure 5.15 illustrates a *correlation coefficient* image revealing shape correlation during the task activation paradigm of Figure 5.5. The waveform of Figure 5.7b was used as a reference vector, as was the case for Figure 5.6e. Note the difference between a cross-correlation image and a correlation coefficient image: the latter has not been scaled by multiplying by σ_f/σ_r and all pixel values lie between +1 and -1. It is observed that the signal at the sagittal sinus

shows minimal correlation. Figure 5.16a shows the same image as in Figure 5.6e, but with thresholding applied so that only responses that demonstrate a correlation coefficient > 0.25 are used to create the brain function correlation image. Figures 5.16 b and c use the same data set, but with thresholds of 0.5 and 0.75, respectively.
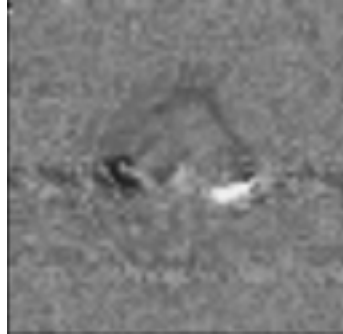

Figure 5.15: Correlation coefficient map of data set from the 0.031 Hz activation paradigm (see text).
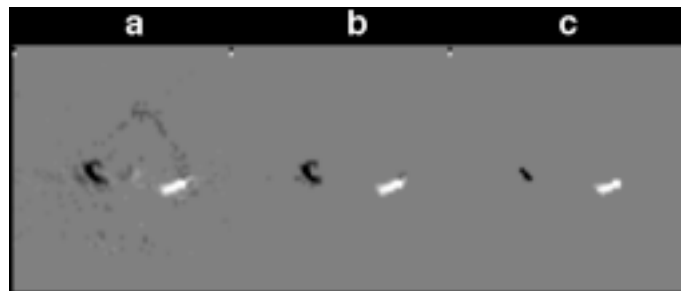

Figure 5.16: Threshold images from the cross-correlation image of Figure 5.6e that correspond to selected correlation coefficient (*cc*) values. In all images, the high signal intensity artifact in the sagittal sinus is removed. Correlation coefficient thresholds: a) 0.25, b) 0.50, and c) 0.75.

While the responses appear, by inspection, highly significant, the statistical significance for acceptance of signals based on the correlation coefficient is not easily determined. Among other variables, the correlation coefficient distribution for all voxels and the temporal correlation of the signal in time need to be considered (274). In addition, the hemodynamic response may vary on a pixel - wise basis depending on hemodynamic factors. Ongoing work is presently being carried out to threshold the data.

A color image at a chosen threshold level may be superimposed upon a reference image chosen from the echo-planar time-course series or from a high-resolution image that was obtained during the same session such that the images are directly registered. The 0.5 correlation coefficient threshold image is superimposed upon the first image in the time-course series (Figure 5.17). The red colors correspond to positive correlation and the blue colors to negative correlation.
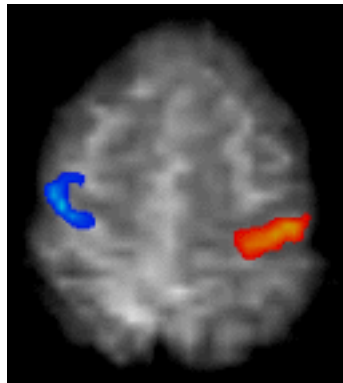

Figure 5.17: The image of Figure 5.16b (0.5 correlation coefficient threshold) is colorized with red, representing positive correlation, and blue, representing negative correlation. The colorized image is then superimposed on and directly registered with the first anatomical image in the time-course series to create a brain activation image with functional and anatomic information.

Frequency domain. Formation of cross-correlation images with thresholding can be carried out using not only time-domain data but also frequency-domain data. This technique was applied to the acquired data using the multiplexed frequency switching paradigm (see Figs. 11-14). Spectral density plots in boxes A and B of Figure 5.13b were used as reference vectors; the threshold was set at $cc = 0.5$; and frequency-domain cross-correlation images were produced; shown in Figs. 5.18a and b, respectively. In this figure, colorized functional images are superimposed on the first anatomical image of the *time-course* data set. Figure 5.18a shows response only in the left motor cortex and Figure 5.18b only in the right. Note that the broadband pulsatile artifacts in the sagittal sinus are removed by the thresholding process.
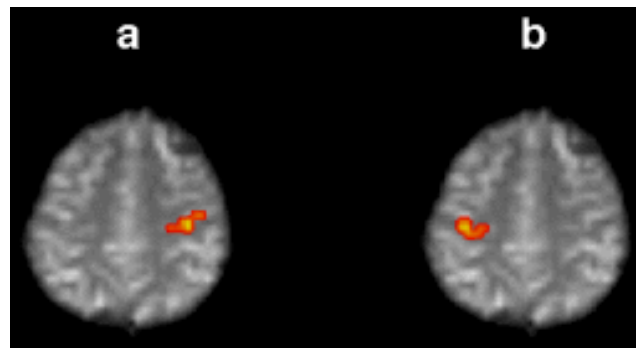
Figure 5.18: Images obtained using a 0.5 correlation coefficient threshold against the reference spectra of Figure 5.13b. Note that the high signal intensity artifacts in the sagittal sinus are removed. The colorized images are superimposed on and directly registered with the first anatomical image in the series. a) Brain activation image obtained using the spectral reference vector with the 0.08 Hz peak. Only the left motor cortex region shows enhancement. b) Brain activation image using the spectral reference vector with the 0.05 Hz peak. Only the right motor cortex region shows enhancement.

5.4 DISCUSSION

Our purpose in this work has been to develop an image processing strategy for fMRI that goes beyond simple subtraction of on- and off-responses to a stimulus. Emphasis has been placed on analysis of data in both the time domain and the frequency domain. In both domains, thresholding according to the correlation coefficient of the data with respect to a reference waveform serves to reject spurious responses. Formation of the cross-correlation image after thresholding provides a high degree of contrast-to-noise. Several approaches to formation of the reference waveform are described, and this is a central aspect of the methods.

Emphasis has been placed on the mathematics of vector spaces. The geometric approach is not a necessity, and its algebraic equivalent is readily written. However, the use of vector spaces is seems appropriate in the context of fMRI. The mathematics is convenient for Gram-Schmidt orthogonalization of artifactual response vectors with respect to activation response vectors.

Information on the temporal response of the brain can be extracted in several ways: 1) Examination of peaks and their relative intensities in the frequency domain display, 2) evaluation of the phase information that is presented in the real and imaginary components of the Fourier transformed data, 3) study of the cross-correlation coefficient as a function of delay using the time-domain data, and 4) variation of rates of activation in the paradigm. Images are readily made that emphasize some aspect of the temporal response. One example, presented here, is an image of the intensity of the second harmonic of the response to a periodic stimulus.

Functional information may be directly registered onto the surface of high-resolution images of the individual's brain. The directly registered information is new to brain imaging modalities.

An array of activation paradigms and post-processing tools tailored to the unique nature of time-course fMRI data and artifacts has been presented. The use of an entire time-course of rapidly obtained images of the same plane immediately gives signal-to-noise advantages. The control of the activation timing and the application of the post-processing methods allow effective removal of the artifactual data and reveal potentially useful information about the relative shapes and phases of the time-course responses to neuronal activation. Spatial and temporal brain function information previously unobtainable by other modalities may now be revealed by effective use of the many advantages of the these fMRI post-processing strategies.

CHAPTER 6

SUSCEPTIBILITY CONTRAST MODEL

6.1 INTRODUCTION

A goal in functional magnetic resonance imaging (fMRI) is the complete understanding of the relationship between brain activation and the observed MR signal changes. In pursuit of this goal, biophysical models that are based on the current understanding of cerebral hemodynamics, blood susceptibility, proton dynamics, and MR physics have been formulated. The model formulation and testing process can give insight into the factors that contribute to the observed activation - induced MR signal changes, and may eventually lead to a quantifiable correlation between the observed signal changes and the underlying neuronal processes.

Several models describing brain activation-induced blood oxygenation level dependent (BOLD) MR signal changes have been published. The models of Ogawa et al. (127), Weisskoff et al. (126, 252), Kennan et al. (116), Yablonsky et al. (118), and Boxerman et al. (124, 190, 192, 210) are particularly instructive in describing specific aspects of BOLD contrast. Most of the models consider two fundamental variables in the context of BOLD contrast: 1) *Magnetic field perturbers.* Red blood cells and blood vessels are considered as magnetic field perturbers. They have a magnetic susceptibility that is sensitive to the oxygen saturation of hemoglobin. During brain activation, the oxygen saturation of hemoglobin is thought to increase locally, causing the magnetic susceptibility of the perturbers to decrease. 2) *Proton dynamics.* The dynamics of protons in the vicinity of these perturbers affects the relative manner in which

irreversible (T2-related) and reversible (T2*-related) dephasing take place. In the context of fMRI- related spin dephasing effects, proton diffusion has been considered to be the most relevant dynamic process. In the above-mentioned models, these diffusion effects are simulated using random walk (Monte Carlo) methods. The positions of the individual spins are tracked over time and their phase histories are recorded.

In this chapter, diffusion is simulated by a deterministic technique first introduced by Wong et al. (128). This technique uses the convolution of a spin density map with a smoothing function, and is deterministic in that no random variables are used.

In this chapter, a simple biophysical model is described which is based on first order approximations of resting and active state cerebral hemodynamics, vessel architecture, blood oxygenation, and proton dynamics. The fundamental variables that are considered include: a) *the susceptibility - induced frequency shift*, which is modulated by blood oxygenation, magnetic field strength, and hematocrit, b) *the vessel geometry*, which includes vessel radii, vessel orientation, and blood volume, and c) *the diffusion coefficient*, which is considered here to be isotropic and unrestricted. The relative and absolute effects of varying these factors on $\Delta R2$ (spin-echo) and $\Delta R2^*$ (gradient-echo) signal are compared with the experimental results reported in the literature.

As a review, the rationale behind the choice of physiological and biophysical variables in the modeling process is first discussed. Second, the relationships, as they have been presented in the literature, between blood oxygenation and spin precession frequency in the vicinity of the particular geometry chosen (infinite cylinder), are then described. Third, the details of formulation and implementation of the deterministic biophysical model are

given. Fourth, an example is presented to illustrate the salient details of the model. Fifth, validation of the deterministic modeling method is carried out by comparison with results of Ogawa et al. (127) which used Monte Carlo methods to simulate spin diffusion. Lastly, several physiological and biophysical parameters are modulated and the effects on the simulated R2 and R2* are observed.

6.2 MODELING CONSIDERATIONS

When attempting to model a physical phenomena, it is ideal to have all of the model parameters accurately represented. Then, the relative significance of each parameter can be precisely determined by repeated simulations in which each parameter value is modulated, keeping all other parameters constant. However, in this particular modeling problem, almost all of the parameters (concerning cerebral hemodynamics, blood oxygenation, and proton dynamics) are not only imprecisely known, but the relative contribution of each parameter to the activation - induced MR signal changes is also not clearly understood. These variables may also vary from voxel to voxel in space. Under these circumstances, the applicability of the model was evaluated by determining whether the simulated results agreed with absolute and relative activation-induced $\Delta R2^*$ and $\Delta R2$ values described in the literature. The relative importance of the various parameters was evaluated by varying one parameter at a time, keeping all the other parameters constant.

Resting State Physiologic Considerations

Hemoglobin Saturation. The susceptibility of blood is linearly proportional to the fractional hemoglobin saturation, Y (108). As blood passes through microvessels in the vicinity of metabolically active cerebral tissue, oxygen is delivered to the tissue, causing the partial pressure of oxygen in the blood, (pO_2), to decrease from approximately 95 mmHg to 30 mmHg (370). The relationship between pO_2 and Y is roughly given by (371):

$$Y \, / \, (1 - Y) = (pO_2/P_{50})^{2.8} \hspace{2cm} [6.1]$$

where P_{50}, the pO_2 at which Y = 0.5, equals 26 mmHg (372). This expression is plotted in Figure 6.1 for illustrative purposes. The fractional saturation of hemoglobin is therefore reduced from 0.97 (arterial side) to 0.59 (venous side) as blood passes through the capillary bed. In the simulations we assume that the MR signal is primarily affected by blood oxygenation changes in the venous end of the capillaries, venuoles, collecting veins, and pial veins. We therefore use a resting Y value of 0.6.
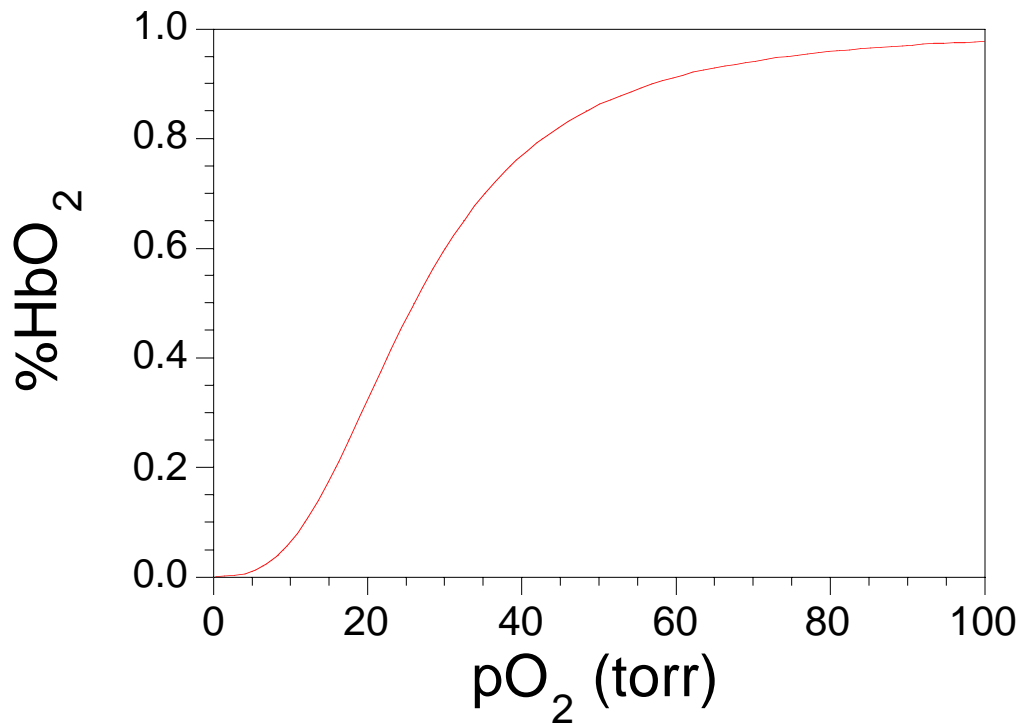
Figure 6.1: The oxygen-hemoglobin dissociation curve. Obtained using equation 6.1 and assuming a P_{50} of 26 mmHg.

Vessel Radius. As described in a study of the anatomical structure of the human cerebral vasculature by Duvernoy et al. (148) , vessel radii vary considerably. Central pial arteries - 130 μm to 140 μm. Peripheral pial arteries - 75 μm to 90 μm. Arterioles at the cortex surface - 25 μm or less. Arteriol anastomoses (connecting arterioles) - 12 μm to 45 μm. Arteries that penetrate the cortical surface have diameters dependent generally on the depth of penetration. Their diameters, at the base, range from 120 μm (deepest arterioles) to 5 μm (most shallow arterioles).

Central pial veins - 140 μm to 190 μm. Peripheral pial veins - 60 μm. The largest principle veins (largest intracortical vein) - 40 μm to 62 μm. As a

side note, principle veins generally penetrate the cortex in a perpendicular manner and drain surrounding cortical areas within a radius of 0.5 to 2 mm. Considering a cortical thickness of about 3 mm, the draining volume would be 0.75 mm^3 to 12 mm^3. Other draining veins have radii which depend on their depth of penetration and cortical drainage area. In the largest of these, the radii are 32 μm. In the smallest, the radii are 10 μm. Other cortical veins branch out tangentially and have radii similar to those of draining veins.

Capillaries have radii ranging from 2.5 μm to 4 μm. Capillary orientation is generally random, but shows some orientation preference in several cortical layers (I - tangental to cortex surface, II - palisading, IV - tangential).

In the simulations presented below, the vessel radii were varied from 2.5 μm to 20 μm. Above 20 μm, as will be discussed, the diffusion effects are minimal and $\Delta R2^*/\Delta R2$ approaches infinity, therefore obviating the need to increase simulated radii any further. When keeping the radius constant and varying other parameters, a radius of 10 μm was chosen for the simulations. The motivation for this choice is related to the fact that when simulation results of Ogawa et al. (127), (Figure 6 of that paper) are compared to data presented in the literature (107, 174, 176, 179, 184, 185, 211), which generally give an $\Delta R2^*/\Delta R2$ ratio between 3/1 and 4/1, the "average" vessel size comes out to be about 10 μm. The simulations presented below also show general agreement with this result. In these preliminary simulations an "average" compartment size (or vessel radius) was chosen with the understanding that it represents a weighted combination of radii ranging from 2.5 μm (capillaries and red blood cells within larger vessels) to 190 μm (central pial veins). Figure 6.2 illustrates shematically the compartments that are considered predominant in the cerebral vasculature.
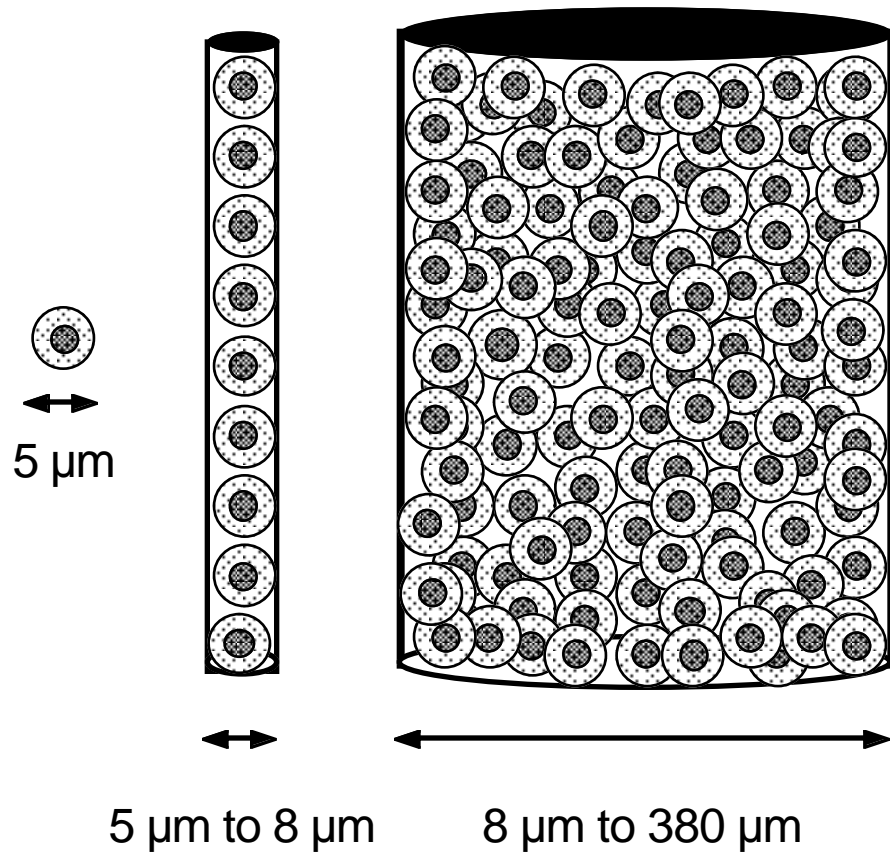
Figure 6.2: Schematic illustration of the predominant cerebral vasculature compartments and their corresponding sizes.

Vessel Orientation. As mentioned above, the cerebral vasculature has some structure and orientation relative to the cortical surface. The larger the vessel, the more likely is it that it will display a single orientation in a voxel. The relative effects on relaxation rate changes by variation of vessel angle was observed in one simulation. In all other simulations, a random vessel orientation distribution, ranging from 0 to $\pi/2$, was used.

Blood Volume. The cerebral blood volumes that are used in other simulations are the range of 2% to 5%. One caveat to this assumption is that if

the brain is divided into voxels, as it is for an imaging experiment, the fraction of the voxel that is blood may vary widely. It is likely that the heterogeneity in the distribution of blood volume in each voxel is smallest for the smallest vessels and largest for larger vessels. It can be assumed that capillary blood volume, about $1/2$ of the total cerebral blood volume, is homogeneously distributed across voxels. In larger vessels, it is very likely that a single vessel may completely fill several voxels, giving a 100% blood volume. In general, larger vessels that change in oxygenation may give a very large signal change simply because of the large blood volume in those particular voxels.

Simulations of the relative effects on activation - induced signal changes by variations in resting state blood volume are carried out. When other parameters were varied, a fractional blood volume value of 4% was used. It is understood that 80% of the total cerebral blood volume is contained in veins and capillaries (19). As will be discussed, activation - induced changes in oxygenation occur primarily in veins and capillaries. Assuming a total (arteries, capillaries, and veins) fractional blood volume of 5%, it is therefore reasonable to use the value of 4% to account for the capillary and venous blood being considered.

Hematocrit. The average hematocrit in healthy humans falls in the range of 30 to 50 (i.e: 30% to 50% of blood volume consists of red blood cells), but varies considerably, in vivo, with vessel diameter (19). It may vary from 50 in the largest vessels, to as low as 30 in capillaries. In these simulations, a hematocrit of 42 was used.

Proton Dynamics. The final model consideration is that of proton dynamics in the presence of magnetic field perturbers. Proton dynamics include diffusion, exchange across red blood cell membranes, and exchange

across capillary walls. Also, movement of red blood cells relative to protons may be considered as proton dynamics since the extent of dephasing is dependent on relative and not absolute dynamics. The diffusion coefficient of free water has been measured to be about 2.5 μm^2/ms (81, 373). In contrast, the diffusion coefficient of protons in the brain was measured to be 1 μm^2/ms (374). Diffusion in gray matter may also be restricted and anisotropic. The average velocity of red blood cells is about 0.3 mm/sec in the capillaries (19, 148).

In the simulations performed, the relative relaxation rate changes are observed as the diffusion coefficient is varied. When other parameters are varied, the diffusion coefficient was set equal to 1 μm^2/ms. Diffusion was also considered to be unrestricted and isotropic.

Activation - Related Physiologic Considerations

During cerebral activation, neuronal and subsequent hemodynamic events take place. Through incompletely understood mechanisms (1, 8-32), arteriolar sphincters open, causing an increase in blood flow. This increase in blood flow is generally accompanied by capillary recruitment, venous vessel distension, and an increase in flow velocity where vessels neither distend nor are recruited. Despite these marked flow changes, it has been demonstrated that the oxidative metabolic rate does not increase proportionally (29) during brain activation.

As discussed by Weisskoff et al. (252), the relationship between resting and activated states of blood oxygenation, blood flow, and oxidative metabolic rate can be described using the principle of conservation of mass or the "Fick principle" which dictates that total oxygen is conserved. The relationship

between resting (*rest*) and active (*act*) flow (F), blood oxygenation in arteries (Qa) and veins (Qv), and tissue oxygen consumption (Q'), is given below.

$$F_{rest} (Qa_{rest} - Qv_{rest}) - Q'_{rest} = F_{act} (Qa_{act} - Qv_{act}) - Q'_{act} \qquad [6.2]$$

During activation, a 5% increase in oxidative metabolic rate has been reported (29). While it is possible that this increase may affect the MR signal in several subtle ways, it is considered to be negligible in these simulations ($Q'_{rest} \approx Q'_{act}$). Equation 6.2 therefore reduces to:

$$(Qa_{act} - Qv_{act}) / (Qa_{rest} - Qv_{rest}) = F_{rest} / F_{act} . \qquad [6.3]$$

This relationship demonstrates that an activation - induced increase in flow, unaccompanied by an increase in oxidative metabolic rate, decreases the arterial - venous oxygenation difference by increasing the venous oxygenation. This decrease in the arterial - venous blood oxygenation difference causes an average increase in blood oxygenation in the vicinity of the activated region.

The relationship between blood volume and blood flow is less clear. From the PET literature, a coupling between flow and volume changes has been characterized in the context of hypercapnic stresses (375). This relationship is given by:

$$V_{act} / V_{rest} = (F_{act} / F_{rest})^{0.5}. \qquad [6.4]$$

Application of equation 6.4 to activation - induced flow and volume changes requires that activation - induced changes follow similar mechanisms as

167

those created as a result of hypercapnic stresses. Figure 6.3 illustrates the above relationships (eq. 6.3 and 6.4) graphically. Whether or not these mechanisms apply to the smaller and more localized activation - induced changes is unknown.
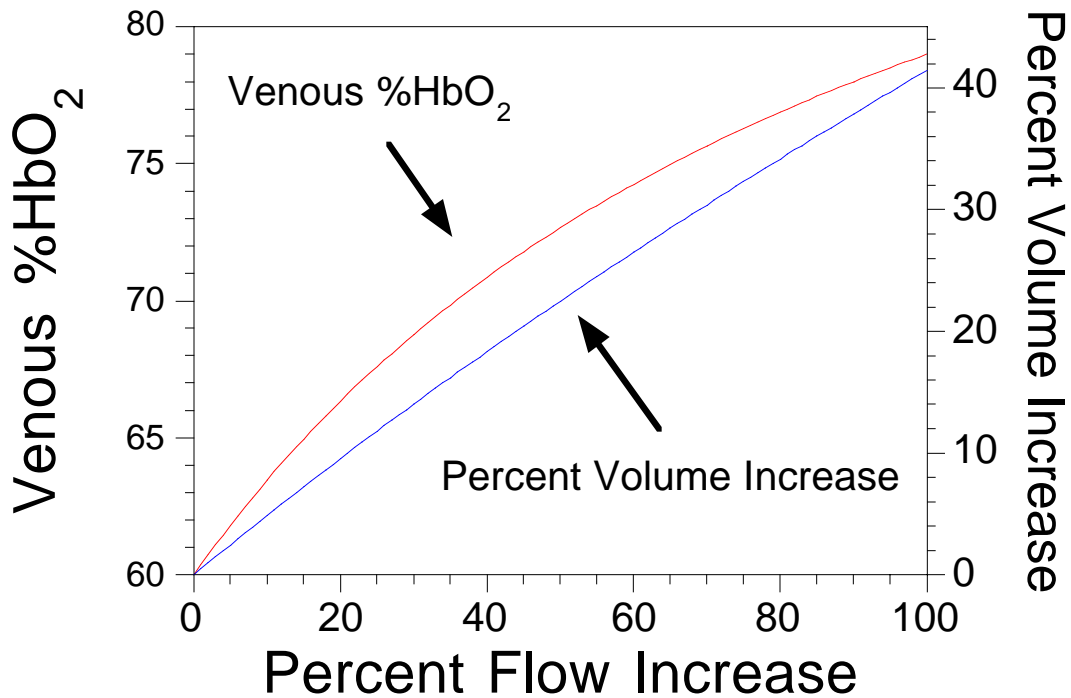

Figure 6.3: Relationship between the fractional flow increase , hemoglobin saturation, and the fractional volume increase, assuming that oxidative metabolic rate does not increase during activation.

Fox et al. (29), using PET, has measured an activation - induced increase in blood flow of about 30%, which, using the above relationships, is associated with a change in venous $\%HbO_2$ from 60% to 65%. Using a bolus-injection of Gd (DTPA) in conjunction with dynamic MRI (27), an average activation - induced blood volume change of $32 \pm 10\%$ was measured. This volume

change is associated with an increase of flow of 75% and a change in venous oxygen saturation from 60% to 76%. In the models of Ogawa et al. (127) and Weisskoff et al. (252), activation - induced increases in blood flow of 70% and 75%, respectively, were assumed. These changes correspond to an increase in venous blood oxygenation from a resting level of 60% to and activated level of about 73% and 74% respectively.

From the literature values, it can be inferred that activation - induced increases in blood flow range from a 30% increase to a 75% increase. This range is quite large, and may depend on many variables, which may include differences in the measurement methods and the type of brain activation. Also, the relationship between blood volume and blood flow is an "ad hoc" estimate which is also dependent on many variables that may not be constant in all regions of activation and between subjects.

The effect of blood oxygenation and blood volume changes on the MR signal are also characterized in this paper. Keeping all other parameters constant, blood volume and oxygenation are varied over a wide range. The effect of flow changes, in themselves, on MR signal, are not explicitly studied. The non-susceptibility related flow effects on MR signal have been extensively modeled (85, 87, 171, 217) and empirically characterized (85, 88, 171, 180, 182, 189). Also, when using a TR $\geq$ 1 sec, non-susceptibility - related MR signal changes, related to flow changes, are minimal relative to susceptibility - related signal changes (180).

When simulating of the dependence of MR signal on parameters other than blood oxygenation and volume, blood oxygenation and volume are either kept fixed at 60% (assumed venous oxygen saturation) and 4%, respectively, or an activation - induced venous oxygen saturation change from 60% to 75% is assumed. Activation - induced changes in blood volume

169

are not considered in most of the simulations (i.e. a constant volume of 4% is assumed), but a demonstration of the relative effects that a combined increase in blood volume and oxygenation has on the MR signal is given. In general, it is shown that activation-induced increases in blood oxygenation greatly outweigh the effect from an increase in blood volume.

Other hemodynamic changes that may be significant and which are not simulated directly include activation-induced changes in blood flow velocity, proton exchange rate, and hematocrit.

Biophysical Considerations

The relationship between the nuclei precession frequency and the applied magnetic field is given by:

$$\omega_O = \gamma\, B_O \qquad\qquad [6.5]$$

where ω_O is the is the Larmor (or precession) frequency in rad/sec. The value, γ, is the gyromagnetic ratio (267.5×10^6 rad/Tesla for protons). The value, B_O, is the strength of the applied magnetic field (Tesla). If, within a voxel, the magnetic field is perturbed (i.e. by an object having a susceptibility not equal to the surrounding medium), a distribution of B_O will be present. The spins will therefore precess at different frequencies and lose coherence (dephase) generally causing a loss of signal. As will be described in more detail, this dephasing depends on several other factors, which include the dynamics of the spins in the vicinity of the field perturber, the geometry of the perturber, and the magnetic susceptibility ($\Delta\chi$) of the perturber.

In the following section, the relationship between blood oxygenation and spin precession frequencies within the vicinity of a vessel containing whole blood is described. First, the relationship between blood oxygenation and resonance frequency, independent of vessel geometry, is considered. Second, geometrical considerations are included.

A recent measurement by Weisskoff et al. (108) of the volume susceptibility difference between fully deoxygenated blood and fully oxygenated red blood cells was 0.18×10^{-6} (cgs units). To obtain the bulk susceptibility of whole blood (blood cells and plasma), it is necessary to multiply the above number (applicable to red blood cells) by the volume fraction of red blood cells in the vasculature. Considering a hematocrit of 42, the susceptibility difference between fully oxygenated and fully deoxygenated whole blood is 0.756×10^{-7}.

Neglecting geometry at this point, the relationship between the frequency offset and the oxygenation of red blood cells is:

$$\Delta\omega = 2\,\pi\,\omega_O\,\Delta\chi\,(1 - Y) \qquad\qquad [6.6]$$

where Y is the fractional blood oxygen saturation, and $\Delta\chi$ is the susceptibility difference between fully deoxygenated red blood cells and surrounding plasma. As a reasonable approximation, the susceptibility of fully oxygenated blood cells and surrounding plasma is considered to be equal. When considering whole blood effects (i.e. the frequency offset induced by a vessel containing blood), it is necessary to multiply the fully deoxygenated red blood cell $\Delta\chi$ by the fraction of red blood cells in the vessel (i.e. hematocrit/100). Equation 6.6 can also be considered as describing the frequency offset induced

at the surface of a infinite cylinder having a susceptibility difference, $\Delta\chi$, and oriented perpendicularly to B_O.

An infinite cylinder having susceptibility difference, $\Delta\chi$, that is placed in a magnetic field causes B_O distortions that are highly dependent on orientation of the cylinder and location in space relative to the cylinder. The geometrical relationships of the cylinder are illustrated in Figure 6.4. The spatial dependence of the induced frequency offset, $\Delta\omega$, on the orientation of the vessel (infinite cylinder) relative to the direction of B_O is given below(122, 127). The variable, $\Delta\omega$', is equal to the $\Delta\omega$ that is given in equation 6.6.

Outside the cylinder:

$$\Delta\omega \ (r, \ \theta, \ \phi) = \Delta\omega' \ \sin^2(\theta) \ (a/r)^2 \ \cos \ (2\phi). \qquad\qquad [6.7]$$

Inside the cylinder:

$$\Delta\omega \ (\theta) \ = \Delta\omega' \ (3 \ \cos^2(\theta) - 1) \ / \ 3. \qquad\qquad [6.8]$$

The angle of the cylinder axis relative to B_O is θ. The radius of the cylinder is a, and the distance from the center of the cylinder to the point of interest, along a plane perpendicular to the cylinder is r. The angle between the vector, r, and the component of Bo on the perpendicular plane is ϕ.
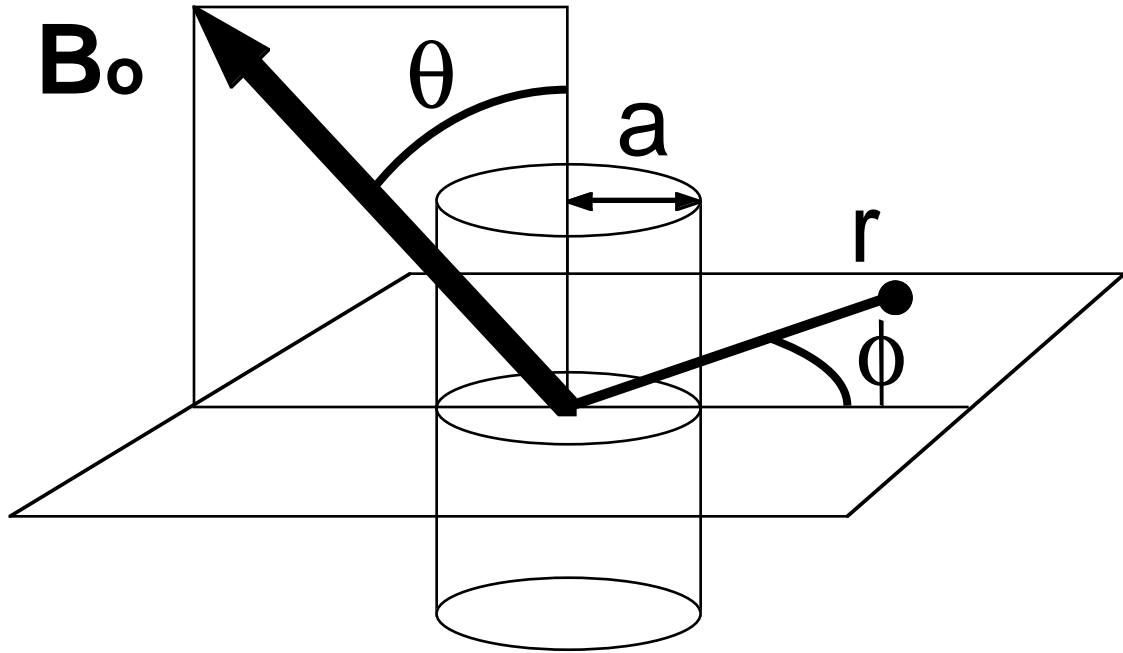
Figure 6.4: Schematic illustration the geometrical relationships that determine resonant frequency shifts in the vicinity of an infinite cylinder placed in a magnetic field, B_O.

Because the magnetic field does not vary along the length of the cylinder, these dephasing effects can be simulated in two dimensions. A subvoxel cell, as described below, is used. In this cell, one cylinder at a time, having a random θ distribution, between 0 and $\pi/2$ was used, and complex addition of the magnetization in each cell was carried out, in each time increment, to compute the degree of dephasing. The effect of overlapping fields was not considered here.

The net phase shift created between intravascular spins and extravascular spins is taken into consideration. Intravascular *dephasing* as a result of susceptibility differences between red blood cells and plasma was not considered here. The amount of intravascular signal can vary considerably as

the T2 and T2* of blood, at a given hematocrit and oxygenation, varies with field strength. Models using Monte Carlo methods (190, 192, 210) and ongoing work using the method presented here consider this potentially significant intravascular dephasing effect.

In general, the significance, regarding the effects on the relative magnitudes of the transverse relaxation rate changes, of curved geometry, overlapping cylinders, intravascular effects, or heterogeneous spin dynamics is unclear. In later stages of modeling work the significance of these parameters should be considered. It is necessary, though, to first construct a simplified model such that the most basic relationships can be understood. This model was formulated as a first step to aid in the clarification of fundamental relationships between basic parameters (which are modulated) and relative gradient-echo and spin-echo dephasing effects.

III. DETERMINISTIC "PHASE ROTATE" AND "SMOOTH" MODEL

In this section, details are given as to how the simulation parameters: diffusion coefficient, vessel radius, blood volume, blood oxygen saturation, field strength, and vessel orientation relative to B_O, are manipulated. Also, a description is given on the manner in which the effects of diffusing spins through microscopic magnetic field gradients are simulated.

Matrix construct: subvoxel map relationships

Computer modeling of diffusion effects has been performed with random walk simulations which track the positions of a group of spins over time and record their phase histories (116, 117, 123, 124, 126, 127, 190). This

requires the calculation of randomized trajectories for a large number of spins in order to arrive at a solution with high precision. In the simulations presented below, diffusion is simulated by convolving a spin density map with a smoothing function. This method, first introduced by Wong et al. (128), is the basis for our method of modeling diffusion effects.

At any instant in time, the state of the spins in a voxel can be described by maps of the magnetization at subvoxel resolution. If these maps are sufficiently fine so that they are smooth over the unit cell, then for the purposes of the MR signal they completely define the state of the spins in that voxel, and it is not necessary to track the phase history of individual spins. In every unit of time, dt, the effects of diffusion and susceptibility can be described by a smoothing function (i.e. a Gaussian distribution) and a spatially dependent phase rotation (i.e. by a rotation matrix derived by the $\Delta\omega$ map), respectively. If dt is small enough so that the distance spins move due to diffusion is small relative to the scale of the field inhomogeneities, then this is a good approximation of the simultaneous diffusion and dephasing process. It was determined that a dt of 1 ms was a sufficiently small time interval, such that, in the range of geometries, susceptibilities, and diffusion coefficients common to the cerebral vasculature, the error due to quantization of time was less than 1% (128).

To simulate diffusion in the presence of a field perturber, three two-dimensional (128 x 128) subvoxel maps were created. The first map is of complex magnetization. At time = 0, this map is real and uniformly one. The second map is the frequency offset or $\Delta\omega$ and is converted into a map of the corresponding rotation martrices for one time interval, dt. The third map is a probability distribution map for diffusing spins in the span of one time interval, dt. As will be demonstrated, the magnetization map is "phase

rotated" and "smoothed" in 1 ms intervals. In each 1 ms step, the magnetization of each voxel evolves in the presence of a specific $\Delta\omega$, and then is smoothed by the probability function. The methods by which these two maps are created and used are described below.

Figure 6.5 graphically shows the relevant variables in the creation of the $\Delta\omega$ map and the Gaussian map.
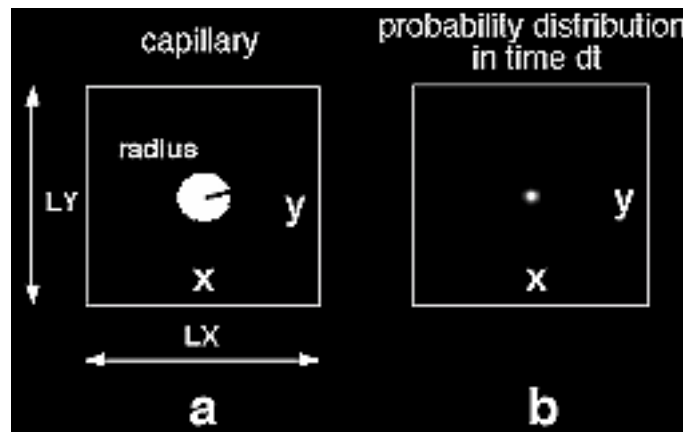

Figure 6.5: Parameters relevant to the subvoxel matrices in the simulations. **a)** The capillary matrix. **b)** The probability distribution matrix.

Figure 6.5a shows the relationships that determine the radius of the capillary relative to the matrix size. Since the map is two dimensional, the fractional blood volume is proportional to the area of the capillary relative to the area of the entire map. This relationship is given by:

$$\text{vessel radius (pixels)} = \sqrt{\frac{\text{LX x LY x } \textbf{fractional blood volume}}{\pi}} \qquad [6.9]$$

where the bold print indicates the value that is entered into the simulation.

Figure 6.5b is the Gaussian probability distribution for a randomly diffusing spin over time interval, dt. As described by Le Bihan et al.(81), the probability that a molecule travels a distance, r, during a time interval, t, can be described, in the case of a simple liquid, by a Gaussian distribution with zero mean. The mean squared path of the diffusing molecule (also the variance of the distance traveled), $<r^2>$, is proportional to the time interval, t, according to the Einstein equation, which, in three dimensions, is:

$$6Dt = <r^2>$$
[6.10]

where D is the diffusion coefficient. Since magnetization does not vary parallel to an infinte cylinder axis, the projection of equation 6.10 onto two dimensions is considered in the simulation. The projection of the mean squared path onto a two - dimensional plane is given by

$$4Dt = <r^2>.$$
[6.11]

The next step is to derive the relationship between the standard deviation, σ, of the Gaussian distribution used in the simulation and the physical parameter that is considered, i.e the diffusion coefficient, D. A Gaussian distribution function, f(r), with mean = 0, and standard deviation = σ, is given below (376):

$$f(r) = \frac{1}{\sqrt{2\pi}\sigma} e^{\left(\frac{-r^2}{2\sigma^2}\right)}$$
[6.12]

The mean squared path of a freely diffusing spin, $<r^2>$, is equal to the expectation value of r^2 in a Gaussian probability distribution. This expectation value is obtained by integration of the Gaussian times r^2 over all space, then by dividing by the integral of the Gaussian only, over all space:

$$4Dt = <r^2> = \frac{\int_0^\infty r^2 \left(\frac{1}{\sqrt{2\pi}\sigma} e^{\left(\frac{-r^2}{2\sigma^2}\right)}\right) r\, dr}{\int_0^\infty \left(\frac{1}{\sqrt{2\pi}\sigma} e^{\left(\frac{-r^2}{2\sigma^2}\right)}\right) r\, dr} \qquad . \qquad [6.13]$$

Equation 6.13 reduces to:

$$4Dt = <r^2> = 2\sigma^2. \qquad\qquad [6.14]$$

The relation between the standard deviation of the Gaussian, σ, and D is given by:

$$\sigma = \sqrt{2Dt} \qquad\qquad [6.15]$$

where t is equal to dt, the time increment used in the simulations. Before equation 6.15 can be used, the diffusion coefficient, D, must be converted from $\mu m^2/ms$ to $pixels^2/ms$. This conversion is:

$$D \ (\text{pixels}^2/\text{ms}) = \frac{\mathbf{D} \ (\mathbf{\mu m^2/ms})}{\left(\dfrac{\text{vessel radius (pixels)}}{\mathbf{vessel \ radius \ (\mu m)}}\right)^2} \qquad [6.16]$$

where, again, the values in bold print are those entered into the simulation. Entering D, in pixels2/ms, and t into equation 6.15, gives a value of σ that is then used in the creation of the Gaussian function in Figure 6.5a. The probability function, after normalization to the matrix dimensions is:

$$\text{prob} \ (x,y) = \left(\frac{LX \times LY}{2 \ \pi}\right) \frac{1}{\sigma^2} \ e^{-\left(\frac{x^2 + y^2}{2\sigma^2}\right)} \qquad [6.17]$$

where LX and LY are the probability density matrix dimensions, and x and y are the coordinates within the matrix.

At this point, it is instructive to give several examples of the dependence of the $\Delta\omega$ maps and the Gaussian maps on the parameters that can be manipulated. The following figures will show how the $\Delta\omega$ maps and the Gaussian maps vary with a) diffusion coefficient, b) vessel radius, c) fractional blood volume, d) fractional blood oxygen saturation, e) magnetic field strength, B_O, and f) the angle between the cylinder axis and the B_O vector. In each example, the parameters that are held constant are given at the bottom of each figure.

Figure 6.6 is an example of how the Gaussian probability density map changes when the diffusion coefficient is varied. The $\Delta\omega$ map remains the same but the width, in pixels, of the Gaussian is increased as D increases from 1 μm^2/ms to 20 μm^2/ms.
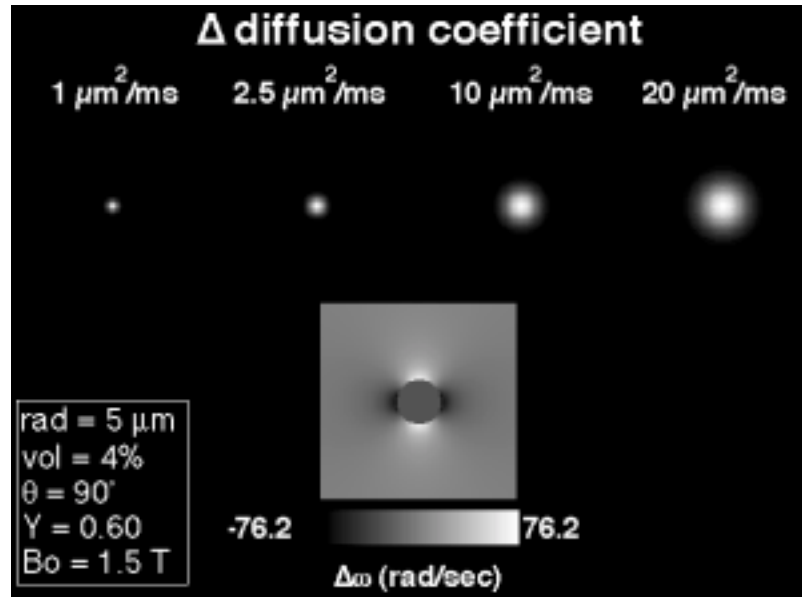

Figure 6.6: Example of the manner in which the Gaussian map changes when the diffusion coefficient is varied.

Figure 6.7 is an example of how the Gaussian map changes when the vessel radius is varied. The $\Delta\omega$ map again remains the same but the width, in pixels, of the Gaussian is decreased as the radius is increased from 2.5 μm to 20 μm.
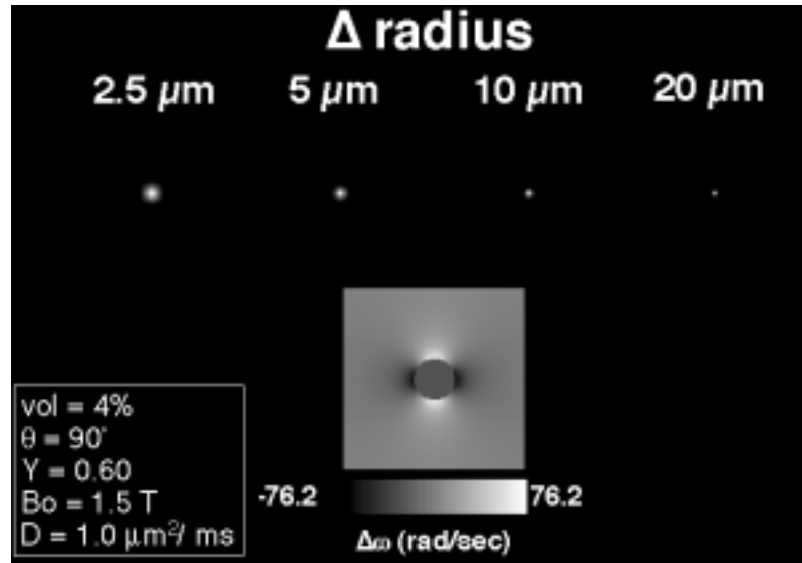
Figure 6.7: Example of the manner in which the Gaussian map changes when the vessel radius is varied.

Figure 6.8 gives an example of how both the Gaussian and Δω maps change when the fractional blood volume is varied. When the fractional blood volume is varied, the vessel radius, in submatrix pixels, is increased (since the area is proportional to the blood volume) and the width of the Gaussian increases accordingly to match the width of the simulated vessel (so that the diffusion distance relative to the vessel radius, is kept constant). Here the blood volume fraction is varied from 2% to 20%.
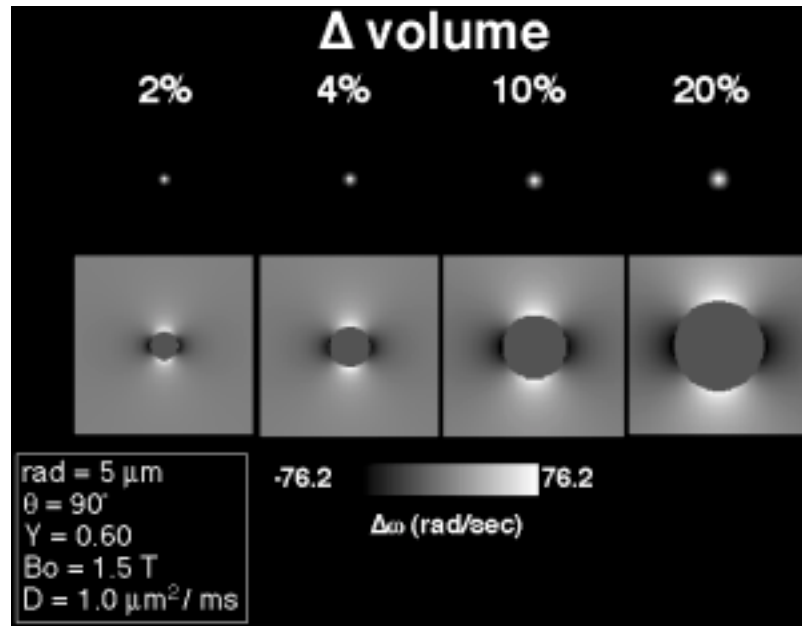
Figure 6.8: Example of the manner in which the Δω and Gaussian maps change when the fractional blood volume is varied.

Figure 6.9 is an example of how the Δω map changes when the fractional blood oxygen saturation is varied. When whole blood becomes less saturated, the frequency offsets in the vicinity of the cylinder are increased. Here, the blood oxygen saturation is varied from 90% to 0%.
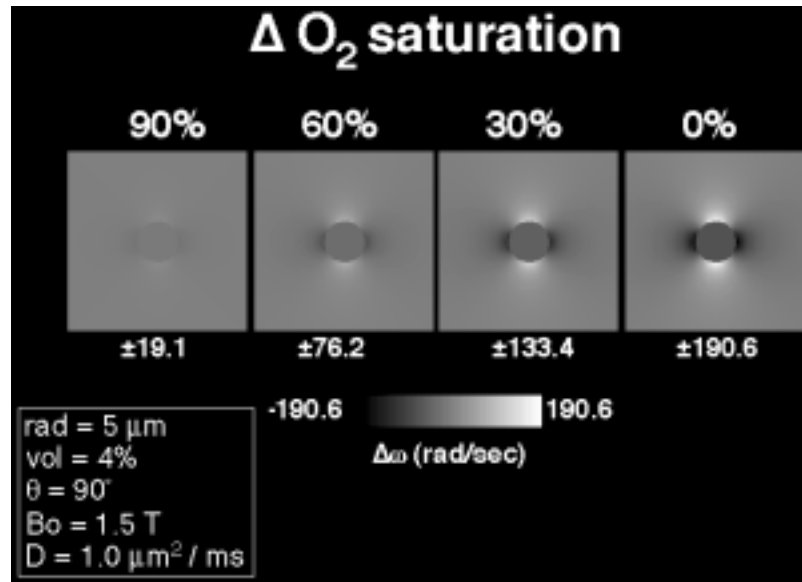
Figure 6.9: Example of the manner in which the Δω map changes when the fractional blood oxygen saturation is varied.

Figure 6.10 is an example of how the Δω map changes when the magnetic field strength, B_O, is varied. When the field strength is increased, the frequency offsets in the vicinity of the cylinder are increased. Here, the field strength is varied from 0.5 Tesla to 4.0 Tesla.
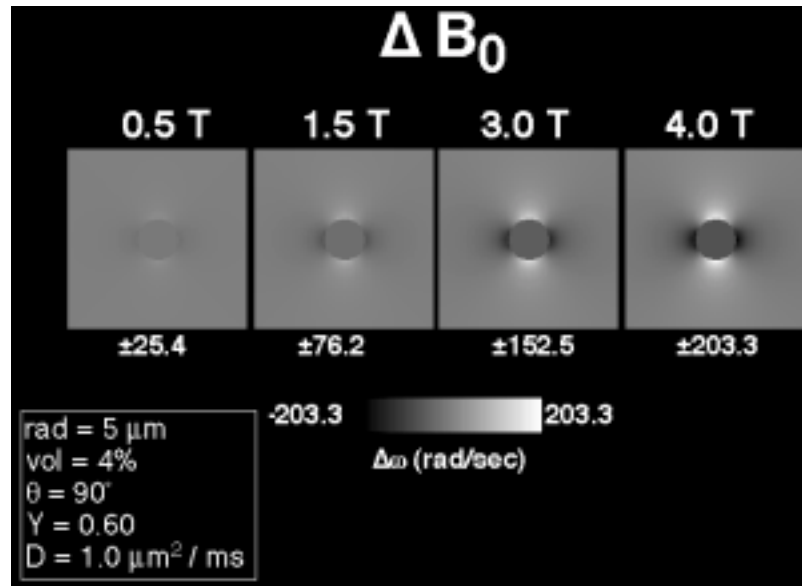
Figure 6.10: Example of the manner in which the $\Delta\omega$ map changes when the magnetic field strength, B_O, is varied.

Lastly, Figure 6.11 is an example of how the $\Delta\omega$ map changes when the angle, θ, between the cylinder axis and the direction of B_O is varied. The field distortions (frequency offsets around the cylinder) are non-existent when the cylinder is parallel to B_O. Here, the angle, θ, is varied from 0° (parallel) to 90° (perpendicular).
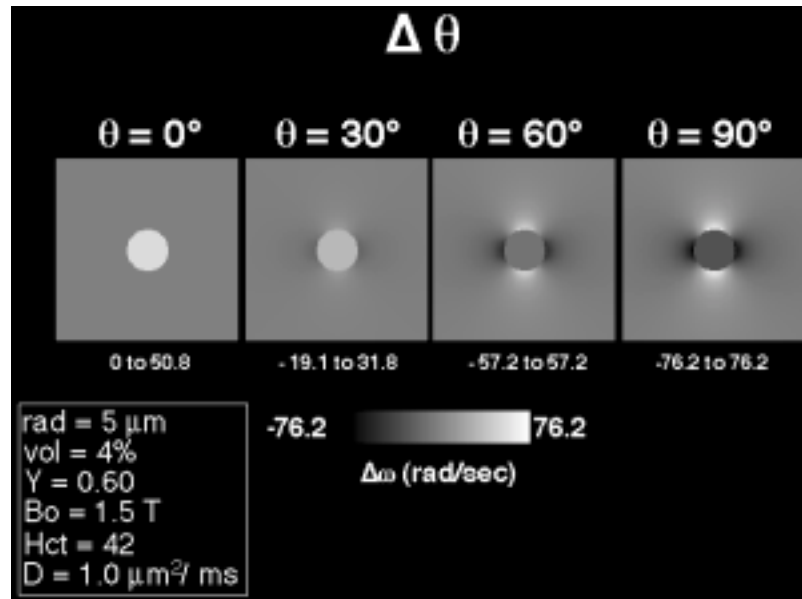
Figure 6.11: Example of the manner in which the Δω map changes when the angle, θ, between the cylinder axis and B_O is varied.

These basic examples illustrate the relationships that have been created to simulate susceptibility effects in the presence of diffusing spins. In the next section, the details of the simulation process are described.

Diffusion simulation methodology

At time zero, uniform and coherent transverse magnetization is placed across the matrix. With each "phase rotate" and "smooth" iteration, every subvoxel in the matrix accumulates a particular real and imaginary component. This iteration process is illustrated schematically in Figure 6.12.
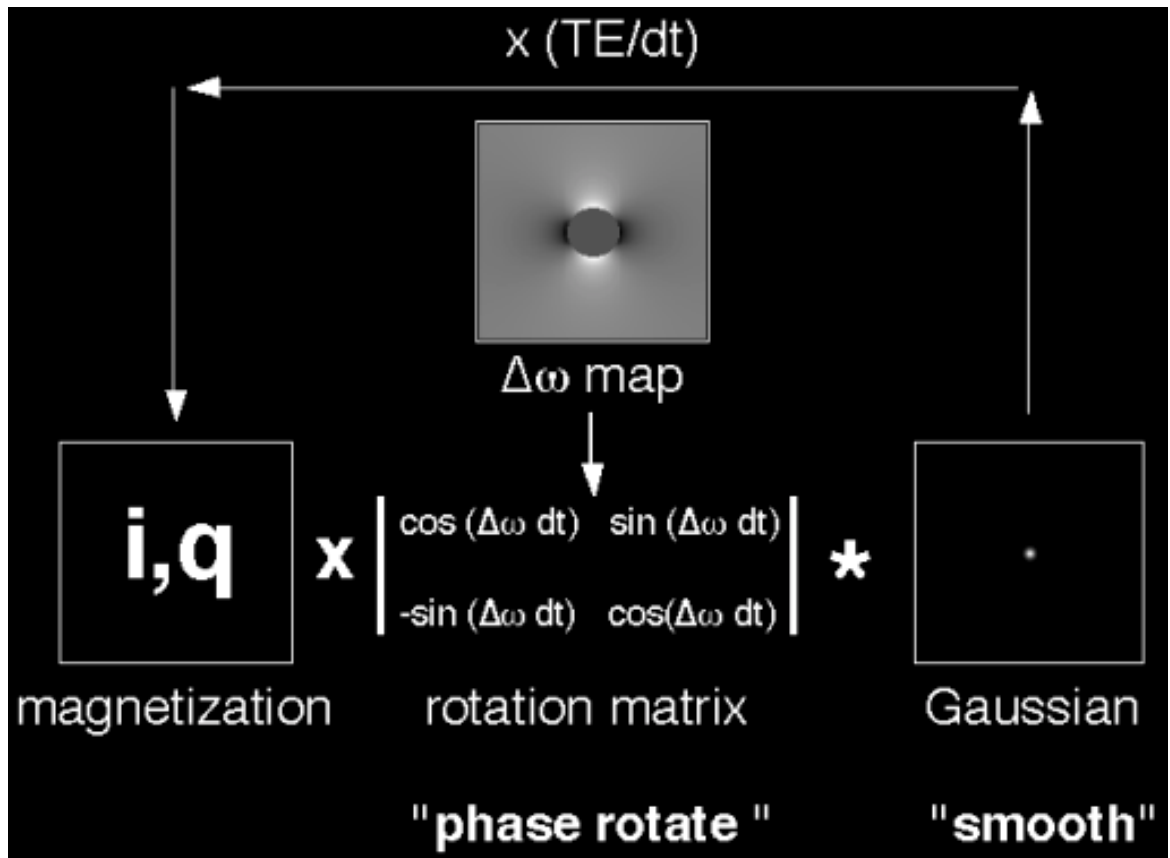
185

Figure 6.12: The basic methodology of the simulation involves an iterative process by which the magnetization map is multiplied by the frequency offset map and subsequently convolved with the Gaussian map. The iteration step, dt, is 1 ms in this simulation.

To simulate a 180° rf pulse, as would be applied for a spin-echo sequence, the imaginary component of the magnetization is multiplied by -1 at time = TE/2.

An example is given to demonstrate the simulation process. In this example, a single cylinder oriented perpendicularly to B_O, is used. The echo time of the experiment is 60 ms. Vessel radius is 10 μm. The diffusion coefficient is 1 $μm^2$/ms. Field strength is 1.5 Tesla. The blood oxygenation

saturation is 0.6, and the hematocrit is 42. Figures 6.13 and 6.14 show the time evolution of the magnetization during gradient - echo and spin - echo sequences respectively. Real (i), imaginary (q), and magnitude (m) maps evolve in time from left to right. Ten iterations take place between each box. In the gradient - echo simulation, the imaginary component begins to resemble a blurred version of the frequency offset map ($\Delta\omega$) used in this simulation. Signal (m) dropout is observed due to subvoxel dephasing over time.
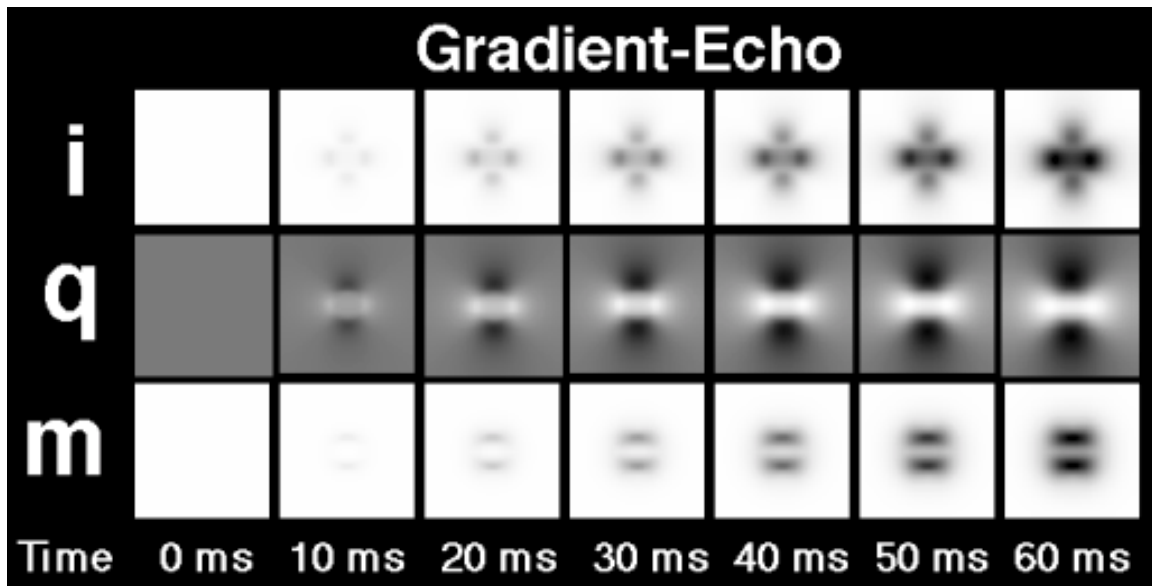

Figure 6.13: Gradient - echo simulation. The time - evolution of the real (i, imaginary (q), and magnitude (m) components of the magnetization as they evolve during the iterative phase rotation and smoothing process.
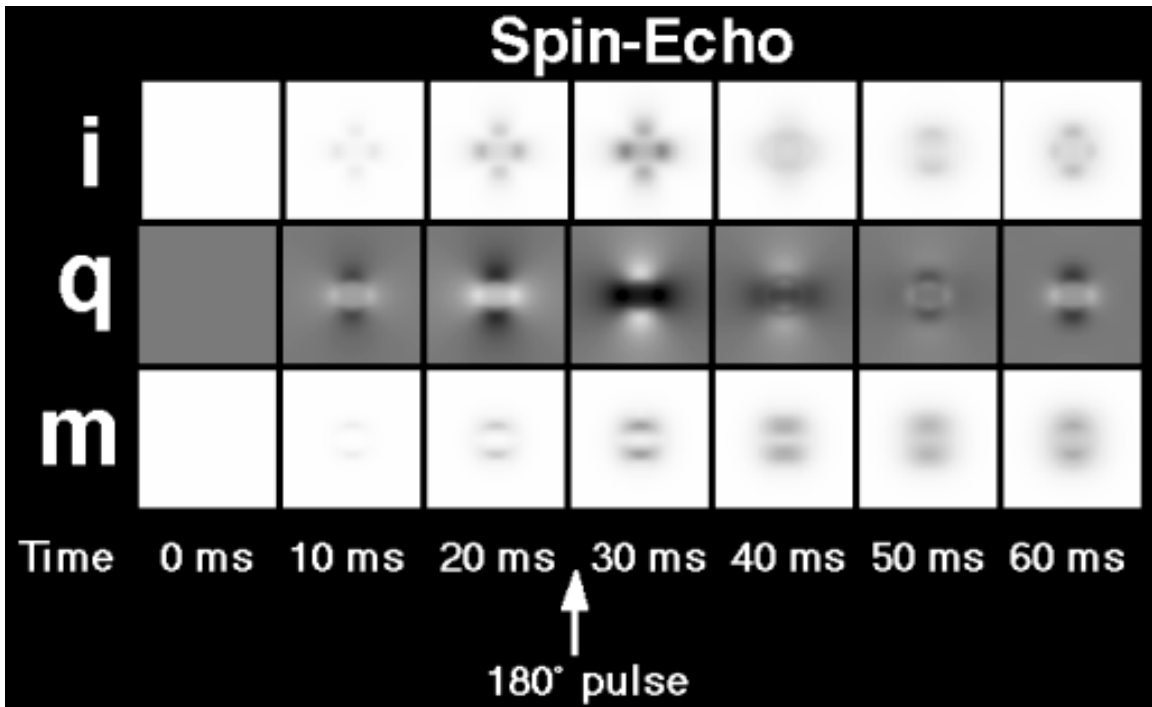
Figure 6.14: Spin - echo simulation. The time - evolution of the real (i), imaginary (q), and magnitude (m) components of the magnetization as they evolve during the iterative rotation and smoothing process. The 180° pulse reverses the sign of the imaginary component, but, because of the diffusion process, the spins are not completely refocussed at the echo time TE.

In the spin-echo map, the sign of the imaginary component map is reversed immediately prior to the maps created at 30 ms. After the application of the 180° pulse, the phase is reversed. If no diffusion were to occur, both the real and imaginary components would return to maps of 1's and 0's, respectively, at the echo time, TE. However, the signal does not completely recover because the diffusion process causes spins to experience different Bo fields, in different locations, before and after the 180° pulse.

Figure 6.15 demonstrates the evolution of the signal intensity over time for the spin-echo and gradient-echo sequences. Signal intensity at each time point is calculated by complex addition of the magnitude.
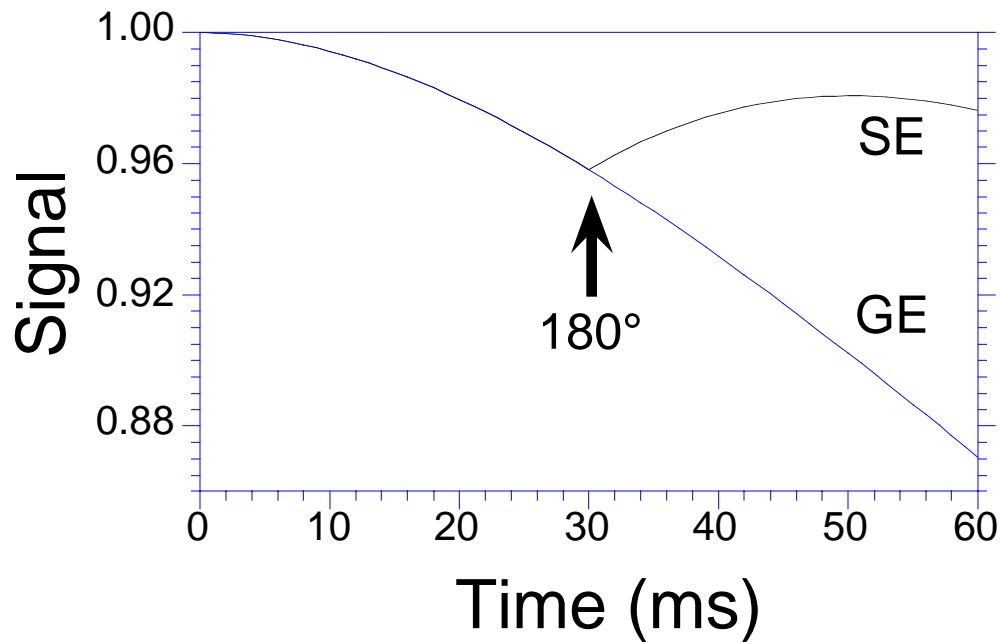
Figure 6.15: Corresponding plots of signal vs. time for the simulated spin-echo and gradient-echo sequences, corresponding to the maps in Figures 6.13 and 6.14. The 180° rf pulse is applied for the spin-echo sequence.

6.4 SIMULATIONS

The goal in these simulations is to characterize the dependencies of $\Delta R2^*$ and $\Delta R2$ on relevant physiologic and biophysical variables. An understanding of these dependencies may allow more accurate interpretation of activation - induced signal changes. This section includes basic simulations, model validation, demonstration of $\Delta R2^*$ and $\Delta R2$ dependence on $\Delta\omega$ and τ, and $\Delta R2^*$ and $\Delta R2$ dependence on physiologic parameters.

Basic simulations

It is instructive to provide a demonstration of the relative (spin - echo to gradient - echo) signal changes that occur if only the vessel radius is varied. Three signal vs. time plots for each pulse sequence corresponding to vessel radii of 2.5 μm, 5 μm, and 20 μm are shown in Figure 6.16a, and 6.16b.
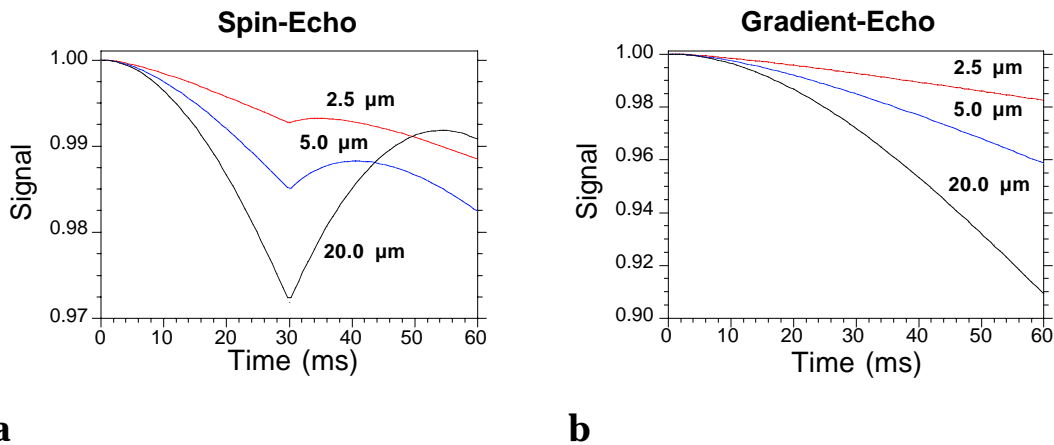

a   **b**

Figure 6.16: The effect of changing the perturber radius on **a.** spin-echo and **b.** gradient-echo signal.

With the spin - echo sequence, the signal intensity remains high for the smaller vessel, then drops for the intermediate sized vessel, and increases when the vessel size is increased to 20 μm. For the smallest vessel, the overall spin coherence remains high due to the relatively rapid diffusion-mediated averaging of field offsets contained in the small region around the 2.5 μm vessel. At the other extreme (20 μm sized vessel), the diffusion effects are minimal due to the relatively large region that the field offset covers, relative to the diffusion distance. In this case, the 180° pulse almost completely

reverses the dephasing effects created by the large vessel, and thus, the diffusional averaging is minimal.

With the gradient - echo sequence, the signal intensity decreases monotonically as the vessel size increases. Diffusional averaging of the field gradients, which maintains spin coherence, decreases as the size of the perturber increases. A 180° pulse is not applied, therefore the spin phase is not reversed.

As the vessel size approaches infinity, the diffusion effects approach zero. In this case, the spin-echo sequence will show complete recovery of signal at the echo time, TE, and the gradient-echo sequence will be maximally dephased, having no motional averaging effects which tend to maintain spin coherence.

The relative effects of perturber size, frequency offset, and diffusion coefficient on relative spin-echo and gradient-echo signals has been categorized roughly into "exchange regimes." This description, given in Table 1.1 (in chapter 1), is an approximation based on spherical geometry, but is also useful when discussing cylindrical geometry. When the radius, R, equals 20 μm and D equals 1 μm^2/ms, the frequency offset at the surface of the vessel, $\Delta\omega$, equals 76.2 rad/sec, (i.e. %HbO_2 = 60%, B_O = 1.5 T, hematocrit = 42, considering that $\Delta\chi$ of completely deoxygenated blood cells equals 0.18 x 10^{-6}), and $\Delta\omega(R^2/D)$ = 30.5. In this "slow exchange" or "linear gradient" regime spin-echo signal shows much less attenuation than gradient-echo signal, as was demonstrated in Figure 6.16 above.

When the vessel radius is changed to 5 μm, (all other parameters remaining the same), $\Delta\omega(R^2/D)$ = 1.90. In this "intermediate exchange" regime, both the spin-echo signal and gradient - echo signal show less attenuation overall.

Lastly, when the vessel radius is changed to 2.5 μm, (all other parameters remaining the same), $\Delta\omega(R^2/D) = 0.476$. In this "fast exchange" or "motionally averaged" regime, both the spin-echo signal and gradient - echo signal show the least attenuation overall.

To apply these effects to *activation - induced signal changes* caused by a *change* in $\Delta\chi$, the simulation was performed at two different blood oxygenation saturation values: 0.60 and 0.75. The relative changes in signal corresponding to a *change* in blood oxygenation from 0.60 to 0.75 are shown in Figure 6.17.
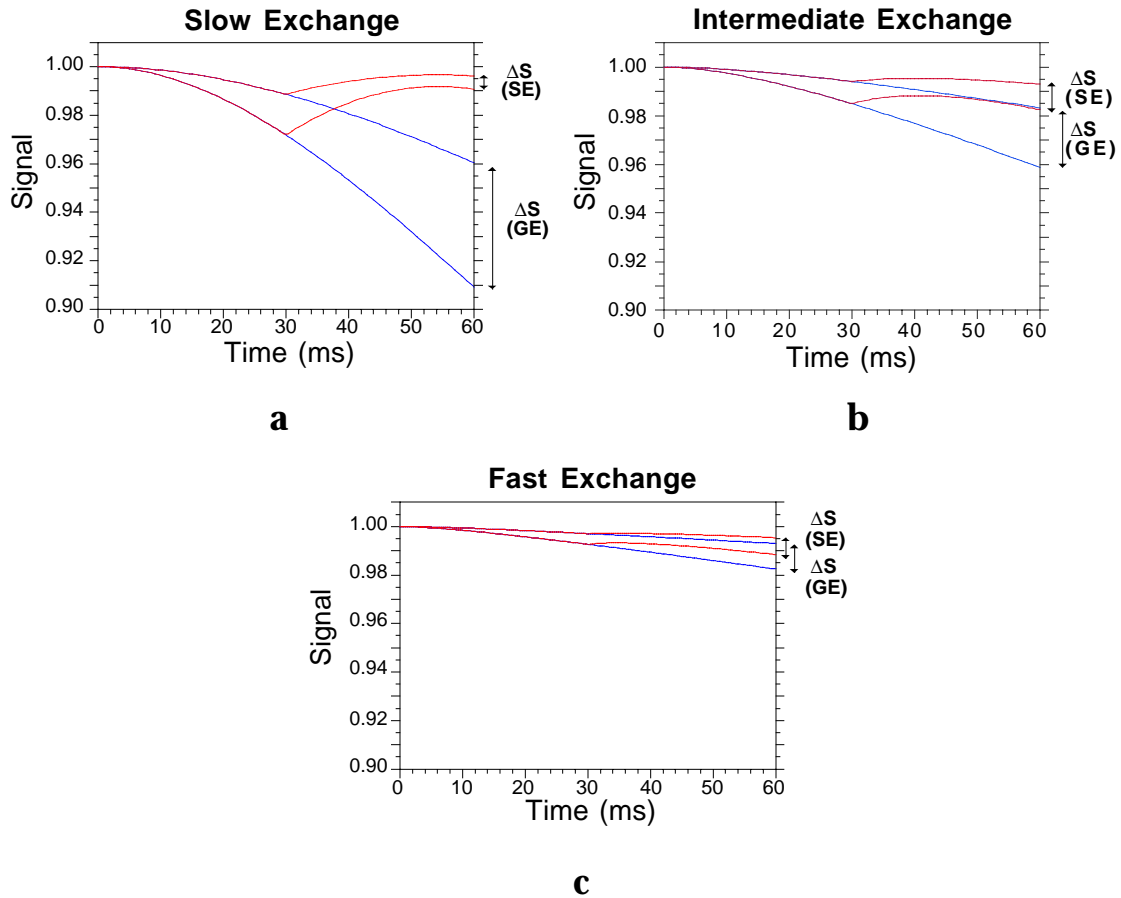
Figure 6.17: Example of signal evolution for spin-echo (SE) and gradient-echo (GE) sequences when the perturber of radius **a.** 20 μm. **b.** 5 μm., and **c.** 2.5 μm. has Δχ altered in a manner corresponding to an activation-induced blood oxygen saturation change from 0.60 to 0.75.

If the assumption is made that the source of the signal change is due to transverse relaxation rate that is modeled as a single exponential, then the relationship between signal and relaxation rate is

$$-Ln(Sa/Sr)/TE = \Delta R2(*).$$

[6.17]

where Sa and Sr are the active and resting state MR signal intensities. $\Delta R2(*)$ stands for either $\Delta R2$ or $\Delta R2^*$. This is a more general manner of describing the relative spin-echo and gradient-echo signal changes, since, given a relaxation rate change, the percent signal change will increase with TE. The relationship between the percent signal change at a given TE and $\Delta R2(*)$ is

$$\text{percent signal change} = 100 \ (e^{-\Delta R2 \ * \ TE} - 1). \qquad [6.18]$$

The percent signal change increases in an approximately linear manner with TE but the signal *difference* reaches a maximum at TE $\approx$ T2(*). It is for this reason that most fMRI studies are performed at TE $\approx$ T2(*).

In all simulations, the active (Sa) and resting (Sr) signal was obtained at a TE of 60 ms. The signal change was then converted to $\Delta R2^*$ and $\Delta R2$ by the use of equation 6.17. It was determined that the fairest spin-echo to gradient-echo comparison would be at TE values which are the same and within the range typically used experimentally. Therefore a TE of 60 ms was chosen.

The $\Delta R2^*/\Delta R2$ ratios from the example above increase from 1.53 (fast exchange) to 2.38 (intermediate exchange), to 9.98 (slow exchange). Figure 6.18 complements the results obtained in Figure 6.17. The frequency offset map is shown on the upper left, and the Gaussian probability distributions relative to the field map for each radius are shown on the right.
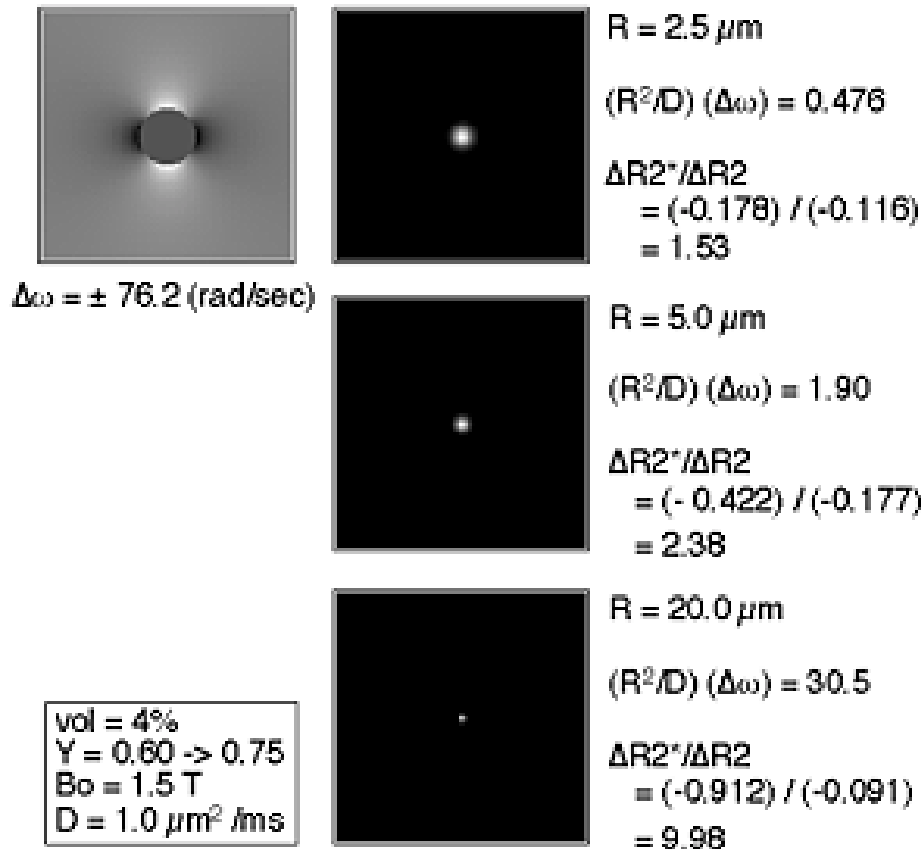
Figure 6.18: Summary of the magnetization map and the Gaussian distributions used for the signal decay plots shown in Figure 6.17. At $(R^2/D)\Delta\omega = 0.476$, ("fast"), $\Delta R2^*/\Delta R2 = (-0.178/-0.116) = 1.53$. At $(R^2/D)\Delta\omega = 1.9$, ("intermediate") $\Delta R2^*/\Delta R2 = (-0.422/-0.177) = 2.38$. At $(R^2/D)\Delta\omega = 30.5$, $\Delta R2^*/\Delta R2 = (-0.912/-0.0091) = 9.98$.


Model Validation

As a validation of the model methodology, a direct comparison was made with results obtained from the Monte - Carlo simulation method of Ogawa et al. (127). Two specific comparisons were made. First, a comparison was made with the study of off-resonant frequencey dependence of $\Delta R2^*$ that

is shown in Figure 3 of Ogawa et al. (127). Second, a comparison was made with the study of spin-echo to gradient-echo fractional signal change ratio dependence on vessel radius that is shown in Figure 6 of the same reference.

For comparison, the units were matched to the studies presented in the work of Ogawa et al. (127). In the first comparison, $\Delta R2^*$ was measured at 5 different Δv (Hz) values. The perturber radius was set to 2.5 μm. The diffusion coefficient used was either zero or 1 μm^2/ms (free diffusion). The blood volume fraction used was 2%. The value of $\Delta R2^*$ was obtained by setting Sa equal to 1 and Sr to the signal intensity obtained from the simulation. The results of the deterministic ("phase rotate" and "smooth") simulation are shown in Figure 6.19a. Here, it is shown that, with D = 0, the change in $\Delta R2^*$ is linear with Δv. In the case that D = 1 μm^2/ms. The dependence of $\Delta R2^*$ on Δv is greater than linear (approximately $B_0^{1.9}$). Both the shapes of the D = 0 and free diffusion D = 1 μm^2/ms curves and but the actual values of $\Delta R2^*$ match the results shown in Figure 3 of (127), shown in Figure 6.20a.

In the second comparison, using the deterministic model, the relative fractional signal attenuation between spin-echo and gradient-echo signal sequences were measured (Figure 6.19b). (TE = 40. Fractional blood volume = 2%. Δv = 40 Hz. D = 1 μm^2/ms.). That these results correspond closely to those shown in Figure 6 from (127), shown in Figure 6.20b.
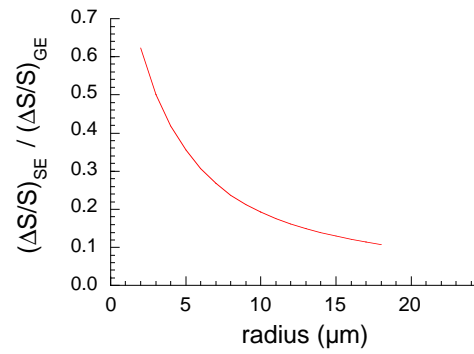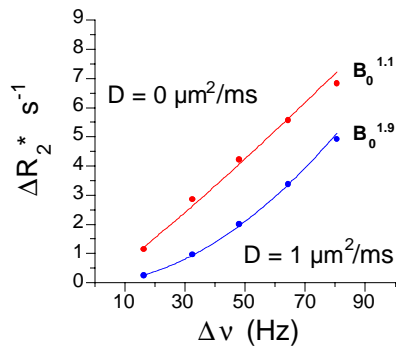
a

b

Figure 6.19: Results from deterministic simulations that are directly compared with Monte Carlo simulations of Ogawa et al. (127). **a.** Comparison with Figure 3 of Ogawa et al. (1). Demonstration of susceptibility - induced R2* change calculated in a voxel containing 2.5 μm blood vessels. **b.** Comparison with Figure 6 of Ogawa et al. (1). The ratio of $\Delta S/S$ for spin echo to $\Delta S/S$ for gradient echo signal as a function of cylinder radius (blood volume = 0.02, TE = 40 ms, $\Delta\nu$ = 40 Hz.
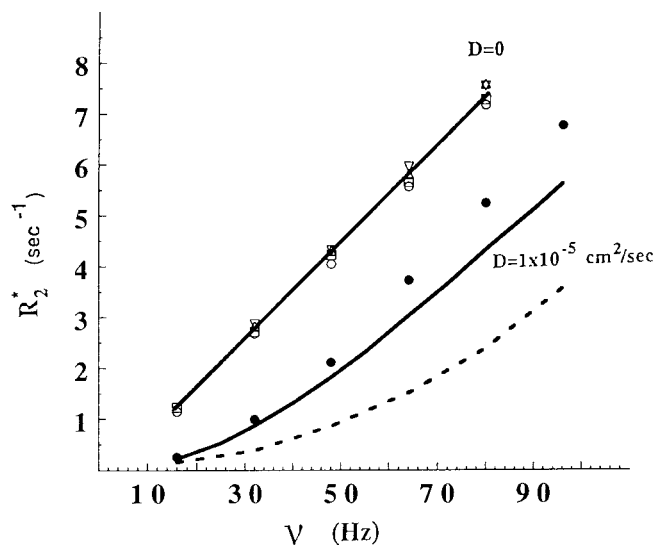
FIGURE 3   The susceptibility-induced R_2^* calculated for a voxel containing 2.5-μm radius blood vessels in the presence and absence of water diffusion. The top straight line is for the case $D = 0$ and a blood volume fraction $b = 0.02$. The rates represented by the open symbols along this line where also calculated for $D = 0$, but for $b = 0.03, 0.04$, and 0.05 and then divided by $b/0.02$ to show a linear dependence of R_2^* on b. The solid middle line for $D = 10^{-5}$ cm^2/s and $b = 0.02$ was calculated using the free diffusion model, whereas the filled circle points were computed with identical parameters but for the constrained diffusion model. The broken line is for the case where diffusion is present but the blood oxygenation level has an exponential variation from 1.0 to Y along the path of the capillary. The plot is made in terms of the shift frequency ν that encompasses the physiological range of venous blood oxygenation level at 4 T field ($\nu = 107.4$ Hz at $Y = 0$).

Figure 6.20a: , Figure 3 from Ogawa et al. (127) (Copied with permission). These results, obtained using a Monte Carlo simulation, show close correspondence with the simulation results shown in Figure 6.19a.
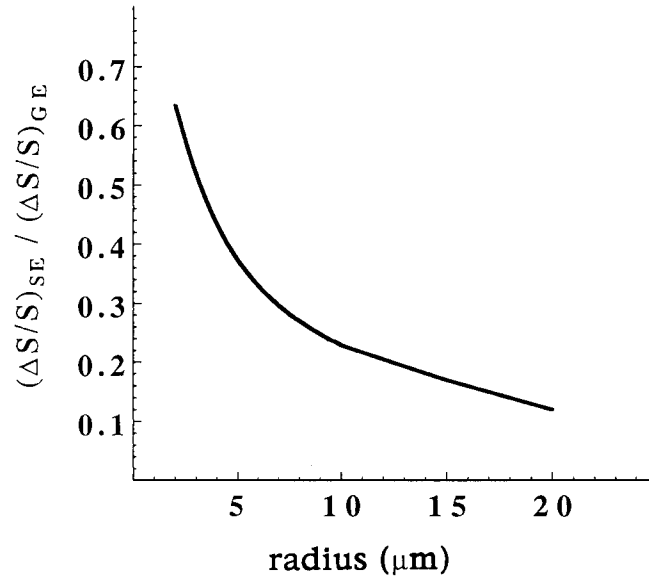
FIGURE 6　The ratio of $\Delta S/S$ for spin echo to $\Delta S/S$ for gradient echo image acquisition as a function of cylinder radius ($b = 0.02$, echo time $t_e = 40$ ms; $\nu = 40$ Hz).

Figure 6.20b: Figure 6 from Ogawa et al. (127). (Copied with permission). These results, also obtained using a Monte Carlo simulation, show close correspondence to the results shown in Figure 6.19b.

In general, though comparisons do not validate the model for every circumstance, the close agreement demonstrated between the results using the deterministic method and the results of Ogawa et al. (127) is encouraging and serves as an approximate validation of the technique.

General $\Delta R2^*$ and $\Delta R2$ dependence on $\Delta\omega$ and τ

In this section, a general description of the dependence of $\Delta R2^*$ and $\Delta R2$ on τ, ($\tau = R^2/D$), is given. However, instead of varying parameters related to $\Delta\omega$, (which include Bo, hematocrit, blood oxygenation, and $\Delta\chi$ of fully

200

deoxygenated red blood cells), $\Delta\omega$ is varied directly. Also, instead of varying parameters related to τ, (including R and D), τ is varied directly.

Figure 6.21 shows $\Delta R2^*$ (Sa = 1, and Sr = signal intensity at 60 ms) vs. $\Delta\omega$ over a range of R^2/D values. The vertical bands indicate the off-resonance frequency range that is covered when the oxygen saturation of whole blood changes from 0.60 (right edge of band) to 0.75 (left edge of band). At higher field strengths, the bands become progressively wider and $\Delta R2^*$ also increases. These results illustrate that, given the same oxygenation change, the activation - induced signal change will be greater at higher field. The assumption is also made that the relative intravascular and extravascular baseline signal intensities are the same across field strengths. As R^2/D increases, $\Delta R2^*$ becomes greater at a given $\Delta\omega$, but the slope of the curve is nearly linear, especially at high $\Delta\omega$ values.
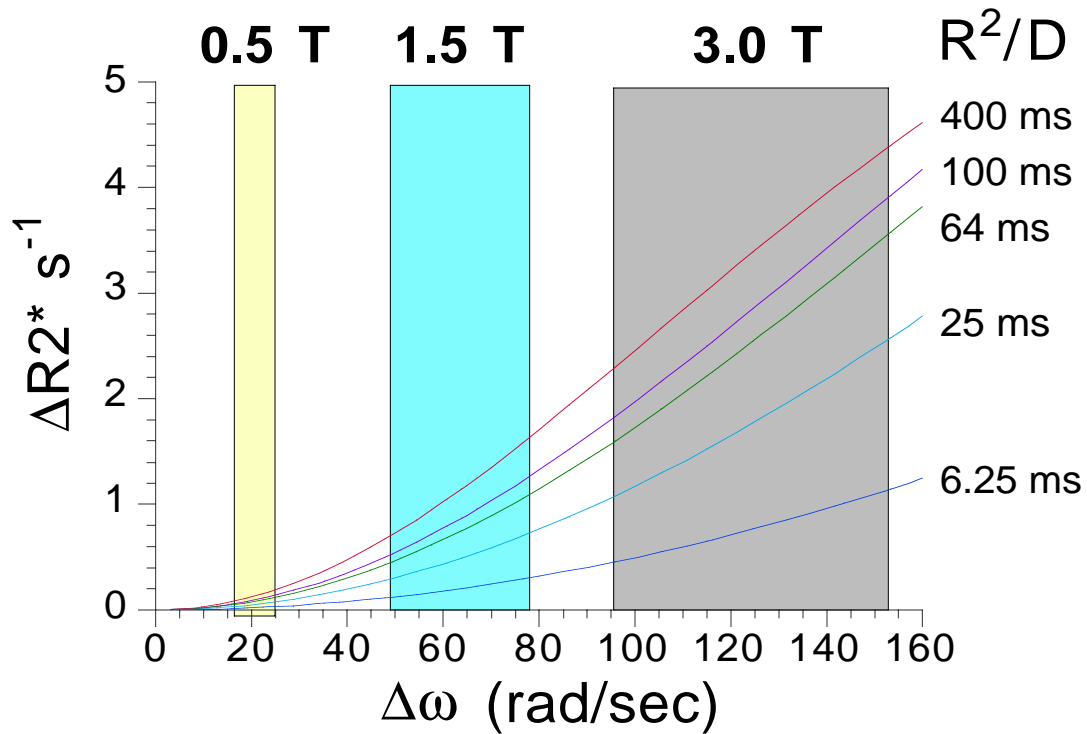
Figure 6.21: Graph of $\Delta R2^*$ vs. $\Delta\omega$ at different values of τ, (R^2/D). The increase in $\Delta R2^*$ is monotonic with frequency and τ. The vertical bands indicate the maximum frequency shift at each field strength that corresponds to a change in hemoglobin saturation from 0.6 to 0.75.

Figure 6.22 shows $\Delta R2$ vs. $\Delta\omega$ over a range of R^2/D values. At a given $\Delta\omega$, $\Delta R2$ is lowest at high R^2/D (slow exchange), then increases until a maximum is reached at $R^2/D = 25$ ms (intermediate exchange), then decreases again as R^2/D decreases further.
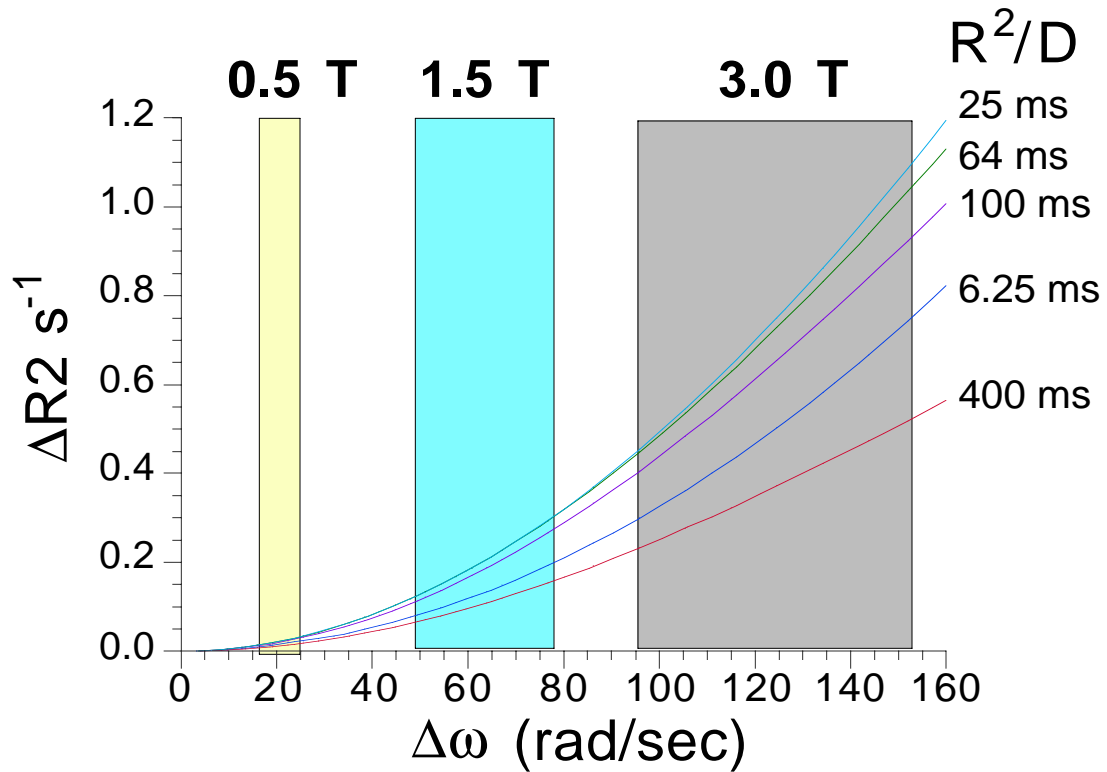
Figure 6.22: Graph of ΔR2 vs. Δω at different values of τ, (R^2/D). As τ is increased, ΔR2 increases, reaching a peak at τ = 25 ms, then decreases at higher τ values.

Figure 6.23 shows ΔR2*/ΔR2 measured across Δω and R^2/D. The ratios increase with increasing R^2/D. The ratios show a relative insensitivity to Δω, which is in agreement with the reported ratios in the literature (185) and in chapter 7, demonstrating that the measured ΔR2*/ΔR2 ratio is relatively field strength - insensitive.
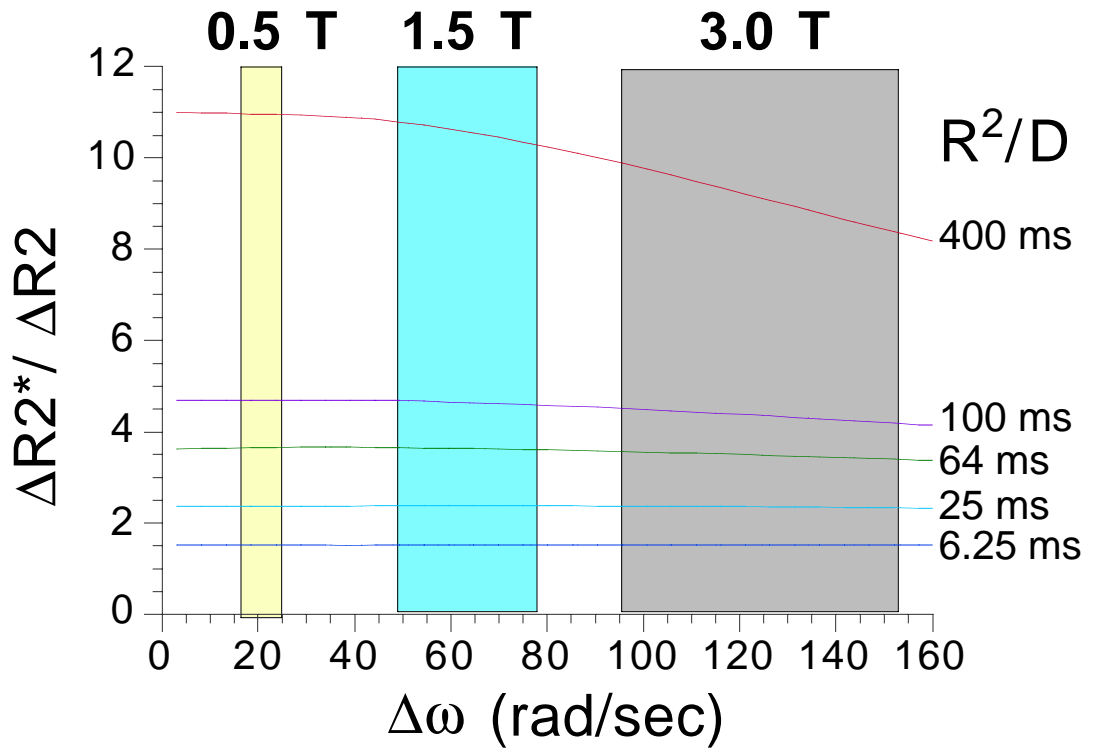
Figure 6.23: Graph of the ΔR2*/ΔR2 demonstrating that the ratio is relatively insensitive to Δω.

ΔR2* and ΔR2 Dependence on Physiologic Parameters

In this section, specific physiological parameters are modulated, one at a time. Specifically, an analysis is made of the absolute and relative ΔR2* and ΔR2 changes that occur when 1) vessel radius is varied at three field strengths, 2) diffusion coefficient is varied, 3) blood volume is varied, 4) vessel orientation, relative to B_o, is varied, and 5) blood oxygenation is varied. The parameters and their corresponding values, when not being modulated, are given in Table 6.1.

Parameter	Value
Blood Oxygen Saturation	0.60 (resting) to 0.75 (active)
Vessel Radius	10 μm
Blood Volume	4%
$\Delta\chi$ of deoxygenated red blood cells	0.18×10^{-6} cgs
Vessel Orientation	Random distribution
Diffusion Coefficient	1 μm2/ms (isotropic & unrestricted)
Field Strength (B_O)	1.5 Tesla
Hematocrit	42

Table 6.1: Table of the constant variable values used. The radius, field strength, diffusion coefficient, blood volume, angle, and blood oxygen saturation are modulated systematically below.

Figure 6.24 shows the effects of varying vessel radius from 2.5 μm to 20 μm at 0.5 T, 1.5 T, and 3T. Figure 6.24a is of ΔR2 and Figure 6.24b is of ΔR2*. The ΔR2 values generally increase with field strength, but peak at a vessel radius of about 6 μm at all field strengths. The ΔR2* values increase monotonically with vessel radius. These relaxation rate changes simulated across the entire range of radii and field strengths are comparable to those measured in active cortical regions (107, 174-176, 179, 180, 185, 211).
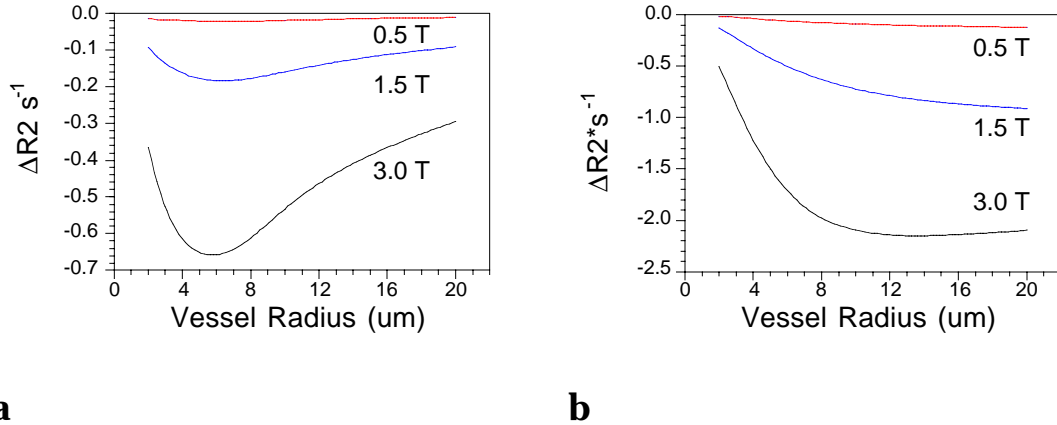
Figure 6.24: Effect of varying field strength on activation - induced changes in **a.** R2 and **b.** R2*.

Figure 6.25 shows the simulated $\Delta R2^*/\Delta R2$ ratios at all field strengths. As the vessel radius approaches 0, the ratio approaches 1 and both of the relaxation rate changes approach zero. This illustrates an important concept regarding endogenous susceptibility contrast. At the limit where the perturber size is small and homogeneously distributed, susceptibility gradients will not exist and dephasing due to spins processing at different frequencies in the vicinity of field inhomogeneities will not occur. Other mechanisms not modeled here may still contribute. Only bulk susceptibility contrast of a compartmentalized field perturber that is large relative to the surrounding spin dynamics can account for the differences between $\Delta R2^*$ and $\Delta R2$ that are consistently observed. The box in Figure 6.25 indicates the ratios typically measured experimentally at the three field strengths (174, 175, 179, 180, 184, 185). The average compartment size (likely some combination of large vessels and intravascular red blood cell effects) is in the range of 7 to 12 μm.
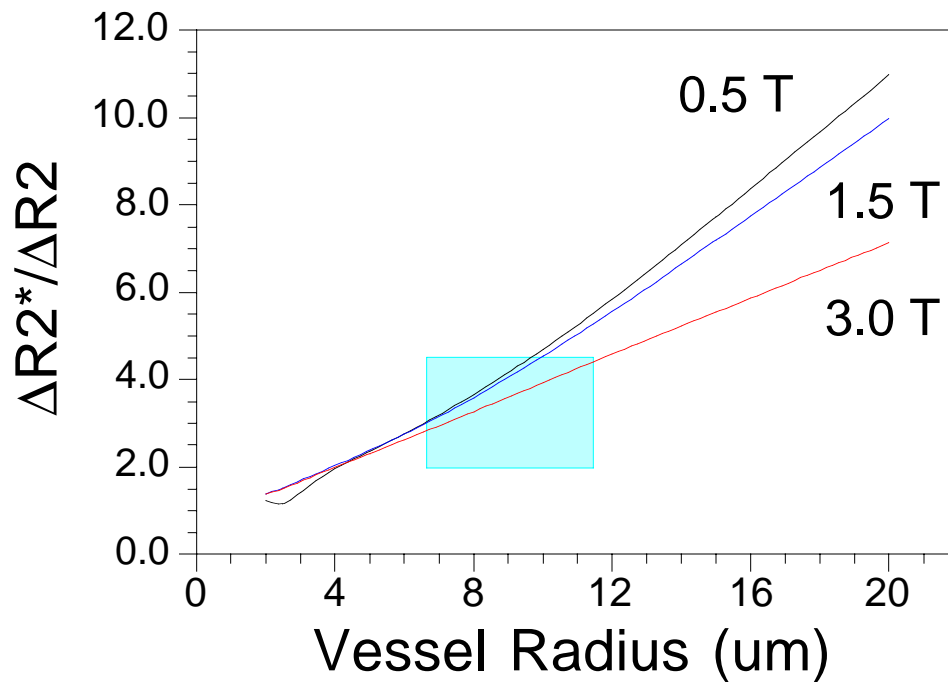
Figure 6.25: Ratio of ΔR2* (shown in Figure 6.25 a) to ΔR2 (shown in Figure 6.25 b) at 0.5 T, 1.5 T, and 3.0 T. The box indicates the typical ΔR2*/ΔR2 ratios reported in the literature.

Studies by Hoppel et al. (107) of ΔR2*/ΔR2 on whole blood during changes in oxygenation report a ratio of 1.5, which corresponds, in the simulated results, to a radius of 2.5 μm - about the radius of a red blood cell. These similarities to the whole blood data may be a) incidental given the vastly different geometries, field overlap, and proton dynamics, or b) indicative that these geometrical differences are not a large factor when considering dephasing in the fast exchange regime. More modeling studies, using this deterministic approach, of the effects of varying oxygenation on blood T2* and T2 are currently being pursued to answer some of the above -

mentioned questions and to complement modeling studies such as those of Gilles et al. (131) and experimental studies on whole blood such as those of Thulborn et al (97) and Wright et al. (105). Some of these studies are presented at the end of this chapter.

Figure 6.26a shows the effect of the diffusion coefficient on $\Delta R2^*$ and $\Delta R2$. Without diffusion, $\Delta R2 = 0$ and $\Delta R2^*$ is maximum for the $\Delta\omega$ and blood volume used. As the diffusion coefficient increases, the $\Delta R2^*$ decreases and $\Delta R2$ first increases then decreases as D is increased further. Measured values of $\Delta R2^*$ and $\Delta R2$ are comparable to the simulated values at $D = 0$ to 5 $\mu m^2/ms$.

Figure 6.26b shows the $\Delta R2^*/\Delta R2$ ratio vs. D. Most experimentally obtained data lies in the elbow of the curve, where the diffusion coefficients are comparable to those found in the brain and in water. As D becomes large the slope flattens considerably near 1.5. The values and ratios simulated for diffusion coefficients greater that 5 $\mu m2/ms$ may be less accurate due to digitization errors when using a step size of 1 ms.

a   **b**
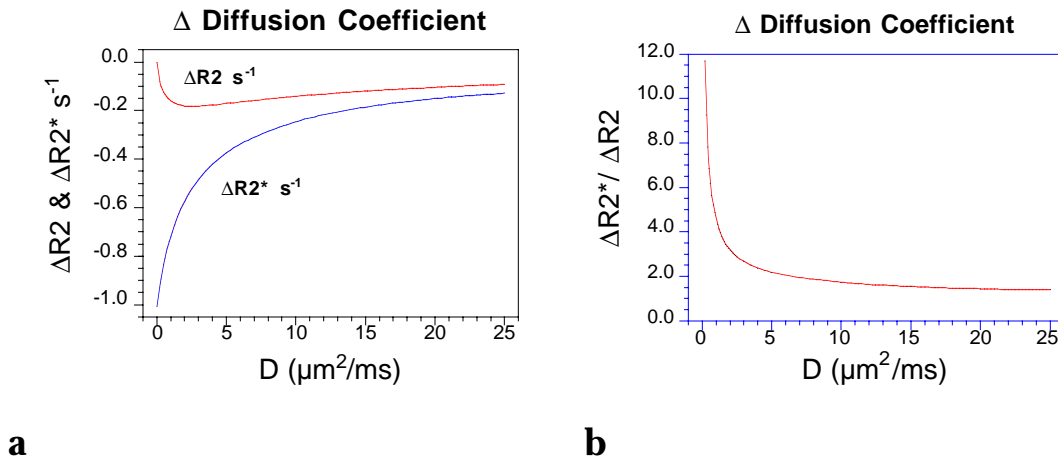
Figure 6.26: Effect of varying diffusion coefficient on activation - induced changes in R2 and R2*. **a:** Relative R2 and R2* vs. D. **b.** $\Delta R2^*/\Delta R2$ vs. D.

As mentioned, the blood volume may vary considerably from voxel to voxel. Figure 6.27a shows the simulated relaxation rate changes as they relate to resting state blood volume. $\Delta R2^*$ and $\Delta R2$ show a strong dependence on blood volume. The $\Delta R2^*$ and $\Delta R2$ values typically observed correspond to blood volumes between 2% and 7%. Figure 6.27b shows the change in $\Delta R2^*/\Delta R2$ with volume change. Here, the ratio changes little.

a   **b**
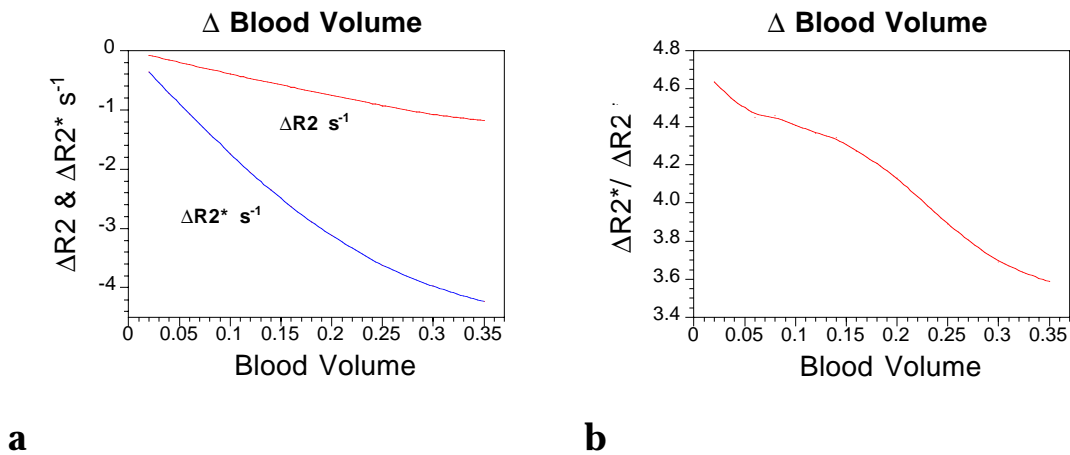
Figure 6.27: Effect of varying fractional blood volume on activation - induced changes in R2 and R2*. **a:** Relative R2 and R2* vs. blood volume. **b.** $\Delta R2^*/\Delta R2$ vs. blood volume.

In the brain and most likely in larger vessels, the predominant vessel orientation may vary considerably from voxel to voxel. The changes in relative relaxation rates that occur with varying the vessel angle are shown in Figure 6.28a. As described in equations 6.7 and 6.8, and shown in Figure 6.11, the external gradients and the intravascular frequency offsets vary considerably with angle. The values of $\Delta R2^*$ and $\Delta R2$ appear largest at 90° - the angle in which the surrounding gradients are largest. The effects are

minimal at 45° - the angle in which the combined effect of the gradients and the internal frequency offset are minimal. The $\Delta R2^*$ and $\Delta R2$ values appear to increase as the angle is reduced to 0° - the angle in which the external gradients do not exist and the intravascular frequency offset is maximal.

The $\Delta R2^*/\Delta R2$ ratio change vs. angle is shown in Figure 6.28b. The ratio increases then reaches a plateau. This is likely related to the fact that the vessel is freely permeable and that the sharp $\Delta\omega$ difference (no gradient: just a step) that begins to form in the immediate vicinity of the vessel wall (below 45°) contributes somewhat to spin-echo irreversible dephasing.

a   **b**
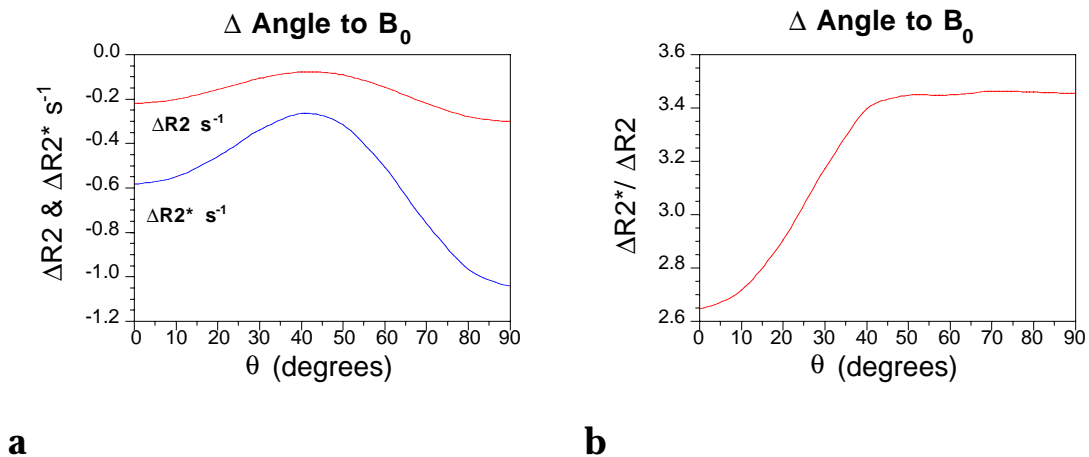
Figure 6.28: Effect of varying cylinder orientation relative to Bo on activation - induced changes in R2 and R2*. **a:** Relative R2 and R2* vs. angle to B_O. **b.** $\Delta R2^*/\Delta R2$ vs. angle to B_O.

The resting blood oxygenation may vary considerably, from voxel to voxel, along with the activation - induced blood oxygenation changes. If the slope of $\Delta R2^*$ or $\Delta R2$ vs. %HbO2 changes, then this may have a large effect on activation - induced signal changes. In the brain, the resting venous oxygen

saturation is assumed to be 60%. The changes in $\Delta R2^*$ and $\Delta R2$ that occur as %HbO$_2$ is increased to 75% were simulated. Figure 6.29a shows $\Delta R2^*$ and $\Delta R2$ vs. %HbO$_2$. Below 60% blood oxygenation, the slopes appear to become somewhat constant. Above a blood oxygen saturation of 60%, the slopes appear to decrease. Figure 6.29b demonstrates that the $\Delta R2^*/\Delta R2$ ratio is not strongly sensitive to %HbO$_2$.

a   **b**
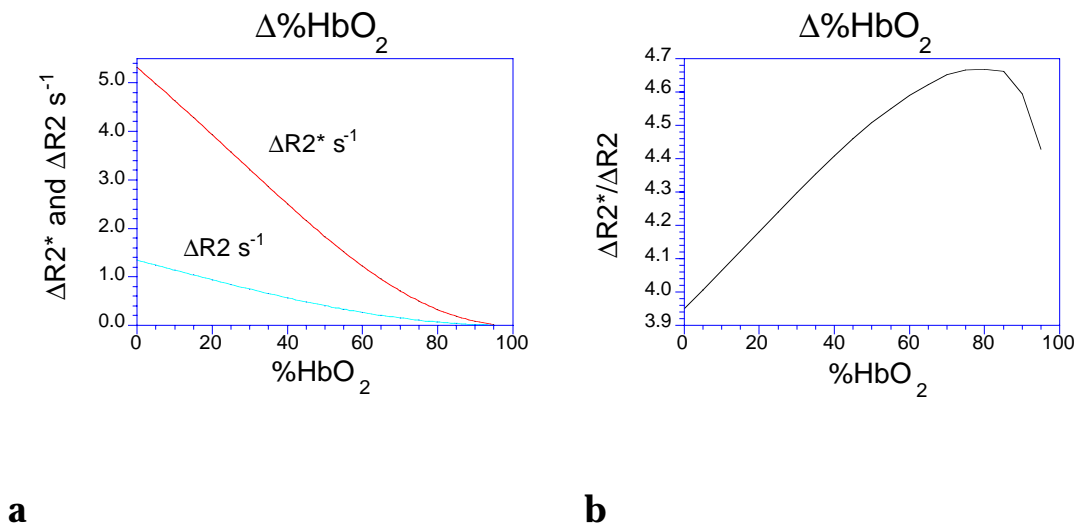
Figure 6.29: Effect of varying hemoglobin oxygen saturation on relative transverse relaxation rate. **a:** Relative R2 and R2* vs. %HbO$_2$. **b.** $\Delta R2^*/\Delta R2$ vs. %HbO$_2$.

Blood oxygenation changes vs. blood volume changes

In this section, it is demonstrated that the concomitant activation - induced change in blood volume contributes much less significantly to the overall signal change than does the change in blood oxygen saturation. A common question that is asked in regard to the activation - induced MR signal change is: "Given constant oxygenation and an increase in volume, the

MR signal drops, but given a constant blood volume and an increase in oxygenation, the MR signal increases. Since both hemodynamic events happen during activation, which effect dominates?" To answer this question, it is necessary to determine the effects of simultaneous changes in blood volume and oxygenation.

Figure 6.30 shows a graph of Y vs. $\Delta R2^*$, similar to Figure 6.30a, but having one curve for each blood volume ranging from 2 to 20%, as shown on the left of the graph. These graphs most closely resemble the phsyiologic process of vessel recruitment, since the vessel radii are not varied when the volume is increased. In this figure, the simultaneous relationship between blood volume and blood oxygen saturation, Y, is shown. At the lowest oxygenation shown, a blood volume increase of an order of magnitude causes a change in $\Delta R2^*$ of 8 s^{-1}. At the highest blood volume, a similar change in $\Delta R2^*$ is caused only by decreasing the %HbO2 by 50%.
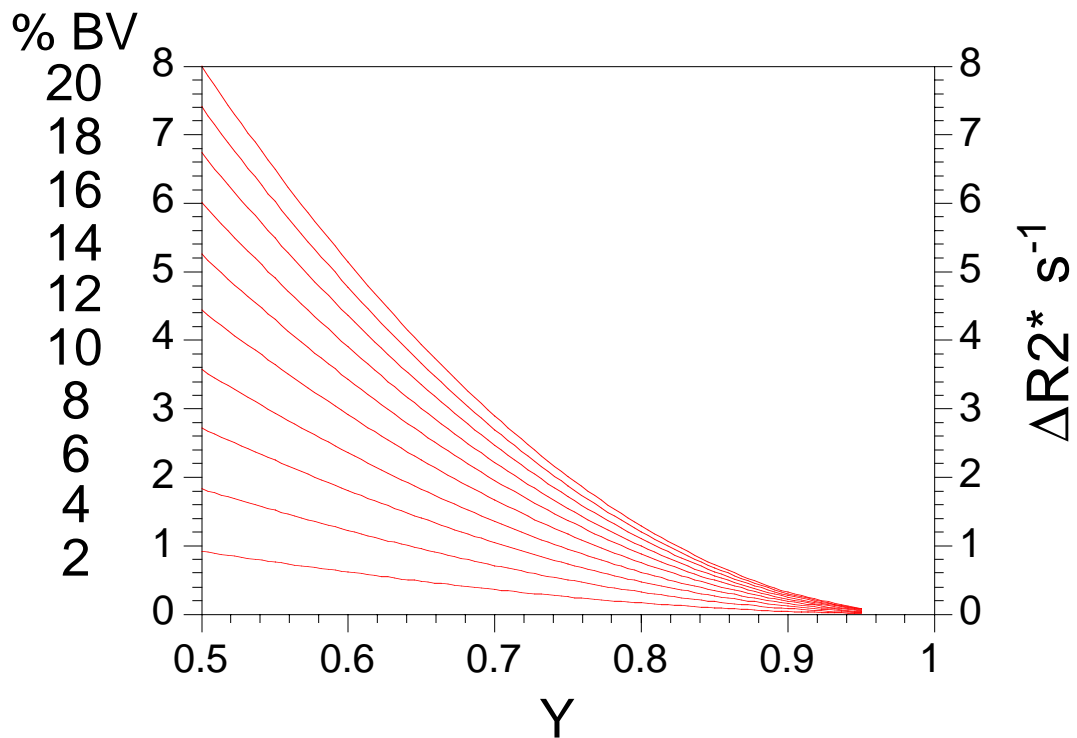
Figure 6.30: The relationship between blood oxygenation saturation (Y) and $\Delta R2^*$ at different fractional blood volumes.

Using the physiological relationships in equations 6.3 and 6.4, it is determined that with an activation - induced increase in flow (69% increase), the venous blood oxygen saturation would increase from 60% to 75%, and the blood volume would increase from 4% to 5.2%. Figure 6.31 is a graph of $\Delta R2^*$ vs. %HbO$_2$, for the resting and active blood volumes, and spanning a %HbO2 range from 0.6 (resting) to 0.75 (active). For the resting state blood volume, $\Delta R2^*$ (difference between 60% blood oxygen saturation and 100% blood oxygen saturation) is about 1.32 s^{-1}. During activation, considering changes in blood oxygen saturation only, the value of $\Delta R2^*$ decreases along the same

curve to 0.5 s^{-1}: a difference of -0.82 s^{-1} (activation - induced signal change of 3.3% at a TE of 40 ms). If changes in blood volume are considered, the ΔR2* value is measured at the same blood oxygenation but on the curve representing the higher blood volume. Here the ΔR2* value is about 0.62 s^{-1}: a difference of -0.70 s^{-1} (an activation - induced signal change of 2.8% at a TE of 40 ms). In general, the small increase in blood volume causes a small reduction in the activation - induced signal increase, but the increase in blood oxygen saturation dominates.

Figure 6.31: Hypothesized activation - induced changes in blood volume and blood oxygen saturation (Y). The effect of an increase in oxygenation and blood volume are opposite in sign, but the oxygenation effect dominates.

Simulating Oxygenation Changes in Whole Blood

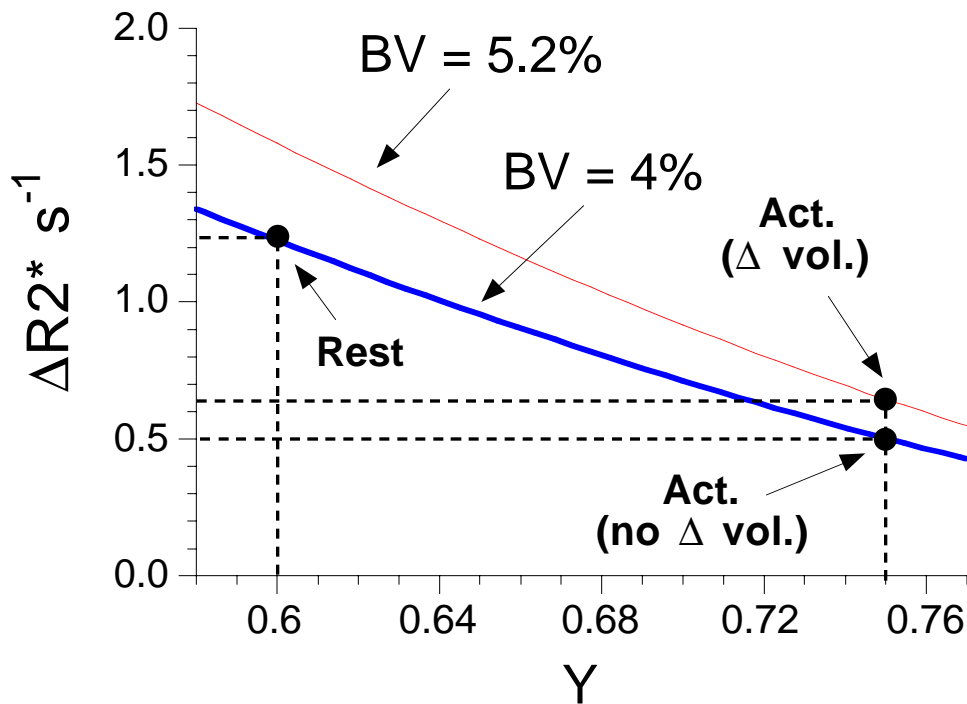Currently, four classes of BOLD models have been published. The first class is that which only takes into consideration the dephasing effects on extravascular spins by gradients outside the simulated vessels (123, 124, 126, 127, 252). The second class is that which takes into consideration the intravascular phase shift effect, neglecting the effects of external gradients on dephasing(186) (186). In this second class , the cause for intravoxel dephasing is the phase difference that accrues between the intravascular spins and extravascular spins. The third class is a combination of the first two classes, taking into consideration both the external gradient dephasing effects and the internal phase shift effects. The deterministic diffusion model presented in this chapter falls into this third class. The fourth class is identical to the third class, yet, in addition, intravascular dephasing due to red blood cell effects on blood plasma spins, is also considered (118, 190, 192, 210). It appears that this fourth class is the most realistic class of models so far. Work is being performed to incorporate intravascular dephasing effects into the deterministic diffusion model presented. Studies of the T2 of blood have been published (97, 100, 105, 131), but none, to date, have directly studied blood T2*. Below is a first attempt to model, using the above - described methodology, the oxygenation - dependent dephasing effects (T2* and T2) in whole blood.

The unknowns involved in modelling intravascular effects include geometry and proton dynamics. The precise shape of red blood cells is known and has been used in other simulations (131). In these simulations this geometry was simplified to randomly orentated and distributed infinite cyliners. It is understood that, at higher diffusion coefficients (fast exchange regieme) the dependence of dephasing effects on geometry of the magentic

field pertuber decreases. The strategy in these simulations was use a simplified geometry but then allow the plasma spin diffusion coefficient to vary until the simulations matched the current experimental T2 and T2* results in the literature (105, 107). With these matched results, one can then not only simulate T2* effects directly but also explore other blood relaxation dependencies not yet tested experimentally. Ultimately these results can be inserted into the simulations in the manner schematically depicted in Figure 6.32.
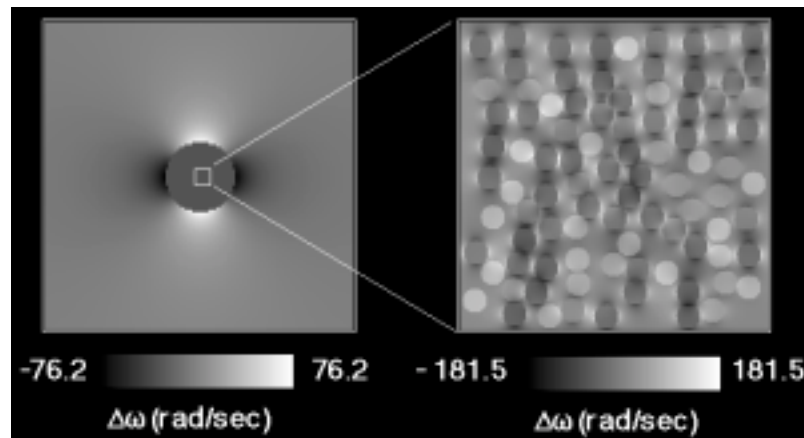
Figure 6.32: Illustration of the intravascular and extravascular magnetic field perturbations. Intravascular effects include a coherent frequency shift, illustrated on the left and frequency dispersion caused by red blood cells in plasma, as shown on the right. Extravascular effects include the gradients sourrounding the vessel. Ideally, all of the illustrated effects would be considered. The simulations described below describe only the intravascular frequency dispersion effects shown on the right.

It is understood that the choice of non-exact geometry and a 2-dimensional simulation may lead to the convergence on an incorrect

diffusion coefficient when trying to match experimental results. It is beleived however, that, while, individually, the parameters are incorrect, their combined effects, which is matched to experimental results, may give an accurate assessment of intravascular dephasing and subsequently allow more accurate prediction and interpretion of activation - induced signal changes.

The basic simulation methodology involved, as described, is a stepwise 2-dimensional Gaussian convolution and phase rotation to simulate diffusion in the presence of off-resonance effects. Field overlap from adjacent red blood cells was considered. Blood susceptibility values of Weisskoff et al. (108) were used. Red blood cell geometry was simplified to randomly oriented and distributed infinite cylinders having 2.5 μm radii. Field strength = 1.5 T. Hematocrit = 44. $T2_O$ = 250 ms. The hematocrit and T2o were approximately those reported in Wright et al. (105). Figure 6.33 illustrates the $\Delta\omega$ map and corresponding Gaussian probability density function (for D = 1.8 μm2/ms and inter step time or dt = 0.25 ms) used in the simulation.
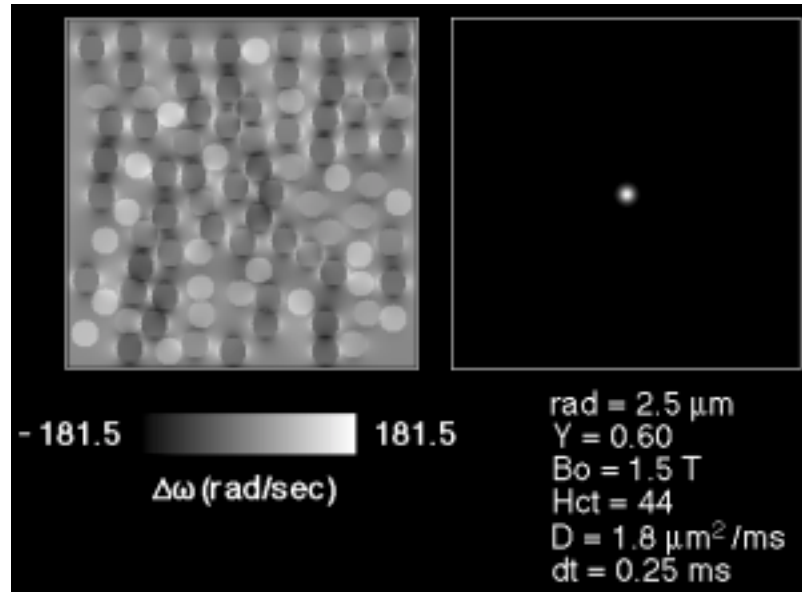
Figure 6.33: Illustion of Δω map and corresponding Gaussian probablility density map for the simulation of intravascular dephasing effects.

First, using a multi-echo (5 echo) simulation with identical parameters to those used experimentally in (105), blood T2 vs. %HbO$_2$ curves were generated, by a linear fit of ln(signal) vs TE (Press et al..numerical recipies) at different inter - 180 pulse times (τ). The best fit to the data of Wright et al. (105) was obtained using D equal to 1.8 μm^2/ms. The T2 vs %HbO$_2$ curves curves generated at this D value are shown in Figure 6.34.
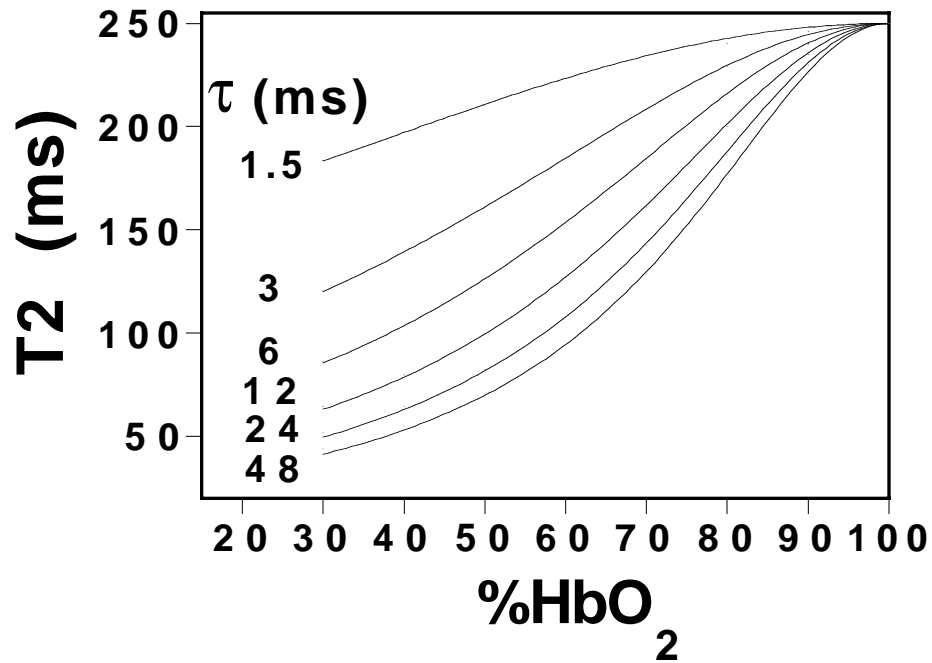
Figure 6.34: Hct = 44, B_O = 1.5 T, $T2_O$ = 250 ms, cell radius = 2.5 µm. Curves obtained at this value of D (1.8 μm^2/ms), give the best fit to those of Wright et al. (105).

The $\Delta R2^*$ and $\Delta R2$ that occur with a change in whole blood $\%HbO_2$ from 60% to 70% were also simulated at different values of D. Figure 6.35 shows $\Delta R2^*$ and $\Delta R2$ on the left axis and $\Delta R2^*/\Delta R2$ on the right axis. At D = 1.8 μm^2/ms, the ratio was 1.5; corresponding to the $\Delta R2^*/\Delta R2$ ratio for whole blood reported by Hoppel et al. (107) using a similar oxygenation perturbation.
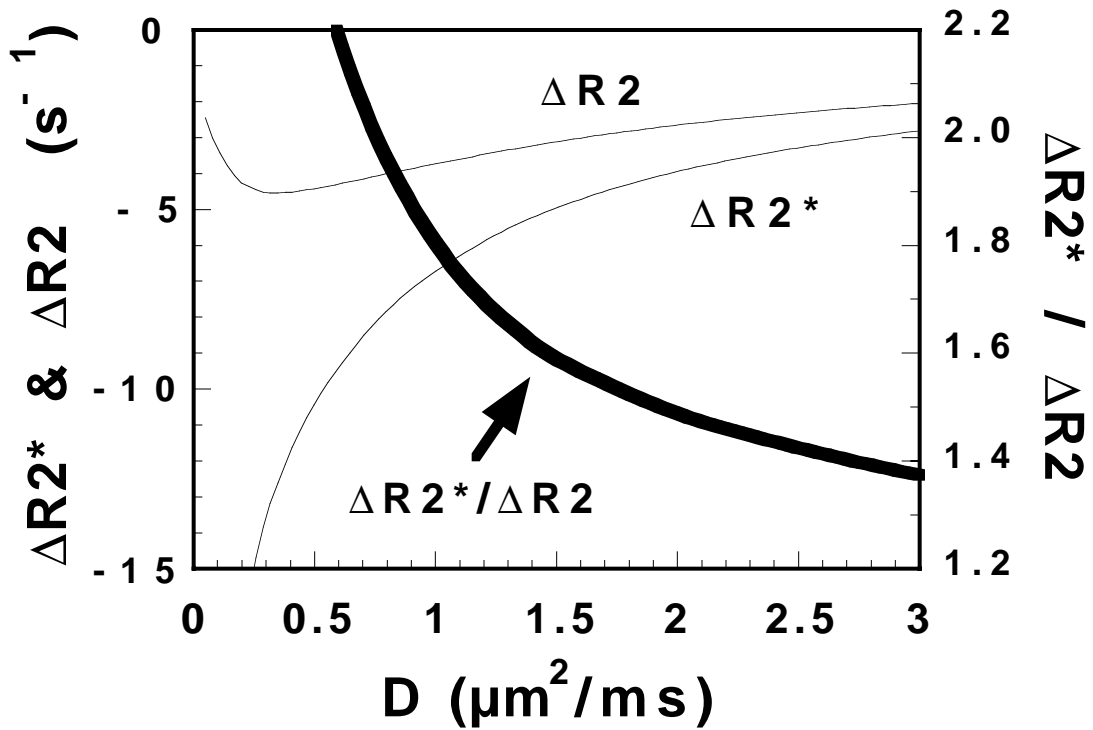
Figure 6.35: Dependence of ΔR2* and ΔR2 (left axis) and ΔR2*/ΔR2 (right axis) on D. The change in %HbO$_2$ was from 60% to 70%. Hct = 44. T2$_O$ = 250 ms, t = 48 ms. The ratio at D = 1.8 μm^2/ms (≈1.5) matches reported results of Hoppel et al. (107).

As illustrated in Figure 6.34 and 6.35, the simulations convergently match the experimental results with a diffusion coefficient of 1.8 μm^2/ms. This does not mean that this is what the diffusion coefficinet in plasma actually is, but it does mean that, given imprecise geometrical considerations, an estimate of the plasme diffusion coefficint can be obtained witch allows convergent agreement with experiment. This extimate can can allow further simulations to be performed and predictions to be made where experimental data is lacking.

The implications of these studies are important in the context of fMRI: whole blood T2 and T2* effects are significant in several ways. One is regarding voxels that are completely contained within a draining vein (100% blood volume - as may be the case for many voxels in high resolution fMRI studies). With an activation - induced %HbO2 change from 60% to 70%, simulated gradient-echo and spin-echo percent signal changes (TE=60ms) are 30% and 18% respectively. These "large vessel effects," which are caused by frequency shifts within red blood cells and are which are vessel orientation - independent, are not removed by the use of spin-echo sequences.

Even in voxels that have a relatively small blood volume fraction, the intravascular component of fMRI signal changes is highly significant (192). Accurate determination of blood relaxation rates is necessary for the assessment of these intravascular dephasing effects.

Ongoing work is being performed to assess the dependence of whole blood on hematocrit, cell integrity, and field strength. In particular, a strong blood T2* dependence on field strength, (stronger than gray matter T2* dependence), as implied by preliminary resluts of these and other (192) simulations, may cause a significantly reduced intravascular contribution to activation - induced signal changes at higher field strenths, therefore possibly helping to explain the linear or sublinear field strength dependence (185) described in chapter 8.

These simulations serve as a means by which the mechanisms underlying activation - induced MR signal changes can begin to be clarified. The simulation methodology presented here provides a flexible and computationally efficient alternative to Monte Carlo techniques. In these simulations, the significance of physiologic and biophysical parameters on activation induced changes in R2* and R2 were assessed.

The simulation method was first compared with a Monte Carlo modelling method (127), giving strongly matching results. Secondly, when using approximate estimates of physiologic and biophysical phenomena during resting and activated states, general agreement was obtained between simulated and measured ΔR2 and ΔR2* values (107, 174-176, 179, 180, 185, 211). These results support the hypothesis that activation - induced signal changes can be explained primarily by a bulk susceptibility contrast mechanism.

More specific conclusions can also be made. The first is that modulation of resting state blood volume and of field strength had the strongest effects on the ΔR2* and ΔR2 values. This conclusion has important implications for fMRI. Blood volume varies considerably from voxel to voxel. These variations across voxels likely modulate fMRI signal change magnitude more strongly than spatial differences in activation-induced oxygenation changes. For example, a large vessel "downstream" from an activated region, yet filling a voxel, may experience a much smaller oxygenation change than the capillaries and venuoles in the immediate vicinity of the activated region, but, because of the large blood volume in that particular voxel, may still show the largest activation - induced signal change

for both spin-echo and gradient-echo sequences. These "large vessel effects" have been alluded to by several investigators (178, 182, 206, 212, 214). Methods for removing these effects have ranged from vein identification methods (178, 180, 182, 187, 205, 206, 214) to normalization of activation-induced signal change maps to a blood volume map created by global vasodilatation accompanying hypercapnia (198).

The strong simulated field strength dependence indicates that a gain in functional contrast can be obtained by performing functional imaging at high fields. Experimental evidence is conflicting; both $B_o^{0.8}$ (185) and $B_o^{1.6}$ dependencies (183) of activation - induced $\Delta R2*$ have been reported. The stronger B_O dependence of the smaller radii vessels may indicate that, at higher field strengths, smaller compartments (capillaries and red blood cells) may contribute more predominantly.

The second specific conclusion that can be made is that the modulation of the diffusion coefficient and compartment size radius had the greatest effect on the $\Delta R2*/\Delta R2$ ratio. Experimental studies have observed large spatial heterogeneity in $\Delta R2*/\Delta R2$ (176, 180, 377), suggesting a large heterogeneity in predominant compartment size or diffusion coefficient. The average ratio measured, in vivo, has been in the range of 3/1 to 4/1 (174, 175, 179, 180, 184, 185), suggesting, with the assumed proton dynamics and susceptibilities, that the "average" compartment size is about 8 to 10 μm.

Modulation of field strength did not strongly affect the simulated $\Delta R2*/\Delta R2$ values. These results are also in approximate agreement with preliminary studies (184, 185).

This model also demonstrates that even though blood oxygenation and blood volume increases during activation cause opposite sign effects, blood oxygenation changes dominate the signal change. This effect should not be

223

confused with the strong effect that resting state blood volume has on $\Delta R2^*$ and $\Delta R2$, given an oxygenation change and fixed volume.

Lastly, this chapter illustrates first steps taken to consider intravascular dephasing effects. Dephasing effects in whole blood are simulated using randomly oriented and distributed infinite cylinders having 2.5 μm radii. The diffusion coefficient was adjusted such that the closest match to experimental results were obtained. In fact, the simulations convergently matched experimental results of Wright et al. (105) and Hoppel et al. (107). Using this simulation, it was determined that, given voxels completely contained in a vessel, the fractional signal changes in both gradient-echo and spin-echo sequences would be quite high. Ongoing work is being performed to incorporate these intravascular effects into the model to better predict the activation - induced signal change dependence on field strength and the relative activation - induced $\Delta R2^*/\Delta R2$ ratios.

The ultimate goal of all fMRI contrast models is a complete understanding of the variables that contribute to the signal changes such that accurate localization of brain activation can be made; quantification of flow, volume, and oxygenation changes can be made, and; other useful neuronal, hemodynamic, or biophysical information can be obtained. Both careful experimentation and modelling are essential to achieve this goal. The science and art of fMRI interpretation is advanced at each iterative step of this experimentation and modeling process.

CHAPTER 7

TRANSVERSE RELAXATION RATE COMPARISONS

7.1 INTRODUCTION

Many variables can influence the magnitude, location, and timing of activation–induced MR signal intensity changes. These variables include a decrease in R2* and R2, an increase in proton density, movement during activation, a net frequency shift causing a subvoxel shifts in signal or periodic intravoxel dephasing, and a decrease in the average RF saturation within a slice caused by an increase in the inflow rate of unsaturated spins have into the imaging plane, and an increase in apparent T1 relaxation rate.

Based on previous studies in whole blood, on animal models, on mathematical simulations, and on human studies involving modulation of contrast weighting and field strength, the evidence exists that the predominant mechanism of signal changes in susceptibility – weighted sequences having TR $\geq$ 1 sec, is from changes in spin–spin relaxation rate due to changes in the susceptibility of hemoglobin during activation.

Accurate interpretation of activation – induced MR signal changes is still problematic due to the existence of several still not fully understood effects. For a complete overview of the current status of these issues, please refer to chapter 1, section 4 (current functional MRI research). A few of these issues are briefly mentioned below. One issue concerns flow vs. oxygenation contrast. How much of the signal change (or what areas) are related primarily to oxygenation changes and how much is due to non–susceptibility related

flow changes? Basically, it is a question of localization. Changes in flow velocity (on the arterial side) are thought to occur more distal from the regions of activation. A second issue regards the predominant vascular size contributing to the BOLD contrast. Do large draining veins or parenchyma contribute, and where? The question is again primarily one of localization: large draining veins may cause oxygenation – related signal changes far removed from regions of activation due to the fact that the blood volume in each voxel heavily weights the magnitude of susceptibility – related signal change. Even if the large vessel is relatively close, it may give an artificial "hot spot" that may be misinterpreted. Please refer to chapter 10 for the analysis of blood volume weighting on fMRI signal changes. Other issues include the following: What is the contribution of motion to fMRI signal changes? What is the reliability of fMRI data? Careful determination of underlying contrast mechanisms might put to rest some of these general concerns.

In this chapter, several of the above issues are directly addressed by pulse – sequence modulation. Specifically, spin–echo (SE) and gradient–echo (GE) EPI sequences (TR = 1 sec) are used to determine the predominant susceptibility compartment size and non–susceptibility contribution in a region of interest and on a voxel – wise basis.

This chapter is divided into two parts. The first part is earlier work (174, 175, 179) (performed in 1992 – submitted paper in Oct. 1993) that used separate SE and GE pulse sequences in the collection of time courses of 15 mm thick images at one TE per time course. The second part is more recent work which used a combined GE and SE pulse sequence in which the TE was systematically varied every sequential image allowing highly sampled

transverse magnetization decay curves to be obtained simultaneously and in a spatially registered manner (176, 180).

7.2 PART 1: ΔR2* AND ΔR2 COMPARISON

GE sequences were the first used for non–invasive MRI mapping of human brain activation (171-173, 227) primarily because of their high sensitivity to susceptibility effects. SE sequences, while having less BOLD contrast than GE sequences, may have nevertheless have a few advantages. The irreversible dephasing that occurs as a result of diffusion of spins through susceptibility induced gradients is maximized with compartments having similar dimension to the diffusion distance in an echo time (i.e. 2 to 7 μm radius) (124, 126-128). If BOLD contrast arising from SE sequences reflects changes in oxygenation in micro vessels in close vicinity to the activated tissue, and not large draining veins which may be distant from the activated brain tissue, a higher *functional* spatial resolution may be obtained with the use of susceptibility – weighted SE sequences. One consideration, though, is that changes in R2 in voxels containing large vessels, and therefore greater blood volume, may be large due to diffusion of water through gradients induced around individual erythrocytes *within* the vessels, irrespective of the diffusion of spins through gradients *around* vessels, suggesting that if draining veins are large enough to fill a voxel, the intrinsic R2 changes in the blood with oxygenation changes may cause significant signal changes in addition to changes in micro vessels in parenchyma.

SE sequences also have considerably less susceptibility – related signal dropout from macroscopic field offsets occurring within a voxel, such as in the case of a poorly shimmed magnet or at interfaces of air, bone, and/or

tissue. Susceptibility – related signal dropout in GE sequences increases with field strength and is especially problematic in the study of deep brain structures, due to the air/tissue interfaces at the base of the brain.

It has been demonstrated that SE and asymmetric SE (268) techniques have less pulsatility artifacts from large vessels. The reason for this is most likely that the slice – selective 180° pulse 10 to 100 ms after the initial 90° does not refocus rapidly flowing spins, therefore creating a signal void where artifactual signal changes would occur with the use of GE sequences.

The precise nature of BOLD contrast is not entirely understood primarily because a relatively small amount of information is known about the control of human cerebral blood blow, volume and oxygenation with neuronal activation. Other unknowns about the nature of BOLD contrast in general are that blood velocity changes may affect R2 and R2* regardless of oxygenation changes. A change in red blood cell velocity might be considered as similar to a change of the diffusion coefficient magnitude and orientation in the vicinity of red blood cells. From models of the susceptibility induced dephasing effect, it is well understood that the extent of dephasing that occurs is closely linked to the extent of diffusion of spins through the susceptibility induced field gradients. Any alteration of the extent of diffusion of spins through gradients around individual red blood cells, caused by blood velocity changes, may cause alterations in T2 and T2*. Please refer to chapter 6 for a discussion of these issues.

It is also understood that flow changes accompanying neuronal activation alter the apparent T1 of perfused tissue (171). The use of short TR values and large flip angles may introduce sensitization to inflow – related changes (182, 189, 214) in addition to T2* signal changes. This may make

interpretation of signal enhancement magnitude and location additionally problematic in such techniques.

In this study, we observe, at 1.5 Tesla, activation – induced changes in SE and GE signal from identical regions in the motor cortex as a function of echo time. From these results, we compare relaxation rate changes and changes in functional contrast between the two sequences. Comparisons are made with the biophysical models of the BOLD contrast effect.

7.3 METHODS: PART 1

Four subjects (3 males, 1 female: ages 20 to 27) were imaged using single – shot SE and GE EPI (shown in Figure 2.5 and 2.6, respectively) on a standard 1.5 Tesla GE Signa scanner (GE Medical Systems, Milwaukee) equipped with an inserted three–axis balanced torque head gradient coil designed for rapid gradient switching (302). A shielded quadrature elliptical endcapped transmit/receive birdcage RF coil (254) was used for high sensitivity whole brain imaging.

For each subject, 11 to 19 time courses of 100 sequential SE or GE images of a single axial slice containing the primary motor cortex were obtained. A different TE value was used for each time course series. For the SE time course series, TE (kx,ky = 0,0) was varied from 40 to 200 ms, and for the GE time course series, TE was varied from 20 ms to 120 ms. Each image was obtained with a readout window of 40 ms and a sampling rate of 8 us per IQ pair. Slice thickness = 15 mm, FOV = 24 cm, and matrix size = 64 x 64. Voxel dimensions were 3.75 x 3.75 x 15 mm. For more detailed information regarding the hardware and pulse sequences used, please refer to chapter 2.

During each time course, the subjects were instructed to perform a motor cortex activation task of tapping each finger to thumb, bilaterally, in a sequential and self–paced manner. Care was taken so that tapping frequency and pressure remained constant throughout each imaging session. The timing of the activation was alternating 20 sec rest (three episodes), with 20 sec movement (two episodes).

All measurements from SE and GE time course series were made in each subject from the identical regions of interest obtained in the following manner: a) Assuming that the optimum functional contrast is obtained at TE $\approx$ T2* or T2, a SE and a GE time course series in which TE was closest to T2 ($\approx$ 100ms) and T2* ($\approx$ 40 ms) was chosen from each set of time courses. b) Temporal cross correlation was calculated on each of the two time course series (220) against the reference waveform illustrated in Figure 7.1. c) For both time course series, all voxels which had a correlation coefficient < 0.6 were removed. d) Voxels common to both the SE and GE correlation coefficient images, after thresholding , were used as the region of interest for all of the SE and GE time course series for each subject. Figure 7.2 illustrates the slice chosen for each subject and the region of interest used (superimposed in white) for all measurements. Note that the regions of interest corresponded closely to the primary motor cortices. Activated regions of interest from subjects 1 through 4, corresponding to Figures 7.2a through 7.2d, contained 43, 38, 24, and 15 voxels respectively.
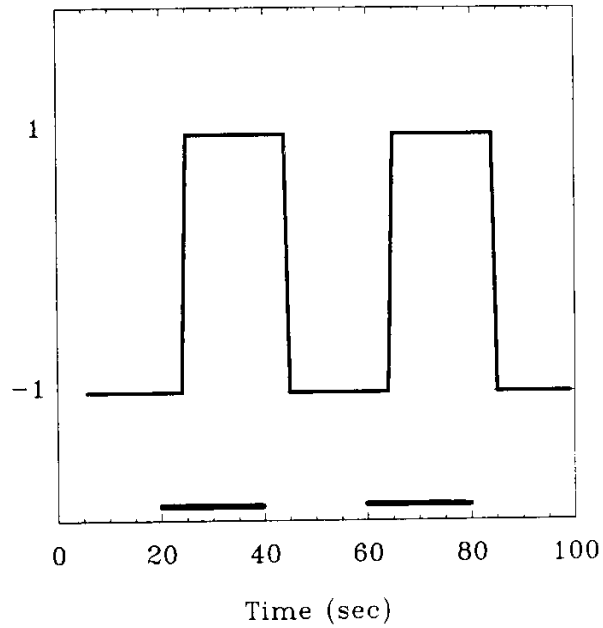
Figure 7.1: Illustration of the reference waveform that was used for all temporal cross correlation calculations (images in Figure 7.7) and temporal correlation coefficient calculations (activation masks in Figure 7.2). Dark lines at the bottom indicate the periods during which subjects performed self–paced finger tapping. Because the activation – induced signal enhancement generally occurs about 4 to 8 seconds after neuronal activation, a five second delay is introduced into the waveform analysis.
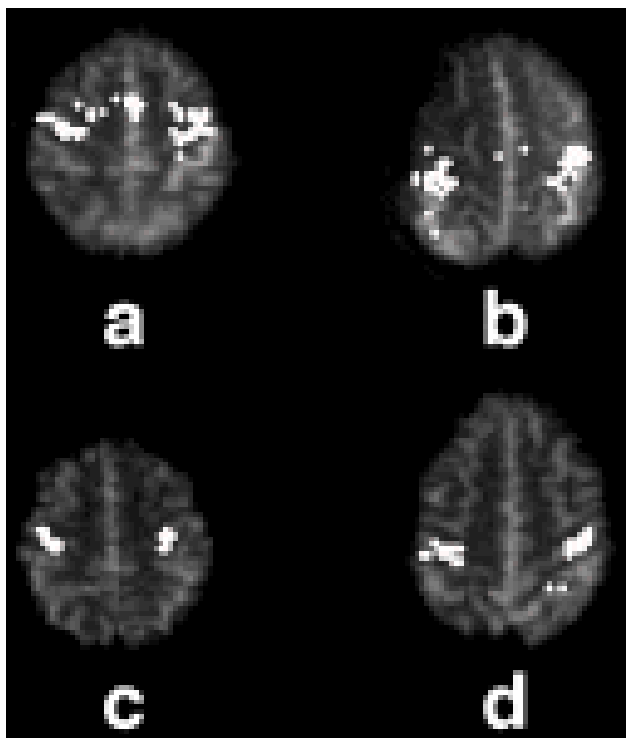
Figure 7.2: Spin–echo echo–planar images (TE/TR = 100/∞) of the axial slice chosen for each subject with the regions used for measurement superimposed in white. For selection of the regions of interest in each subject, two respective time course series were chosen, from each set of time course series, at TE values closest to the TE for maximal contrast (TE ≈ T2* and T2). The regions include the voxels that had a correlation coefficient > 0.6 with the reference waveform in Figure 7.1 for a GE *and* a SE activation time course series. Regions of interest in Figure 7.2a through Figure 7.2d corresponded to subjects 1 through 4, and contained 43, 38, 24, and 15 voxels respectively.

All measurements of resting and active state signal for SE and GE sequences at each TE were made from the time course plots from the regions of interest. From the time course plots, points 10 through 20 were averaged to obtain the baseline signal and points 30 through 40 and 70 through 80 were

averaged to obtain the activated state signal. A linear fit of the natural log of the signal intensities versus TE was used to obtain the respective relaxation rates during rest and activation. This linear fitting technique for determining relaxation rate works best when the tissue has a decay that can be characterized by a single exponential, which may not be the case for many of studies. Regions of interest and voxels may have a combination of blood, gray matter, white matter, and csf – all with different decay rates. Also, single tissue types may have multiexponential decay rates intrinsically or as a result of poor shim within the region. A multiexponential fitting procedure would likely give a better fit but, in most cases, the underlying reason for the multiexponential behavior is unclear. So, in this first analysis, a simple single exponential fit was used with the understanding that it may not be optimal, but also that the alternative approaches are outside the goal of this analysis.

7.4 RESULTS: PART 1

Figure 7.3 illustrates three GE EPI time course plots, from subject 4, at echo times ranging from 20 to 100 ms. Note that the percent signal change shows an increase with increased TE. Figure 7.4 illustrates three SE EPI time course plots from the same region of interest at echo times ranging from 40 ms to 160 ms. The percent signal changes also show an increase with increased TE , and, while easily observable, are significantly less than those observed in the gradient echo EPI time course series at corresponding TE values.
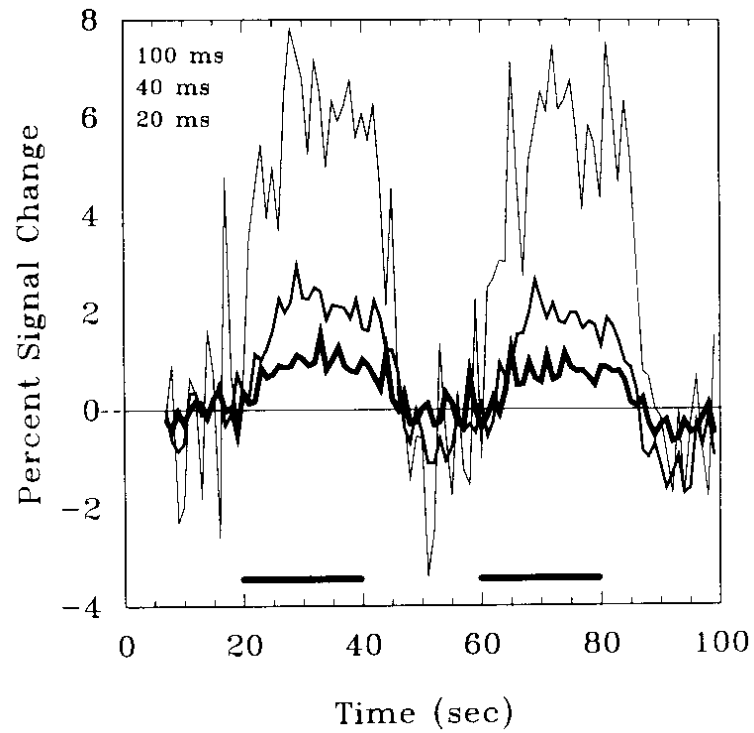
Figure 7.3: Three time course plots of the averaged signal from the region of interest (white) in Figure 7.2d, obtained using GE EPI at echo times of 20ms (most bold) to 100ms (lightest). TR = 1000ms. Horizontal bars at the bottom indicate when finger tapping was performed. The percent signal change increases with echo time.
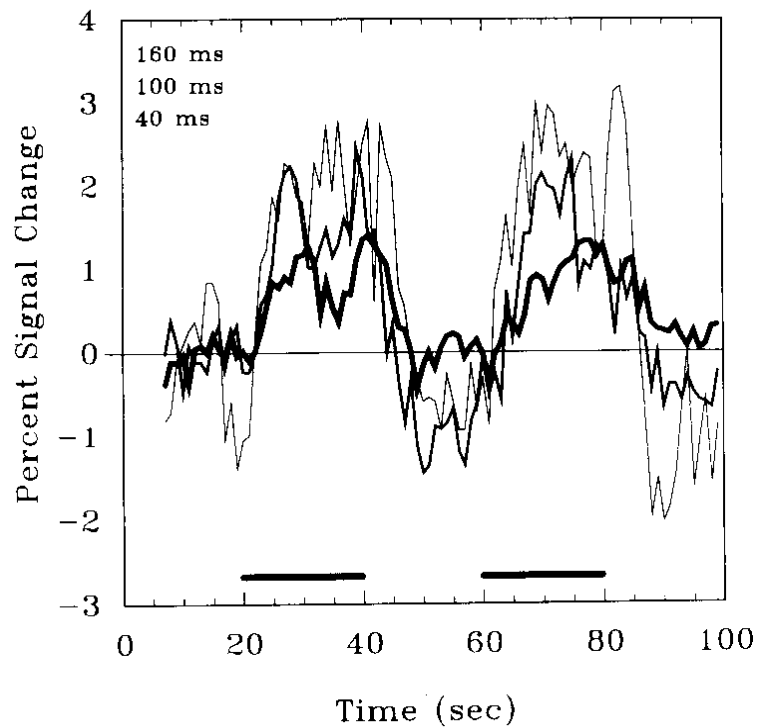
Figure 7.4: Three time course plots of the averaged signal from the region of interest in Figure 7.2d, obtained using SE EPI at echo times of 40ms (most bold) to 160ms (lightest). TR = 1000ms. Horizontal bars at the bottom indicate when finger tapping was performed. The signal changes are easily seen and increase with echo time, yet are much smaller than those observed at corresponding echo times using GE EPI (Figure 7.3).

Figure 7.5 illustrates the T2 and T2* decay curves for each subject. Error bars, (± standard error), are within the data points. A close correspondence to a single exponential decay is observed within the range of echo times used. The regions of interest used were likely to contain signal from cerebral spinal fluid, blood, gray matter, and white matter. The T2 rates are generally more consistent across the subjects than T2* rates. This is most likely due to the sensitivity of T2* to variations in magnet shim and voxel size.
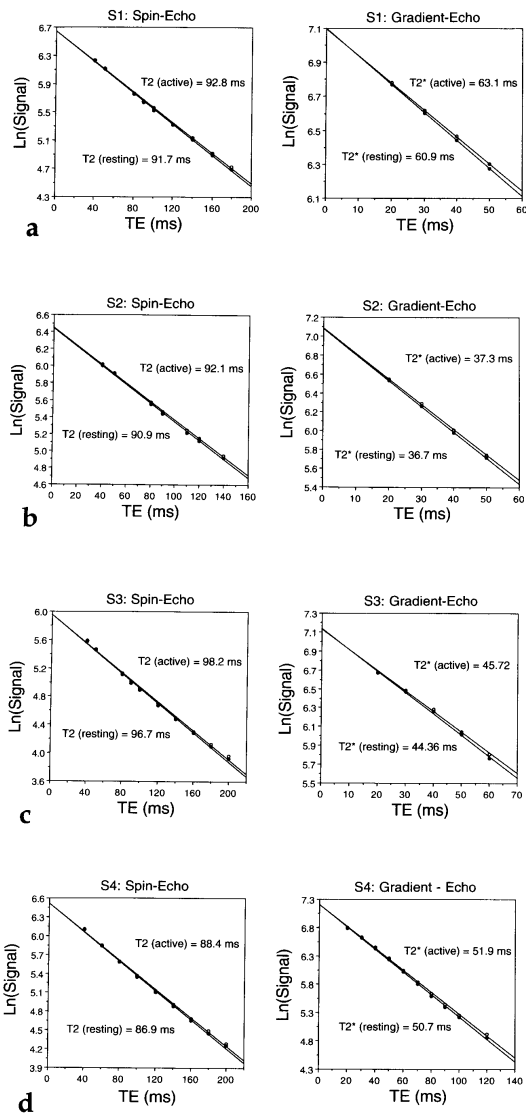
Figure 7.5: Resting and active state T2 and T2* decay curves for subjects 1 through 4. Figures 7.5a through 7.5d were created from time course plots of averaged signal from the regions of interest in Figure 7.2a though 7.2d respectively. From each time course plot, time points of 20 through 30 seconds were averaged for the resting state measurements. Time points of 30 through 40 and 70 through 80 were averaged for the active state measurements. Error bars are within most of the data points.

Table 7.1 summarizes the results shown in Figure 7.5. Based upon differences in linear fits to the decay curves, significant ($p < 0.05$) changes in R2 were observed in two subjects and significant changes in R2* were observed in 3 subjects. The average value of ΔR2 was -0.16 $\pm$ 0.02 s^{-1} ($\pm$ standard error) and the average value of ΔR2* was -0.55 $\pm$ 0.08 s^{-1}. The average ratio (ΔR2*/ΔR2) of the relaxation rate changes was 3.52 $\pm$ 0.56. From this ratio, a comparison with a biophysical model was made to discern the vessel radius that predominantly contributed to the BOLD signal change. The model of Ogawa et al. (127), suggests that this relaxation rate ratio roughly corresponded to a vessel radius of $\approx$ 8 μm. Studies which have been performed to map, voxel for voxel, the relative changes in relaxation rates using a combined SE and GE EPI sequence (176, 180) have shown that the ratio of relaxation rates varies significantly across active voxels, suggesting that the predominant vascular scale contributing to BOLD contrast varies considerably in space. Relaxation rate mapping in a voxel by voxel manner may allow predominant vessel scale to be characterized more accurately.

Subject	R_2 active (1/s)	R_2 resting (1/s)	R_2^* active (1/s)	R_2^* resting (1/s)	ΔR_2 (1/s)	ΔR_2^* (1/s)	$\Delta R_2^*/\Delta R_2$	at $TE=T_2$ calculated spin-echo ΔS	at $TE=T_2^*$ calculated gradient-echo ΔS	at $TE=T_2^*$ and T_2 calculated $\Delta S_{GE}/\Delta S_{SE}$
1	10.77±0.10	10.91±0.14	15.84±0.12	16.42±0.07	NS −0.13±0.07	** −0.58±0.08	4.35	0.0046	0.0133	2.89
2	10.86±0.13	11.01±0.17	26.83±0.25	27.26±0.13	** −0.14±0.04	NS −0.42±0.12	2.96	0.0048	0.0057	1.19
3	10.19±0.19	10.34±0.20	21.81±0.59	22.54±0.62	NS −0.16±0.12	** −0.75±0.04	4.56	0.0059	0.0124	2.10
4	11.31±0.19	11.51±0.20	19.29±0.20	19.72±0.22	** −0.20±0.03	** −0.44±0.04	2.21	0.0064	0.0082	1.28

From these measurements, ΔR_2 and ΔR_2^* calculations are made. Significant differences in R_2 and R_2^* are indicated by **. Ratios of relaxation rate changes ($\Delta R_2^*/\Delta R_2$) are displayed. In addition normalized signal differences (at $TE = T_2$ or T_2^*), calculated from R_2 and ΔR_2 (spin-echo) and from R_2^* and ΔR_2^* (gradient-echo), are displayed. Gradient-echo/spin-echo signal difference ratios are displayed as a measure of relative BOLD contrast.

Table 7.1

It is potentially misleading, due to differences in baseline T2 and T2*, to consider relative activation – induced relaxation rate changes between SE and GE sequences as measures of the relative magnitudes of the BOLD contrast. If it is assumed that T2 and T2* follow single exponentials, and that activation – induced $\Delta R2$ and $\Delta R2*$ are small compared to R2 and R2*, the optimum TE for the detection of a maximal signal difference would occur at TE $\approx$ T2* for GE sequences and TE $\approx$ T2 for SE sequences. Table 7.1 shows R2 and R2* – related absolute signal changes calculated at optimum TE for every subject after normalizing the calculated signal to 1 at TE = 0. The average signal difference ratio (GE/SE) was calculated to be 1.87 ± 0.40 (± standard error), which is considerably smaller than the relaxation rate change ratio.

Relative BOLD contrast changes with TE are illustrated in an example in Figures 7.6 and 7.7.
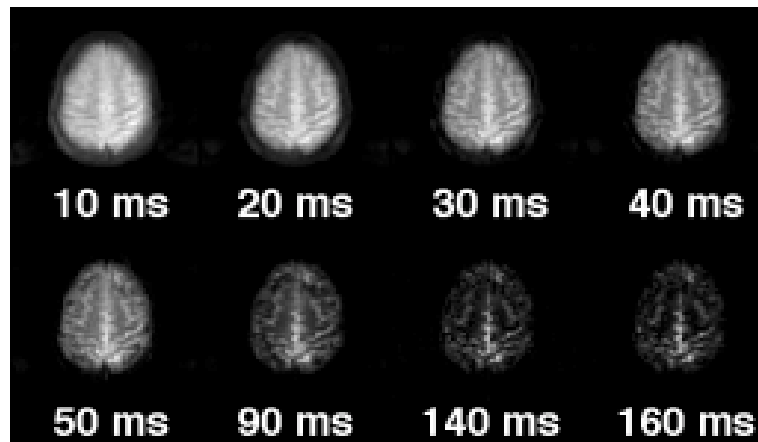
Figure 7.6a: The first images (TR = ∞) in time course series from subject 4. The GE images illustrate a rapid and spatially non–uniform decay of signal as echo time is increased.
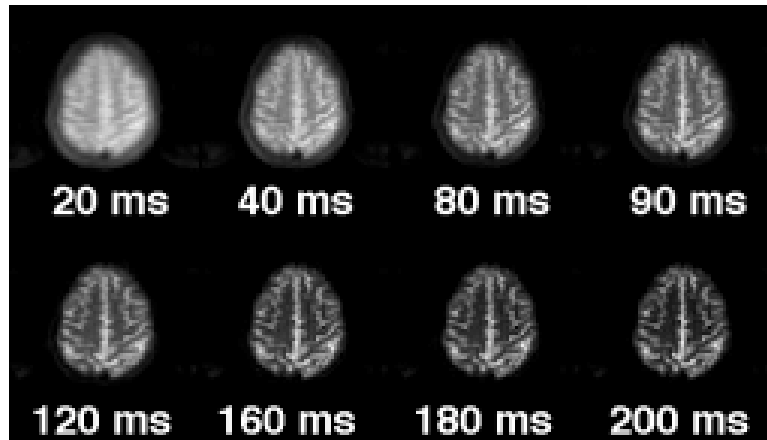
Figure 7.6b: The first images (TR = ∞) in time course series from subject 4. The SE images illustrate a more uniform decay as the echo time is increased, demonstrating less signal dropout with variations in B_O in the image.
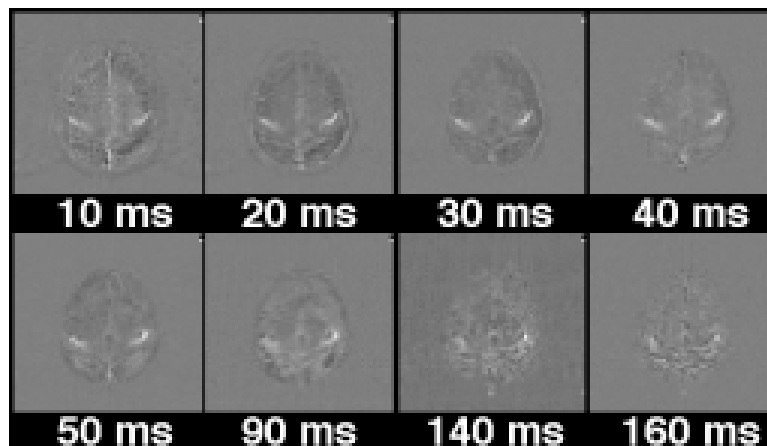
Figure 7.7a: Gradient – echo brain activation images (bilateral motor cortex activation) obtained by temporal cross correlation of the reference waveform in Figure 7.1 with every voxel in the time course series. Images correspond to the anatomical images shown in Figure 7.6a. GE brain activation images demonstrate that the highest BOLD contrast to noise occurs at a TE in the range of the measured T2* values (Figure 7.5d).
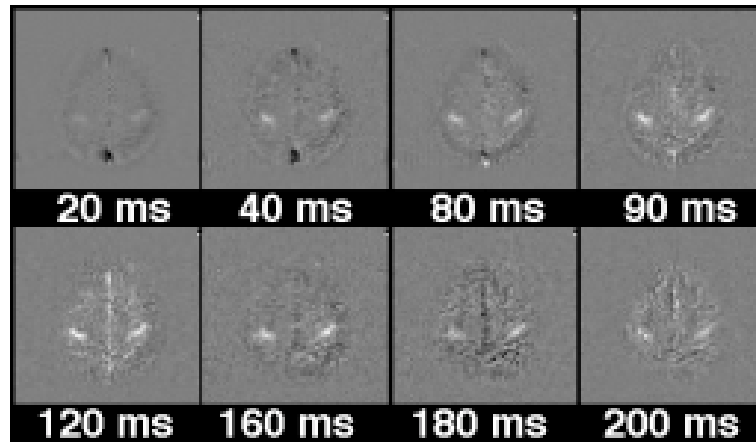
Figure 7.7b: Spin–echo brain activation images (bilateral motor cortex activation) obtained by temporal cross correlation of the reference waveform in Figure 7.1 with every voxel in the time course series. The images demonstrate that the highest BOLD contrast to noise occurs at a TE in the range of the measured T2 values (Figure 7.5d). The SE brain activation images have less BOLD contrast than the GE brain activation images. The active regions in the SE images appear slightly more diffuse. Many areas showing signal enhancement are unique to either the SE or GE brain activation images.

Figures 7.6a and 7.6b are the first images, from subject 4, at incremented TE values, in the GE and SE time course series respectively. Note that the signal decay in the GE images was not as spatially uniform as in the SE images. The T2* decay rates differed not only between tissues but between areas having different Bo field homogeneity. Figures 7.7a and 7.7b are correlation images from of GE and SE sequences respectively, corresponding to the anatomical images in Figure 6a and 6b. They were obtained by scalar product calculation of the reference waveform, illustrated in Figure 7.1, with every voxel in each time course series. No thresholding was applied. Figure

7.7a shows the GE correlation images. Signal enhancement is easily observed at short TE values, and the activation – induced signal changes with highest contrast to noise ratios are at TE values of 40 to 50 ms, which correspond to the T2* measurements from the region of interest (Figure 7.5d). At longer TE values, the signal decays into the noise, and activation – induced signal changes are therefore less readily apparent, even though the fractional signal change increases with TE. Figure 7b shows SE correlation images. Overall, BOLD contrast was less than that produced by GE time course series, but was still high enough so that active regions were easily seen. Activation – induced BOLD contrast to noise appears to peak in the SE sequences between 80 and 120 ms, which corresponds closely to the corresponding T2 measurements from the region of interest (Figure 7.5d).

7.5 DISCUSSION: PART 1

MRI of human brain activation has been observed using SE and GE EPI sequences. All active and resting state signals were obtained from the same region of interest in each subject. Identical brain activation timing and post processing methods were used to obtain resting and active state signals. From these signals, obtained using time course series with different TE values, relative R2, R2*, ΔR2, and ΔR2* rates were obtained. All calculations of relaxation rate change ratios and absolute signal difference ratios between GE and SE sequences were based upon these measurements.

Because of the relatively large slice thickness and large regions of interest used, a substantial amount of partial volume averaging of active with inactive tissue probably occurred. The effect the slice thickness on the magnitude of activation – induced signal change has been studied (186, 188).

Slice thicknesses on the order of the cortical thickness (3 to 4 mm) would prevent most partial volume averaging problems. The choice of slice thickness in this study was related, in part, to the uncertainty of the location and size of the activated motor cortex region in combination with the acquisition of only one slice. Assuming similar slice profiles, the large slice thickness most likely caused an underestimation of the absolute magnitudes of the relaxation rate changes rather than the relative differences between SE and GE sequences since the same regions are being observed.

Potential errors involved with the comparison of SE and GE activation – induced signal changes include systematic errors due to movement and shifting between or during runs, and variations in activation timing and intensity across or during runs. Artifactual signal changes in pulsatile vessels, which depend upon heartbeat timing relative to image acquisition timing, may also vary across runs. Analysis is underway in our laboratory with the use of a spatially and temporally registered GE and SE EPI sequence to make more accurate comparisons, on a voxel–wise basis, of relative relaxation rate changes and absolute signal changes with brain activation (176, 180). These studies are presented in part 2 of this chapter.

One primary conclusion from this study is that the GE/SE activation – induced BOLD contrast ratio was about 2 when considering the use of each pulse sequence at the optimal TE for detection of BOLD signal changes.

Spin–echo sequences are a) preferentially sensitized to smaller vessels. b) less sensitive to pulsatile flow artifacts, and c) less sensitive to macroscopic field gradients created by poor shim and tissue/brain/air interfaces. Although the intrinsic BOLD contrast is less in SE sequences than in GE sequences, the advantages of less sensitivity to intravoxel dephasing in combination with

sophisticated post processing techniques make SE EPI a good alternative to GE EPI for functional activation studies.

From this comparative study, it is apparent that SE techniques, sensitized to BOLD signal changes, show promise in the more extensive application of MRI to non invasive assessment of human brain activation.

7.6 PART 2: SIMULTANEOUS ΔR2*, ΔR2, AND ΔS$_O$ COMPARISON

As mentioned, an ongoing issue in fMRI is the characterization of the effects of activation – induced changes in blood flow and oxygenation on the MR signal. Signal changes corresponding to changes in blood oxygenation (T2 and T2* lengthening effects) are generally observed with T2 and T2* – weighted sequences, while changes in blood perfusion (apparent T1 shortening effects) are generally observed with T1 – weighted sequences. The contribution of "inflow" effects (activation – induced increases in the velocity of unsaturated spins entering into an RF saturated imaging plane) to signal changes in susceptibility – weighted sequences have been observed at relatively short TR values and high flip angles (182, 189). Several unresolved questions exist in regard to the relative certainty of functional contrast weighting (inflow, oxygenation, perfusion) and to the relative locations (large veins, arteries, parenchyma) and magnitudes (signal magnitude $\propto$ activation magnitude) of hemodynamic events that cause the MR signal changes.

In this part of the chapter, a question that is specifically addressed is: "What are the relative signal change contributions using either SE or GE echo planar imaging (EPI) at TR = 1 second?"

Assuming that a SE or GE sequence is used, the resting and activated signal, Sr and Sa respectively, may be approximated by:

$$Sr = Sr_O \, e^{-(R2r \, TE)} \quad and \quad Sa = Sa_O \, e^{-(R2a \, TE)}. \qquad [7.1]$$

Resting and activated signal at TE=0, Sr_O and Sa_O, respectively are modulated by changes in proton density and/or T1. Transverse relaxation rates, R2r (1/T2r) and R2a (1/T2a) are modulated, in this context, by changes in the magnetic susceptibility of blood which causes changes in R2' (1/T2') on different spatial scales. Temporally and spatially registered time course measurements of R2, R2*, and S_O during rest and activation have allowed, in this study, separation of flow (non–susceptibility) and oxygenation (susceptibility) effects.

7.7 METHODS: PART 2

A combined SE and GE EPI sequence (176), (SEGE–EPI), shown in Figure 2.7, was used to collect single shot, SE and GE echo–planar image pairs of an axial slice through the motor cortex. Imaging was performed on a 1.5 Tesla GE Signa scanner using a local three–axis gradient coil and a quadrature transmit/receive birdcage RF coil. The voxel volume was 3.75 x 3.75 x 5 mm^3. TR = 1 sec. First, SEGE–EPI time course series was obtained during cyclic on/off finger movement using single TE values of 30 (GE) and 110 (SE). This was performed to find the regions that demonstrate significant signal changes with activation. Second, time course series consisting of 20 to 50 sequential R2 and R2* decay curves were obtained using 5 to 100 TE increments per curve.

Regions of interest consisting of voxels that demonstrated significant signal changes during the time course collection of SE and GE images, were used. From these ROI's and maps, resting and active R2, R2*, and So

245

measurements were made. In the graphs, fitting of the trends was performed using KaleidaGraph™ software. In addition, maps of resting and activation – induced changes in R2*, R2, R2', and So were created by fitting, on a voxel– wise basis, the decay curves to a single exponential using a linear lest squares fitting subroutine (378). During sequential collection of the R2 and R2* curves, subjects alternated periods of rest and finger tapping. Sr_O and Sa_O were calculated by extrapolation of the decay curves to TE=0. The activation – induced changes in $\Delta R2$ and $\Delta R2*$ were compared with the model presented in chapter 6.

7.8 RESULTS: PART 2

A SEGE–EPI time course of axial T2–weighted (SE TE = 110 ms) and T2*–weighted (GE TE = 30 ms) image pairs was first collected during cyclic on–off finger movement. Figure 7.8 shows the simultaneously obtained time courses from the same motor cortex region.
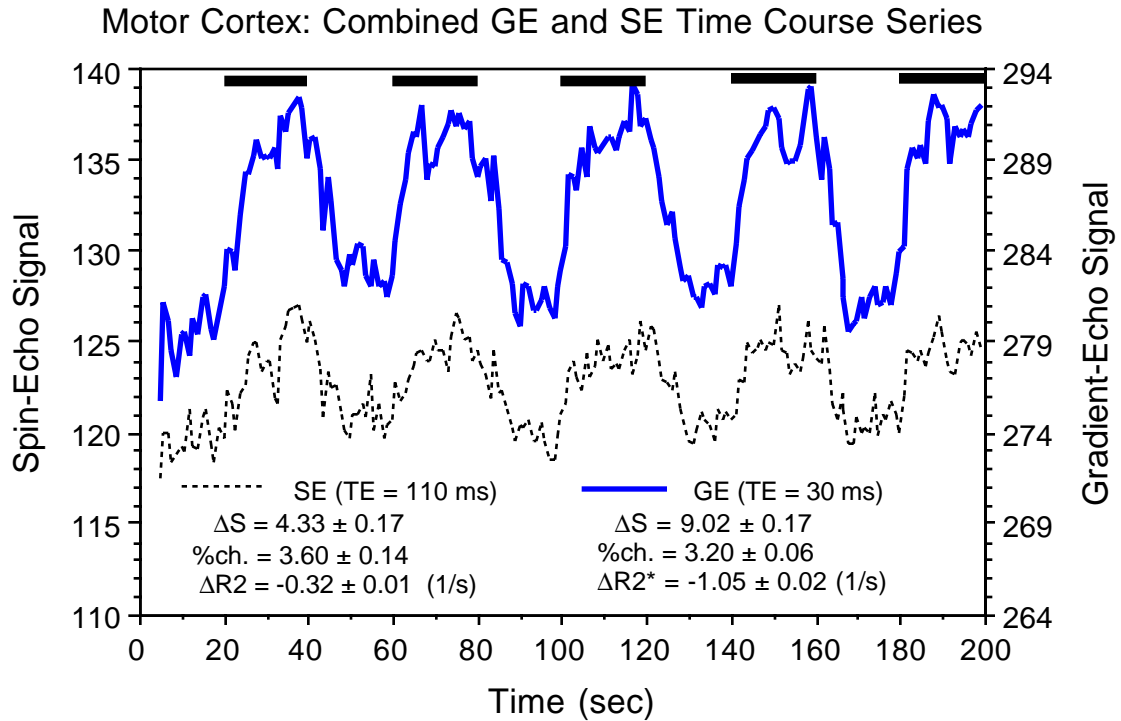
Figure 7.8: Simultaneously – obtained T2* and T2 weighted time course series from motor cortex (ROI is colored region in Figure 7.9) during bilateral cyclic on – off finger movement.

Vertical scales have the same range. The average percent changes were 3.60 ± 0.14 for the SE time course and 3.20 ± 0.06 for the GE time course. The calculated $\Delta R2^*$ and $\Delta R2$ (from the time course series) using Sr (resting signal) and Sa (active signal) and equation 1.9 are -1.05 ± 0.02 s^{-1} and -0.32 ± 0.01 s^{-1} respectively. These relaxation rate values will later be compared to direct $\Delta R2^*$ and $\Delta R2$ measurements, which are insensitive to non–susceptibility related effects. Figures 3.1, 3.2, and 3.3 show the high resolution image of the slice chosen, the first anatomical SE and GE images obtained, and the corresponding functional images, (created by calculation of the scalar product of each time course with the same reference waveform), respectively.

Note the differences in functional contrast to noise and the differences in signal change locations, suggesting different susceptibility compartment size weightings. After a threshold was applied, the percent change images were calculated. These images are shown in Figure 7.9.
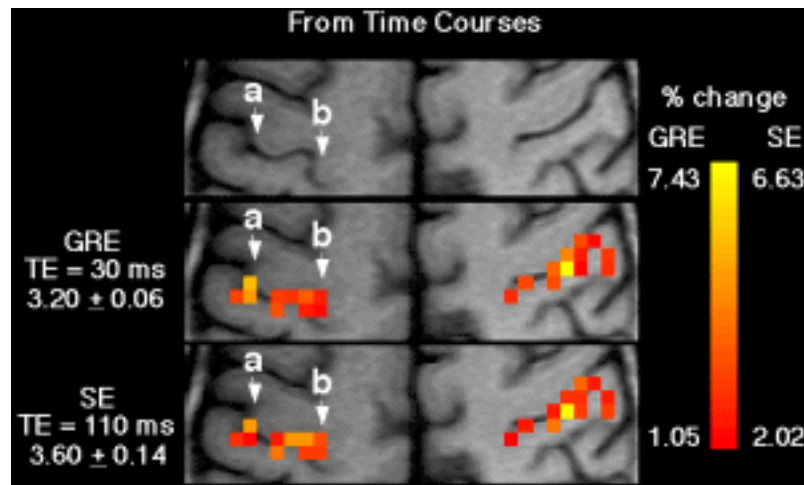
Figure 7.9: Simultaneously – obtained SE and GE percent change images.

The images appear similar in pattern within the regions of interest. Note the "hot spot," indicated by letter "a," in the left side of the image near the large sulcal opening suggestive of a vein. Some differences do appear to exist though. The more medially located area of the left motor cortex region (left motor cortex = left side of image), indicated by the letter "b," shows relatively greater activation for the SE sequences.

Relaxation rate change images were also calculated from the time course (using only Sa and Sr at one TE) which basically normalized for the different TE values used for the SE and GE images. Figure 7.10 shows the relaxation rate change images. The GE image shows considerably higher

relaxation rate changes values, with the highest change in the sulcal area identified above.
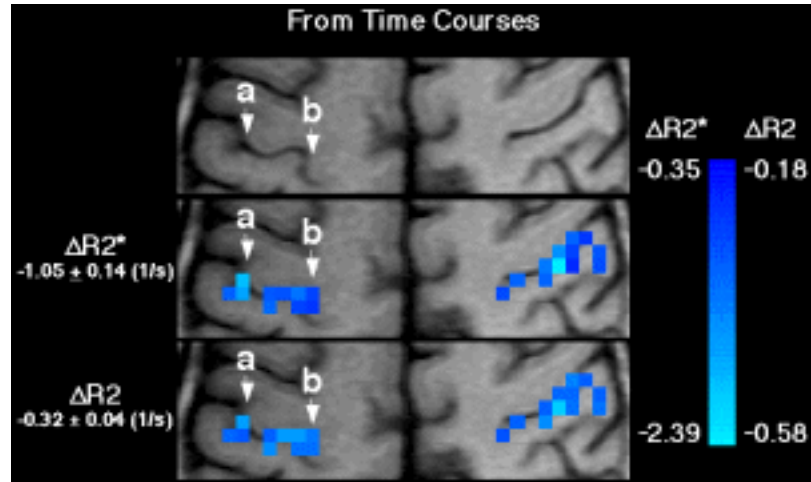
Figure 7.10: Simultaneously – obtained ΔR2* and ΔR2 images. These were calculated using the relationship in equation 1.9.

The ΔR2* and ΔR2 images, shown in Figure 7.10, were used to create a ΔR2*/ΔR2 map, shown in Figure 7.11. Based on the models, the higher this ratio the larger the "average" susceptibility compartment size in a voxel. The highest ratio is observed in a voxel adjacent to the "hot spot" identified in the previous images. This may reflect a susceptibility – induced gradient in the vicinity of a larger vessel. The reason why it may not occur directly on the "hot spot" is because large vessels have small compartments internally (red blood cells) which may reduce the ΔR2*/ΔR2 ratio. The adjacent voxel may not contain the large vessel. Instead, it may only be experiencing the gradients surrounding the large vessel.
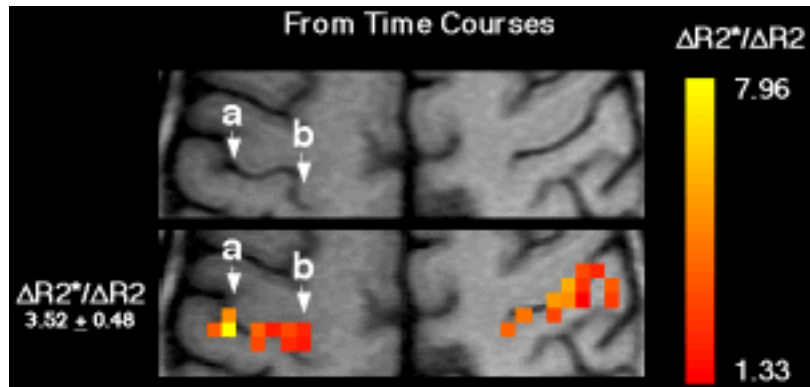
Figure 7.11: $\Delta R2^*/\Delta R2$ map calculated from the images in Figure 7.10.

It is important to note at this point that the $\Delta R2^*$ and $\Delta R2$ maps that were created above may be affected by non–susceptibility related signal changes. The assumption was that $So_a = So_r$ in equation 7.1. In the next step, that assumption is tested. A time course of images, from the same plane, consisting of 50 sequentially obtained R2 and R2* decay curves having 5 incremented TE values per curve (GE TE = 25 to 65 ms , SE TE = 100 to 180 ms) were collected from the same slice. Signal intensity vs. time, from the same ROI is shown in Figure 7.12.
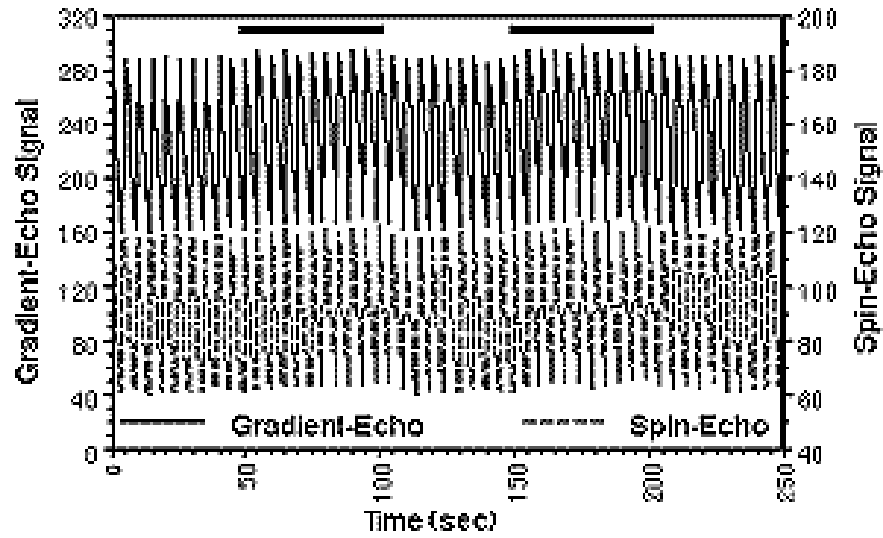
Figure 7.12: GE and SE signal intensities in the motor cortex during time course collection of 50 consecutive transverse relaxation rate curves of five images each.

Finger movement was performed during 2 sections of the time course, indicated by the horizontal bars. Plots of R2*, R2, and So for SE and GE sequences are shown in Figure 7.13. From the average resting and average values of signal at each TE, plots of percent signal change vs. TE, shown in Figure 7.14a, were made. As can be seen, the TE = 0 intercept is positive. To obtain ΔR2*, ΔR2 and the TE = zero intercepts, the slope of -ln(Sa/Sr) vs. TE was obtained. This plot is shown in Figure 7.14b.
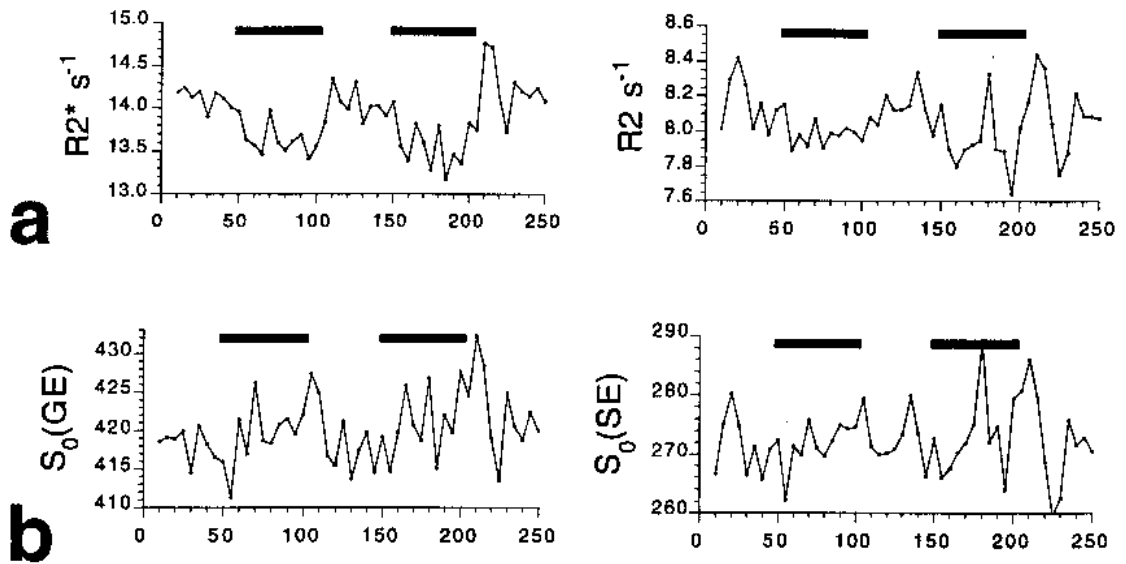
Figure 7.13: Graphs created from the signal in Figure 7.12, of **a.** the slopes of ln(signal) vs TE: R2* and R2*, and **b.** the zero intercept values: So (GE and SE).

a   b
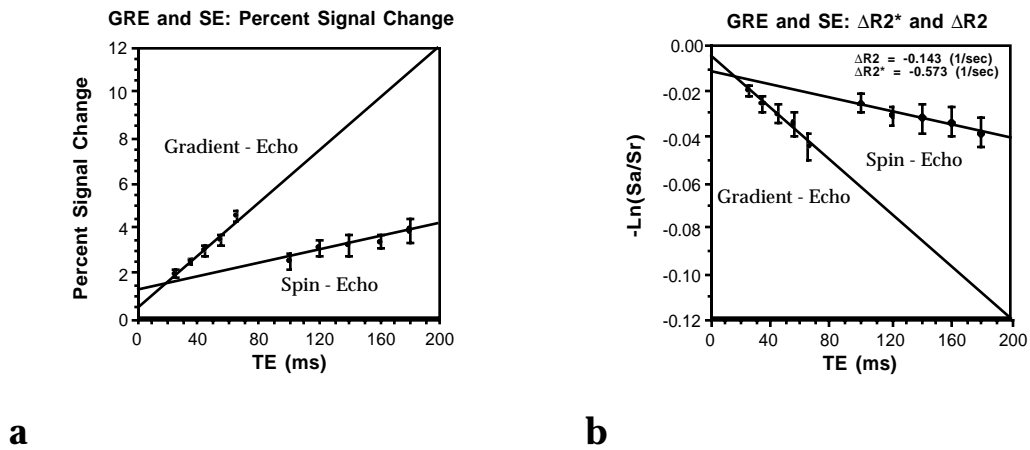
Figure 7.14a Percent signal change (during finger movement) vs. TE obtained from the time course signal shown in Figure 7.12. **b** Plot of average -ln(Sa/Sr) vs. TE. The slopes give $\Delta R2^*$ and $\Delta R2$. The intercepts give ΔSo.

252

From these data, it is apparent that the $\Delta R2^*$ and $\Delta R2$ values are less than the values obtained from the time course series. The reason is that changes in So were not separated from changes in transverse relaxation rate. Here, the effects are differentiated. The average $\Delta R2^*/\Delta R2$ ratio is still in the range of 3/1 to 4/1.

This same data is again reformatted to show ΔS (signal contrast) vs. TE. Two curves were used to fit the data. One curve assumed that $So_a = So_r$ and the other used the individual So_a and So_r values obtained from the zero intercept of the relaxation rate curves. The plot and curve fits are shown in Figure 7.15.
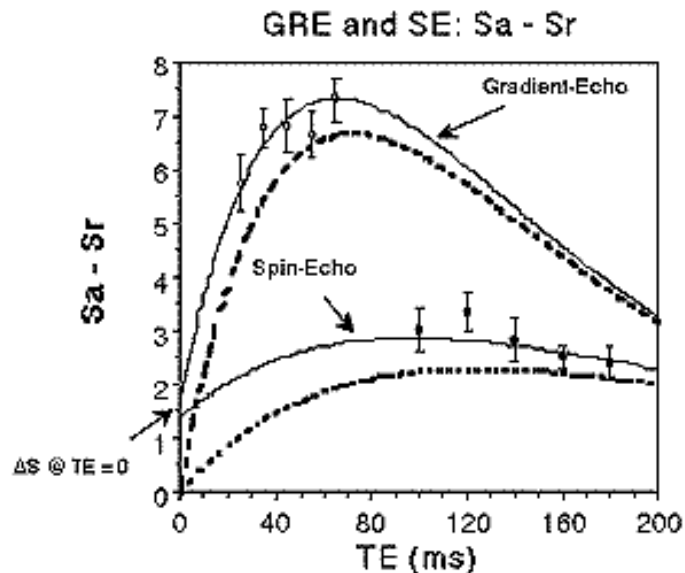
Figure 7.15: Plot of ΔS vs. TE. The curve used to fit the data used equation 7.1. The dotted curve fits assume $So_a = So_r$. The solid curve fits use the So values obtained from an interpolation of the relaxation rate curves to TE = 0.

The curve fit that is created not assuming $So_a = Sa_r$ (ΔS @ TE = 0) fits the data more accurately. The implication is that a non–susceptibility related

component is present in the MR signal change since if a TE of 0 were used, no signal change would be apparent if the source of the change were simply due to changes in transverse relaxation rate.

One other observation is that the contrast in the GE sequence is higher than the SE sequence by a factor of about 3, which is slightly larger than the contrast ratio mentioned in part 1 using separate SE and GE sequences for comparison.

Using the same time course series of images as above, the values of $R2^*$, $R2$, and S_o were calculated on a voxel – wise bases. In addition, $R2'$ maps (direct measure of proton resonance linewidth) were calculate by $R2^* - R2$. These maps are shown in Figure 7.16.
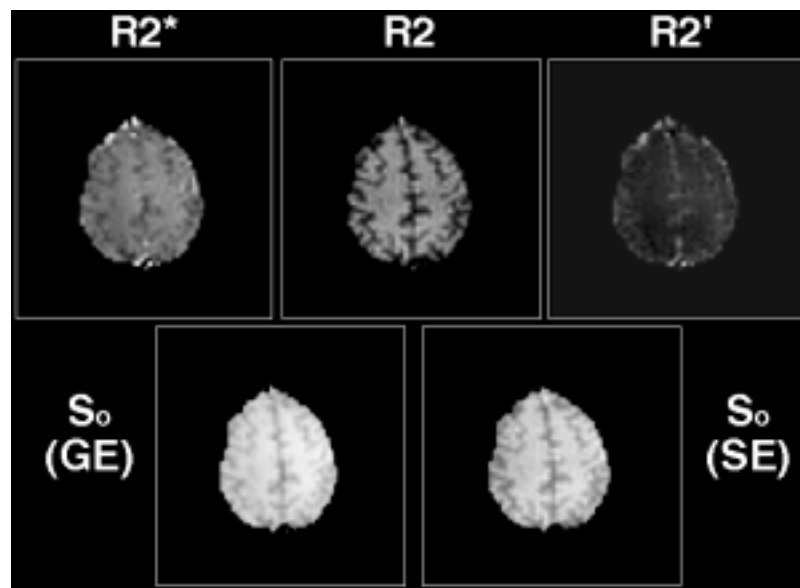
Figure 7.16: Resting state transverse relaxation rate and S_o images. The $R2'$ image ($= R2^* - R2$) indicates regions where macroscopic field inhomogeneities are.

Corresponding maps depicting activation–induced *changes* in these values are shown in Figure 7.17. Note that decreases in R2* and R2' are observed most easily. Using this method of analysis, a decrease in R2 is minimally perceptible, and S_O changes are relatively imperceptible.
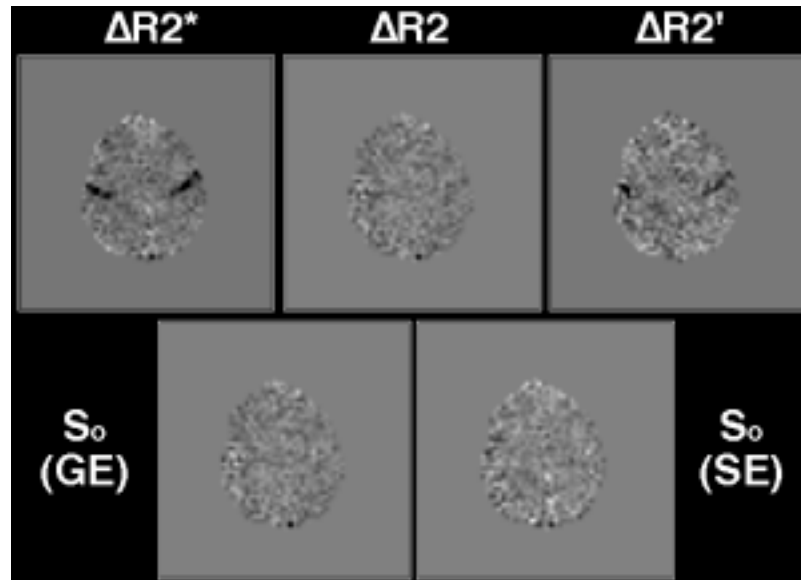
Figure 7.17: Images of transverse relaxation rate change during bilateral finger tapping. Largest changes are seen in R2* and R2'. Smaller changes are seen in R2, and almost no change is seen in So.

A blowup of these maps is shown in Figure 7.18. The "hot spot" in the ΔR2' map (indicating a change in macroscopic gradient) corresponds closely with the largest ΔR2*/ΔR2 ratio indicated in Figure 7.11. The evidence indicates that this region is likely a vessel. The regions of small ΔR2' and larger ΔR2 are likely smaller vessels or capillaries.
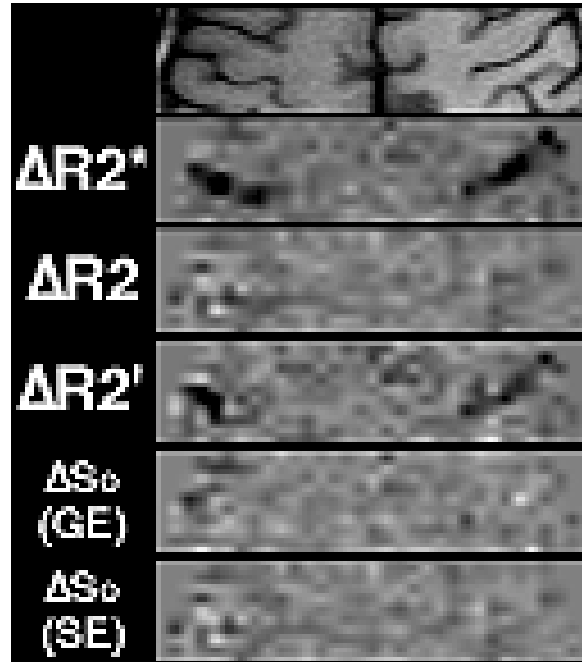
Figure 7.18: Magnification of Figure 7.17.

Regions showing activation in both the SE and GE time course series were selected for further voxel–wise quantitative mapping, shown in Figure 7.19. The average values (over space) are again lower than those obtained using only a single TE value in the time course in Figure 7.8. Nevertheless, when averaged over space, the ΔSo values are not significant. A small contribution from So is present at TR = 1 sec, but appears highly heterogeneous over space. The region showing the relatively higher SE percent change also shows the highest ΔR2 and lowest ΔR2'.
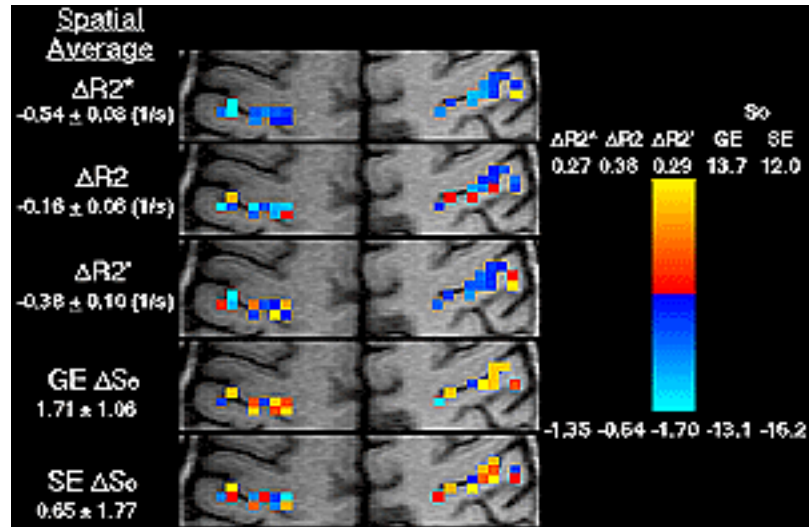
Figure 7.19: Quantitative maps of Figures 7.17 and 7.18 from regions of significant MR signal changes common to both SE and GE sequences.

A $\Delta R2^*/\Delta R2$ map was created using the $\Delta R2^*$ and $\Delta R2$ maps shown in Figure 7.20. This map looks generally similar to the map created from the time course series that used a single TE measurement sequence (Figure 7.11), but differences may exist because of the removal of S_O changes and because a fit of an exponential may introduce more systematic errors and noise into the data. Nevertheless, the maps do agree in that the medial left cortex region also shows the smallest $\Delta R2^*/\Delta R2$ ratio.
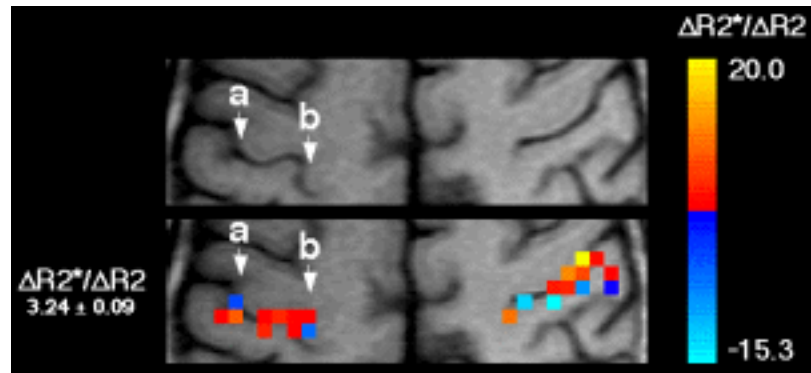
Figure 7.20: $\Delta R2^*/\Delta R2$ map created from the maps shown in Figure 7.19.

In a second study a time course consisting of 20 R2 and R2* decay curves having 100 incremented TE values per curve (GE TE = 25 to 74.5 ms, SE TE = 100 to 199 ms) were obtained. Figure 7.21 shows a plot of the averaged R2* and R2 values collected during rest and activation.
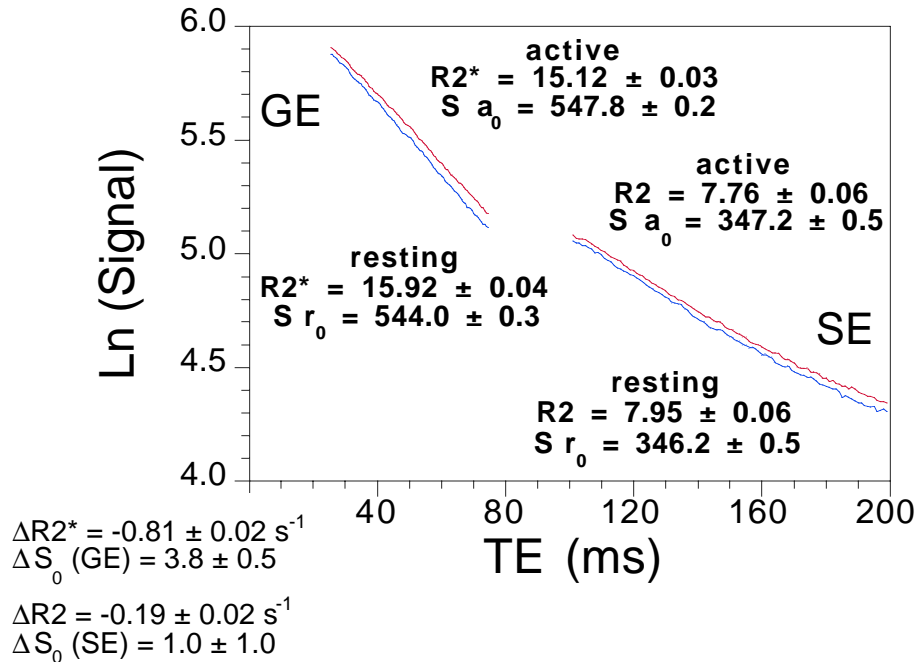
Figure 7.21: R2, R2*, and So values obtained simultaneously during rest and activation from identical regions in motor cortex.

It is observed that So values between GE and SE sequences should be equal but are not. Two possible reasons for this are that a) The 180° pulse for the SE sequence caused signal loss due to an imperfect slice profile. b) The T2 curve has more strongly multiexponential decay characteristics that reveal themselves at longer echo times (csf, which has a very long T2, is in the region of interest) contributing to more error in true So when using a single exponential fit. A multiexponential fit would likely give So values which are closer. Nevertheless, changes in So are considered to be accurately measurable in the presence on an inaccurate curve fit.

Using this same data set as above, the percent signal change vs. TE is shown in Figure 7.22. The percent change again shows a linear TE dependence. This dependence is extremely close to that shown in Figure 1.3 of

simulated transverse relaxation rate changes. Also, a positive TE=0 or ΔSo value is again apparent. The ΔSo value is significant for the GE curve fit. This TE=0 change corresponds closely to fractional apparent T1–related signal changes predicted for SE and GE sequences at TR = 1 sec (≈ 0.6%) using the perfusion effect model of Kwong et al. (171).

GE int. = 0.64 ± 0.15 %
SE int. = 0.24 ± 0.38 %
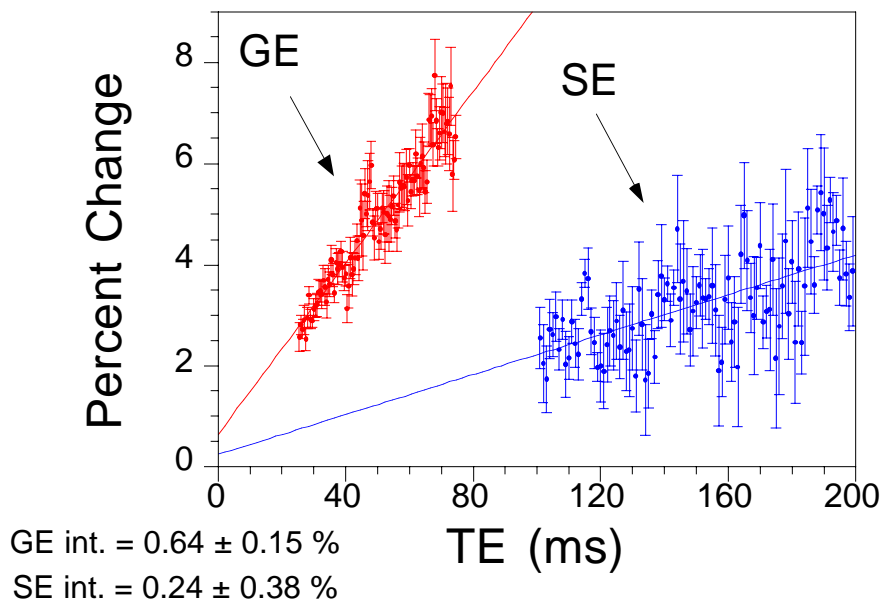
Figure 7.22: Percent GE and SE signal change vs. TE. The dependence of the fraction al signal change is linear, and the zero intercept shows a positive change with activation.

A plot of Sa - Sr vs. TE is shown in Figure 7.23. Bold lines indicate Sa - Sr values calculated using the measured $\Delta R2^*$, $\Delta R2$ as well as extrapolated ΔS_O values. Lighter lines are calculated using only the measured $\Delta R2^*$, $\Delta R2$ values.
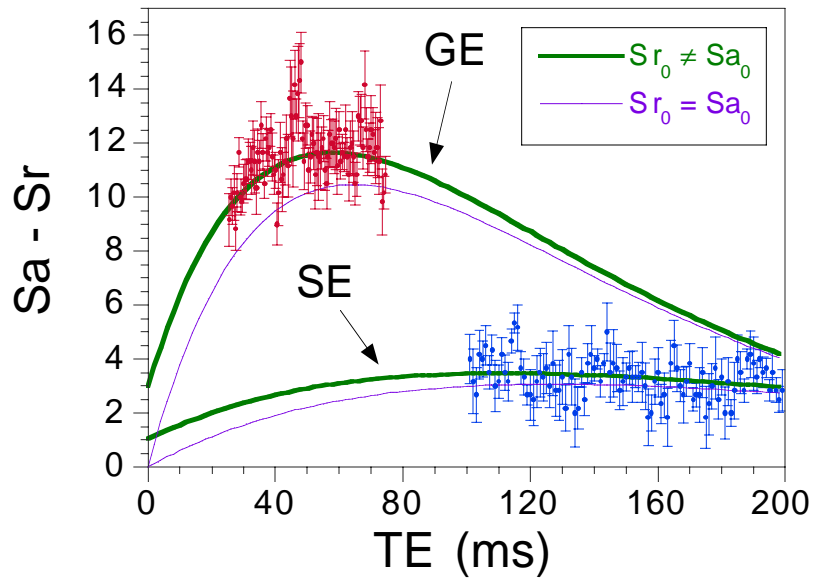
Figure 7.23: Signal difference vs. TE. Bold lines are calculated using the measured resting and active R2, R2*, and So values. Lighter lines are calculated using the measured R2 and R2* values and assuming that $Sa_0 = Sr_0$.

From Figure 7.23, difference in contrast, at $TE \approx T2^*$, between GE and SE sequences is about 3.5 to 1. This is also a slightly higher value than that obtained in part 1. Once again, the more precise fit to the ΔS curve was that which used the So_r and So_a values obtained by interpolation of the decay curves to $TE = 0$.

SEGE–EPI allows for spatially and temporally registered measurements of R2* and R2. In this study, R2*, R2, and interpolated TE=0 signal were measured over time in the brain during rest and activation. These studies typically find large spatial $\Delta R2^*/\Delta R2$ heterogeneity, with an average ratio of 3/1 to 4/1, indicating, with several assumptions, an "average" susceptibility compartment size of 8 to 10 μm.

For a more precise determination of predominant vessel size from these data, it may be useful to consider the average $\Delta R2^*/\Delta R2$ to be a combination of intravascular and extravascular effects. Since all vessels contain red blood cells, and since it has already been shown in simulations (chapter 6) and in data (107) that $\Delta R2^*/\Delta R2$ in blood (radius = 2.5 μm) is about 1.5, this combination of a low intravascular ratio with the ratio created by extravascular effects may actually reveal that actual "average" compartment size may be significantly larger than 10 μm. Ongoing simulation work is being performed so that this measured ratio may be more meaningfully interpreted.

Lastly, these studies indicate that, while susceptibility effects dominate when using TR ≥ 1 sec. in GE or SE sequences, a small non–susceptibility related component, So, contributes.

CHAPTER 8

FIELD STRENGTH COMPARISON

8.1 INTRODUCTION

A primary goal in functional MRI is the characterization of the mechanisms which contribute to activation–induced signal changes. Studies have suggested several sources of functional contrast which may contribute in various degrees, depending on MR parameters. Published models describing the effect of compartmentalized susceptibility changes on MR signal (113, 116-129) generally agree that, with a given activation–induced susceptibility change, the change in R2* increases with B_O at a rate which is between linear and quadratic, depending on the exchange regime, as described in chapter 1 and 6. In the case of the fast exchange regime, the field strength dependence will approach quadratic, and in the case of the slow exchange regime, the dependence approaches linear.

Ogawa et al. (127) and Ugurbil et al. (251) provide an approximate expression for activation–induced R2* changes in the presence of water diffusion and susceptibility–induced field gradients:

$$R2^* = \alpha[\gamma\Delta\chi B_O]\, b_L + \beta(\gamma\Delta\chi B_O)^2 (b_S)^q p \qquad [8.1]$$

where b_L and b_S are blood volume fractions for large vessels and small vessels, α, β, and q are constants; and p is the fraction of active capillary vessels so that b_S is the blood volume when all capillaries have been

recruited. As implied by this equation, the activation–induced dependence on field strength is between linear (large vessels: b_L) and quadratic (small vessels: b_S).

Results published by Turner et al. (183), by which a direct comparison in activation–induced $\Delta R2^*$ was made using photic stimulation at 1.5 T and 4.0 T indicated a power of 1.5 to 1.8 dependence on B_O. These measurements, which used one TE, one ROI, and were carried out on a single subject, are far from conclusive.

In this chapter, experiments to determine activation–induced $\Delta R2^*$ at 0.5 T, 1.5 T, and 3.0 T are carried out. The field strength dependence of $R2^*$, and S_O/N is also measured.

8.2 METHODS

The hardware used for imaging at all three field strengths is described in chapter 2. At all field strengths, a blipped gradient–echo echo–planar imaging sequence, also described in chapter 2, was used. The readout window was 40 ms, and the sampling rate was 8 µs per complex point. Voxel volume = 3.75 x 3.75 x 5 mm^3. TR = 1000 ms. θ = 90°. The TE was varied from 10 ms to 250 ms. The same subject was used for all three field strengths.

At each TE value used, a time–course series of 200 to 500 sequential images of one axial plane through the motor cortex was obtained during cyclic (20 sec on, 20 sec off) bilateral finger tapping. A single functional image was created, using the time–course series at which TE $\approx$ T2*, and used as a mask in the averaging of pixels for time–course measurements. The correlation coefficient threshold was varied such that the size of the active regions were approximately the same. While spatial heterogeneity exists in the

measurements, the similar sized regions (9 to 15 voxels) from which the averaged signals were obtained allowed for a fair comparison. In a second step in this analysis, seven of the voxels demonstrating the strongest activation–induced signal changes were chosen manually. The signal from all seven voxels, the three demonstrating the highest signal changes, and the three demonstrating the lowest signal changes, were also compared. From the regions of interest, spatially averaged signal vs. time plots were created. From these time–course series, resting (Sr) and active (Sa) signal values were obtained. $\Delta R2^*$ values were calculated by a linear fit (fitting routine in KaleidaGraph™ software) to the slope of $-\ln(Sa/Sr)$ vs. TE. Also, functional contrast to physiologic noise and system noise were measured by dividing the activation induced signal differences, ΔS, by the standard deviation, over time, of signal from regions in resting cortex and regions outside of the brain, respectively.

8.3 CONTRAST MECHANISM STUDY

The first gradient echo echo–planar anatomical images from a time–course series at each field strength (TR = ∞, TE = 80 ms) are shown in Figure 8.1. Care was also taken so that image quality and slice location was similar across field strengths. At 0.5 T, controlling for off resonance effects in the slice select direction (manifested primarily as signal dropout), was much less of a difficulty than at 3.0 T.
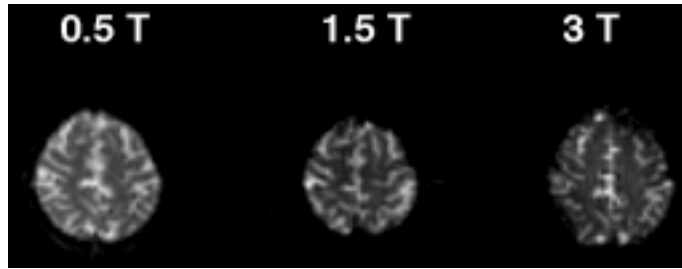
Figure 8.1: Gradient–echo anatomical images the of same slice location and subject at 0.5, 1.5, and 3.0 Tesla. TE = 80 ms. TR = 1000 ms, θ = 90°. Voxel volume = 3.75 x 3.75 x 5 mm^3.

Correlation images were created using a time–shifted (5 sec. latency), box car reference waveform. These images, shown in Figure 8.2, were created from the time series corresponding to the images in Figure 8.1. Bilateral activation appears in similar regions at all field strengths. Contrast to noise at 0.5 T appears lower. The difference in contrast to noise between 1.5 T and 3 T, by inspection, is less.
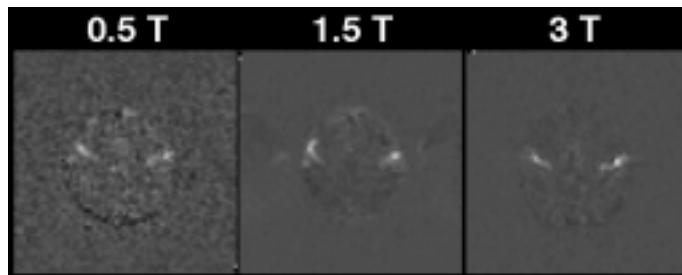
Figure 8.2: Correlation images (bilateral finger tapping) created from the TE = 80 ms time–course series at each field strength.

After a threshold was applied (thresholds were chosen such that the sizes of the activated regions were similar), the surviving voxels were

superimposed on the first anatomical images. These functional correlation overlays are shown in Figure 8.3.
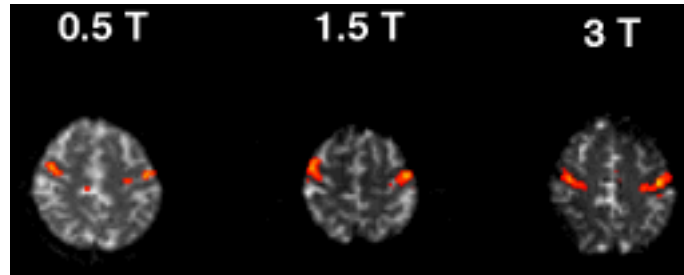
Figure 8.3: Threshold correlation images corresponding to those obtained in Figure 8.2.

Across the activated voxels shown in Figure 8.3, the signal intensity was averaged at each time point. A plot of the percent signal change (TE = 80 ms) vs. time at each field strength is shown in Figure 8.4.
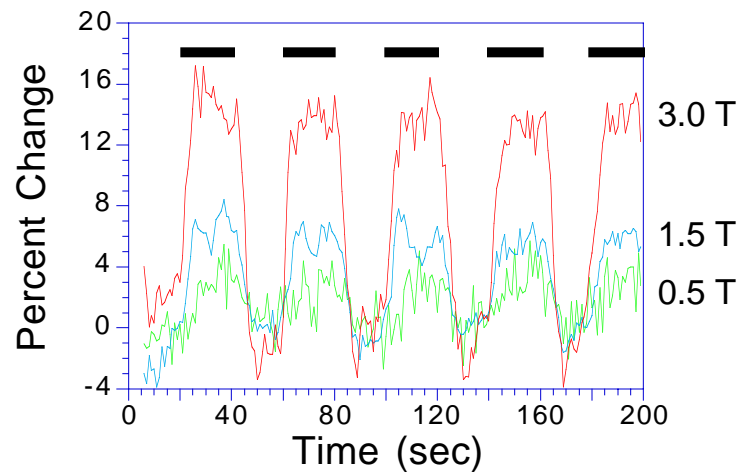
Figure 8.4: Time–course series from selected regions of interest in the motor cortex during cyclic bilateral finger tapping. Active and resting signal was obtained from the average of the on and off states.

As shown in Figure 8.4, the activation–induced percent signal change increases with field strength. At a given TE, activation–induced signal changes may also include flow–related (susceptibility–independent) effects. The slope of -ln(Sa/Sr) vs. TE gives $\Delta R2^*$, separate from flow–related effects. Any non–susceptibility related effects would give a non–zero intercept value at TE = 0, but would not alter the slope of the curve since flow weighting is kept constant across all TE values. At each field strength, Sa and Sr were measured at six different TE values. The plots of -ln(Sa/Sr) vs. TE at three field strengths are shown in Figure 8.5. The slopes appear linear and the zero–intercepts appear negligible.
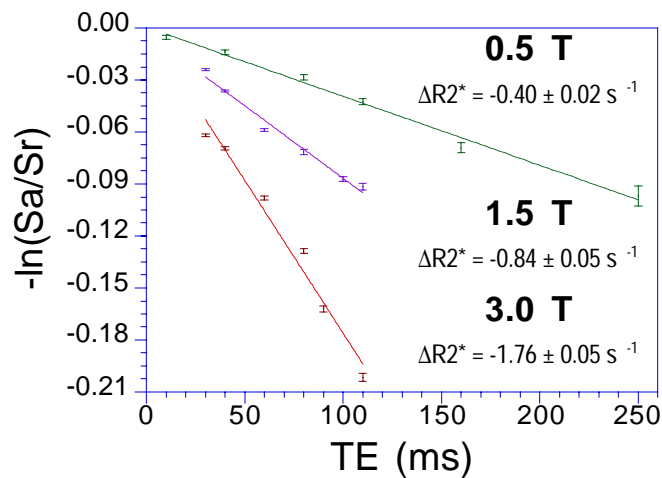
Figure 8.5: $\Delta R2^*$ values obtained from the slopes of -ln(Sa/Sr) vs. TE.

Figure 8.6, which shows the absolute value of the relaxation rate change (the rate changes are negative) plotted vs. TE, shows a B_0 dependence of $\Delta R2^*$ that appears slightly less than linear.
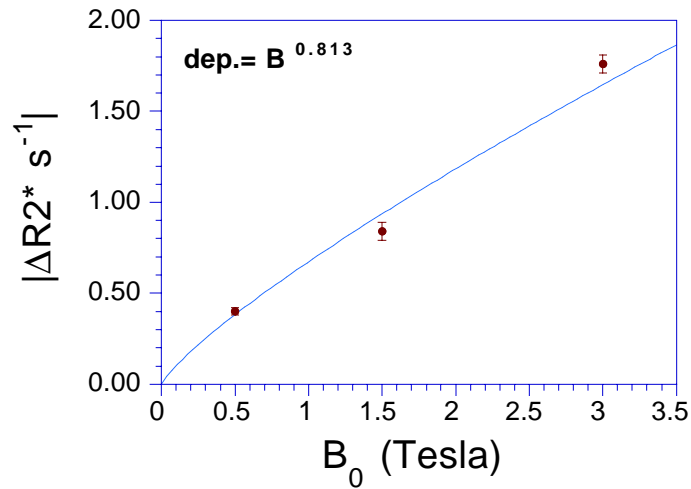
Figure 8.6: $\Delta R2^*$ vs. B_O. An approximately linear dependence of $\Delta R2^*$ on field strength is observed.

The schematic diagram Figure 8.7 serves to illustrate a possible source of error that may be present in these measurements. The entire region represents a uniformly activated region of cortex. Each box represents a voxel. The region of three concentric circles represents the significantly activated volume obtained at 0.5 T. The region of only two concentric circles represents the additional volume showing activation at 1.5 T, and the entire matrix represents the volume that shows significant activation at 3.0 T.
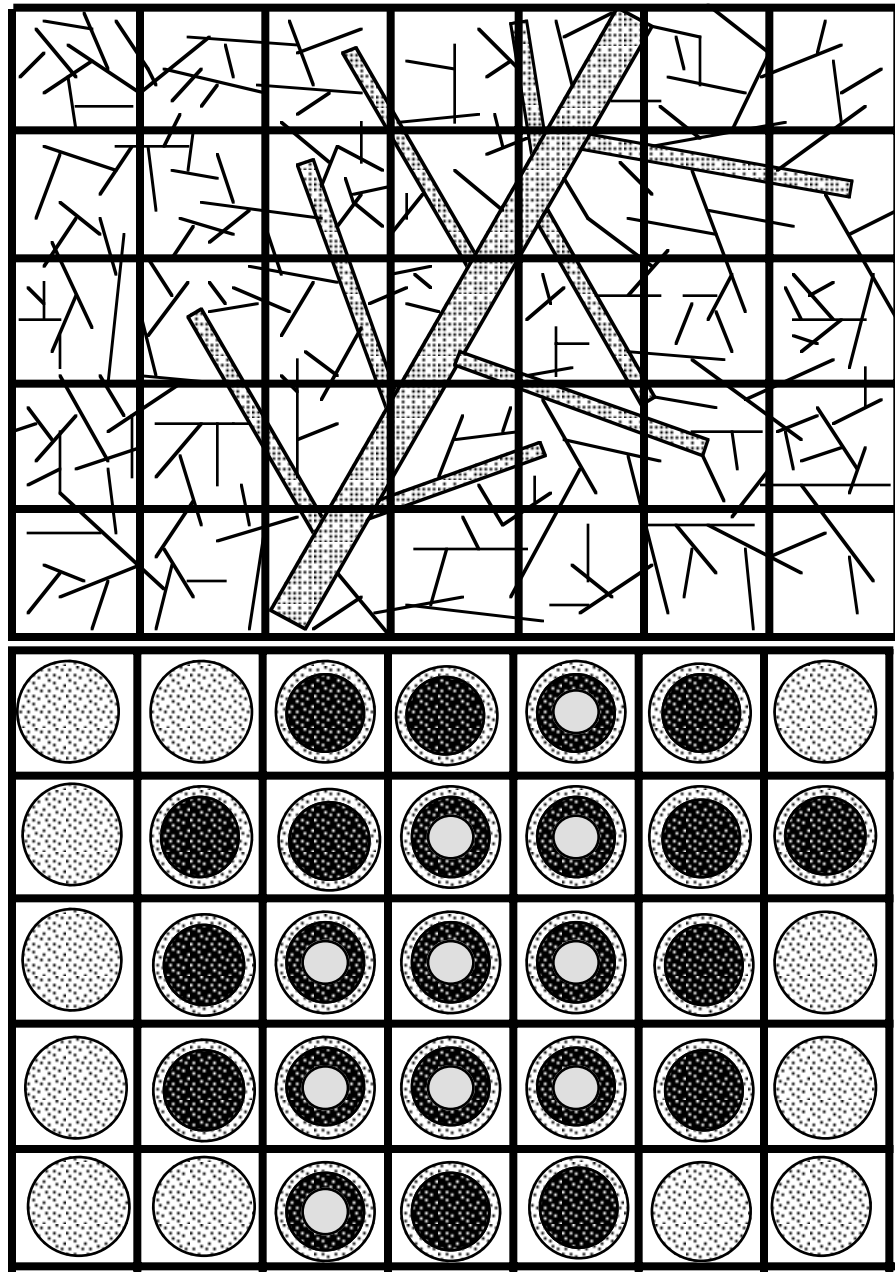
Figure 8.7: Schematic illustration of possible methodological source of error involved in choosing ROI's of different sizes at different field strengths. Artificial weighting may be placed on larger vessels (voxels with higher blood volume) and therefore higher changes, at low field strengths.

Because of the lower susceptibility effect and signal–to–noise ratio, activated regions obtained at lower field strengths (0.5 T) are hypothesized to reside predominantly in voxels having large vessels and larger blood volumes, (i.e. only voxels with large vessels that show the strongest effect would be above the noise). Activated regions obtained at higher field strengths, because of the greater susceptibility effect and higher signal to noise, are hypothesized to reside not only in the large vessel regions but also in regions of relatively small blood volumes such as voxels containing predominantly microvessels. Because of this effect, some weighting is placed on lower field strength effects by allowing the size and location of the region of interest to vary somewhat across field strengths.

To account for this possible error, the number of voxels observed was kept constant. It is hardly possible to pick, based on anatomy, regions at 0.5 T that do not show activation but would show activation at higher field strengths. It is also hardly possible to pick identical regions across field strengths. The manual choice of the seven voxels showing the greatest signal changes only ensured, at best, that large vessel weighting was somewhat evenly placed, at all field strengths. The voxels were most likely those having high blood volume and large vessels.

Figure 8.8 shows the field strength dependence of the absolute values of $\Delta R2^*$ measured using the highest 3, lowest 3, and all seven of the most strongly activated voxels. The dependence of $\Delta R2^*$ on B_O appears essentially linear for all the regions observed.

Figure 8.8 graph showing:

Hi 3 Vox: dep.= B$^{0.998}$
All 7 Vox: dep. = B$^{0.950}$
Low 3 Vox: dep. = B$^{1.02}$

Y-axis: $|\Delta R2^* \, s^{-1}|$ (0.00, 1.00, 2.00, 3.00, 4.00)
X-axis: B_0 (Tesla) (0, 0.5, 1, 1.5, 2, 2.5, 3, 3.5)
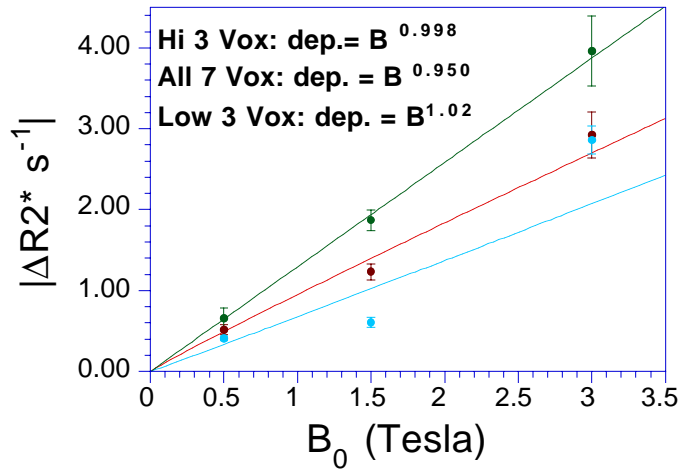
Figure 8.8: Dependence of $\Delta R2^*$ on field strengths measured using ROI's consisting seven voxels demonstrating the highest percentage change. Of the seven, three voxels demonstrating the highest percentage change and the three voxels demonstrating the lowest percentage change are also compared.

For, comparison, a simulation was carried out using the deterministic method described in chapter 6. First, it was necessary to decide upon the average vessel radius to use in the simulation. The data used is this decision are the $\Delta R2^*/\Delta R2$ ratio values obtained at all field strengths. These data are summarized in Table 8.1. The ratios obtained in this table were compared with the simulated plot of $\Delta R2^*/\Delta R2$ vs. radius (Figure 6.25). The box in Figure 6.25 represents the ratios shown in Figure 8.1.

Field Strength	$\Delta R2^*/\Delta R2$	n
0.5 Tesla	2.35 ± 1.32	1
1.5 Tesla	3.38 ± 0.12	11
3.0 Tesla	3.31 ± 0.34	4

Table 8.1: Summary of $\Delta R2^*/\Delta R2$ ratios (in a region of interest) and number of experiments performed, n, at each field strength.

These measured ratios are relatively field strength insensitive, as is suggested by the simulations in chapter 6 (within the range of radii measured and field strengths used), and also mentioned by Ogawa et al. (127). The box in that figure spans a $\Delta R2^*/\Delta R2$ ratio of about 2/1 to 5/1 corresponding to radii of 6 µm to 10 µm. Based in the data in Table 8.1 and the simulation results in Figure 6.25, a radius of 8 µm was used in the present simulation. An oxygenation change of 0.60 to 0.75 was used at the three field strengths. Details of the simulation methods are described in chapter 6. The values of $\Delta R2^*$ were obtained in the same manner as the experimental data were obtained above. The slopes of the simulated -ln(Sa/Sr) vs. TE, shown in Figure 8.9, were obtained. A fit of the absolute value of $\Delta R2^*$ vs. TE to a power of B_O is shown in Figure 8.10. The dependence on B_O is considerably higher: about 1.63. This serves to illustrate that some discrepancy or discrepancies exist between the demonstrated model and the observed results. The differences in results may be many: ranging from oversimplifications in the simulations to systematic errors in the experimental measurements or in the simulations.
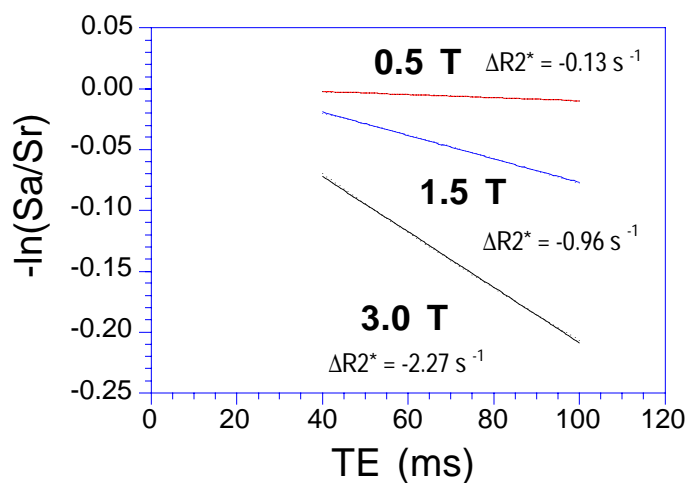
Figure 8.9: Simulated values of -ln(Sa/Sr) vs. TE using 8 μm vessel radius, 0.60 to 0.75 oxygenation saturation change, and a 1.0 μm^2/ms diffusion coefficient.
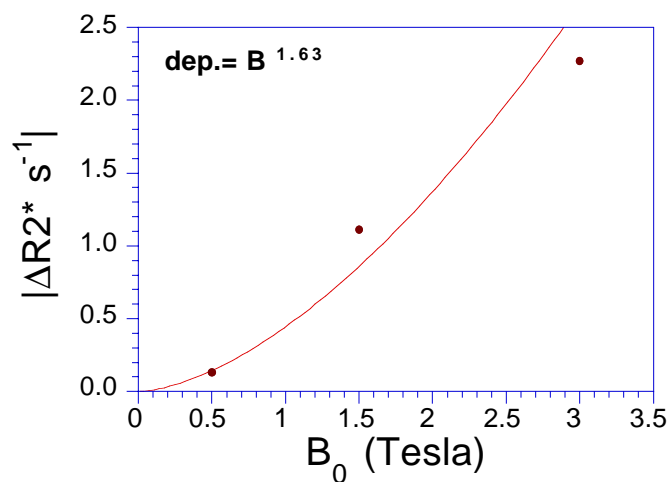
Figure 8.10: Simulation of ΔR2* vs. field strength. The values were obtained from Figure 8.9.

One possible reason for this discrepancy is that, in the simulations, intravascular dephasing effects (resting state and activation–induced changes) were not considered. A recent publication (190) has suggested that, at 1.5T, up to two thirds of activation–induced BOLD signal changes are intravascular. Given that blood T2* decreases more rapidly with increased field strength than tissue T2*, less blood signal is present at higher field strengths. Therefore, the intravascular effect will be reduced, therefore reducing somewhat the activation–induced signal change. Ongoing work is being pursued to clarify these issues.

8.4 CONTRAST TO NOISE STUDY

At any TE value, the contrast to noise in a gradient–echo time–course experiment can be given by (251):

$$\Delta S/N = \{(So/N) \exp[-(TE)R2^*]\} \times \{\exp[-(TE)\Delta R2^*] - 1\} \qquad [8.2]$$

which reduces to:

$$\approx (S_O/N) \ [(TE)\Delta R2^*]\{\exp[-(TE)R2^*]\}. \qquad [8.3]$$

At TE ≈ T2*, (where contrast is maximized) the expression reduces to:

$$\Delta S/N = (S_O/N) \ (\Delta R2^*/R2^*)[\exp(-1)]. \qquad [8.4]$$

The determining factor in contrast to noise is not only activation–induced $\Delta R2^*$ but also baseline values in signal and noise. In addition to

measuring activation–induced ΔR2* values from the activated regions of interest, baseline relaxation rate, baseline R2*, values were obtained.

R2* values were obtained from the same data set by measurement of the slope of a linear fit to plots of $\ln(S_r)$ vs. TE, shown in Figure 8.11. Because a constant TR was used in the measurement of these values, a small increase in the partial volume averaging of cerebral spinal fluid at 0.5 Tesla was expected (T1 rate increases at lower field strengths, causing more complete relaxation for a given TR). More cerebral spinal fluid signal is therefore present at lower field strengths at a constant TR. Nevertheless, these measurements are consistent with the typical fMRI protocol that is kept relatively constant in practice. T2*, in general, is also highly dependent on voxel volume and shim. A good shim is more easily achievable at low field strengths. As mentioned, voxel volume was kept constant and the shim was adjusted so that image quality was also kept relatively constant across field strengths. As shown in Figure 8.11, the signal decays appear to be well fitted well by single exponentials.
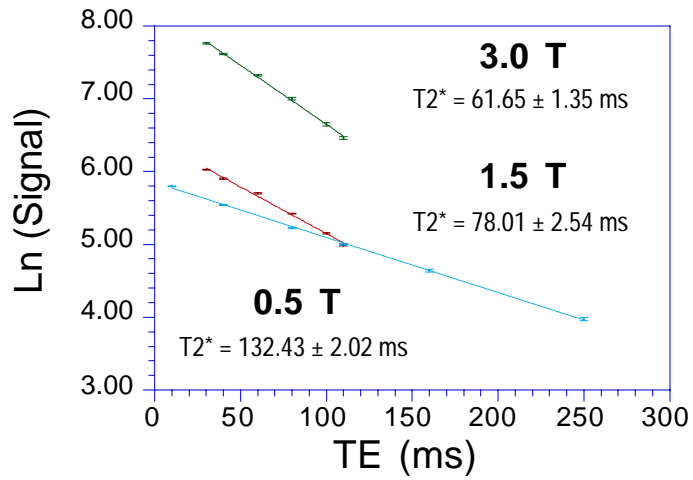
Figure 8.11: Measurement of T2* values from same region of interest as used in Figure 8.5.

A plot of R2* vs. B_O is shown in Figure 8.12. R2* appears to increase at a slightly less than linear rate with B_O.
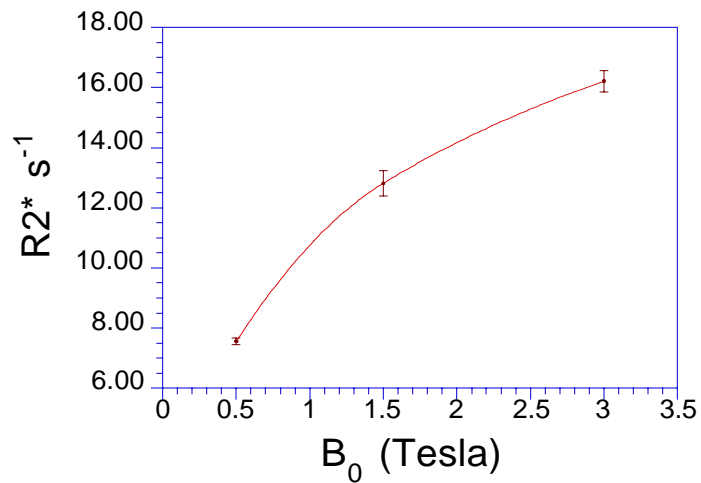
Figure 8.12: Plot of resting state R2* (from the motor cortex region) vs. B_O.

Using the measured R2* and ΔR2* values in conjunction with the assumption of a single exponential decay rate, the signal differences or contrasts can be approximated and compared. Figure 8.13 is a plot of normalized (S_O set to 1) signal difference (ΔS) data. The solid lines, shown in Figure 8.13, are calculated Sa - Sr values assuming that $\Delta S = e^{-(TE \ (R2 + \Delta R2))} - e^{-(TE \ R2)}$. Note that the peak in ΔS occurs at TE ≈ T2*. It has been shown in chapter 1 that, in the limit that ΔR2* approaches 0, ΔS is maximized at TE = T2*. It is at this TE value that relative contrasts should be compared.
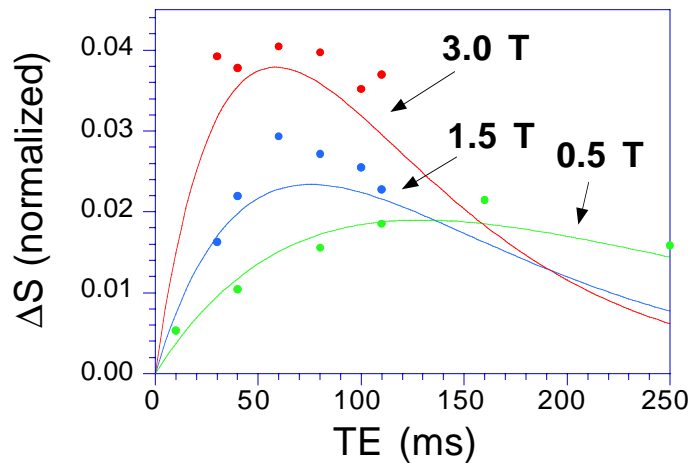
Figure 8.13: ΔS values with curves calculated using the baseline R2* values and measured activation–induced ΔR2* values.

It is apparent from Figure 8.13 that contrast increases with field strength. Lastly, contrast to noise is measured. If noise scales similarly with field strength, then gains in contrast to noise are be minimal. The standard deviation of signal over time from within non–activated cortical regions of the brain were measured to estimate noise. The contrast was divided by the

standard deviation, in time, of the signal from resting cortex. The contrast to noise values are shown in Figure 8.14. The contrast to noise values at TE $\approx$ T2* vs. B_O are shown in Figure 8.15.
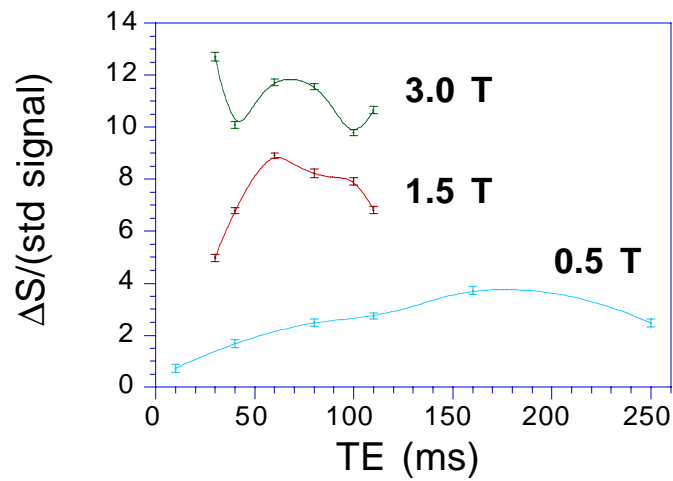
Figure 8.14: Measured $\Delta S/$(std signal) vs. TE. The standard deviation of the signal was measured over time from resting cortical regions.
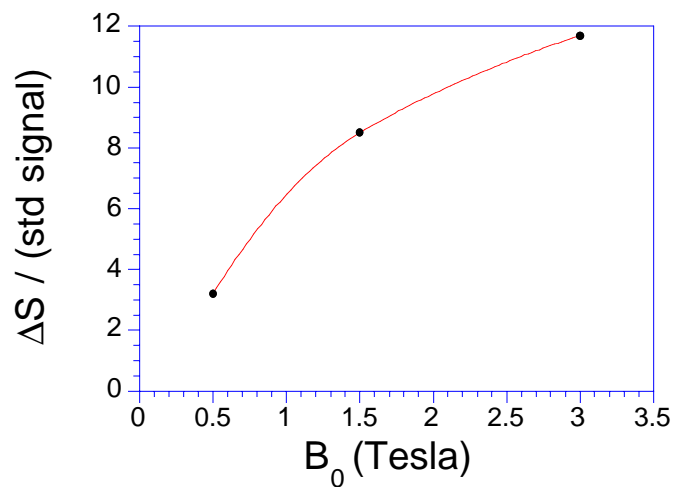
Figure 8.15: Measured $\Delta S/N$ at TE $\approx$ T2* vs. B_O.

It is apparent that gains in contrast to noise. at 3.0 T are made. It should be cautioned that these results only apply to these specific pulse sequence parameters. Factors such as relative noise power are highly pulse–sequence and system dependent.

It is interesting to characterize the nature of the noise in the brain. Figure 4.17 and 4.18 and other work (257, 258, 260) suggest that most of the noise power in much of the brain is at the heart rate and respiration frequencies, and is due to time–of–flight signal enhancement from motion of blood, csf, and brain.

A comparison of the standard deviation of the signal fluctuations in time within the brain to the standard deviation of the signal fluctuations in time outside of the brain, shown in Figure 8.16, gives a measure of the degree to which "physiological fluctuations" contribute to the noise. Time–course signal from a region of resting cortex and from a region in space were compared. The ratios were divided by 1.52 to account for noise rectification (after Fourier transformation) in regions of very low signal intensity (379).

(brain noise / background noise) / 1.52
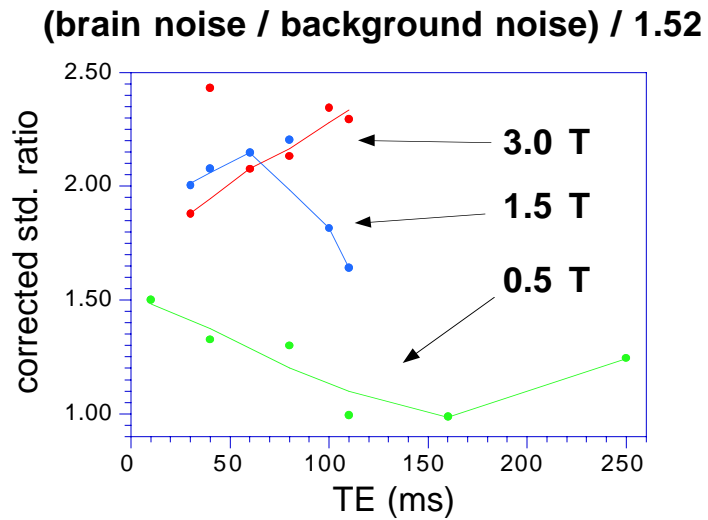
Figure 8.16: Standard deviation of signal inside resting cortex / standard deviation of signal outside brain. (and normalized) vs. TE.

It is apparent that, at 1.5 T and 3.0 T, the noise inside resting cortex (mixed with csf and pulsating blood) has approximately twice the magnitude as that outside the brain. At 0.5 Tesla, non–physiologic noise remains the dominant noise source. Some preliminary conclusions from these data are that the noise does not significantly change with TE (therefore is not primarily based on susceptibility–related changes such as oscillations in oxygenation) and is not significantly different between 1.5 T and 3.0 T. As mentioned that, because of the hypothesized origin of these fluctuations, the relative magnitudes of the noise are likely to be extremely pulse–sequence dependent (TR, θ, resolution, outer volume saturation, flow compensation, motion correction). Gains in functional contrast to noise can therefore be obtained if physiologic noise can be removed or reduced.

8.5 DISCUSSION

From these measurements, it appears that $\Delta R2^*$ increases approximately linearly with field strength. It is not conclusive that $\Delta R2^*$ in voxels containing predominately capillaries increases in a greater than linear fashion since it is very difficult to identify from anatomical images at low field strengths, the vascular structures or to compare activated with adjacent non–activated regions across field strengths.

It is also apparent that functional contrast to noise (ΔS/standard deviation of signal in resting cortex), as it was measured, also increases with field strength. This increase in contrast to noise can translate into more successful application of fMRI at higher spatial and temporal resolution without significant loss in functional image quality.

Figure 8.17 shows a comparison of correlation images obtained at 3T using single shot EPI at 3.75 x 3.75 x 5 mm^3 resolution (64 x 64) and at 2.50 x 2.50 x 5.0 mm^3 (96 x 96). The high contrast to noise and signal to noise appears maintained at the higher resolution.
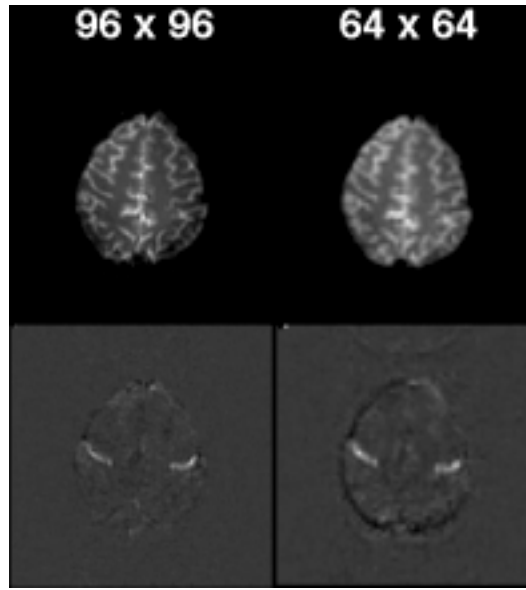
Figure 8.17: Anatomical and corresponding correlation images obtained at 3T using single–shot EPI at 3.75 x 3.75 x 5 mm^3 resolution (64 x 64) and at 2.50 x 2.50 x 5.0 mm^3 (96 x 96).

Higher functional contrast to noise also allows more sensitivity to subtle signal changes arising from higher cognitive activity or to more subtle hemodynamic events. Such information may be useful and possibly essential in the unraveling of fMRI contrast mechanisms and of study of higher cognitive function.

CHAPTER 9

PARTIAL VOLUME AND INFLOW EFFECTS

9.1 INTRODUCTION

In this chapter the effects of three pulse sequence modulations are described. The pulse sequence modulations include: a) alteration of voxel volume from 3.75 x 3.75 x 20.0 mm^3 to 3.75 x 3.75 x 2.0 mm^3, b) application of a 10 mm thick outer volume RF saturation on either side of the imaging plane, and c) variation of TR from 6000 ms to 200 ms, with concurrent variation of flip angle from 90° to 6° when using a TR of 300 ms. For all pulse modulations, a time course series of T2*–weighted images was collected during which the subject performed bilateral cyclic finger movement. The degree of partial volume averaging that occurs at typical resolutions used was assessed by (a), and, the extent or degree that "inflow effects" contribute to the activation–induced signal changes by (b) and (c).

9.2 PARTIAL VOLUME AVERAGING

The effects on activation–induced MR signal change by variation of the MR voxel volume, keeping all other parameters constant, are considered in this section. Other investigators performing direct comparisons of activation–induced signal changes at different voxel volumes (177, 186, 188) have observed that the fractional signal change increased as voxel volume decreased. The hypothesized reason for these phenomena is that within a

284

smaller voxel, less partial volume averaging takes place with either non activated tissue or with unaffected spins outside the range of microscopic field gradients that are modulated as a result of oxygenation changes.

In this study, the fractional activation–induced signal change and the activated volume (the volume that showed a temporal correlation coefficient threshold above a fixed threshold) were measured as the MR voxel volume was decreased.

Five time–course series, consisting of 50 sequential 64 x 64 gradient–echo echo–planar images (TE = 40 ms, TR = 2000 ms, $\theta = 90°$, FOV = 24 cm), were obtained during which two 20 sec. periods of bilateral finger movement were performed. The first time course series was of a single 20 mm thick slice. The second was of two 10 mm thick slices. The third was of four 5 mm thick slices. The fourth was of five 4 mm thick slices. The last time course series was of ten 2 mm thick slices. In the multislice studies, no interslice spacing was used and the spatial order of slice acquisition was interleaved to minimize RF saturation at the slice edges which occurs as a result of imperfect slice profiles and no inter–slice spacing. The study was performed in this manner because a variation of in–plane resolution in EPI changes other variables such as readout window length and/or filter bandwidth. In order to keep these variables constant, it was necessary to keep in–plane resolution and the volume of the observed region constant. The anatomical images are shown in Figure 9.1.
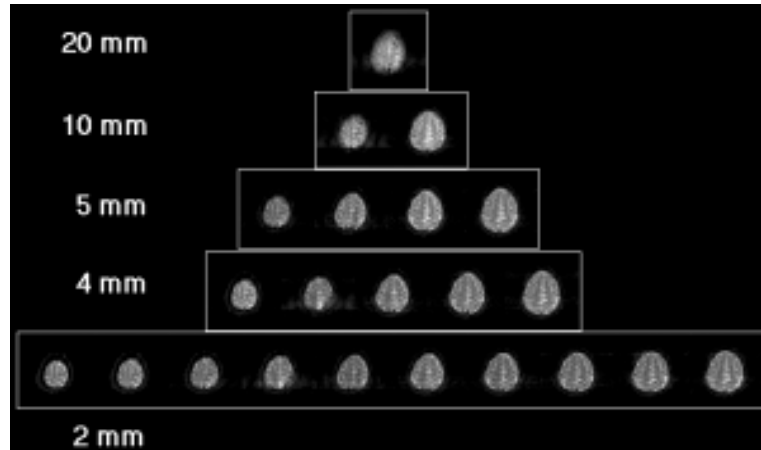
Figure 9.1: Anatomical images from voxel volume variation study. All rows contain the same total volume. Voxel volume in the top image is 3.75 x 3.75 x 20 mm^3, and the voxel volume of the ten images on the bottom row are 3.75 x 3.75 x 2 mm^3

Corresponding functional correlation images are shown in Figure 9.2. Activation was observed within in every slice.
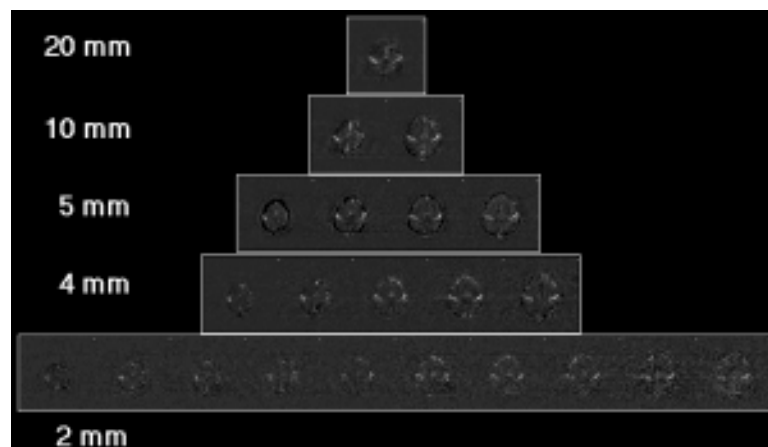
Figure 9.2: Correlation images (bilateral finger movement) corresponding to the anatomical images in Figure 9.1.

From voxels having a correlation coefficient above 0.7 with an reference vector, the average baseline signal was measured. Figure 9.3 shows a plot of intensity vs. voxel volume. The signal intensity at the thickest slices seems to taper off slightly from a linear dependence on voxel volume. This small deviation may be due to susceptibility or shim–related signal dropout that increases as voxel volume is increased. Also, the small deviation from linearity at the thinnest slices may be caused by slice cross–talk effects.
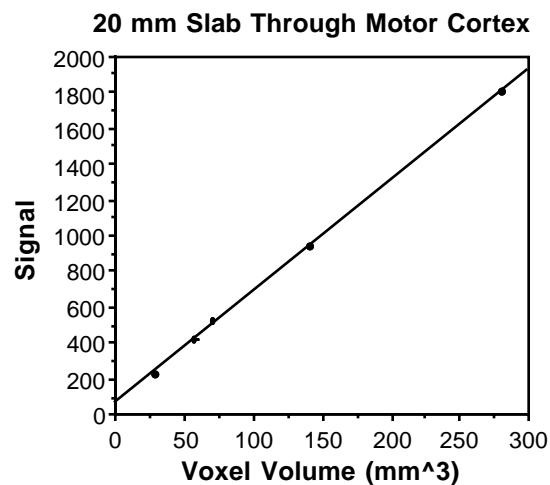
Figure 9.3: Plot of MR signal intensity vs. voxel volume, demonstrating a linear proportionality. The signal intensity was averaged from the motor cortex region in all slices.

From the time course data sets, the fractional signal change was calculated. The averaged fractional signal change is shown in Figure 9.4. The bar locations correspond to relative anatomical slice location. The bar thickness is not indicative of actual slice thickness and the actual slices are also contiguous. Left = superior and right = anterior.
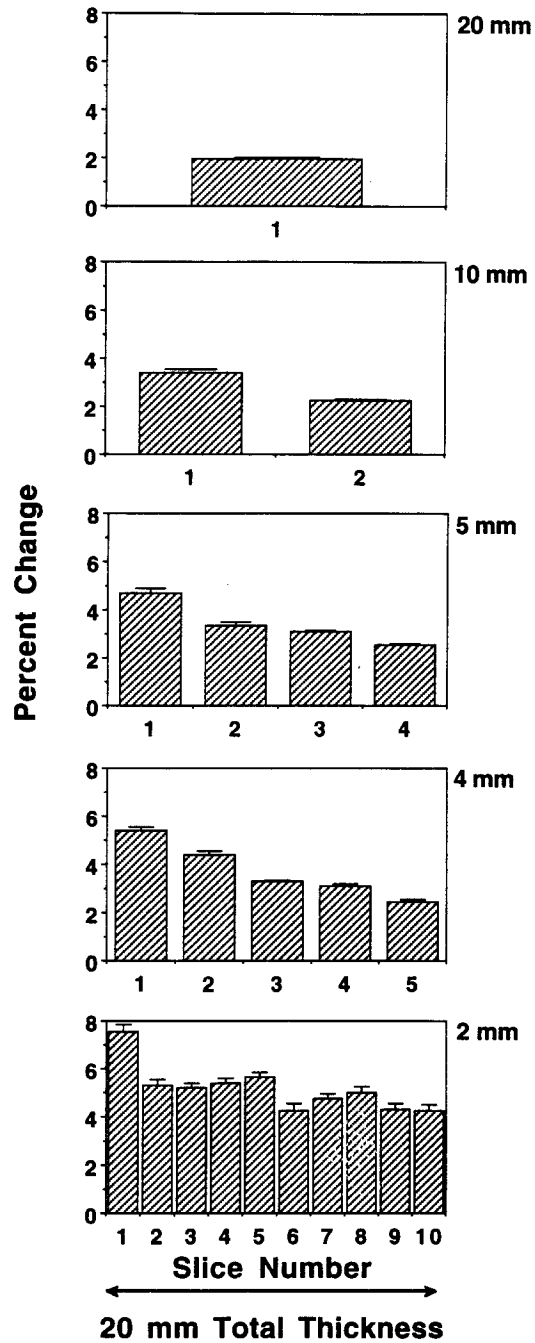
Figure 9.4: Fractional signal change in activated motor cortex in each slice. Slice thickness is indicated to the right of each graph. The slice ordering is from superior (left) to posterior (right). All of the slices were contiguous.

Figure 9.5 shows the average fractional signal change vs. voxel volume, demonstrating an increase in fractional signal change corresponding to the number of slices used.

20 mm Axial Slab Through Motor Cortex
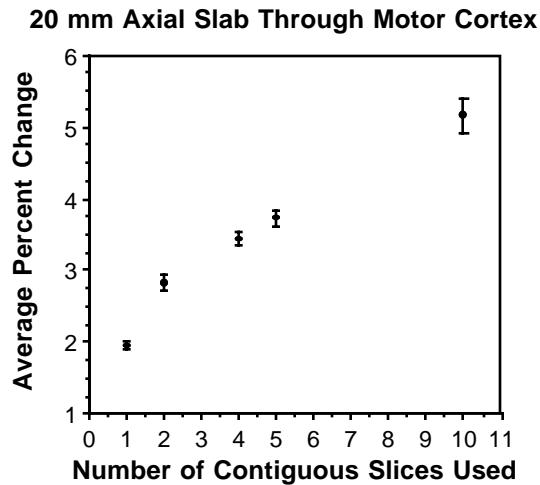
Figure 9.5: Summary of Figure 9.4 demonstrating an increase in the fractional activation–induced signal change as the voxel volume is decreased.

The volume showing activation, as determined voxels having a correlation coefficient above a threshold of 0.7, decreased in a manner that was proportional to voxel volume, as shown in Figure 9.6. This demonstrates either that a) a large amount of partial volume averaging occurs at larger voxel volumes or that b) small activation–induced signal changes fall below the correlation coefficient threshold as overall signal intensity decreases (relative noise increases). The assessment physiologic noise magnitudes and variations across slice thicknesses were outside the immediate goals of this study and therefore not carefully addressed here. With these parameters, noise should be invariant of slice thickness. Any changes in noise would be

indicative of changes in physiologic fluctuation sensitization, and therefore a potentially useful method for probing the sources of these effects.
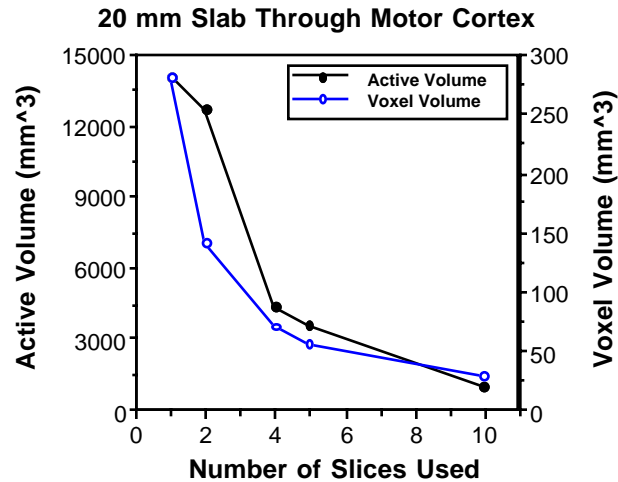
Figure 9.6: Demonstration of a proportional decrease in voxel volume and activated volume.

Lastly, a qualitative assessment of activated region characteristics and contrast to noise values is given below. The voxel dimensions were varied from 1.67 x 1.67 x 1.50 mm^3 to 6.25 x 6.25 x 2.00 mm^3. The first image of each time course series is shown in Figure 9.7. Corresponding correlation images displaying regions activated by bilateral finger tapping are shown in Figure 9.8. It appears that, as resolution is increased, the activated regions decrease in size and increase in intensity, relative to the noise. It is not clear from these studies whether the larger apparent regions of activation at low resolution are only due to partial volume averaging of large vessel effects (187) or if these larger regions include capillary effects that are so small that, at high resolutions, are at the level of the noise and therefore do not appear. A proposed study to help answer this question would be one that involves

matching the functional contrast (activation–induced signal change) to noise across resolutions by making the high resolution runs longer. As more averaging is performed the active region in the high resolution scans should increase in size if more subtle capillary effects are, in fact, present and in different locations than the large vessel effects.
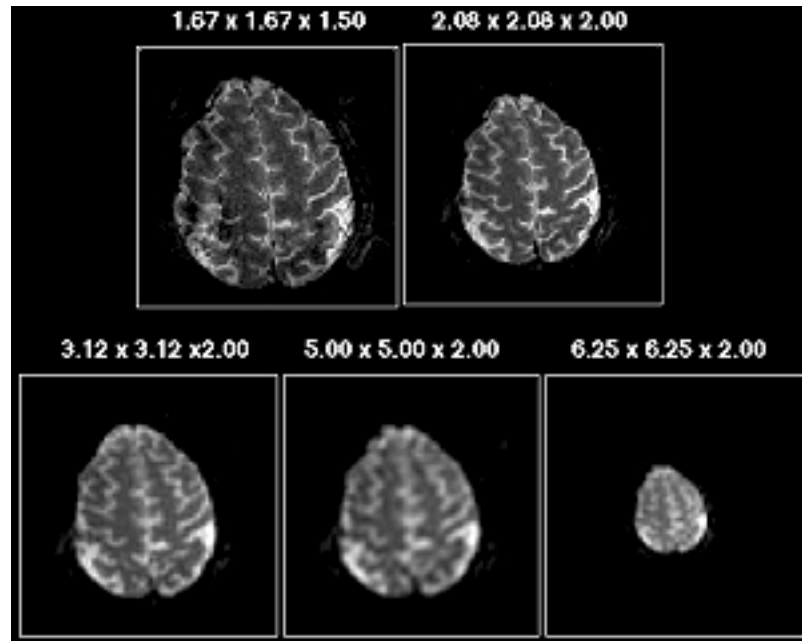
Figure 9.7: Anatomical images of progressively higher resolution single–shot gradient–echo EPI.
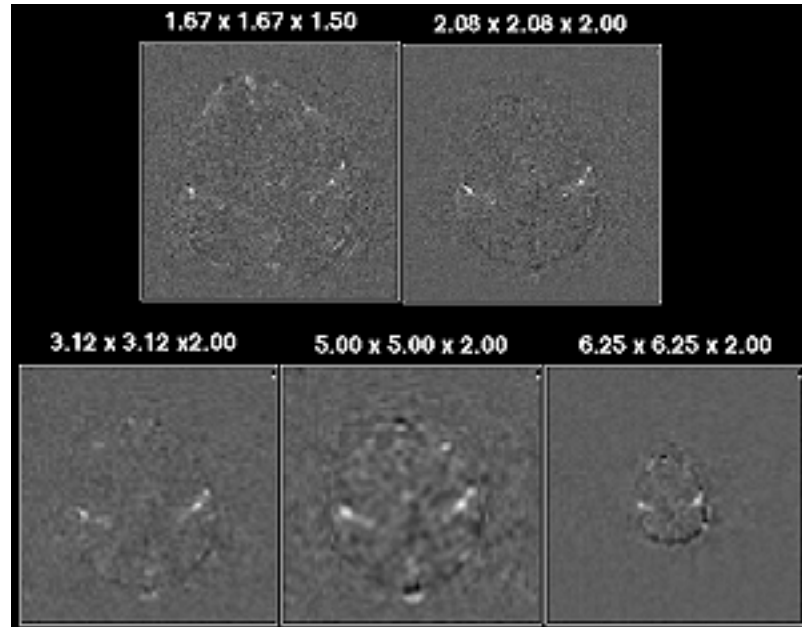
Figure 9.8: Functional correlation images obtained from time–course series of images following the first anatomical image displayed in Figure 9.8. The task was bilateral finger movement.

9.3 INFLOW EFFECTS

Inflow effects have been described as susceptibility–independent activation–induced signal changes that are observed primarily when using a) short TR (relative to T1), b) high flip angle, or c) linear phase encoding steps in FLASH–type sequences (short TR). Previous studies (178, 182, 189, 214) have discussed inflow effects. The basic explanation for inflow effects is that, when using pulse–sequence parameters (a through c) mentioned above, steady–state magnetization within the slice is less than that outside of the slice. Fresh, unsaturated flowing spins enter the imaging plane and cause signal enhancement that is highly flow velocity sensitive (380). An activation–induced increase in flow velocity can therefore cause a change in

signal. Methods that have been used to reduce the inflow effect include a) outer volume RF saturation (182, 189), b) low flip angles (182), c) long TR values (typical of EPI studies), and c) centric–ordered phase encoding (214) when using multi–shot imaging methods.

In this section, using EPI, we make an assessment of the extent and degree of inflow effects. First, two time course series of 100 sequential axial echo–planar images (voxel volume = 2.08 x 2.08 x 2.5 mm^3) were collected during cyclic, bilateral finger movement (TE = 40 ms, TR = 1 sec., θ = 90) The second of the two time course series was collected during application of 10 mm thick outer volume RF saturation pulses on each side of the imaging plane. Correlation images were created from the two time course series in an identical manner. Figure 9.9 shows the first anatomical image in the first time course series and also the correlation images with and without the use of the outer volume RF saturation pulse. The only observed difference is in the spatial pattern of activation. The functional image created using the time course series with no RF saturation has more pronounced "hot spots" or regions of higher activation–induced signal change and the functional image created using the time course series with no RF saturation has more of a "flat" region of activation. It is hypothesized that this high intensity region may be either from a) pure inflow effects or b) more signal within a large draining vein from which an intravascular BOLD signal change arises. Studies in chapter 7 suggest that very small non–BOLD signal changes arise at TR = 1 sec. In this study, the most that can be said is that the signal from inflowing spins (which can alter apparent T1 and T2*) is apparently reduced. It is expected that, when using a shorter TR, the effect of outer volume saturation on fMRI activation will be more dramatic due to an increased RF saturation in the imaging plane.
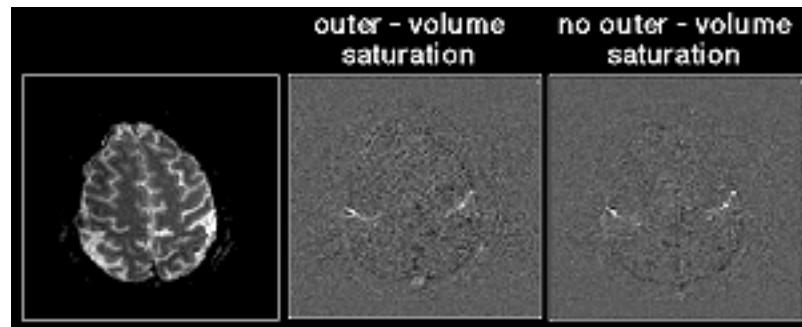
Figure 9.9: Anatomical image and corresponding correlation images with (center) and without (far right) outer volume saturation.

A second strategy used to assess inflow effects is modulation of TR and θ, which alters the difference in magnetization between the imaging plane and unsaturated spins outside of the imaging plane.

In the following study, performed at 3T to enhance inflow effects (longer T1 values), time course series of images (TE = 27 ms, voxel volume = 3.75 x 3.75 x 5 mm^3) were collected, keeping the imaging time and task activation timing constant. Total imaging time was 134 seconds, during which two episodes of bilateral finger movement were performed. The TR was decreased from 6000 ms to 300 ms, and, at a TR of 300 ms, the flip angle was decreased from 90° to 6°. The fractional signal change from the same region of interest was measured. Figure 9.10 shows, at each TR and θ used, the fractional signal change between the first image (TR = ∞) and the average steady–state signal along with the fractional activation–induced signal change.
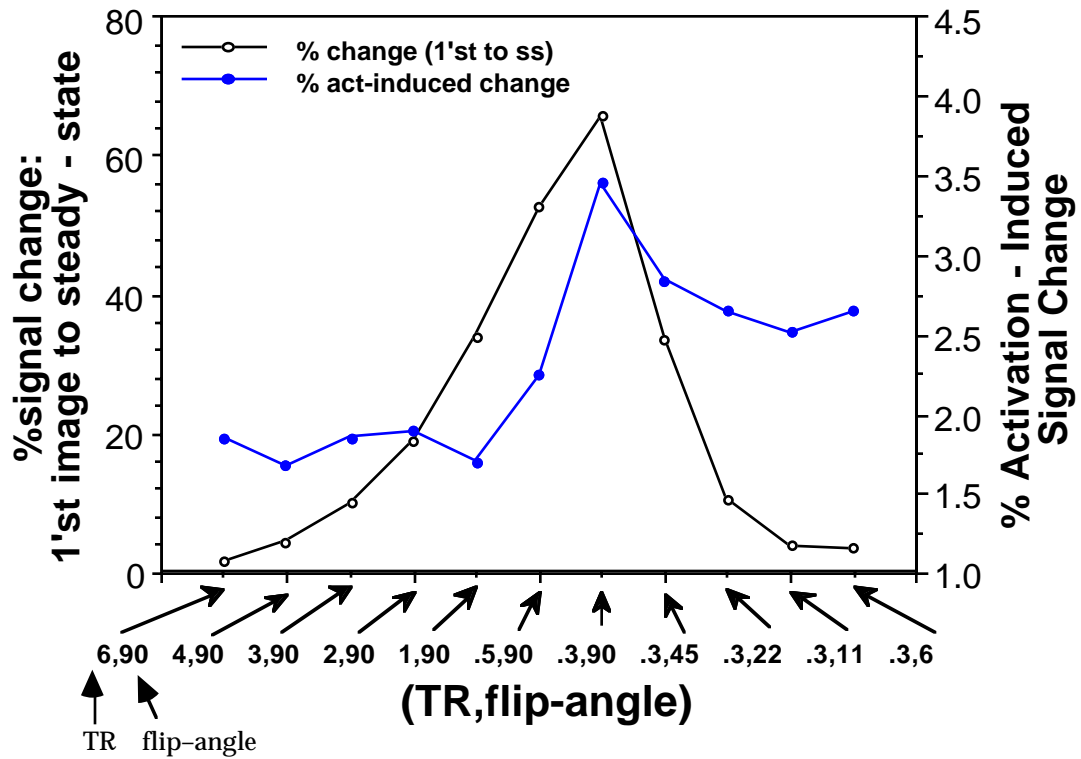
Figure 9.10: Signal from the same region in motor cortex as TR (sec.) is shortened, then as flip angle (degrees) is decreased. The activation–induced fractional signal change appears to have a similar dependency on TR and flip angle as the fractional signal difference between the signal in the first image (TR = ∞) and the steady state signal.

The fractional magnetization difference between the unsaturated spins and steady state follows the activation–induced fractional signal change, possibly indicating that enhancement from inflowing spins is increased as the magnetization difference increases. One other possible interpretation is that the shorter TR values cause greater saturation with cerebral spinal fluid, which shares most voxels with gray matter. The greater fractional signal

enhancement may be due to less partial volume averaging with cerebral spinal fluid.

9.4 DISCUSSION

It is clear that many factors influence the activation–induced MR signal change in addition to the hemodynamic transfer function as characterized in chapters 3, 4, 5, 6, 7, and 8. This chapter serves to illustrate the effects of changing resolution, TR, and flip angle. Hypothesized explanations for the changes in activation volume, distribution, and magnitude have been considered. While it is clear that the dominant source of signal change elicited when using susceptibility–weighted sequences is BOLD contrast (as suggested, for example, by the strong TE dependence of the fractional signal change in Figure 7.22), it is also clear that other factors may significantly contribute to the changes and therefore need to be taken into careful consideration when any quantitative analysis of activation–induced MR signal changes is performed.

CHAPTER 10

HYPERCAPNIA AND HYPOXIA

10.1 INTRODUCTION

The work described in this chapter involves the study of the effects of hypercapnia and hypoxia on T2*–weighted MR signal in the human brain during rest and also during neuronal activation. This study is divided into two parts. In part 1, the hemodynamic mechanisms which contribute to activation–induced MR signal changes are further characterized, and in part 2, a normalization method which may allow more accurate localization of brain activation–induced vasodilatation sources is demonstrated.

10.2 INTRODUCTION TO PART 1

As discussed in chapter 6, neuronal activation causes local vasodilatation but is accompanied by relatively small increase in oxidative metabolic rate (29). The Fick principle dictates that the resulting increase in flow rate causes a decrease in the arterial–venous $\%HbO_2$ difference, causing susceptibility–weighted MR signal to increase (decreased paramagnetic deoxy–Hb concentration). This mechanism of signal change may be mimicked by hypercapnia (increase in blood CO_2 concentration) which results in global vasodilatation and subsequent increase in flow. This flow increase is not accompanied by a corresponding increase in oxidative metabolic rate, therefore the venous oxygenation is also globally increased. These signal

increases which accompany hypercapnia are dependent on voxel–wise differences in hemodynamics (blood volume, oxygenation) and vessel architecture (radii, orientation, vascular patency) (107, 171, 198, 244). If the mechanism of action (vasodilatation) is similar to that accompanying neuronal activation, then the competitive effect should damp activation–induced MR signal changes.

Hypoxia, (decrease of blood O_2 saturation), causes a global MR signal decrease (increase in deoxy–Hb concentration), with similar dependence on hemodynamics and vessel architecture (107, 146, 147, 168, 169, 196, 197, 240). However, because mild hypoxia does not cause strong vasodilatation, activation–induced signal changes should not be as strongly damped.

10.3 INTRODUCTION TO PART 2

One difficulty in interpretation of neuro–functional MR images is that hemodynamic and vessel architecture variations across voxels lead to uncertainty of true activation foci locations, magnitudes, and distributions. Specifically, given a constant oxygenation change, the signal changes across voxels will depend on regional vascular differences. Assuming that hypercapnia and neuronal activation cause similar hemodynamic events; one global and the other local, then division of a "fractional change during brain activation" image by a "fractional change during hypercapnia" image would give a ratio map that is normalized to the signal change accompanying global vasodilatation.

10.4 METHODS

Sequential single shot gradient–echo echo–planar images containing the motor cortex were obtained at 1.5 T. Voxel volume = 3.75 x 3.75 x 5 mm^3, TE = 40 ms, TR = 2 sec. This study is of one subject, but involving seven trials. In all of seven trials, a time course of 120 sequential images were collected in 4 minutes each. Each trial was separated by a five minute rest period. The trials are listed below.

1 & 2: Hypoxia (breathing of 12% O$_2$) for a duration of 3 minutes, starting at 30 sec. No finger movement is performed.

3 & 4: Hypercapnia (breathing of 5% CO$_2$) for a duration of 3 minutes, starting at 30 sec. No finger movement is performed.

5: Cyclic bilateral finger movement (10 sec "on" and 20 sec "off") during the entire time course, while breathing room air.

6: Cyclic bilateral finger movement combined with hypoxia.

7: Cyclic bilateral finger movement combined with hypercapnia.

10.5 RESULTS TO PART 1

Figure 10.1a shows an anatomical echo–planar image of the slice chosen. Figure 10.1b shows a brain activation image obtained by calculation of the dot product or correlation of a reference function representing the expected activation–induced response with the time course of images from trial #5. Figures 10.1c and 10.1d show images obtained by subtraction of the average of images #10 to #20 (baseline) from the average of images #40 to #120 in time courses of trials #1 and #2 (hypoxia) respectively. Figures 10.1e

and 10.1f show images obtained by subtraction of the average of images #10 to #20 (baseline) from the average of images #40 to #120 in time course series from trials #3 and #4 (hypercapnia) respectively. The results are highly reproducible and show that the patterns of signal change during hypercapnia and hypoxia are similar in magnitude yet opposite in sign. Regions of highest blood volume (sinuses and other large vessels) appear to show the largest signal changes with the global stresses *and* during finger movement.
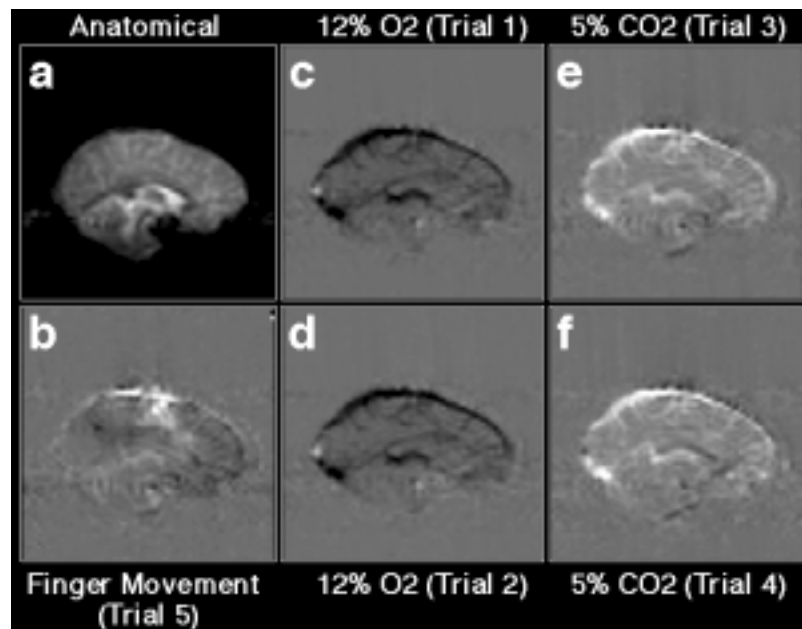
Figure 10.1: a. anatomical echo–planar image. **b.** brain activation image (finger movement) from trial 5 **c. & d.** average stress (hypoxia: image #40 to #120)– average baseline (image #10 to #20) from trials 1 & 2. **e. & f.** average stress (hypercapnia: image #40 to #120)–average baseline (image #10 to 20) from trials 3 & 4.

Time course plots from a single 15 voxel region of interest, corresponding to trials 1 through 4 are shown in Figure 10.2.
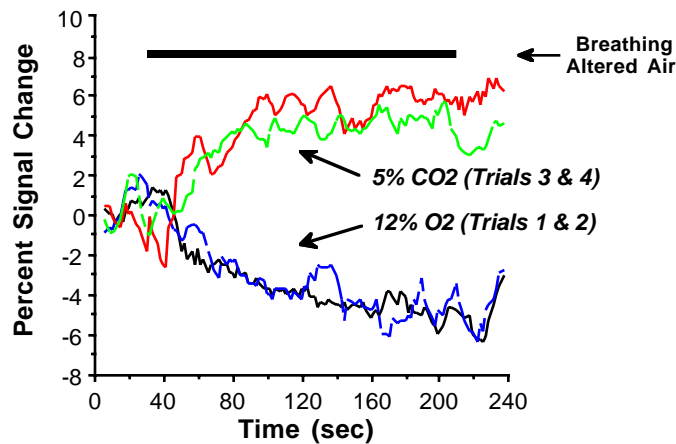
Figure 10.2: MR signal from 15 voxel region in motor cortex during two trials (trials 1 & 2) of hypoxia (12% O_2) and two trials (trials 3 & 4) of hypercapnia (5% CO_2).

During hypercapnia, a signal increase is observed, suggesting that an increase in flow without an increase in the oxygen extraction rate caused an overall increase in oxygenation. During hypoxia, the overall signal decreased, suggesting that the arterial oxygenation decreased without significant compensatory vasodilatation, thus causing the blood oxygenation to decrease. This study helps to further establish that these MR pulse sequences with these parameters are sensitive primarily to oxygenation changes and not to flow changes. If the pulse sequence were flow sensitive, it would be difficult to explain the signal drop with hypoxia, since hypoxia is known to not cause a decreases in flow but is known to cause a decrease in oxygenation.

Time course plots corresponding to trials 5 through 7 are shown in Figure 10.3.
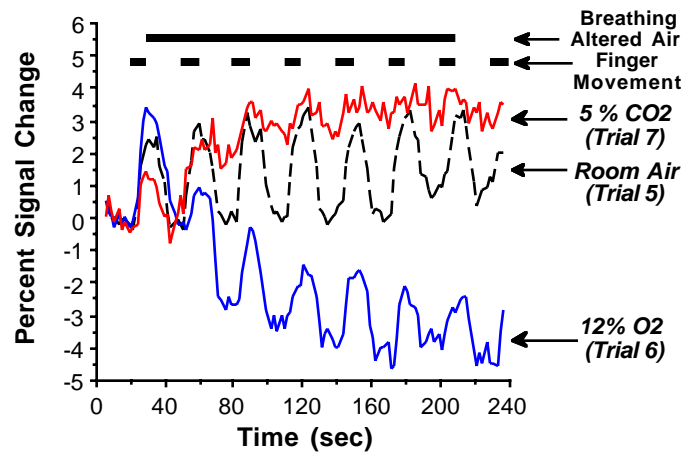
Figure 10.3: MR signal from a 15 voxel region in motor cortex during combinations of cyclic on–off finger movement and breathing room air (trial 5), finger movement and hypoxia (trial 6), finger movement and hypercapnia (trial 7).

The amplitude of the activation–induced signal change was significantly damped during hypercapnia. During hypoxia, the amplitude of the activation–induced signal change was only slightly damped, potentially supporting the hypothesis that because hypoxia does not cause significant increases in flow, it does not damp activation–induced signal changes. In addition, the evidence suggests either that a feedback mechanism for supplying an adequate oxygen supply during activation is either not strong or is nonexistent, since the fractional activation induced signal changes do not increase during a decreased steady state oxygenation level.

A voxel–wise comparison was also made between activation–induced signal changes (while breathing room air) and signal changes caused by hypoxia and hypercapnia (during no finger movement). A region demonstrating activation during cyclic finger movement was obtained from trial 5. This region was used as a mask in the voxel–wise comparison of activation–induced signal changes with hypoxia, and hypercapnia. Figure 10.4 shows the region obtained and the corresponding fractional signal changes corresponding to finger movement.
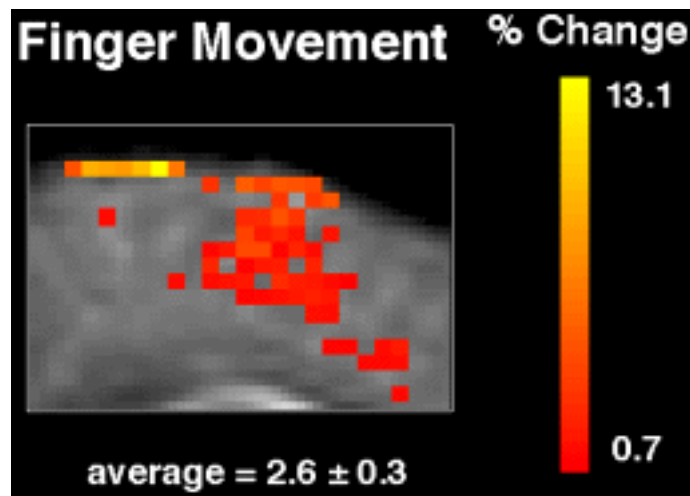
Figure 10.4: Region showing activation during finger movement. Note that largest fractional signal changes appear to be in the sagittal sinus.

Note that the highest signal changes appear to occur in the sagittal sinus. Figure 10.5 shows the fractional signal changes in the same region during hypoxia (trials 1 and 2) and hypercapnia (trials 3 and 4) respectively.
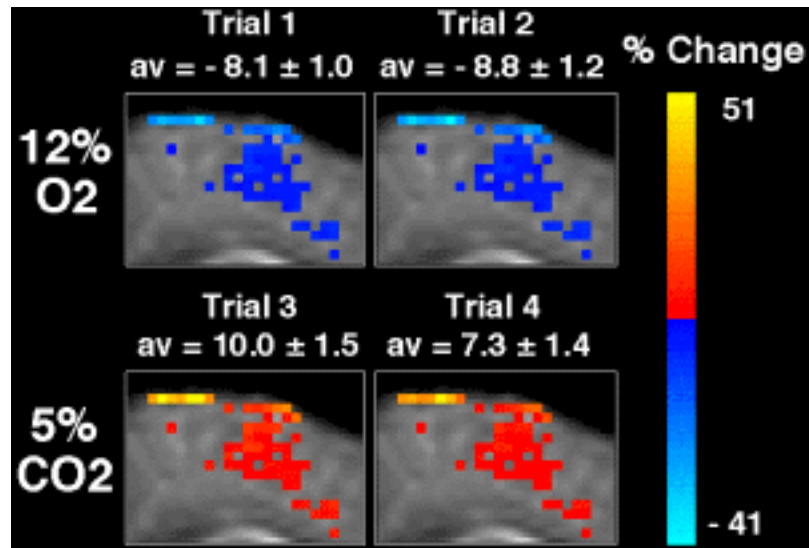
Figure 10.5 Fractional change during hypoxia (trials 1 and 2) and hypercapnia (trials 3 and 4) selectively observed *only in the voxels activated during trial 5* (finger movement only). Note the similar relative signal change magnitudes in all images to that shown in Figure 4 (finger movement only).

The magnitude of the signal changes during the hemodynamic stresses are higher than the changes in most pixels during finger movement, but the relative magnitudes of the signal changes within this region show an extremely similar pattern (i.e. highest changes in sagittal sinus).

Figure 10.6 is a voxel–wise comparison of signal change during finger movement with the signal changes during hypoxia (average of 1 & 2) or hypercapnia (average of 3 & 4).
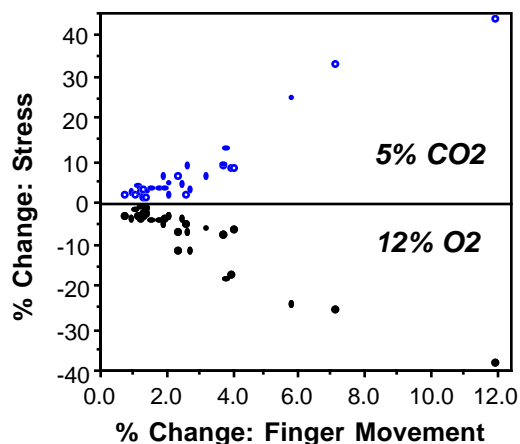
Figure 10.6: Voxel–wise comparison (32 voxels in motor cortex) of % change during finger movement (room air: trial 5) vs. % change during either hypoxia (average of trials 1 & 2) or hypercapnia (average of trials 3 & 4). The changes appear to be proportional to one another, suggesting that hemodynamic and vessel architecture differences primarily determine the relative signal change magnitudes.

Figure 10.7 is a voxel–wise plot of "fractional change during finger movement" vs. "fractional change during finger movement ÷ fractional change during hypercapnia" from 32 voxels in the region showing activation.

305
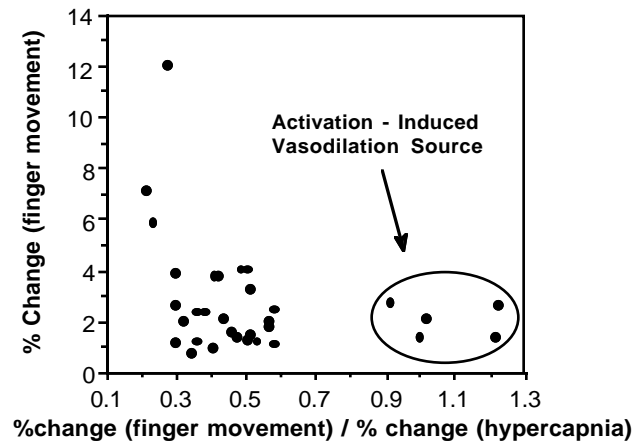
Figure 10.7: Voxel–wise comparison of "% change during finger movement" (y–axis)vs. % change during finger movement" ÷ "% change during finger hypercapnia" (x–axis). Voxels with the highest *normalized* change (x–axis) are hypothesized to be the source of activation–induced vasodilatation. The highest pre–normalized changes (y–axis) have low ratios.

Several voxels have a ratio ≈ 1. It is hypothesized that, in these voxels, the strongest activation–induced vasodilatation has taken place. Note that the largest changes prior to normalization (y–axis), have nearly the smallest ratios (x–axis), indicating that the actual activation–induced oxygenation change in these voxels may have been minimal (downstream), but possibly a large blood volume in these particular voxels has amplified the fractional signal change. The relative signal change magnitudes before and after division of the activation–induced fractional signal change map by the hypercapnia fractional signal change map, (here trial 4 is used), are shown in Figure 10.8.
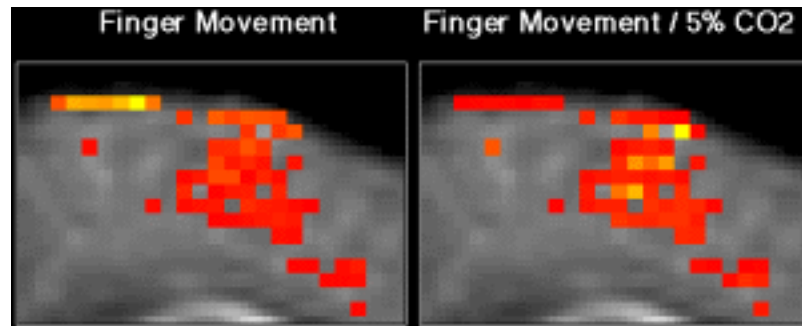
Figure 10.8: Brain activation map before and after division by a "% change during hypercapnia" mask. The highest signal change moves from the sagittal sinus to a region in cortex. It is hypothesized that this post processing step can eliminate the effects of relative spatial hemodynamics and vessel architecture differences from activation maps.

The region of highest signal change, after division by a "fractional change during hypercapnia" mask, has moved from the sagittal sinus to a region apparently in cortex.

10.7 DISCUSSION

Several conclusions may be drawn from this study. Positive and negative changes in global MR signal corresponded to changes in *oxygenation* with hypercapnia and hypoxia respectively and not to flow since, for both hypercapnia and hypoxia, flow increased (hypoxia is known to slightly increase flow rate if it changes flow at all). This, in itself, demonstrates higher sensitivity of this pulse sequences to oxygenation and not to flow changes. Hypercapnia increased the overall signal intensity, and damped activation–induced signal changes, demonstrating a competitive, and possibly identical, signal change mechanism as that caused by neuronal activation. These results

alone may suggest a feedback mechanism, but, in light of the hypoxia results, a feedback mechanism is unlikely. Hypoxia decreased overall signal intensity but did not as strongly damp the activation–induced signal changes as hypercapnia did. The lack of apparent competition with activation–induced signal changes is supported by the understanding that mild hypoxia does not cause large flow increases. Activation–induced signal change magnitudes (relative to absolute baseline) from an averaged ROI did not increase during trial 7 (activation with hypoxia), suggesting a lack of a strong feedback system in the regulation of cerebral blood oxygenation during activation.

Within the observed motor cortex region, the spatial pattern of signal change caused by finger movement was similar to the pattern created by the global stresses, suggesting that the primary cause for spatial variation in signal change during activation is spatial heterogeneity in hemodynamics and vessel architecture. The small gradient in blood oxygenation that extends away from the activation–induced source of vasodilatation only secondarily contributes to relative signal change differences. The implication is that brain activation maps created using gradient–echo sequences are highly blood volume weighted. This applies to maps obtained using spin–echo sequences as well when considering intravascular effects. Division of activation–induced fractional change maps by hypercapnia–induced fractional change maps removed the artifactual contributions to signal changes, leaving behind, as the highest signal intensity region, the area of activation–induced vasodilatation. This method may be necessary to increase the functional resolution (meaning the resolution with which one can distinguish discrete regions of activation–induced signal changes) of fMRI and, in the future, may be useful in quantification of activation–induced flow changes, assuming the ability to quantify global hypercapnia–induced flow changes.

CHAPTER 11

APPLICATIONS

11.1 INTRODUCTION

In the following chapter, several applications of fMRI using BOLD contrast are demonstrated. Primary and higher order activity associated with the motor, visual and auditory cortices are observed. First, whole brain and extended time course methods are used to map regions associated with the performance and imagination of complex finger movement tasks. Secondly, regions activated by reading, listening to spoken words, and generating words are also mapped.

11.2 GENERAL METHODOLOGY

All the studies presented in this chapter were performed using single shot 64 x 64 echo planar imaging (EPI) on a standard 1.5 Tesla GE Signa scanner. Figure 11.1 shows the setup as it would appear before the subject and coil are placed into the magnet. In spite of the apparent inaccessibility, visual and auditory stimuli are able to be presented to the subject.

Figure 11.1: Gradient and radio frequency coil setup with subject.

In all studies, sequential time series of susceptibility–weighted gradient–echo images (TE = 40 ms) were obtained. Single or multi–slice EPI was performed using time course series ranging from 64 to 1024 images. The TR value used ranged was from 1 to 2 seconds. The field of view was always 24 cm and the slice thickness ranged from 3 to 10 mm.

In all studies, brain activation tasks were presented in a repetitive on/off fashion for several cycles (from 2 to 12 cycles of approximately 8 to 20 sec "off" and 8 to 20 sec "on") throughout the EPI time course. Foci of brain activation were identified by cross correlation of the time course of each pixel with a reference wave form resembling the expected activation–induced response(220). Pixels having a temporal correlation coefficient below 0.4 to 0.6 were removed. These activation images were then colorized and

superimposed upon high resolution anatomical scans of the same slice obtained in the same imaging session.

11.3 MAPPING OF COMPLEX MOTOR CONTROL

During the past decade, an increase in cerebral blood flow in the primary and non–primary motor cortex in response to voluntary movements has been demonstrated (22, 322, 332, 381-386). Roland et al. (385), showed that simple finger movements resulted in increases in regional cerebral blood flow confined to the contralateral sensorimotor hand region. In this study, it was also shown that performance of a complicated finger sequencing task, while also producing an increase in cerebral blood flow in the contralateral sensorimotor area, produced a cerebral blood flow increase in the supplementary motor area and bilateral premotor cortex. Imagination of the complex finger task performance produced cerebral blood flow changes within the supplementary motor area, but not within the primary sensorimotor cortex.

Previous work in fMRI has demonstrated contralateral activation, and to a smaller degree, ipsalateral activation of the primary motor cortex, especially in the non–dominant hand (173, 322, 332). Recently, a study (341) has demonstrated additional activation in the supplementary motor area and bilaterally in the premotor cortex associated with the task of tapping out specified finger sequences, termed "complex" finger movement. Activation was also observed in the supplementary motor area during mental rehearsal of complex finger movement tasks.

In the present study, cortical and subcortical regions activated by simple, complex, and mental rehearsal of complex finger tapping paradigms

were observed using extended time course (one slice) and multi–slice (whole brain) fMRI (230, 363). All tasks were performed in a repetitive on/off manner. The on/off cycle length was 32 seconds. Simple finger movement involved tapping of fingers in no particular order against the patient table. Complex finger movement involved repetitively tapping out, for the duration of each activation time (16 seconds), a different five digit sequence (with numbers 1 through 5 representing each finger) presented at the onset of every activation cycle. Mental rehearsal of complex finger movement was performed using the same digit presentation paradigm as with complex finger movement. During mental rehearsal, the subject was instructed not to move in any manner.

11.4 SINGLE SLICE EXTENDED TIME COURSE ANALYSIS

In the single slice extended time course study, six finger movement paradigms were cyclically presented in six 320 second sections. One subject was studied. 960 axial images (slice thickness = 10 mm) of the same plane were collected (TR = 2 sec). The total time course duration was 1920 sec (32 minutes). During each section, the subject performed the specific paradigm for ten on/off cycles. Figure 11.2 is a high resolution anatomical image of the slice selected for the study. The time course signals from the seven indicated regions are shown in Figure 11.3, with the activation paradigm shown above each of the six sections.
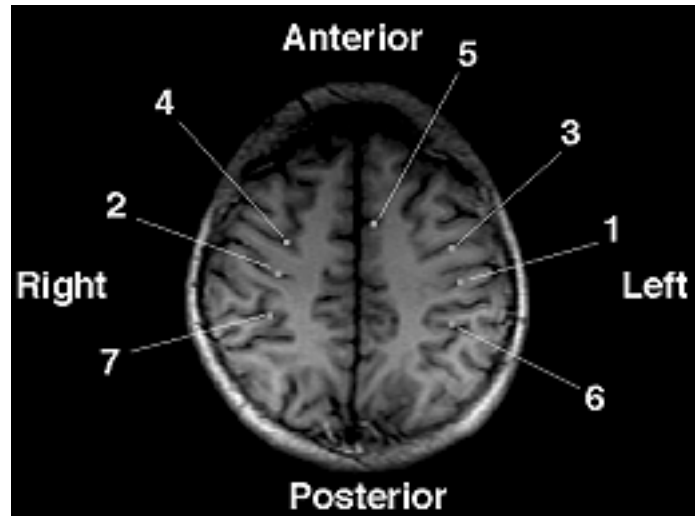
Figure 11.2: High resolution image of the axial slice selected for an extended time–course study in which a subject performed simple, complex, and imagination of complex finger movements on each hand during different periods of the same time course. The time courses of the indicated regions are shown in Figure 11.3.
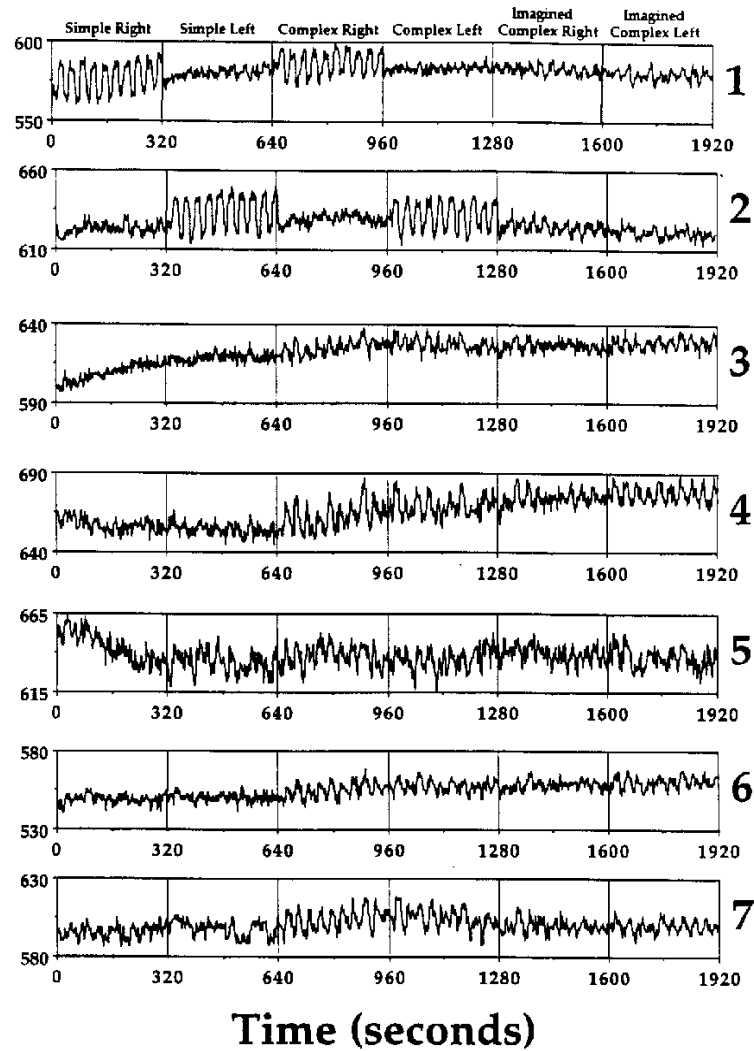
Figure 11.3: Signal intensity versus time from the regions in Figure 11.2. The 32 minute–long time course was divided into 6 sections of 160 images each. During each of the six sections, the subject performed the specific paradigm, indicated at the top, for ten on/off cycles, lasting 32 seconds each. Regions in the primary motor cortex [1 and 2] showed well behaved cyclic activation for the complex and imagined complex movement on the contralateral hand. Premotor [3 and 4], supplementary [5], and posterior parietal [6 and 7] regions showed increased cyclic activity, bilaterally, during the performed and imagined complex finger movement sections.

314

Functional images, shown in Figure 11.4, were created from the extended time course in the manner described in the general methodology section. The only difference was that the time course was divided into six sections corresponding to each paradigm, on each of which the cross correlation with a 160 point (320 second duration) reference waveform was calculated. Any pixels having a correlation coefficient below 0.4 were removed. The remaining pixels were used to create the brain activation images.
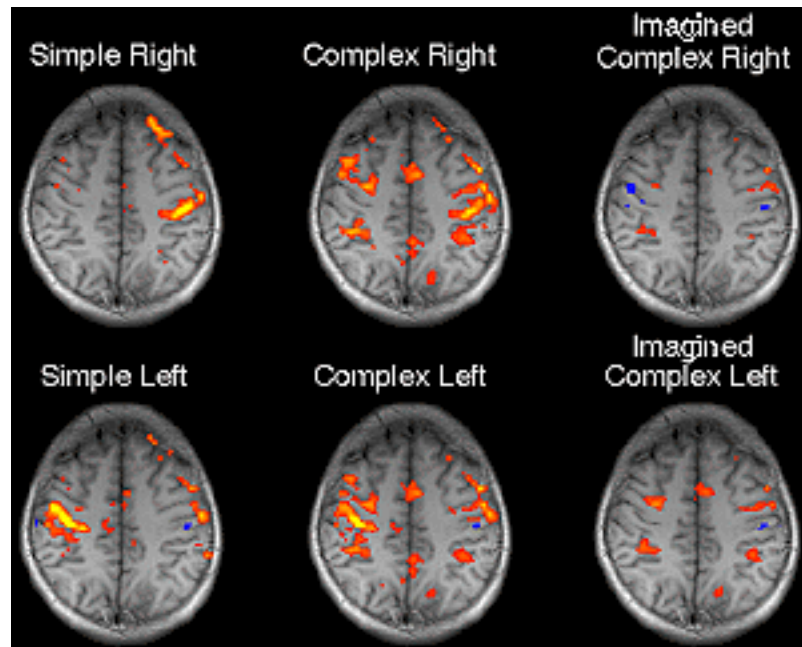
Figure 11.4: Axial brain activation images created from the study shown in Figures 11.2 and 11.3. The images of simple, complex, and mental rehearsal of complex finger movement were created by temporal cross–correlation of a reference waveform with each of the six segments of the time course shown in Figure 11.3.

It is helpful to observe the time courses in Figure 11.3 as well as the functional images in Figure 11.4 to obtain a better understanding of the spatial and dynamic characteristics of the signal changes corresponding with the particular tasks.

Regions 1 and 2 in Figure 11.2 are approximately in the left and right primary motor cortex. These regions demonstrated, in Figure 11.3, a strong and well–behave cyclic response on the contralateral side during both the simple and complex finger movement tasks. A small negative correlation was observed in primary motor cortex during the imagined tasks. It is hypothesized that tonic activation may actually have been inhibited in the primary motor cortex during imagination as the subject concentrated on *not* moving the fingers.

Regions 3 and 4 are approximately within the left and right pre motor cortex. Signal enhancement followed the time course during the complex and imagined complex tasks but not during the simple tasks. Also, the timing and amplitude of the activation–induced signal changes were not as high in amplitude nor as precisely time–locked as in the primary motor cortices. The functional images in Figure 11.4 illustrate bilateral activation of the premotor cortex during complex finger movement and imagined complex finger movement.

Region 5 is approximately in the supplementary motor area. The chosen slice may actually have been below most of the supplementary motor area, but activation–induced signal enhancement was still observed. It appears that the supplementary motor area was activated to some extent throughout the time course. The functional images in Figure 11.4 also show that complex and imagined complex finger movement caused more

activation in the supplementary motor area than did the simple finger movement tasks.

Regions 6 and 7 are in the posterior parietal region. Simple finger movement caused no activation in these regions, yet complex and imagined complex finger movement caused relatively strong signal changes. It is hypothesized that these regions may be involved with finger positional planning. The regions are posterior and medial to the primary sensory cortices. The functional images in Figure 11.4 illustrate that similar patterns of posterior parietal activation were manifested in the complex and imagined complex finger movement. These may also be activated by attentional or arousal mechanisms that may be more active during the complex finger movement and imagination sections.

Several other aspects of the functional images in Figure 11.4 are significant. Simple right finger movement caused mostly contralateral activation and minimal ipsalateral activation. Simple left finger movement caused a large amount of contralateral activation, but generally more ipsalateral activation than during simple right finger movement. The cortical activation patterns with complex left and right finger movements differed only in the primary motor cortex region. Left and right complex finger movement demonstrated a similar activation pattern in the premotor, supplementary, and posterior parietal regions. Imagination of left and right finger movement resulted in similar cortical activation patterns regardless of the hand used. In addition, the pattern exhibited with imagination of the complex finger movement task was similar, other than in the primary motor cortex, to the complex finger movement task. The non–primary regions involved with planning, execution, and learning complex sequences of finger

317

movement were the same regardless of the hand on which the task was performed.

Lastly, during some simple and most during complex finger movement, correlated signal decreases tended to appear in the ipsalateral primary motor cortex. During imagined finger movement, correlated signal decreases appeared bilaterally in the primary motor cortex. Given that "artifactual" sources can be ruled out, it is not entirely clear exactly what a localized MR signal decrease (blood oxygenation decrease) during activation means. It is possible, that, given a tonic vasodilatory state, a "suppression" or decrease in local cortical activity may cause a decrease in flow without a decrease in oxidative metabolic rate, thus causing blood oxygenation to locally decrease.

11.5 ENTIRE BRAIN ANALYSIS

The use of single shot EPI in combination with a TR of 2 seconds allows for the extension of single slice acquisition to as many as 20 slices with no compromise in total imaging time or image quality. In the study presented, finger movement tasks were cyclically presented in separate time course series (TR = 2 sec) consisting of 100 images of each plane. The data set collected consisted of 10 sagittal slices (slice thickness = 8 mm) with an interplane spacing of 2 mm. For each of the time course series, a total of 1000 images were collected. In each time course series, the subject alternated 16 sec of activation with 16 sec baseline for six on/off cycles. The paradigms performed were the same as those described in the previous section. The results from the time course series involving simple, complex, and imagined complex finger movement on the right and left hands are shown.

Figure 11.5 shows the first echo–planar images in the time course series. Figures 11.6 through 11.8 show high resolution anatomical images with regions of activation superimposed in color. The slice sequence proceeds from a view of the left lateral aspect of the brain in panel 1 to the right lateral aspect in panel 10. Slices 5 and 6 straddle the midline, with slice 5 being positioned slightly closer to midline.
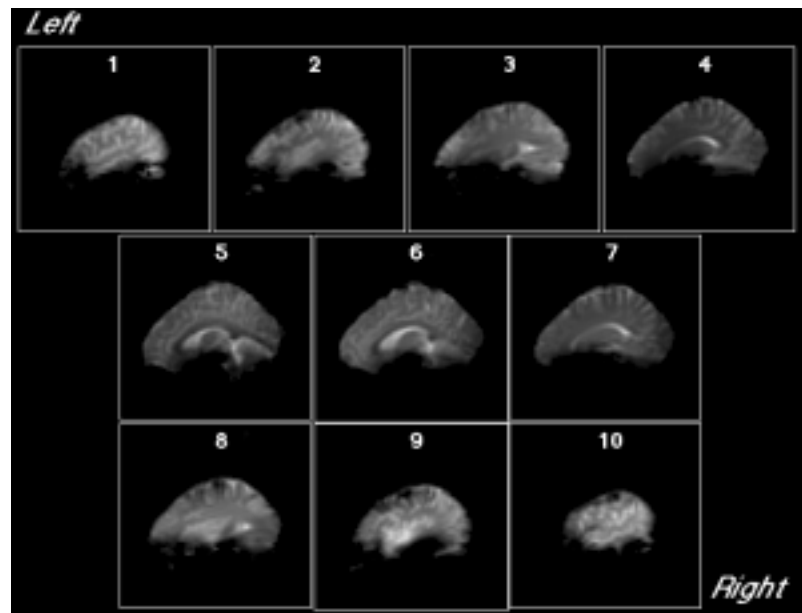
Figure 11.5: First echo planar images in the whole brain time course series.

Figures 11.6a and 11.6b show activation with simple finger movement on the right and left hands respectively. The contralateral motor cortex showed activation during simple finger movement. In addition, the cerebellum was activated on the ipsalateral side. Regions near the caudate nucleus of the basal ganglia also appeared to show activation. A small amount of activation was apparent in the supplementary motor area. Figures 11.7a and 11.7b show activation with complex finger movement on the right

and left hands respectively. More extensive activation was apparent both anterior and posterior to the primary motor cortex. Activation was also more extensive in the cerebellum and supplementary motor area. Activation in the premotor region and in the posterior parietal region was bilateral. Figures 11.8 a and 11.8 b shows activation with imagination of complex finger movement on the right and left hands respectively. Activation was apparent in the supplementary motor area and cerebellum.
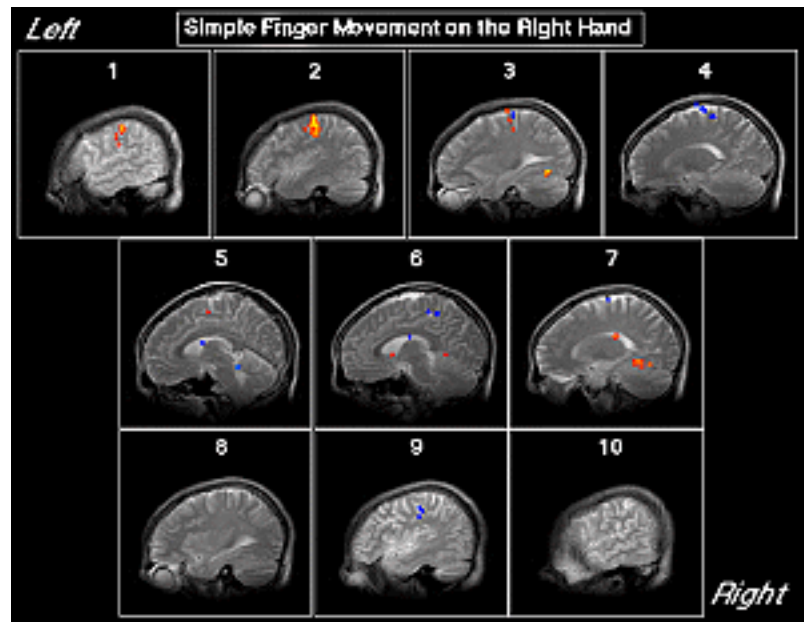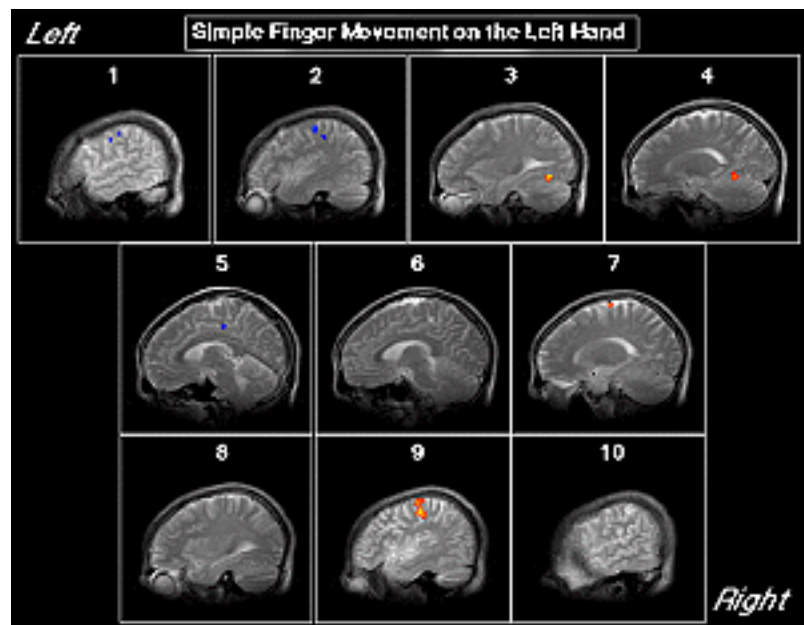
Figure 11.6: Sagittal brain activation images containing the entire brain. Simple finger movement was performed on the **a)** right and **b)** left hands respectively.
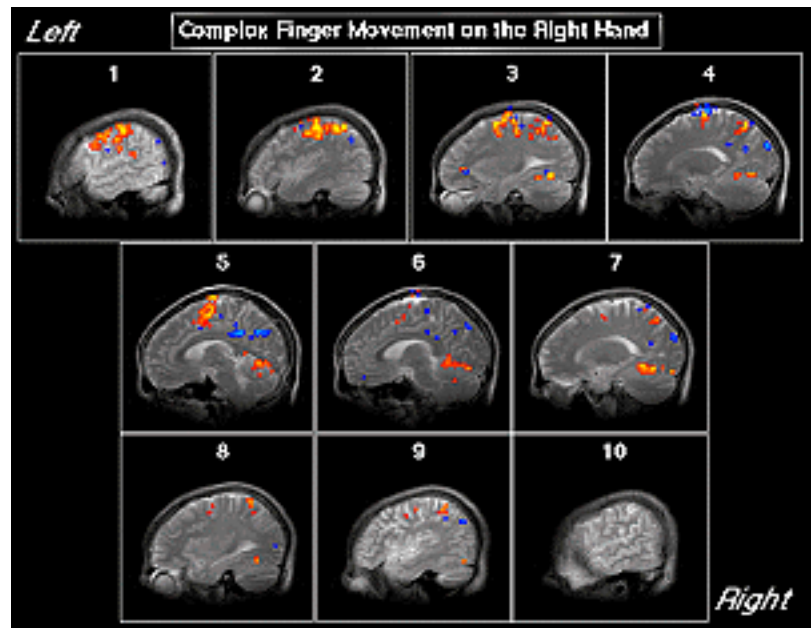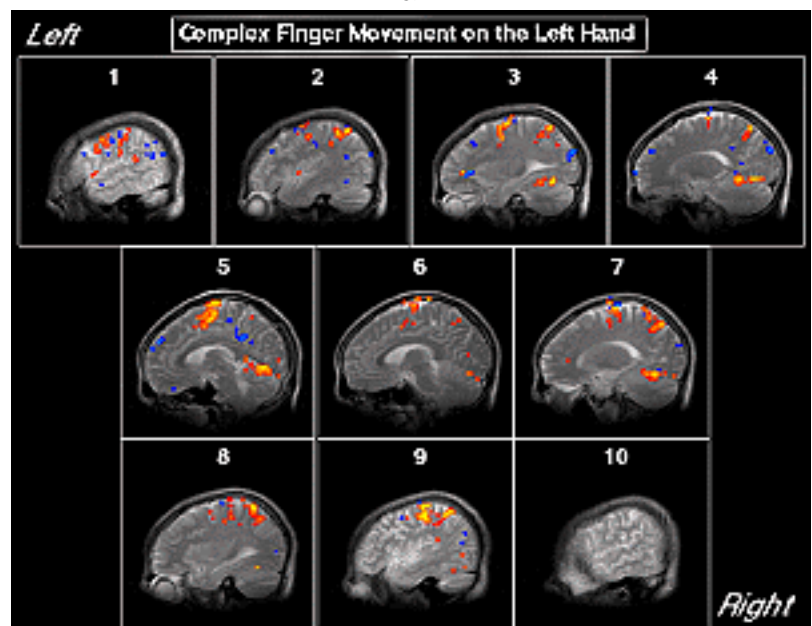
Figure 11.7: Sagittal brain activation images containing the entire brain. Complex finger movement was performed on the **a)** right and **b)** left hands respectively.
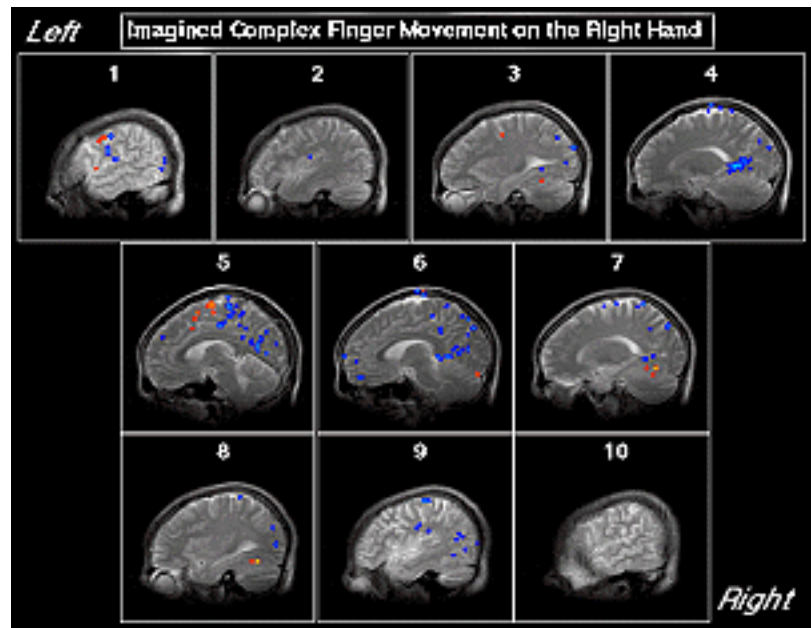
a
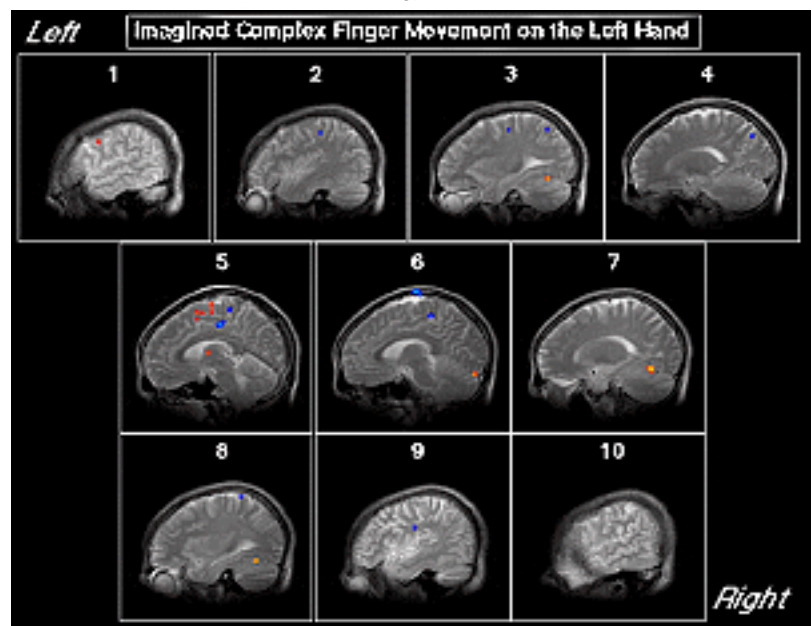
b

Figure 11.8: Sagittal brain activation images containing the entire brain. Imagination of complex finger movement was performed on the **a)** right and **b)** left hands respectively.

Non–primary regions activated during both complex finger movement and imagination of complex finger movement appeared to be common between hands.

It is possible to perform entire brain fMRI primarily because of the high sensitivity quadrature coil used and the ability to easily obtain high B_O homogeneity over a large volume at 1.5 Tesla. With the use of multislice EPI, a functional study of the entire brain involving an array of tasks and/or stimuli may be carried out in essentially the same amount of time as most standard clinical MRI scans.

Though susceptibility contrast is improved at higher field strengths, the pulse sequence, imaging hardware, system stability, and post–processing methodology also are extremely important in determining the quality of the brain activation images. From these results, it appears that susceptibility contrast is sufficient at 1.5 Tesla to carry out mapping of higher cognitive function in the human brain.

11.6 READING, LISTENING TO WORDS, AND GENERATING WORDS

In the above sections, results from carefully controlled experiments regarding higher order motor function were presented. In this section, data from three uncontrolled pilot experiments are presented demonstrating the ease with which activation–induced signal changes can be obtained in single studies using equipment already in place in most clinical scanners, (lights inside the bore and a patient intercom).

Two contiguous axial sections (slice thickness = 10 mm) through the auditory and visual cortices were obtained. During the sequential acquisition of 128 images (TR = 1 sec) for each of the two planes, stimuli were oscillated in

an on/off manner for five cycles. Each cycle consisted of 12 seconds of baseline and 12 seconds of activation. Functional images were created as described in the general methodology section. All pixels having a correlation coefficient below 0.4 were removed.

The activation tasks consisted of a) reading silently, b) listening to spoken words, and c) generating words that began with a letter spoken through the patient intercom at the onset of each cycle. During the baseline periods of the studies, the subject had eyes closed. During the active state of the first study, the subject silently read text, using only the light inside the scanner for illumination. During the active state of the second study, the subject listened to single syllable words spoken through the patient intercom. During the active state of the third study, the subject attempted to come of with as many words as possible that began with the letter heard at the beginning of the 12 second "on" period. To avoid motion artifacts and to avoid activating regions involved with mouth and tongue movement, the subject did not speak the words that were generated.

Figure 11.9 illustrates the activation images, through the same two sections, obtained by reading, listening to words, and word generation respectively. The left hemisphere is located on the right side of the image. The area activated during the reading tasks covered a region extending from the primary visual cortex anterior to the temporal lobes. Bilateral temporal lobe activation was observed during the listening task. Left hemisphere cortical regions and subcortical regions were activated during the word generation task. Also, some negative signal changes were observed. Some spatial overlap was also observed in activated regions.
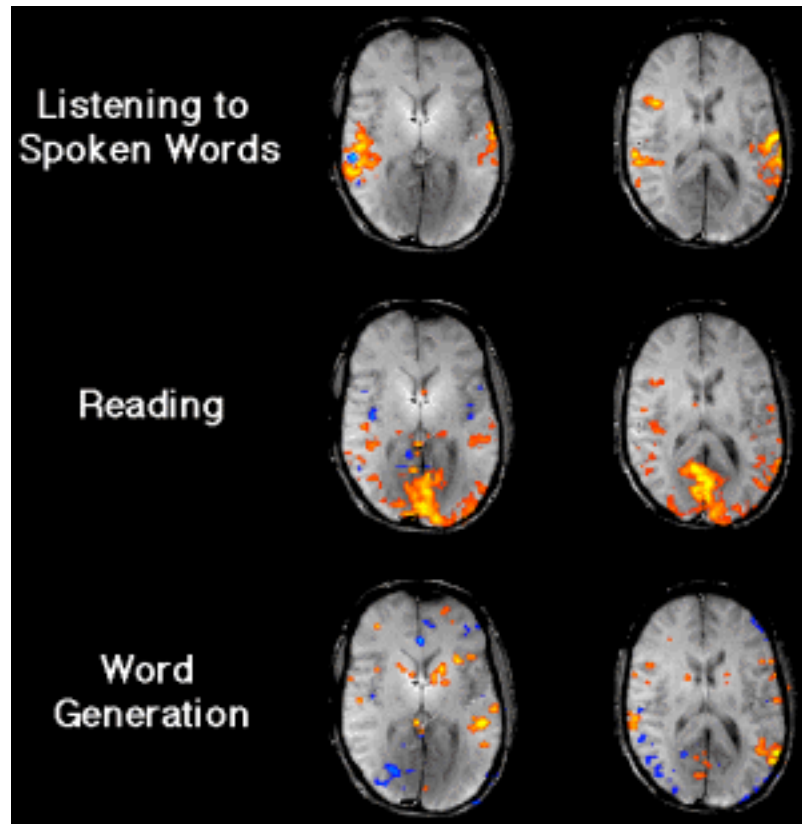
Figure 11.9: Axial brain activation images through the visual cortex and temporal lobe. The left hemisphere is located on the right side of the image. In the first row, the subject was reading text, using only the ambient light inside the scanner. In the second row, the subject was hearing words spoken through the intercom of the scanner. In the third row the subject was trying to come up with as many words as possible that started with a given letter. The subject did not speak the words.

11.7 DISCUSSION

Functional MRI using BOLD contrast is a relatively new method for observing brain activation. Accompanying the novelty of the technique are

many unknowns regarding the upper limits of spatial and temporal resolution as well as an unclear understanding of physiological and the biophysical mechanisms which regulate hemodynamic changes. In addition, the ways in which the hemodynamic changes affect the MR signal are incompletely understood. Nevertheless, the applications described here and elsewhere empirically establish the utility of this approach.

These studies have demonstrated only a few applications of BOLD contrast based fMRI to the understanding of human brain activation. Regions involved with performance and mental rehearsal of complex motor tasks have been imaged. Also regions activated by the tasks of reading and listening to spoken words have been observed.

Much additional work will be necessary to understand completely the precise nature of BOLD contrast. Nevertheless, it appears that fMRI using the BOLD approach holds great promise in uncovering unique and useful information about brain function and physiology.

CHAPTER 12

CONCLUSIONS

The work in this dissertation was directed primarily at the goal of understanding of the correlation between neuronal activation and MRI signal change characteristics. The MRI signal change location, distribution, and magnitude were observed as neuronal, physiologic, and MRI parameters were systematically modulated. These observations were also compared with a simulation which considered several potentially relevant MRI and physiological parameters. In addition, the implementation of post processing strategies and the application of fMRI in the context of brain function research were carried out.

12.1 DISSERTATION SUMMARY

Activation–induced signal change locations, while generally similar between contrast weightings, had small systematic differences that seem to suggest that particular contrast weightings are sensitive to underlying hemodynamic events that appear to occur in proximate but not identical locations.

Activation–induced signal change dynamics also demonstrated general similarities yet subtle differences across contrast weightings, tasks, and locations in the brain. The onset latency was generally longer than the return to baseline latency. A latency spread across tasks and across brain regions was observed. Brief activation times of 0.5 sec were detectable. The signal change magnitude stayed elevated during entire tonic activation times of up to 6

minutes. The hemodynamic response amplitude began to become reduced above on/off rates of 0.06 Hz., and did not follow the on/off timing (becoming saturated in the "on" state) above 0.13 Hz.

Post–processing strategies, tailored to the MRI signal change dynamics and based on cross–correlation methodology, were implemented. These techniques generally allow robust extraction of activation–induced MRI signal changes from a background that consists of noise and artifact that arise from pulsatile flow and motion, gross motion, system instabilities, and limitations in scanner hardware.

A biophysical/physiologic model was constructed to test the relative effects of physiologic and MRI parameters on activation–induced signal changes. A deterministic method involving repeated convolution and phase rotation was used to simulate the time evolution of diffusing spins in the presence of magnetic field distortions. The relative changes in transverse relaxation rates were measured as physiologic parameters (vessel radii, diffusion coefficient, blood oxygenation, vessel orientation, and blood volume) and MR parameters (field strength, pulse sequence, and TE) were modulated. The simulations showed a general agreement with the observed results, demonstrating the utility of the model and its potential future use. Specifically, the strongest effects on $\Delta R2^*$ and $\Delta R2$ were caused by changing blood volume, blood oxygenation, and field strength. The strongest effects on the $\Delta R2^*/\Delta R2$ ratio were caused by changing diffusion coefficient and the vessel radius.

Transverse relaxation rate changes, $\Delta R2^*$ and $\Delta R2$, were measured using either separate or combined gradient–echo and spin–echo sequences in which the TE was incremented. These measurements were then compared with the above–mentioned simulation and with the results of other models.

The average $\Delta R2^*/\Delta R2$ ratio, at 1.5 Tesla, was found to be 3.38 ± 0.12. This ratio suggests an "average" compartment size of 8 to 10 μm.

Using a combined spin–echo and gradient–echo sequence, the relaxation rates and rate changes were measured in a temporally and spatially registered manner by systematic variation of the TE during the time course collection of images. These results gave similar average $\Delta R2^*$ and $\Delta R2$ values as the studies using separate pulse sequences, but, in addition, demonstrated that, over a region of interest. much spatial heterogeneity of $\Delta R2^*/\Delta R2$ exists, suggesting differences in vessel radii across voxels.

Projection of the single exponential decay fits in the relaxation rate data (collected using up to 100 different TE data points) to TE = 0 allowed for simultaneous assessment of non–susceptibility contributions to the signal change. Using a TR of 1 sec, the non–susceptibility effects contributed, at most, an additional 0.5% to the signal change. This study demonstrated that, when using a TR of 1 sec, changes in transverse relaxation rate primarily contributed to the activation–induced MRI signal change.

The dependence of $\Delta R2^*$ from a region of interest on field strength was determined. Time course image collection was carried out at several TE values at 0.5 Tesla, 1.5 Tesla, and 3.0 Tesla. The dependence of $\Delta R2^*$ on field strength, from the region of interest, was determined to be approximately linear. The $\Delta R2^*/\Delta R2$ ratio at 3 Tesla was 3.31 ± 0.34. In agreement with the simulations, the dependence of the relaxation ratio was not strongly field strength dependent. The linear field strength dependence of $\Delta R2^*$ suggests that the predominant vessel size that contributes to the signal change has a radius greater than 20 μm, but the relaxation rate ratio data suggests a radius of about 8 μm to 10 μm. This discrepancy may be a result of the fact that measurements from regions of interest at different field strengths had vessel

size weightings which depended on the field strength, therefore skewing the results. At lower fields, only largest vessel effects (highest blood volume in the voxel) may have been detected, and, at high fields, more subtle effects, arising from smaller vessels may have been detected and averaged into the measurements. The possibility also exists that intravascular dephasing effects, not considered in the simulations, may be significant.

The effects of changing voxel volume, outer volume saturation, and TR and flip angle on activation–induced signal changes were determined. The active volume size decreased and the percent signal change increased with a decrease in voxel volume used, suggesting, under the assumption that contrast to noise was sufficient to detect all activation–induced signal changes at all voxel sizes, significant partial volume averaging of non–active tissue or non–vascularized tissue at larger voxel volumes.

Reduction of TR caused a slight increase in activation induced signal change. Reduction of flip angle, when using a small TR value, caused a decrease in activation induced signal change. The activation–induced signal changes were approximately proportional to the percentage difference between the signal in the imaging plane at steady state and the first image (TR $= \infty$) in the time course series, suggesting the contribution of inflow–effects at shorter TR. One other possible interpretation is that the partial volume averaging with cerebral spinal fluid was decreased at shorter TR values and lower flip angles (csf T1 > gray matter T1).

Outer volume RF saturation, which reduces the contribution of inflowing spins, had minimal effects, at a TR of 1 sec, on the activation–induced signal change. Some regions of high signal intensity changes were slightly reduced. In general, the lack of effect was in agreement with the previous data suggesting that, at a TR of 1 sec, inflow effects are minimal.

The effects of respiratory stresses of hypoxia and hypercapnia on resting MRI signal and activation–induced MRI signal changes (using T2*–weighted sequences) were observed. Hypoxia and hypercapnia caused positive and negative global signal changes, respectively, strongly suggesting that the signal change was proportional to blood oxygenation and not flow effects since oxygenation, and not flow, is reduced during hypoxia.

These global signal changes appeared to be proportional to blood volume. A voxel–wise comparison also demonstrated that the relative magnitude of the signal changes in an activated region of the brain and the magnitude of signal change during either of the stresses were proportional to one another, suggesting that the activation–induced signal changes are strongly weighted by relative blood volume across voxels. Assuming that hypercapnia and neuronal activation caused similar hemodynamic events; one global and one local, division of a "percent change during brain activation" image by a "percent change during hypercapnia" image gave a ratio map of task–induced activation which was normalized to the signal change accompanying global vasodilatation. Division of the activation image by the hypercapnia image caused the largest signal changes to move from the sagittal sinus to a region in cortex.

Hypercapnia also significantly reduced the relative activation–induced MRI signal changes, suggesting a competitive vasodilatation effect. Hypoxia did not as strongly decrease the activation–induced signal change. Hypoxia, within the values used, does not increase flow as much as hypercapnia does, therefore does not as highly suppress activation–induced signal changes.

Lastly, several applications of fMRI were demonstrated. These included whole brain and extended time course studies in which a comparison between regions activated during simple, complex, and mental

rehearsal of complex finger movement was made. In addition, regions activated by reading listening to spoken words, and word generation were observed. These studies demonstrated the utility of fMRI for use in human brain research.

12.2 FUTURE WORK

Co–evolution of fMRI Parts

The field of fMRI appears to have four highly interdependent and complementary parts, illustrated in Figure 12.1. These parts are co–evolving in that an advancement in one area will likely result in advancement in the other areas, and a lack of development in one area will either hinder advancement in the other areas or cause the other areas to compensate.
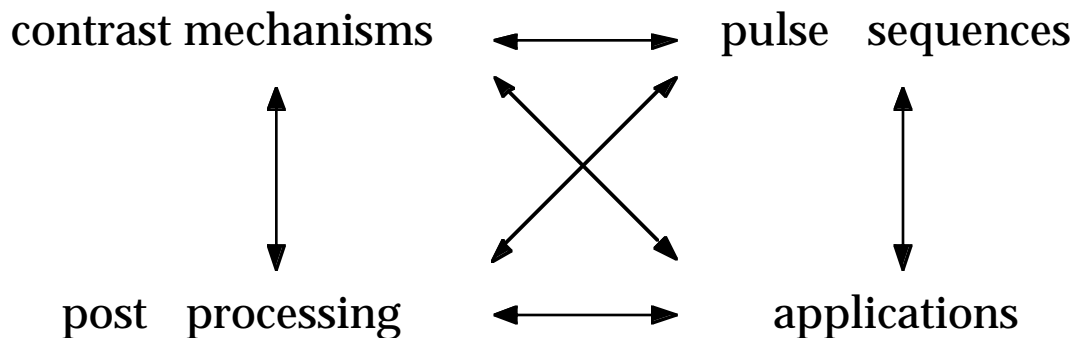
Figure 12.1: Schematic illustration of the four co–evolving fMRI parts.

An advancement in understanding of fMRI contrast mechanisms may likely a) lead to more sophisticated post processing methods which use more

a priori information, and therefore are more robust and powerful, b) lead to the development of pulse sequences which are tailored to selectively observe or suppress the specific type of contrast now understood more fully, and c) regarding all applications, will lead to more precise and insightful data interpretation and therefore the ability to perform more sophisticated neurological, pharmacologic, and clinical studies–knowing what signal changes are artifact and what changes contain information.

Pulse sequence development in itself may lead to a) unique strategies by which details of contrast mechanisms may be unraveled, or may allow higher contrast to noise, higher resolution, higher stability, and/or higher speed, therefore allowing more precise measurements to be made. b) the opportunity to implement more powerful post processing techniques, based on higher spatial or temporal resolution, and c) the implementation of applications that were previously impossible, because of pulse sequence related limitations.

The development of post–processing methods may allow for more powerful extraction of subtleties of the time course signal, lending itself to a) contrast mechanism research or b) applications. Pulse sequences that are tailored to specific types of contrast but lack sensitivity, etc.. may become more usable as a result of increased data extraction power arising from new post–processing methods.

As more applications are found for fMRI (clinical, neurological, pharmacological, physiological) more feedback will be provided to contrast–mechanism research, post–processing development, and pulse sequence development. More rapid feedback usually translates to more rapid evolution.

Each specific fMRI application will determine the supportive requirement in the other areas. For example, initial clinical applications may need whole brain coverage and minimal distortion, but may not need exquisitely high spatial resolution or sensitivity. Each of the four parts will evolve a specific set of minimal requirements for its development.

General fMRI Development

It is most certain that advancements will be made in fMRI primarily by improvements in contrast to noise. Contrast to noise is improved by either improving signal to noise (better RF coils, higher fields), contrast (contrast enhancement agents, higher fields), or by reduction of noise (filtering, motion correction/compensation). Improvements in fMRI contrast to noise will directly carry over into the improvements in resolution, sensitivity, and speed, which will translate into more robust and extensive applications .

Also, fMRI and other brain function monitoring methodologies may be combined in a synergistic fashion (such as EEG and fMRI) to explore high resolution spatial (fMRI) and temporal (EEG using fMRI localize activated regions) information therefore uncovering details of neural network relationships.

The development of activation paradigms tuned such that the unique characteristics of fMRI signal changes are optimally exploited and artifacts are optimally minimized is still in its infancy.

Revolutionary improvements are hard to predict. The amount of information in the time–course signal may be much larger than imagined. Careful study of the MRI signal in time and space over resting and activated states may provide revolutionary new directions in fMRI research.

The technique of fMRI is relatively fast, has relatively high resolution, and is non–invasive. Functional data is also registered with underlying anatomical data. Whole brain fMRI mapping is also possible. A unique "temporal resolution / spatial resolution / invasiveness" niche in brain function exploration methodologies is therefore filled by fMRI. Because of this niche, the probability for uncovering principles human brain function and development by fMRI appears quite high.

In general, fMRI is still in its infancy. Much needs to be done regarding: a) the uncovering of functional contrast mechanism details, b) the development of robust and rigorous post–processing methodologies, c) the development MR pulse sequences tailored to specific types of functional contrast or to specific types of applications, and d) the number and refinement of applications of fMRI in the exploration of the human brain.

References

1. P. E. Roland, "Brain Activation," Wiley-Liss, Inc., New York, 1993.

2. P. S. Churchland, T. J. Sejnowski, "The Computational Brain," MIT Press, Cambridge, 1992.

3. S. W. Kuffler, J. G. Nicholls, A. R. Martin, "From Neuron to Brain," Sinauer Associates Inc., Sunderland, MA, 1984.

4. K. Krnjevic, *in* "Brain Work" (D. H. Ingvar, N. A. Lassen, Eds.), p.65, Munksgaard, Copenhagen, 1975.

5. S. G. Hillyard, T. W. Picton, *in* "Handbook of Physiology, Section 1: Neurophysiology", p.519, American Physiological Society, New York, 1987.

6. R. Hari, On brain's magnetic responses to sensory stimuli. *J. Clinical Neurophysiology* **8**, 157-169 (1991).

7. L. Kaufman, S. J. Williamson, Magnetic location of cortical activity. *Annals of the New York Academy of Sciences* **388**, 197-213 (1982).

8. C. S. Roy, C. S. Sherrington, On the regulation of the blood-supply of the brain. *J. Physiol* **11**, 85-108 (1890).

9. F. Gotoh, K. Tanaka, *in* "Handbook of Clinical Neurology" (P. J. Vinkin, G. W. Bruyn, H. L. Klawans, Eds.), p. 47, Elsevier Science Publishing Co., Inc., New York, 1987.

10. W. Kushinsky, Coupling between functional activity, metabolism, and blood flow in the brain: state of the art. *Microcirculation* **2**, 357-378 (1982-1983).

11. D. W. Busija, D. D. Heistad, "Factors Involved in the Physiological Regulation of the Cerebral Circulation," Springer Verlag, Berlin, 1984.

12. M. Ursino, Mechanisms of cerebral blood flow regulation. *Critical Reviews in Biomedical Engineering* **18**, 255-288 (1991).

13. H. C. Lou, L. Edvinsson, E. T. MacKenzie, The concept of coupling blood flow to brain function: revision required? *Ann Neurol* **22**, 289-297 (1987).

14. W. Kuschinsky, Physiology of cerebral blood flow and metabolism. *Arzneimittel-Forschung* **41**, 284-288 (1991).

15. C. Estrada, E. Mengual, C. Gonzalez, Local NADPH-diaphorase neurons innervate pial arteries and lie close or project to intracerebral blood vessels: a possible role for nitric oxide in the regulation of cerebral blood flow. *J. Cereb. Blood Flow Metab.* **13**, 978-984 (1993).

16. Y. E. Moskalenko, G. B. Weinstein, I. T. Demchenko, Y. Y. Kislyakov, A. I. Krivchenko, "Biophysical Aspects of Cerebral Circulation," Pergamon Press, Oxford, 1980.

17. U. Dirnagl, U. Lindauer, A.Villringer, Role of nitric oxide in the coupling of cerebral blood flow to neuronal activation in rats. *Neuroscience Letters* **149**, 43-46 (1993).

18. C. Iadecola, Regulation of cerebral microcirculaton during neural activity: is nitric oxide the missing link? *TINS* **16**, 206-214 (1993).

19. G. Mchedlishvili, "Arterial Behavior and Blood Circulation in the Brain," Plenum Press, New York, 1986.

20. D. H. Ingvar, *in* "Brain Work" (D. H. Ingvar, N. A. Lassen, Eds.), p.397, Munksgaard, Copenhagen, 1975.

21. S. T. Grafton, R. P. Woods, J. C. Mazziotta, M. E. Phelps, Somatotopic mapping of the primary motor cortex in humans: activation studies with cerebral blood flow and positron emission tomography. *J. Neurophysiol* **66**, 735-743 (1991).

22. J. G. Colebatch, M.-P. Deiber, R. E. Passingham, K. J. Friston, R. S. J. Frackowiack, Regional cerebral blood flow during voluntary arm and hand movements in human subjects. *J. Neurophysiol* **65**, 1392-1401 (1991).

23. P. T. Fox, M. E. Raichle, Stimulus rate determines regional brain blood flow in striate cortex. *Ann. Neurol* **17**, 303-305 (1985).

24. P. T. Fox, M. E. Raichle, Stimulus rate dependence of regional cerebral blood flow in human striate cortex, demonstrated by positron emission tomography. *J. Neurophysiol* **51**, 1109-1120 (1991).

25. O. G. Cameron, J. G. Modell, R. D. Hichwa, B. W. Agranoff, R. A. Koeppe, Changes in sensory-cognitive input: effects on cerebral blood flow. *J. Cereb. Blood Flow Metab* **10**, 38-42 (1990).

26. C. A. Sandman, J. P. O'Halloran, R. Isenhart, Is there an evoked vascular response? *Science* **224**, 1355-1356 (1984).

27. J. W. Belliveau, D. N. Kennedy, R. C. McKinstry, B. R. Buchbinder, R. M. Weisskoff, M. S. Cohen, J. M. Vevea, T. J. Brady, B. R. Rosen, Functional mapping of the human visual cortex by magnetic resonance imaging. *Science* **254**, 716-719 (1991).

28. A. Villringer, J. Planck, C. Hock, L. Scheinkofer, U. Dirnagl, Near infrared spectroscopy (NIRS): a new tool to study hemodynamic changes during activation of brain function in human adults. *Neuroscience Letters* **154**, 101-104 (1993).

29. P. T. Fox, M. E. Raichle, Focal physiological uncoupling of cerebral blood flow and oxidative metabolism during somatosensory stimulation in human subjects. *Proc. Natl. Acad. Sci. USA* **83**, 1140-1144 (1986).

30. R. D. Frostig, E. E. Lieke, D. Y. Ts'o, A. Grinvald, Cortical functional architecture and local coupling between neuronal activity and the microcirculation revealed by in vivo high-resolution optical imaging of intrinsic signals. *Proc. Natl. Acad. Sci. USA* **87**, 6082-6086 (1990).

31. A. Grinvald, R. D. Frostig, R. M. Siegel, E. Bratfeld, High - resolution optical imaging of functional brain architecture in the awake monkey. *Proc. Natl. Acad. Sci. USA* **88**, 11559 - 11563 (1991).

32. R. D. Frostig, *in* "Cerebral Cortex, vol. 10" (A. Peters, K. S. Rockland, Eds.), p.331, Plenum Press, New York, 1994.

33. H. Chertkow, D. Bub, *in* "Localization and Neuroimaging in Neuropsychology" (A. Kertesz, Ed.), p.151, Academic Press, San Diego, 1994.

34. S. E. Peterson, P. T. Fox, M. I. Posner, M. Mintun, M. E. Raichle, Positron emission tomographic studies of the cortical anatomy of single-word processing. *Nature* **331**, 585-589 (1988).

35. P. T. Fox, M. A. Mintun, M. E. Raichle, F. M. Miezin, J. A. Allman, D. C. V. Essen, Mapping the visual cortex with positron emission tomography. *Nature* **323**, 806-809 (1986).

36. P. T. Fox, F. M. Miezin, J. M. Allman, D. C. V. Essen, M. E. Raichle, Retinotopic organization of human visual cortex mapped with positron - emission tomography. *The Journal of Neuroscience* **7**, 913-922 (1987).

37. M. E. Raichle, Positron emission tomography. *Ann. Rev. Neurosci.* **6**, 249-267 (1983).

38. M. E. Phelps, J. C. Mazziotta, Positron emission tomography: Human brain function and biochemistry. *Science* 799-809 (1985).

39. W. Lang, D. Cheyne, R. Kristeva, G. Lindinger, L. Deeke, *in* "Event-Related Brain Research" (C. H. M. Brunia, G. Mulder, M. N. Verbaten, Eds.), p.97, Elsevier Science Publishers, 1991.

40. E. J. Potchen, M. J. Potchen, The imaging of brain function: positron emission tomography, single-photon emission computed tomography, and some prospects for magnetic resonance. *Invest. Radiol.* **26**, 258-265 (1990).

41. S. J. Williamson, Z. L. Lu, D. Karron, L. Kaufman, Advantages and limitations of magnetic source imaging. *Brain Topography* **4**, 169-180 (1991).

42. S. Sato, M. Balish, R. Muratore, Principles of magnetoencephalography. *J. Clinical Neurophysiology* **8**, 144-156 (1991).

43. C. C. Gallen, D. F. Sobel, J. D. Lewine, J. A. Sanders, B. L. Hart, L. E. Davis, W. W. Orrison, Neuromagnetic mapping of brain function. Radiology. *Radiology* **187**, 863-867 (1993).

44. M. E. Brandt, Topographic mapping of brain electromagnetic signals: a review of current technology. *American Journal of Physiologic Imaging* **7**, 160-174 (1992).

45. P. K. Wong, Topographic representation of event-related potentials. *Electroencephalography & Clinical Neurophysiology* **S-42**, 5-12 (1991).

46. D. Swick, M. Kutas, H. J. Neville, *in* "Localization and Neuroimaging in Neuropsychology" (A. Kertesz, Ed.), p.73, Academic Press, San Diego, 1994.

47. I. A. Shevelev, E. N. Tsicalov, A. M. Gorbach, K. P. Budko, G. A. Sharaev, Thermoimaging of the brain. *J. Neuroscience Methods* **46**, 49-57 (1993).

48. I. A. Shevelev, Temperature topography of the brain cortex: thermoencephaloscopy. *Brain Topography* **5**, 77-85 (1992).

49. M. R. Nuwer, Intraoperative electroencephalography. *J. Clinical Neurophysiology* **10**, 437-444 (1993).

50. I. Fried, A. Katz, G. McCarthy, K. J. Sass, P. Williamson, S. S. Spence, D. D. Spencer, Functional organization of human supplementary motor cortex studied by electrical stimulation. *J. Neuroscience* **11**, 3656-3666 (1991).

51. W. Penfield, E. Boldrey, Somatic motor and sensory representation in the cerebral cortex of man as studied by electrical stimulation. *Brain* **60**, 389-443 (1937).

52. G. A. Ojemann, *in* "Localization and Neuroimaging in Neuropsychology" (A. Kertesz, Ed.), p.35, Academic Press, San Diego, 1994.

53. M. M. Haglund, G. A. Ojemann, D. W. Hochman, Optical imaging of epileptiform and functional activity in human cerebral cortex. *Nature* **358**, 668-671 (1992).

54. M. S. Gazzinga, Organization of the human brain. *Science* **245**, 947-952 (1989).

55. M. I. Posner, S. E. Peterson, P. T. Fox, M. E. Raichle, Localization of cognitive operations in the human brain. *Science* **240**, 1627-1631 (1988).

56. S. Zeki, S. Shipp, The functional logic of cortical connections. *Nature* **335**, 311-317 (1988).

57. S. Kosslyn, Aspects of a cognitive neuroscience of mental imagery. *Science* **240**, 1621-1626 (1988).

58. H. Damasio, A. R. Damasio, "Lesion Analysis in Neuropsychology," Oxford University Press, Oxford, 1989.

59. J. L. Haxby, C. L. Grady, L. G. Ungerleider, B. Horowitz, Mapping the functional neuroanatomy of the intact human brain with brain work imaging. *Neuropsychologia* **29**, 539-555 (1991).

60. J. C. Mazziotta, M. E. Phelps, *in* "Brain Imaging and Brain Function" (L. Sokoloff, Ed.), p.121, Raven Press, New York, 1985.

61. M. E. Phelps, D. E. Kuhl, J. C. Mazziotta, Metabolic mapping of the brain's response to visual stimulation: studies in humans. *Science* **211**, 1445-1448 (1981).

62. P. T. Fox, M. E. Raichle, M. A. Mintun, C. Dence, Nonoxidative glucose consumption during focal physiologic neural activity. *Science* **241**, 462- (1988).

63. K.-D. Merboldt, H. Bruhn, W. Hanicke, T. Michaelis, J. Frahm, Decrease of glucose in the human visual cortex during photic stimulation. *Magn. Reson. Med.* **25**, 187-194 (1992).

64. J. Prichard, D. Rothman, E. Novotny, O. Petroff, T. Kuwabara, M. Avison, A. Howsman, C. Hanstock, R. Shulman, Lactate rise detected by 1H NMR in human visual cortex during physiologic stimulation. *Proc. Natl. Acad. Sci. USA* **88**, 5829-5831 (1991).

65. P. C. Lauterbur, Image formation by induced local interactions: examples employing nuclear magnetic resonance. *Nature* **242**, 190-191 (1973).

66. P. Mansfield, P. K. Grannell, NMR diffraction in solids ? *J. Phys. C., Solid State Phys* L422-L426 (1973).

67. P. Mansfield, P. K. Grannell, "Diffraction" and microscopy in solids and liquids by NMR. *Phys. Rev. B* **12**, 3618-3634 (1975).

68. P. Mansfield, P. G. Morris, "NMR Imaging in Biomedicine," Academic Press, New York, 1982.

69. P. G. Morris, "Nuclear Magnetic Resonance Imaging in Medicine and Biology," Oxford University Press, Oxford, 1986.

70. W. A. Edelstein, P. A. Bottomly, H. R. Hart, L. S. Smith, Signal, noise, and contrast in nuclear magnetic resonance (NMR) imaging. *J. Comput. Assist. Tomogr* **7**, 391-401 (1983).

71. I. R. Young, M. Burl, B. M. Bydder, Comparative efficiency of different pulse sequences in MR imaging. *J. Comput. Assist. Tomogr* **10**, 271-286 (1986).

72. R. A. Fox, P. W. Henson, A general method for optimizing tissue discrimination in magnetic resonance imaging. *Med. Phys.* **13**, 635-643 (1986).

73. R. B. Buxton, R. R. Edelman, B. R. Rosen, G. L. Wismer, T. J. Brady, Contrast in rapid MR imaging: T1- and T2- weighted imaging. *J. Comput. Assist. Tomogr* **11**, 7-16 (1987).

74. F. W. Wehrli, J. R. MacFall, G. H. Glover, N. Grigsby, V. Haughton, J. Johanson, The dependence of nuclear magnetic resonance (NMR) image contrast on intrinsic and pulse sequence timing parameters. *J. Magn. Reson. Imag.* **2**, 3-16 (1984).

75. C. T. W. Moonen, P. C. M. vanZijl, J. A. Frank, D. LeBihan, E. D. Becker, Functional Magnetic Resonance Imaging in Medicine and Physiology. *Science* **250**, 53-61 (1990).

76. R. R. Edelman, H. P. Mattle, D. J. Atkinson, H. M. Hoogewood, MR angiography. *AJR* **154**, 937-946 (1990).

77. J. Listerud, First principles of magnetic resonance angiography. *Magn. Reson. Quart.* **7**, 136-170 (1991).

78. SMRM workshop: magnetic resonance imaging of blood flow. *Magn. Reson. Med.* **14**, 171-315 (1990).

79. H. Y. Carr, E. M. Purcell, Effects of diffusion on free procession in nuclear magnetic resonance experiments. *Phys. Rev.* **94**, 630-635 (1954).

80. E. O. Stejskal, J. E. Tanner, Spin-diffusion measurements: spin echoes in the presence of a time-dependent field gradient. *J. Chem. Phys.* **42**, 288-292 (1965).

81. D. LeBihan, R. Turner, C. T. Moonen, J. Pekar, Imaging of diffusion and microcirculation with gradient sensitization: design, strategy, and significance. *JMRI* **1**, 7-28 (1991).

82. D. LeBihan, E. Breton, D. Lallemand, M.-L. Aubin, J. Vignaud, M. Laval-Jeantet, Separation of diffusion and perfusion in intravoxel incoherent motion MR imaging. *Radiology* **168**, 497-505 (1988).

83. SMRM workshop: future directions in MRI of diffusion and perfusion. *Magn. Reson. Med* **19**, 209-333 (1991).

84. D. LeBihan, Magnetic resonance imaging of perfusion. *Magn. Reson. Med.* **14**, 283-292 (1990).

85. J. A. Detre, J. S. Leigh, D. S. WIlliams, A. P. Koretsky, Perfusion imaging. *Magn. Reson. Med.* **23**, 37-45 (1992).

86. D. LeBihan, Theoretical principles of perfusion imaging: applications to magnetic resonance imaging. *Invest Radiol* **27**, S6-S11 (1992).

87. J. A. Detre, W. Zhang, D. A. Roberts, A. C. Silva, D. S. Williams, D. J. Grandis, A. P. Koretsky, J. S. Leigh, Tissue - specific perfusion imaging using arterial spin labeling. *NMR in Biomedicine* **7**, 75-82 (1994).

88. R. R. Edelman, B. Sievert, P. Wielopolski, J. Pearlman, S. Warach, Noninvasive mapping of cerebral perfusion by using EPISTAR MR angiography. *JMRI* **4(P), [Abstr.]**, 68 (1994).

89. R. Edelman, P. Wielopolski, F. Schmitt, Echo-planar MR imaging. *Radiology* **192**, 600-612 (1994).

90. R. R. Edelman, B. Siewert, M. Adamis, J. Gaa, G. Laub, P. Wielopolski, Signal targeting with alternating radiofrequency (STAR) sequences: application to MR angiography. *Magn. Reson. Med.* **31**, 233-238 (1994).

91. S. D. Wolff, R. S. Balaban, Magnetization transfer tcontrast (MTC) and tissue water proton relaxation in vivo. *Magn. Reson. Med.* **10**, 135-144 (1989).

92. R. S. Balaban, T. L. Ceckler, Magnetization transfer contrast imaging. *Magn. Reson. Quart.* 116-137 (1992).

93. T. R. Brown, B. M. Kincaid, K. Ugurbil, NMR chameical shift imaging in three dimensions. *Proc. Natl. Acad. Sci. USA* **79**, 3523-3526 (1982).

94. A. A. Maudsley, S. K. Hilal, W. H. Perman, H. E. Simon, Spatially resolved high resolution spectroscopy by "four dimensional" NMR. *J. Magn. Reson. Med.* **52**, 147-151 (1983).

95. J. F. Schenck, Health and physiological effects of human exposure to whole-body four-tesla magnetic fields during MRI. *Annals of the New York Academy of Sciences* **649**, 285-301 (1992).

96. L. Pauling, C. D. Coryell, The magnetic properties and structure of hemoglobin, oxyhemoglobin, and carbonmonoxyhemoglobin. *Proc. Natl. Acad. Sci. USA* **22**, 210-216 (1936).

97. K. R. Thulborn, J. C. Waterton, P. M. Matthews, G. K. Radda, Oxygenation dependence of the transverse relaxation time of water protons in whole blood at high field. *Biochim. Biophys. Acta.* **714**, 265-270 (1982).

98. K. M. Brindle, F. F. Brown, I. D. Campbell, C. Grathwohl, P. W. Kuchell, Application of spin-echo nuclear magnetic resonance to whole-cell systems. *Biochem. J.* **180**, 37-44 (1979).

99. R. A. Brooks, G. D. Chiro, Magnetic resonance imaging of stationary blood: a review. *Med. Phys* **14**, 903-913 (1987).

100. J. M. Gomori, R. J. Grossman, C. Yu-Ip, T. Asakura, NMR relaxation times of blood: dependence on field strength, oxidation state, and cell integrity. *Journal of Computer Assisted Tomography* **11**, 684-690 (1987).

101. N. A. Matwiyoff, C. Gasparovic, R. Mazurchuk, G. Matwiyoff, The line shapes of the water proton resonances of red blood cells containing carbonyl hemoglobin, deoxyhemoglobin, and methemoglobin: implications for the interpretation of proton MRI at 1.5 T and below. *Magn. Reson. Imag.* **8**, 295-301 (1990).

102. L. A. Hayman, J. J. Ford, K. H. Taber, A. Saleem, M. E. Round, R. N. Bryan, T2 effects of hemoglobin concentration: assessment with in vitro MR spectroscopy. *Magn. Reson. Imag.* **168**, 489-491 (1988).

103. P. A. Janick, D. B. Hackney, R. I. Grossman, T. Asakura, MR imaging of various oxidation states of intracellular and extracellular hemoglobin. *AJNR* **12**, 891-897 (1991).

104. G. A. Wright, D. G. Nishimura, A. Macovski, Flow-independent magnetic resonance projection angiography. *Magn. Reson. Med.* **17**, 126-140 (1991).

105. G. A. Wright, B. S. Hu, A. Macovski, Estimating oxygen saturation of blood in vivo with MR imaging at 1.5 T. *JMRI* **1**, 275-283 (1991).

106. K. R. Thulborn, T. J. Brady, Iron in magnetic resonance imaging of cerebral hemorrhage. *Magn. Reson. Quart.* **5**, 23-38 (1989).

107. B. E. Hoppel, R. M. Weisskoff, K. R. Thulborn, J. B. Moore, K. K. Kwong, B. R. Rosen, Measurement of regional blood oxygenation and cerebral hemodynamics. *Magn. Reson. Med* **30**, 715-723 (1993).

108. R. M. Weisskoff, S. Kiihne, MRI susceptometry: image - based measurement of absolute susceptibility of MR contrast agents and human blood. *Magn. Reson. Med.* **24**, 375-383 (1992).

109. R. B. Lauffer, Magnetic resonance contrast media: principles and progress. *Magn. Reson. Quart.* **6**, 65-84 (1990).

110. SMRM workshop: contrast enhanced magnetic resonance. *Magn. Reson. Med.* **22**, 177-378 (1991).

111. N. Bloembergen, E. M. Purcell, R. V. Pound, Relaxation effects in nuclear magnetic resonance absorption. *Phys. Rev.* **73**, 679 (1948).

112. B. R. Rosen, J. W. Belliveau, D. Chien, Perfusion imaging by nuclear magnetic resonance. *Magn. Reson. Quart* **5**, 263-281 (1989).

113. A. Villringer, B. R. Rosen, J. W. Belliveau, J. L. Ackerman, R. B. Lauffer, R. B. Buxton, Y.-S. Chao, V. J. Wedeen, T. J. Brady, Dynamic imaging with lanthanide chelates in normal brain: contrast due to magnetic susceptibility effects. *Magn. Reson. Med.* **6**, 164-174 (1988).

114. B. R. Rosen, J. W. Belliveau, J. M. Vevea, T. J. Brady, Perfusion imaging with NMR contrast agents. *Magn. Reson. Med.* **14**, 249-265 (1990).

115. K. M. Donahue, D. Burstein, W. J. Manning, M. L. Gray, Studies of Gd-DTPA relaxivity and proton exchange rates in tissue. *Magn. Reson. Med.* **32**, 66-76 (1994).

116. R. P. Kennan, J. Zhong, J. C. Gore, Intravascular susceptibility contrast mechanisms in tissues. *Magn. Reson. Med.* **31**, 9-21 (1994).

117. C. R. Fisel, J. L. Ackerman, R. B. Buxton, L. Garrido, J. W. Belliveau, B. R. Rosen, T. J. Brady, MR contrast due to microscopically heterogeneous magnetic susceptibility: numerical simulations and applications to cerebral physiology. *Magn. Reson. Med.* **17**, 336-347 (1991).

118. D. A. Yablonsky, E. M. Haacke, Theory of NMR signal behavior in magnetically inhomogenous tissues: the static dephasing regime. *Magn. Reson. Med* **32**, 749-763 (1994).

119. P. Gillis, S. H. Koenig, Transverse relaxation of solvent protons induced by magnetized spheres: applications to ferritin, erythrocytes, and magnetite. *Magn. Reson. Med.* **5**, 323-345 (1987).

120. P. A. Hardy, R. M. Henkleman, On the transverse relaxation rate enhancement induced by diffusion of spins through inhomogeneous fields. *Magn. Reson. Med.* **17**, 348-356 (1991).

121. P. A. Hardy, R. M. Henkleman, Transverse relaxation rate enhancement caused by magnetic particulates. *Magn. Reson. Imag* **7**, 265-275 (1989).

122. S. C.-K. Chu, Y. Xu, J. A. Balschi, C. S. S. Jr, Bulk magnetic susceptibility shifts in NMR studies of compartmentalized samples: use of paramagnetic reagents. *Magn. Reson. Med* **13**, 239-262 (1990).

123. R. M. Weisskoff, B. J. Hoppel, B. R. Rosen, Signal changes in dynamic contrast studies: theory and experiment in vivo. *JMRI* **2(P) [Abstr.]**, 77 (1992).

124. J. L. Boxerman, R. M. Weisskoff, B. E. Hoppel, B. R. Rosen, MR contrast due to microscopically heterogeneous magnetic susceptibility: cylindrical geometry, *in* "Proc., SMRM, 12th Annual Meeting, New York, 1993," p. 389.

125. W. B. Edmister, R. M. Weisskoff, Diffusion effects on T2 relaxation in microscopically inhomogeneous magnetic fields, *in* "Proc., SMRM, 12th Annual Meeting, New York, 1993," p. 799.

126. R. M. Weisskoff, C. S. Zuo, J. L. Boxerman, B. R. Rosen, Microscopic susceptibility variation and transverse relaxation: theory and experiment. *Magn. Reson. Med.* **31**, 601-610 (1994).

127. S. Ogawa, R. S. Menon, D. W. Tank, S.-G. Kim, H. Merkle, J. M. Ellerman, K. Ugurbil, Functional brain mapping by blood oxygenation level - dependent contrast magnetic resonance imaging: a comparison of signal characteristics with a biophysical model. *Biophysical J* **64**, 803-812 (1993).

128. E. C. Wong, P. A. Bandettini, A deterministic method for computer modelling of diffusion effects in MRI with application to BOLD contrast imaging, *in* "Proc., SMRM, 12th Annual Meeting, New York, 1993," p. 10.

129. C. S. Li, T. A. Frisk, M. B. Smith, Computer simulations of susceptibility effects: implications for lineshapes and frequency shifts in localized spectroscopy of the human head, *in* "Proc., SMRM, 12th Annual Meeting, New York, 1993," p. 912.

130. P. A. Bandettini, E. C. Wong, The effects of biophysical and physiologic parameters on brain activation - induced R2* and R2 changes: simulations using a deterministic diffusion model. *International Journal of Imaging Systems and Technology* (in press).

131. P. Gilles, S. Peto, F. Moiny, J. Mispelter, C.-A. Cuenod, Proton transverse nuclear magnetic relation in oxidized blood: a numerical approach. *Magn. Reson. Med.* **33**, 93-100 (1995).

132. S. Posse, Direct imaging of magnetic field gradients by group spin-echo selection. *Magn. Reson. Med* **25**, 12-29 (1992).

133. J. Lian, D. S. Williams, I. J. Lowe, Magnetic resonance imaging of diffusion in the presence of background gradients and imaging of background gradients. *J. Magn. Reson.* **106**, 65-74 (1994).

134. T. J. Mosher, M. B. Smith, Magnetic susceptibility measurement using a double-DANTE tagging (DDT) sequence. *Magn. Reson. Med.* **18**, 251-255 (1991).

135. J. Frahm, K.-D. Merboldt, W. Hanicke, Direct flash imaging of magnetic field inhomogeneities by gradient compensation. *Magn. Reson. Med* **6**, 474-480 (1988).

136. K. M. Ludke, P. Roschmann, R. Tishler, Susceptibility artefacts in NMR imaging. *Magn. Reson. Imag.* **3**, 329-343 (1985).

137. I. J. Cox, G. M. Bydder, D. G. Gadian, I. R. Young, E. Proctor, S. R. Williams, I. Harts, The effect of magnetic susceptibility variations in NMR imaging and NMR spectroscopy in vivo. *J. Magn. Reson.* **70**, 163-168 (1986).

138. J. C. Ford, F. W. Wehrli, H.-W. Chung, Magnetic field distribution in models of trabecular bone. *Magn. Reson. Med.* **30**, 373-379 (1993).

139. R. Bhagwandien, R. vanEe, R. Beersma, C. J. C. Bakker, M. A. Moerland, J. J. W. Lagendijk, Numerical analysis of the magnetic field for arbitrary magnetic susceptibility distributions in 2D. *Magn. Reson. Imag* **10**, 299-313 (1992).

140. S. Majumdar, Quantitative study of the susceptibility difference between trabecular bone and bone marrow: computer simulations. *Magn. Reson. Med.* **22**, 101-110 (1991).

141. S. Majumdar, J. C. Gore, Studies of diffusion in random fields produced by variations in susceptibility. *J. Magn. Reson.* **78**, 41-55 (1988).

142. D. T. Edmonds, M. R. Wormwald, Theory of resonance in magnetically inhomogeneous specimens and some useful calculations. *J. Magn. Reson.* **77**, 223-232 (1988).

143. F. W. Wehrli, J. C. Ford, M. Attie, H. Y. Kressel, F. S. Kaplan, Trabecular structure: preliminary application of MR interferometry. *Radiology* **179**, 615-621 (1991).

144. S. Majumdar, D. Thomasson, A. Shimakawa, H. K. Genant, Quantitation of the susceptibility difference between trabecular bone and bone marrow: experimental studies. *Magn. Reson. Med.* **22**, 111-127 (1991).

145. T. A. Case, C. H. Durney, D. C. Ailion, A. G. Cutillo, A. H. Morris, A mathematical model of diamagnetic line broadening in lung tissue and similar heterogeneous systems: calculations and measurements. *J. Magn. Reson.* **73**, 304-314 (1987).

146. S. Ogawa, T.-M. Lee, A. S. Nayak, P. Glynn, Oxygenation - sensitive contrast in magnetic resonance image of rodent brain at high magnetic fields. *Magn. Reson. Med.* **14**, 68-78 (1990).

147. S. Ogawa, T.-M. Lee, Magnetic resonance imaging of blood vessels at high fields: in vivo and in vitro measurements and image simulation. *Magn. Reson. Med* **16**, 9-18 (1990).

148. H. M. Duvernoy, S. Delon, J. L. Vannson, Cortical blood vessels of the human brain. *Brain Research Bulletin* **7**, 519-579 (1981).

149. J. R. Ewing, C. A. Branch, J. A. Helpern, M. B. Smith, S. M. Butt, K. M. A. Welch, Cerebral blood flow measured by NMR indicator dilution in cats. *Stroke* **20**, 259-267 (1989).

150. J. J. H. Ackerman, C. S. Ewy, N. N. Becker, R. A. Shalwitz, Deuterium nuclear magnetic resonance measurements of blood flow and tissue

perfusion employing $2H_2O$ as a freely diffusable tracer. *Proc. Natl. Acad. Sci. USA* **84**, 4099-4102 (1987).

151. J. Pekar, L. Ligeti, Z. Ruttner, R. C. Lyon, T. M. Sinnwell, P. v. Gelderen, D. Fiat, C. T. W. Moonen, A. C. McLaughlin, In vivo measurement of cerebral oxygen consumption and blood flow using 17O magnetic resonance imaging. *Magn. Reson. Med.* **21**, 313-319 (1991).

152. K. K. Kwong, A. L. Hopkins, J. W. Belliveau, D. A. Chesler, L. M. Porkka, R. C. McKinstry, D. A. Finelli, G. J. Hunter, J. B. Moore, R. G. Barr, B. R. Rosen, Proton NMR imaging of cerebral blood flow using $H_2^{17}O$. *Magn. Res. Med.* **22**, 154-158 (1991).

153. J. W. Belliveau, B. R. Rosen, H. L. Kantor, R. R. Rzedzian, D. N. Kennedy, R. C. McKinstry, J. M. Vevea, M. S. Cohen, I. L. Pykett, T. J. Brady, Functional cerebral imaging by susceptibility-contrast NMR. *Magn. Reson. Med.* **14**, 538-546 (1990).

154. M. K. Stehling, R.Turner, P. Mansfield, Echo-planar imaging: magnetic resonance imaging in a fraction of a second. *Science* **254**, 43-50 (1991).

155. P. Mansfield, Multi-planar image formation using NMR spin echoes. *J. Phys.* **C10**, L55-L58 (1977).

156. A. Haase, J. Frahm, D. Matthaei, W. Haenicke, K.-D. Ferboldt, Flash imaging: rapid NMR imaging using low flip - angle pulses. *J. Magn. Reson* **67**, 258-266 (1986).

157. F. W. Wehrli, Fast-acan magnetic resonance: principles and applications. *Magn. Reson. Quart.* **6**, 165-236 (1990).

158. B. R. Rosen, J. W. Belliveau, H. J. Aronen, D. Kennedy, B. R. Buchbinder, A. Fischman, M. Gruber, J. Glas, R. M. Weisskoff, M. S. Cohen, F. H. Hochberg, T. J. Brady, Susceptibility contrast imaging of

cerebral blood volume: human experience. *Magn. Reson. Med.* **22**, 293-299 (1991).

159. J. W. Belliveau, D. N. Kennedy, R. C. Mckinstry, B. R. Buchbinder, R. M. Weisskoff, M. S. Cohen, J. M. Vevea, T. J. Brady, B. R. Rosen, Functional mapping of the human visual cortex by nuclear magnetic resonance imaging, *in* "Proc., SMRM, 10th Annual Meeting, San Francisco, 1991," p. 115.

160. T. J. Brady, Future prospects for MR imaging, *in* "Proc., SMRM, 10th Annual Meeting, San Francisco, 1991," p. 2.

161. K. K. Kwong, J. W. Belliveau, C. E. Stern, D. A. Chesler, I. E. Goldberg, B. P. Poncelet, D. N. Kennedy, R. M. Weisskoff, M. S. Cohen, R. Turner, H.-M. Cheng, T. J. Brady, B. R. Rosen, Functional MR imaging of primary visual and motor cortex. *JMRI* **2(P) [Abstr.]**, 76 (1992).

162. M. Stehling, M. Fang, R. Ladebeck, F. Schmitt, Functional echo-planar MR imaging at 1 T. *JMRI* **2(P) [Abstr.]**, 76 (1992).

163. P. A. Bandettini, E. C. Wong, R. S. Tikofsky, R. S. Hinks, J. S. Hyde, Echo-planar imaging of cerebral capillary percent deoxyhemoglobin change on task activation. *JMRI* **2(P) [Abstr.]**, 76 (1992).

164. S. Ogawa, T. M. Lee, Functional brain imaging with physiologically sensitive image signals. *JMRI* **2(P)-WIP suppliment, [Abstr.]**, S22 (1992).

165. K. Kwong, B. Hoppel, R. Weisskoff, S. Kiihne, B. Barrere, J. Moore, B. Poncelet, B. Rosen, K. Thulborn, Regional cerebral tissue oxygenation studied with EPI at clinical field strengths. *JMRI* **2(P), [Abstr.]**, 44 (1992).

166. A. J. deCrespigny, M. E. Moseley, M. F. Wendland, Echo-planar imaging of blood oxygenation contrast in focal ischemia of cat brain. *JMRI* **2(P)-WIP suppliment, [Abstr.]**, S4 (1992).

167. A. J. deCrespigny, M. Tsuura, M. E. Moseley, Gradient-echo imaging of blood oxygenation effects in locally ischemic rat brain at 4.7 T. *2(P)-WIP suppliment, [Abstr.]* **JMRI**, S23-S24 (1992).

168. S. Ogawa, T. M. Lee, A. R. Kay, D. W. Tank, Brain magnetic resonance imaging with contrast dependent on blood oxygenation. *Proc. Natl. Acad. Sci. USA* **87**, 9868-9872 (1990).

169. R. Turner, D. LeBihan, C. T. W. Moonen, D. Despres, J. Frank, Echo-planar time course MRI of cat brain oxygenation changes. *Magn. Reson. Med.* **27**, 159-166 (1991).

170. B. E. Hoppel, R. M. Weisskoff, K. R. Thulborn, J. Moore, B. R. Rosen, Measurement of regional brain oxygenation state using echo planar linewidth mapping, *in* "Proc., SMRM, 10th Annual Meeting, San Francisco, 1991," p. 308.

171. K. K. Kwong, J. W. Belliveau, D. A. Chesler, I. E. Goldberg, R. M. Weisskoff, B. P. Poncelet, D. N. Kennedy, B. E. Hoppel, M. S. Cohen, R. Turner, H. M. Cheng, T. J. Brady, B. R. Rosen, Dynamic magnetic resonance imaging of human brain activity during primary sensory stimulation. *Proc. Natl. Acad. Sci. USA.* **89**, 5675-5679 (1992).

172. S. Ogawa, D. W. Tank, R. Menon, J. M. Ellermann, S.-G. Kim, H. Merkle, K. Ugurbil, Intrinsic signal changes accompanying sensory stimulation: functional brain mapping with magnetic resonance imaging. *Proc. Natl. Acad. Sci. USA.* **89**, 5951-5955 (1992).

173. P. A. Bandettini, E. C. Wong, R. S. Hinks, R. S. Tikofsky, J. S. Hyde, Time course EPI of human brain function during task activation. *Magn. Reson. Med* **25**, 390-397 (1992).

174. P. A. Bandettini, E. C. Wong, R. S. Hinks, L. Estkowski, J. S. Hyde, Quantification of changes in relaxation rates $R2^*$ and $R2$ in activated

brain tissue, *in* "Proc., SMRM, 11th Annual Meeting, Berlin, 1992," p. 719.

175. P. A. Bandettini, E. C. Wong, L. Estkowski, R. S. Hinks, J. S. Hyde, Spin-echo echo-planar imaging of localized signal enhancement in the human brain during task activation. *JMRI* **3(P), [Abstr.]**, 63 (1993).

176. P. A. Bandettini, E. C. Wong, A. Jesmanowicz, R. S. Hinks, J. S. Hyde, Simultaneous mapping of activation - induced $\Delta R2^*$ and $\Delta R2$ in the human brain using a combined gradient-echo and spin-echo EPI pulse sequence, *in* "Proc., SMRM, 12th Annual Meeting, New York, 1993," p. 169.

177. J. Frahm, K.-D. Merboldt, W. Hanicke, Functional MRI of human brain activation at high spatial resolution. *Magn. Reson. Med.* **29**, 139-144 (1993).

178. R. S. Menon, S. Ogawa, D. W. Tank, K. Ugurbil, 4 tesla gradient recalled echo characteristics of photic stimulation - induced signal changes in the human primary visual cortex. *Magn. Reson. Med.* **30**, 380-386 (1993).

179. P. A. Bandettini, E. C. Wong, A. Jesmanowicz, R. S. Hinks, J. S. Hyde, Spin-echo and gradient-echo epi of human brain activation using BOLD contrast: a comparative study at 1.5 tesla. *NMR in Biomedicine* **7**, 12-19 (1994).

180. P. A. Bandettini, E. C. Wong, R. W. Cox, A. Jesmanowicz, R. S. Hinks, J. S. Hyde, Simultaneous assessment of blood oxygenation and flow contributions to activation induced signal changes in the human brain, *in* "Proc., SMR, 2nd Annual Meeting, San Francisco, 1994," p. 621.

181. A. M. Blamire, S. Ogawa, K. Ugurbil, D. Rothman, G. McCarthy, J. M. Ellermann, F. Hyder, Z. Rattner, R. G. Shulman, Dynamic mapping of

the human visual cortex by high-speed magnetic resonance imaging. *Proc. Natl. Acad. Sci. USA* **89**, 11069-11073 (1992).

182. J. Frahm, K.-D. Merboldt, W. Hanicke, A. Kleinschmidt, H. Boecker, Brain or vein-oxygenation or flow? On signal physiology in functional MRI of human brain activation. *NMR in Biomedicine* **7**, 45-53 (1994).

183. R. Turner, P. Jezzard, H. Wen, K. K. Kwong, D. L. Bihan, T. Zeffiro, R. S. Balaban, Functional mapping of the human visual cortex at 4 and 1.5 tesla using deoxygenation contrast EPI. *Magn. Reson. Med.* **29**, 277-279 (1993).

184. A. Jesmanowicz, P. A. Bandettini, E. C. Wong, G. Tan, J. S. Hyde, Spin-echo and gradient-echo EPI of human brain function at 3 Tesla, *in* "Proc., SMRM, 12th Annual Meeting, New York, 1993," p. 1390.

185. P. A. Bandettini, E. C. Wong, A. Jesmanowicz, R. Prost, R. W. Cox, R. S. Hinks, J. S. Hyde, MRI of human brain activation at 0.5 T, 1.5 T, and 3 T: comparisons of $\Delta R2^*$ and functional contrast to noise ratio, *in* "Proc., SMR, 2nd Annual Meeting, San Francisco, 1994," p. 434.

186. E. M. Haacke, A. Hopkins, S. Lai, P. Buckley, L. Friedman, H. Meltzer, P. Hedera, R. Friedland, L. Thompson, D. Detterman, J. Tkach, J. S. Lewin, 2D and 3D high resolution gradient-echo functional imaging of the brain: venous contributions to signal in motor cortex studies. *NMR in Biomedicine* **7**, 54-62 (1994).

187. S. Lai, A. L. Hopkins, E. M. Haacke, D. Li, B. A. Wasserman, P. Buckley, L. Friedman, H. Meltzer, P. Hedera, R. Friedland, Identification of vascular structures as a major source of signal contrast in high resolution 2D and 3D functional activation imaging of the motor cortex at 1.5T: preliminary results. *Magn. Reson. Med* **30**, 387-392 (1993).

188. J. R. Baker, M. S. Cohen, C. E. Stern, K. K. Kwong, J. W. Belliveau, B. R. Rosen, The effect of slice thickness and echo time on the detection of signal changes during echo-planar functional neruroimaging, *in* "Proc., SMRM, 11th Annual Meeting, Berlin, 1992," p. 1822.

189. J. H. Duyn, C. T. W. Moonen, G. H. vanYperen, R. W. d. Boer, P. R. Luyten, Inflow versus deoxyhemoglobin effects in BOLD functional MRI using gradient-echoes at 1.5 T. *NMR in Biomedicine* 7, 83-88 (1994).

190. J. L. Boxerman, P. A. Bandettini, K. K. Kwong, J. R. Baker, T. L. Davis, B. R. Rosen, R. M. Weisskoff, The intravascular contribution to fMRI signal change: monte carlo modeling and diffusion-weighted studies in vivo. *Magn. Reson. Med.* 34, 4-10 (1995).

191. A. W. Song, E. C. Wong, P. A. Bandettini, J. S. Hyde, The effect of diffusion weighting on task-induced functional MRI, *in* "Proc., SMR, 2nd Annual Meeting, San Francisco, 1994," p. 643.

192. J. L. Boxerman, R. M. Weisskoff, K. K. Kwong, T. L. Davis, B. R. Rosen, The intravascular contribution to fMRI signal change. Modeling and diffusion-weighted in vivo studies, *in* "Proc., SMR, 2nd Annual Meeting, San Francisco, 1994," p. 619.

193. R. S. Menon, X. Hu, G. Adriany, P. Anderson, S. Ogawa, K. Ugurbil, Comparison of spin-echo EPI, asymmetric spin-echo EPI and conventional EPI appled to functional neuroimaging. The effect of flow crushing gradients on the BOLD signal, *in* "Proc., SMR, 2nd Annual Meeting, San Francisco, 1994," p. 622.

194. H. Bruhn, A. Kleinschmidt, H. Boecker, K.-D. Merboldt, W. Hanicke, J. Frahm, The effect of acetazolamide on regional cerebral blood

oxygenation at rest and under stimulation as assessed by MRI. *J.Cereb Blood Flow Metab.* **14**, 742-748 (1994).

195. S. Ogawa, T. M. Lee, B. Barrere, The sensitivity of magnetic resonance image signals of a rat brain to changes in the cerebral venous blood oxygenation. *Magn. Reson. Med.* **29**, 205-210 (1993).

196. A. J. deCrespigny, M. F. Wendland, N. Derugin, E. Kozniewska, M. E. Moseley, Real - time observation of transient focal ischemia and hyperemia in cat brain. *Magn. Reson. Med.* **27**, 391-397 (1992).

197. A. J. deCrespigny, M. F. Wendland, N. Derugin, Z. S. Vexler, M. E. Moseley, Rapid MR imaging of a vascular challenge to focal ischemia in cat brain. *JMRI* **3**, 475-481 (1993).

198. P. A. Bandettini, E. A. Aaron, E. C. Wong, T. F. Lowry, R. S. Hinks, J. S. Hyde, H. V. Forster, Hypercapnia and hypoxia in the human brain: effects on resting and activation-induced MRI signal, *in* "Proc., SMR, 2nd Annual Meeting, San Francisco, 1994," p. 700.

199. F. Prielmeier, Y. Nagatomo, J. Frahm, Cerebral blood oxygenation in rat brain during hypoxic hypoxia. Quantitative MRI of effective transverse relaxation rates. *Magn. Reson. Med.* **31**, 678-681 (1994).

200. J. R. Binder, S. M. Rao, T. A. Hammeke, J. A. Frost, P. A. Bandettini, J. S. Hyde, Effects of stimulus rate on signal response during functional magnetic resonance imaging of auditory cortex. *Cognitive Brain Research* **2**, 31-38 (1994).

201. S. M. Rao, P. A. Bandettini, J. Bobholz, J. R. Binder, T. A. Hammeke, J. A. Frost, J. S. Hyde, Relationship between movement rate and functional magnetic resonance signal change in primary motor cortex. (submitted).

202. P. A. Bandettini, E. C. Wong, J. R. Binder, S. M. Rao, A. Jesmanowicz, E. A. Aaron, T. F. Lowry, H. V. Forster, R. S. Hinks, J. S. Hyde, *in* "Diffusion and Perfusion: Magnetic Resonance Imaging" (D. LeBihan, Ed.), pp. 335-349, Raven Press, New York, 1995.

203. P. A. Bandettini, E. C. Wong, E. A. DeYoe, J. R. Binder, S. M. Rao, D. Birzer, L. D. Estkowski, A. Jesmaniowicz, R. S. Hinks, J. S. Hyde, The functional dynamics of blood oxygen level dependent contrast in the motor cortex, *in* "Proc., SMRM, 12th Annual Meeting, New York, 1993," p. 1382.

204. P. A. Bandettini, *in* "Functional MRI of the Brain" , p.143, Society of Magnetic Resonance in Medicine, Berkeley, 1993.

205. A. T. Lee, G. H. Glover, C. H. Meyer, Discrimination of large venous vessels in time-course spiral blood-oxygen-level-dependent magntic-resonance functional neuroimaging. *Magn. Reson. Med.* **33**, 745 -754 (1995).

206. A. T. Lee, C. H. Meyer, G. H. Glover, Discrimination of large veins in time-course functional neuroimaging with spiral k-space trajectories. *JMRI* **3(P), [Abstr.]**, 59-60 (1993).

207. J. A. Sanders, J. D. Lewine, J. S. George, A. Caprihan, W. S. Orrison, Correlation of FMRI with MEG., *in* "Proc., SMRM, 12th Annual Meeting, New York, 1993," p. 1418.

208. A. Connelly, G. D. Jackson, R. S. J. Frackowiak, J. W. Belliveau, F. Vargha-Khadem, D. S. Gadian, Functional mapping of activated human primary cortex with a clinical MR imaging system. *Radiology* **188**, 125-130 (1993).

209. C. R. Jack, R. M. Thompson, R. K. Butts, F. W. Sharbrough, P. J. Kelly, D. P. Hanson, S. J. Riederer, R. L. Ehman, N. J. Hangiandreou, G. D.

Cascino, Sensory motor cortex: correlation of presurgical mapping with functional MR imaging and invasive cortical mapping. *Radiology* **190**, 85-92 (1994).

210. J. L. Boxerman, L. M. Hamberg, B. R. Rosen, R. M. Weisskoff, MR contrast due to intravascular magnetic susceptibility perturbations. *Magn. Reson. Med.* (in press).

211. B. E. Hoppel, J. R. Baker, R. M. Weisskoff, B. R. Rose, The dynamic response of $\Delta R2$ and $\Delta R2'$ during photic activation, *in* "Proc., SMRM, 12th Annual Meeting, New York, 1993," p. 1384.

212. R. Turner, P. Jezzard, D. L. Bihan, A. Prinster, Contrast mechanisms and vessel size effects in BOLD contrast functional neuroimaging, *in* "Proc., SMRM, 12th Annual Meeting, New York, 1993," p. 173.

213. K. K. Kwong, D. A. Chesler, C. S. Zuo, J. R. Baker, Y. C. Chen, R. M. Weisskoff, B. R. Rosen, Spin echo (T2, T1) studies for functional MRI, *in* "Proc., SMRM, 12th Annual Meeting, New York, 1993," p. 172.

214. S.-G. Kim, K. Hendrich, X. Hu, H. Merkle, K. Ugurbil, Potential pitfalls of functional MRI using conventional gradient-recalled echo techniques. *NMR in Biomedicine* **7**, 69-74 (1994).

215. J. V. Hajnal, A. G. Collins, S. J. White, J. M. Pennock, A. Oatridge, C. J. Baudouin, I. R. Young, G. M. Bydder, Imaging of human brain activity at 0.15 T using fluid attenuated inversion recovery (FLAIR) pulse sequences. *Magn. Reson. Med.* **30**, 650-653 (1993).

216. J. V. Hajnal, R. Myers, A. Oatridge, J. E. Schwieso, I. R. Young, G. M. Bydder, Artifacts due to stimulus correlated motion in functional imaging of the brain. *Magn. Reson. Med* **31**, 283-291 (1994).

217. D. S. Williams, J. A. Detre, J. S. Leigh, A. S. Koretsky, Magnetic resonance imaging of perfuusion using spin-inversion of arterial water. *Proc. Natl. Acad. Sci. USA* **89**, 212-216 (1992).

218. A. W. Song, J. C. Wu, E. C. Wong, J. S. Hyde, First-pass Gd-DTPA bolus injection with diffusion weighting in an animal model, *in* "Proc., SMR, 2nd Annual Meeting, San Francisco, 1994," p. 1385.

219. E. A. DeYoe, J. Neitz, P. A. Bandettini, E. C. Wong, J. S. Hyde, Time course of event-related MR signal enhancement in visual and motor cortex, *in* "Proc., SMRM, 11th Annual Meeting, Berlin, 1992," p. 1824.

220. P. A. Bandettini, A. Jesmanowicz, E. C. Wong, J. S. Hyde, Processing strategies for time-course data sets in functional MRI of the human brain. *Magn Reson. Med.* **30**, 161-173 (1993).

221. J. W. Belliveau, K. K. Kwong, D. N. Kennedy, J. R. Baker, R. Benson, D. A. Chesler, R. M. Weisskoff, M. S. Cohen, R. B. H. Tootell, P. T. Fox, T. J. Brady, B. R. Rosen, Magnetic resonance imaging mapping of brain function: human visual cortex. *Invest. Radiol.* **27**, S59-S65 (1992).

222. J. R. Binder, A. Jesmanowicz, S. M. Rao, P. A. Bandettini, T. A. Hammeke, J. S. Hyde, Analysis of phase differences in periodic functional MRI activation data, *in* "Proc., SMRM, 12th Annual Meeting, New York, 1993," p. 1383.

223. H. Wen, S. Wolff, K. Berman, R. Turner, M. Iadarolla, R. Balaban, Phase and magnitude functional imaging of motor tasks and pain stimuli, *in* "Proc., SMRM, 12th Annual Meeting, New York, 1993," p. 9.

224. A. Jesmanowicz, P. A. Bandettini, J. S. Hyde, Frequency shift artifacts in functional echo - planar imaging, *in* "Proc., SMR, 2nd Annual Meeting, San Francisco, 1994," p. 437.

225. J. R. Binder, S. M. Rao, T. A. Hammeke, P. A. Bandettini, A. Jesmanowicz, J. A. Frost, E. C. Wong, V. M. Haughton, J. S. Hyde, Temporal characteristics of functional magnetic resonance signal changes in lateral frontal and auditory cortex, *in* "Proc., SMRM, 12th Annual Meeting, New York, 1993," p. 5.

226. J. W. Belliveau, J. R. Baker, K. K. Kwong, B. R. Rosen, J. S. George, C. J. Aine, J. D. Lewine, J. A. Sanders, G. V. Simpson, J. Foxe, Functional neuroimaging combining fMRI, MEG, and EEG, *in* "Proc., SMRM, 12th Annual Meeting, New York, 1993," p. 6.

227. J. Frahm, H. Bruhn, K.-D. Merboldt, W. Hanicke, D. Math, Dynamic MR imaging of human brain oxygenation during rest and photic stimulation. *JMRI* **2**, 501-505 (1992).

228. G. M. Hathout, K. A. Kirlew, G. J. K. So, D. R. Hamilton, J. X. Zhang, U. Sinha, S. Sinha, J. Sayre, D. Gozal, R. M. Harper, R. B. Lufkin, MR imaging signal response to sustained stimulation in human visual cortex. *JMRI* **4**, 537-543 (1994).

229. C. E. Stern, K. K. Kwong, J. W. Belliveau, J. R. Baker, B. R. Rosen, MR tracking of physiological mechanisms underlying brain activity, *in* "Proc., SMRM, 11th Annual Meeting, Berlin, 1992," p. 1821.

230. P. A. Bandettini, S. M. Rao, J. R. Binder, T. A. Hammeke, A. Jesmanowicz, F. Z. Yetkin, S. Bates, L. D. Estkowski, E. C. Wong, V. M. Haughton, R. S. Hinks, J. S. Hyde, Magnetic resonance functional neuroimaging of the entire brain during performance and mental rehearsal of complex finger movement tasks, *in* "Proc., SMRM, 12th Annual Meeting, New York, 1993," p. 1396.

231. J. Hennig, T. Ernst, O. Speck, G. Deuschl, E. Feifel, Dection of brain activation using oxygenation sensitive functional spectroscopy. *Magn. Reson. Med.* **31**, 85-90 (1994).

232. T. Ernst, J. Hennig, Observation of a fast response in functional MR. *Magn. Reson. Med.* 146-149 (1994).

233. R. S. Menon, S. Ogawa, J. P. Strupp, P. Anderson, K. Ugurbil, BOLD based functional MRI at 4 tesla includes a capillary bed contribution: echo-planar imaging correlates with previous optical imaging using intrinsic signals. *Magn. Reson. Med.* **33**, 453 - 459 (1995).

234. F. Hyder, K. L. Behar, M. A. Martin, R. G. Shulman, Activation of the somatosensory/motor cortex in anesthetized rats during fore-paw stimulation localized by magnetic resonance imaging, *in* "Proc., SMRM, 12th Annual Meeting, New York, 1993," p. 1379.

235. W. Huang, M. S. Albert, N. D. Volkow, C. S. Springer, Functional imaging of the rodent brain at 9.4 T, *in* "Proc., SMRM, 12th Annual Meeting, New York, 1993," p. 1378.

236. R. A. Meyer, R. A. Bernard, T. G. Cooper, E. J. Potchen, Changes accompanying visual stimulation in 4.7 T GRASS images of the occipital cortex in sedated rabbits, *in* "Proc., SMRM, 12th Annual Meeting, New York, 1993," p. 1377.

237. S. Ogawa, T. M. Lee, Blood oxygenation level dependent MRI of the brain: effects of seizure induced by kainic acid in rat, *in* "Proc., SMRM, 11th Annual Meeting, Berlin, 1992," p. 501.

238. N. v. Bruggen, A. R. Gardner-Medwin, M. D. King, S. R. Williams, Propegating waves of spreading depression demonstrated by gradient echo MRI in the anaethetized rat, *in* "Proc., SMRM, 12th Annual Meeting, New York, 1993," p. 54.

239. G. D. Graham, J. Zhong, O. A. C. Petroff, R. T. Constable, J. W. Prichard, J. C. Gore, BOLD MRI monitoring of changes in cerebral perfusion induced by acetazolamide and hypercarbia in the rat. *Magn. Reson. Med.* **31**, 557-560 (1993).

240. P. Jezzard, F. Heinmann, J. Taylor, D. Despres, H. Wen, R. S. Balaban, R. Turner, Comparison of EPI gradient-echo contrast changes in cat brain caused by respiratory challenges with direct simultaneous evaluation of cerebral oxygenation via a cranial window. *NMR in Biomedicine* **7**, 35-44 (1994).

241. M. E. Moseley, A. deCrespigny, T. Roberts, M. E. Wendland, *in* "Functional MRI of the Brain" , p.111, Society of Magnetic Resonance in Medicine, Berkeley, 1993.

242. M. K. Stehling, F. Schmitt, R. Ladebeck, Echo-planar MR imaging of human brain oxygenation changes. *JMRI* **3**, 471-474 (1993).

243. P. A. Bandettini, E. C. Wong, R. S. Hinks, J. S. Hyde, Time-course spin-echo and gradient-echo EPI of the human brain during a breath hold, *in* "Proc., SMRM, Berlin, 1992," p. 1104.

244. E. Rostrup, H. B. W. Larsson, P. B. Toft, K. Garde, C. Thomsen, P. Ring, L. Sondergaard, O. Henricksen, Functional MRI of CO_2 induced increase in cerebral perfusion. *NMR in Biomedicine* **7**, 29-34 (1994).

245. J. R. Binder, S. M. Rao, T. A. Hammeke, J. A. Frost, P. A. Bandettini, J. S. Hyde, Syllable rate determines functional MRI response magnitude during a speech discrimination task, *in* "Proc., SMR, 2nd Annual Meeting, San Francisco, 1994," p. 327.

246. C. Price, R. Wise, S. Ramsay, K. Friston, D. Howard, K. Patterson, R. Frackowiak, Regional response differences within the human auditory

cortex when listening to words. *Neuroscience Letters* **146**, 179-182 (1992).

247. R. B. Buxton, L. R. Frank, A physiological model for the quantitative interpretation of functional MR brain activation studies, *in* "Proc., SMRM, 12th Annual Meeting, New York, 1993," p. 4.

248. Y. Cao, V. L. Towle, D. N. Levin, J. M. Balter, Functional mapping of human motor cortical activation with conventional MR imaging at 1.5 T. *JMRI* **3**, 869-875 (1993).

249. R. T. Constable, G. McCarthy, T. Allison, A. W. Allison, A. W. Anderson, J. C. Gore, Functional brain imaging at 1.5 T using conventional gradient echo MR imaging techniques. *Magn. Reson. Imag* **11**, 451-459 (1994).

250. L. R. Schad, U. Trost, M. V. Knopp, E. Muller, W. J. Lorenz, Motor cortex stimulation measured by magnetic resonance imaging on a standard 1.5 T clinical scanner. *Magn. Reson. Imag* **11**, 461-464 (1994).

251. K. Ugurbil, M. Garwood, J. Ellermann, K. Hendrich, R. Hinke, X. Hu, S.-G. Kim, R. Menon, H. Merkle, S. Ogawa, R. Salmi, Imaging at high magnetic fields: initial experiences at 4 T. *Magn. Reson. Quart.* **9**, 259-277 (1993).

252. R. M. Weisskoff, J. L. Boxerman, C. S. Zuo, B. R. Rosen, *in* "Functional MRI of the Brain" , p.103, Society of Magnetic Resonance in Medicine, Berkeley, 1993.

253. R. S. Menon, X. Hu, P. Anderson, K. Ugurbil, S. Ogawa, Cerebral oxy/deoxy hemoglobin changes during neural activation: MRI timecourse correlates to optical reflectance measurements, *in* "Proc., SMR, 2nd Annual Meeting, San Francisco, 1994," p. 68.

254. E. C. Wong, E. Boskamp, J. S. Hyde, A volume optimized quadrature elliptical endcap birdcage brain coil, *in* "Proc., SMRM, 11th Annual Meeting, Berlin, 1992," p. 4015.

255. E. C. Wong, G. Tan, J. S. Hyde, A quadrature transmit-receive endcapped birdcage coil for imaging of the human head at 125 MHz, *in* "Proc., SMRM, 12th Annual Meeting, New York, 1993," p. 1344.

256. B. Poncelet, V. J. Wedeen, R. M. Weisskoff, M. S. Cohen, Measurement of brain parenchyma motion with cine echo-planar MRI, *in* "Proc., SMRM, 11th Annual Meeting, Berlin, 1992," p. 809.

257. R. M. Weisskoff, J. Baker, J. Belliveau, T. L. Davis, K. K. Kwong, M. S. Cohen, B. R. Rosen, Power spectrum analysis of functionally-weighted MR data: what's in the noise?, *in* "Proc., SMRM, 12th Annual Meeting, New York, 1993," p. 7.

258. P. Jezzard, D. LeBihan, C. Cuenod, L. Pannier, A. Prinster, R. Turner, An investigation of the contributions of physiological noise in human functional MRI studies at 1.5 Tesla and 4 Tesla, *in* "Proc., SMRM, 12th Annual Meeting, New York, 1993," p. 1392.

259. D. C. Noll, J. D. Cohen, C. H. Meyer, W. Schneider, Spiral k-space MR imaging of cortical activation. *JMRI* **5**, 49-56 (1995).

260. B. Biswal, E. A. DeYoe, A. Jesmanowicz, J. S. Hyde, Removal of physiological fluctuations from functional MRI signals, *in* "Proc., SMR, 2nd Annual Meeting, San Francisco, 1994," p. 653.

261. G. H. Glover, A. T. Lee, C. H. Meyers, Motion artifacts in fMRI: comparison of 2DFT with PR and spiral scan methods, *in* "Proc., SMRM, 12th Annual Meeting, New York, 1993," p. 197.

262. D. A. Feinberg, A. S. Mark, Human brain motion and cerebrospinal fluid circulation demonstrated with MR velocity imaging. *Radiology* **163**, 793-799 (1987).

263. G. H. Glover, A. T. Lee, Motion artifacts in fMRI: comparison of 2DFT with PR and spiral scan methods. *Magn. Reson. Med.* **33**, 624-635 (1995).

264. E. V. Golanov, S. Yamamoto, D. J. Reis, Spontaneous waves of cerebral blood flow associated with a pattern of electrocortical activity. *Am. J. Physiol* **266**, R204-R214 (1994).

265. A. G. Hudetz, R. J. Roman, D. R. Harder, Spontaneous flow oscillations in the cerebral cortex during acute changes in mean arterial pressure. *J. Cereb. Blood Flow Metab.* **12**, 491-499 (1992).

266. Ugurbil, Personal communication.

267. K. Butts, S. J. Riederer, Analysis of flow effects in echo-planar imaging. *JMRI* **2**, 285-293 (1992).

268. J. R. Baker, B. E. Hoppel, C. E. Stern, K. K. Kwong, R. M. Weisskoff, B. R. Rosen, Dynamic functional imaging of the complete human cortex using gradient-echo and asymmetric spin-echo echo-planar magnetic resonance imaging, *in* "Proc., SMRM, 12th Annual Meeting, New York, 1993," p. 1400.

269. L. R. Frank, J. C. Stout, S. Archibald, R. B. Buxton, Oblique flow compensation for improved functional imaging, *in* "Proc., SMRM, 12th Annual Meeting, New York, 1993," p. 1375.

270. X. Hu, S.-G. Kim, Reduction of signal fluctuations in functional MRI using navigator echoes. *Magn. Reson. Med.* **31**, 495-503 (1994).

271. R. P. Woods, S. R. Cherry, J. C. Mazziotta, Rapid automated algorithm for aligning and reslicing PET images. *J. Comp. Asst. Tomog.* **115**, 565 - 587 (1992).

272. K. J. Friston, J. Ashburner, C. D. Frith, J.-B. Poline, J. D. Heather, R. Frackowiak, Spatial registration and normalization of images. *Human Brain Mapping* (in press).

273. E. A. DeYoe, P. Bandettini, J. Neitz, D. Miller, P. Winans, Methods for functional magnetic resonance imaging (FMRI) of the human brain. *J. Neuroscience Methods* **54**, 171-187 (1994).

274. K. J. Friston, P. Jezzard, R. Turner, Analysis of functional MRI time-series. *Human Brain Mapping* **1**, 153-171 (1994).

275. J. D. Cohen, D. C. Noll, W. Schneider, Functional magnetic resonance imaging: overview and methods for psychological research. *Behavior Research Methods, Instruments, & Computers* **25**, 101-113 (1993).

276. N. J. Cohen, M. T. Barnich, A. F. Kramer, H. D. Morris, P. C. Lauterbur, C. S. Potter, Y. Cao, D. N. Levin, Assessing test-retest reliability of functional MRI data, *in* "Proc., SMRM, 12th Annual Meeting, New York, 1993," p. 1410.

277. D. LeBihan, P. Jezzard, R. Turner, C. A. Cuenod, L. Pannier, A. Prinster, Practical problems and limitations in using Z-maps for processing of brain function MR images, *in* "Proc., SMRM, 12th Annual Meeting, New York, 1993," p. 11.

278. J. A. Sanders, W. W. Orrison, ANOVA tests for identification of FMRI activation, *in* "Proc., SMRM, 12th Annual Meeting, New York, 1993," p. 1376.

279. W. Schneider, B. J. Casey, D. Noll, Functional MRI mapping of stimulus rate effects across visual processing stages. *Human Brain Mapping* **1**, 117-133 (1994).

280. J. R. Baker, R. M. Weisskoff, C. E. Stern, D. N. Kennedy, A. Jiand, K. K. Kwong, L. B. Kolodny, T. L. Davis, J. L. Boxerman, B. R. Buchbinder, V.

J. Wedeen, J. W. Belliveau, B. R. Rosen, Statistical assessment of functional MRI signal change, *in* "Proc., SMRM, 2nd Annual Meeting, San Francisco, 1994," p. 626.

281. S. D. Forman, J. D. Cohen, M. Fitzgerald, W. P. Eddy, M. A. Mintun, D. C. Noll, Improved assessment of significant activation in functional magnetic resonance imaging (fMRI): use of a cluster–size threshold. *Magn. Reson. Med.* **33**, 636-647 (1995).

282. B. Biswal, E. A. DeYoe, R. W. Cox, J. S. Hyde, FMRI analysis for aperiodic task activation using nonparametric statistics, *in* "Proc., SMR, 2nd Annual Meeting, San Francisco, 1994," p. 624.

283. J. Frahm, K. D. Merboldt, W. Hanicke, A. Kleinschmidt, H. Steinmetz, High-resolution functional MRI of focal subcortical acivity in the human brian. Long - Echo Time FLASH of the Lateral Geniculate Nucleus During Visual Stimulation, *in* "Proc., SMRM, 12th Annual Meeting, New York, 1993," p. 57.

284. S. A. Engel, D. E. Rumelhart, B. A. Wandell, A. T. Lee, G. H. Glover, E. J. Chichilnisky, M. N. Shadlen, fMRI of human visual cortex. *Nature* **369, 370 [erratum]**, 525, 106 [erratum] (1994).

285. R. B. H. Tootell, J. B. Reppas, K. K. Kwong, R. Malach, R. T. Born, T. J. Brady, B. R. Rosen, J. W. Belliveau, Functional analysis of human MT and related visual cortical areas using magnetic resonance imaging. *The Journal of Neuroscience* **15**, 3215-3230 (1995).

286. M. I. Sereno, A. M. Dale, J. R. Reppas, K. K. Kwong, J. W. Belliveau, T. J. Brady, B. R. Rosen, R. B. H. Tootell, Functional MRI reveals borders of multiple visual areas in humans. *Science* **268**, 889 - 893 (1995).

287. J. J. Sychra, P. A. Bandettini, N. Bhatttacharya, Q. Lin, Synthetic Images by Subspace Transforms I: Principal Components Images and Related Filters. *Med. Phys.* **21**, 193-201 (1994).

288. B. Biswal, P. A. Bandettini, A. Jesmanowicz, J. S. Hyde, Time-frequency analysis of functional EPI time-course series, *in* "Proc., SMRM, 12th Annual Meeting, New York, 1993," p. 722.

289. P. A. Bandettini, E. C. Wong, E. A. DeYoe, J. R. Binder, R. S. Hinks, J. S. Hyde, Fourier analysis of functional EPI time-course series. *JMRI* **3(P), [Abstr.]**, 89 (1993).

290. R. W. Cox, A. Jesmanowicz, J. S. Hyde, Real-time functional magnetic resonance imaging. *Magn. Reson. Med.* **33**, 230-236 (1995).

291. R. L. Savoy, K. M. O'Craven, R. M. Weisskoff, T. L. Davis, J. Baker, B. Rosen, Exploring the temporal bourdaries of fMRI: measuring responses to very brief visual stimuli, *in* "Book of Abstracts, Soc. for Neuroscience 24'th Annual Meeting, Miami, 1994," p. 1264.

292. X. Hu, S.-G. Kim, A new T2*-weighting technique for magnetic resonance imaging. *Magn. Reson. Med.* **30**, 512-517 (1993).

293. E. C. Wong, S. G. Tan, A comparison of signal to noise ratio and BOLD contrast between single voxel spectroscopy and echo-planar imaging, *in* "Proc., SMR, 2nd Annual Meeting, San Francisco, 1994," p. 663.

294. K. Butts, S. J. Riederer, R. L. Ehman, R. M. Thompson, C. R. Jack, Interleaved echo planar imaging on a standard MRI system. *Magn. Reson. Med.* **31**, 67-72 (1994).

295. G. Liu, G. Sobering, A. W. Olson, P. v. Gelderen, C. T. Moonen, Fast echo-shifted gradient-recalled MRI: combining a short repetition time with variable T2* weighting. *Magn. Reson. Med.* **30**, 68-75 (1993).

296. C. T. Moonen, G. Liu, P. v. Gelderen, G. Sobering, A fast gradient-recalled MRI technique with increased sensitivity to dynamic susceptibility effects. *Magn. Reson. Med.* **26**, 184-189 (1992).

297. S. Chandra, Z. P. Liang, P. C. Lauterbur, Application of RIGR to efficient bold imaging, *in* "Proc., SMRM, 12th Annual Meeting, New York, 1993," p. 699.

298. D. W. Shaw, E. Weinberger, C. E. Hayes, C. Yuan, J. E. Stark, K. S. White, M. Radvilas, G. Young, T. Foo, Reduced K-space (keyhole) functional imaging without contrast on a conventional clinical scanner, *in* "Proc., SMRM, 12th Annual Meeting, New York, 1993," p. 1430.

299. O. Heid, M. Deimling, W. Huk, TE-interlaced gradient-echo functional imaging, *in* "Proc., SMRM, 12th Annual Meeting, New York, 1993," p. 476.

300. R. T. Constable, R. P. Kennan, A. Puce, G. McCarthy, J. C. Gore, Functioal NMR imaging using fast spin echo at 1.5 T. *Magn. Reson. Med.* **31**, 686-690 (1994).

301. E. C. Wong, Magnetic resonance functional neuroimaging using interleaved SUNBURST, *in* "Proc., SMR, 2nd Annual Meeting, San Francisco, 1994," p. 25.

302. E. C. Wong, P. A. Bandettini, J. S. Hyde, Echo-planar imaging of the human brain using a three axis local gradient coil, *in* "Proc., SMRM, 11th Annual Meeting, Berlin, 1992," p. 105.

303. W. Schneider, D. C. Noll, J. D. Cohen, Functional topographic mapping of the cortical ribbon in human vision with conventional MRI scanners. *Nature* **365**, 150-153 (1993).

304. B. R. Buchbinder, Personal communication.

305. Y. Cao, V. L. Towle, D. N. Levin, R. Grzeszczuk, J. F. Mullian, Conventional 1.5 T functional MRI localization of human hand senserimotor cortex with intraoperative electrophysiologic validation, *in* "Proc., SMRM, 12th Annual Meeting, New York, 1993," p. 1417.

306. J. R. Ives, S. Warach, F. Schmitt, R. R. Edelman, D. L. Schomer, Monitoring the patient's EEG during echo planar MRI. *EEG and Clinical Neurophys* **87**, 417-420 (1993).

307. A. Jesmanowicz, E. C. Wong, E. A. DeYoe, J. S. Hyde, Method to correct anatomic distortion in echo-planar images, *in* "Proc., SMRM, 11th Annual Meeting, Berlin, 1992," p. 4260.

308. R. S. Menon, H. Merkle, K. Ugurbil, A novel multi-slice FLASH sequence for functional magnetic resonance imaging, *in* "Proc., SMRM, 12th Annual Meeting, New York, 1993," p. 1203.

309. J. H. Duyn, V. S. Mattay, R. H. Sexton, G. S. Sobering, F. A. Barrios, G. Liu, J. A. Frank, D. Weinberger, C. T. W. Moonen, 3-Dimensional functional imaging of human brain using echo-shifted FLASH MRI. *Magn. Reson. Med* **32**, 150-155 (1994).

310. J. R. Binder, S. M. Rao, T. A. Hammeke, F. Z. Yetkin, A. Jesmanowicz, P. A. Bandettini, E. C. Wong, L. D. Estkowski, M. D. Goldstein, V. M. Haughton, J. S. Hyde, Functional magnetic resonance imaging of human auditory cortex. *Ann. Neurol.* **35**, 662-672 (1994).

311. J. R. Binder, S. M. Rao, *in* "Localization and Neuroimaging in Neuropsychology" (A. Kertesz, Ed.), p.185, Academic Press, San Diego, 1994.

312. J. R. Binder, S. M. Rao, T. A. Hammeke, J. A. Frost, R. W. Cox, E. C. Wong, P. A. Bandettini, A. Jesmanowicz, J. S. Hyde, A lateralized, distributed network for semantic processing demonstrated with whole

brain functional MRI, *in* "Proc., SMR, 2nd Annual Meeting, San Francisco, 1994," p. 694.

313. J. R. Binder, S. M. Rao, T. A. Hammeke, J. A. Frost, R. W. Cox, P. A. Bandettini, J. S. Hyde, Identification of auditory, linguistic, and attention systems with task subtraction functional MRI, *in* "Proc., SMR, 2nd Annual Meeting, San Francisco, 1994," p. 681.

314. M. Singh, H. Kim, T. Kim, D. Khosla, P. Colletti, Fuctional MRI at 1.5 T during auditory stimulation, *in* "Proc., SMRM, 12th Annual Meeting, New York, 1993," p. 1431.

315. R. Turner, P. Jezzard, D. LeBihan, A. Prinster, L. Pannier, T. Zeffiro, BOLD contrast imaging of cortical regions used in processing auditory stimul, *in* "Proc., SMRM, 12th Annual Meeting, New York, 1993," p. 1411.

316. S. M. Rao, P. A. Bandettini, E. C. Wong, F. Z. Yetkin, T. A. Hammeke, W. M. Mueller, S. Goldman, G. L. Morris, P. G. Antuono, L. D. Estkowski, V. M. Haughton, J. S. Hyde, Gradient-echo EPI demonstrates bilateral superior temporal gyrus activation during passive word presentation, *in* "Proc., SMRM, 11th Annual Meeting, Berlin, 1992," p. 1827.

317. S. R. Bates, F. Z. Yetkin, P. A. Bandettini, A. Jesmanowicz, L. Estkowski, V. M. Haughton, Activation of the human cerebellum demonstrated by functional magnetic resonance imaging, *in* "Proc., SMRM, 12th Annual Meeting, New York, 1993," p. 1420.

318. C. A. Cuenod, T. Zeffiro, L.Pannier, S. Posse, V. Bonnerot, P. Jezzard, R. Turner, J. A. Frank, D. LeBihan, Functional imaging of the human cerebellum during finger movement with a conventional 1.5 T MRI

scanner, *in* "Proc., SMRM, 12th Annual Meeting, New York, 1993," p. 1421.

319. J. M. Ellerman, D. Flament, S.-G. Kim, Q.-G. Fu, H. Merkle, T. J. Ebner, K. Ugurbil, Spatial patterns of functional activation of the cerebellum investigated using high field (4 T) MRI. *NMR in Biomedicine* 7, 63-68 (1994).

320. T. A. Hammeke, F. Z. Yetkin, W. M. Mueller, G. L. Morris, V. M. Haughton, S. M. Rao, J. R. Binder, Functional magnetic resonance imaging of somatosensory stimulation. *Neurosurgery* 35, 677-681 (1994).

321. K. Sakai, E. Watanabe, Y. Onodera, H. Itagaki, E. Yamamoto, H. Koizumi, Y. Miyashita, Functional mapping of the human somatosensory cortex with echo-planar MRI. *Magn. Reson. Med.* 33, 736-743 (1995).

322. S.-G. Kim, J. Ashe, A. P. Georgopoulos, H. Merkle, J. M. Ellermann, R. S. Menon, S. Ogawa, K. Ugurbil, Functional imaging of human motor cortex at high magnetic field. *J. Neurophysiol* 69, 297-302 (1993).

323. S. M. Rao, J. R. Binder, T. A. Hammeke, L. M. Lisk, P. A. Bandettini, F. Z. Yetkin, G. L. Morris, W. M. Meuller, P. G. Antuono, E. C. Wong, V. M. Haughton, J. S. Hyde, Somatotopic mapping of the primary motor cortex with functional magnetic resonance imaging, *in* "Proc., SMRM, 12th Annual Meeting, New York, 1993," p. 1397.

324. S. M. Rao, P. A. Bandettini, J. Bobholz, J. R. Binder, T. A. Hammeke, J. A. Frost, J. S. Hyde, Somatotopic mapping of the human primary motor cortex with functional magnetic resonance imaging. (in press).

325. E. A. DeYoe, J. Neitz, D. L. Miller, P. A. Bandettini, E. C. Wong, A. Jesmanowicz, J. S. Hyde, Mapping striate and extrastriate visual cortex with functional MRI. (submitted).

326. R. B. H. Tootell, K. K. Kwong, J. W. Belliveau, J. R. Baker, C. E. Stern, R. L. Savoy, H. Breiter, R. Born, R. Benson, T. J. Brady, B. R. Rosen, Functional MRI (fMRI) evidence for MT/V5 and associated visual cortical areas in man, *in* "Book of Abstracts, Soc. for Neuroscience 23'rd Annual Meeting, Washington D. C., 1993," p. 1500.

327. A. Karni, L. Ungerleider, J. Haxby, P. Jezzard, C. A. Cuenod, R. Turner, D. LeBihan, Stimulus dependent MRI signals evoked by oriented line-element textures in human visual cortex, *in* "Book of Abstracts, Soc. for Neuroscience 23'rd Annual Meeting, Washington D. C., 1993," p. 1501.

328. A. G. Sorensen, F. Caramia, S. H. Wray, K. Kwong, J. Belliveau, C. Stern, J. Baker, I. Gazit, H. Breiter, B. Rosen, Extrastriate activation in patients with visual field defects, *in* "Proc., SMRM, 12th Annual Meeting, New York, 1993," p. 62.

329. R. B. H. Tootell, J. B. Reppas, A. D. Dale, R. B. Look, R. Malach, T. J. Brady, B. R. Rosen, Visual motion aftereffect in human cortical area MT/V5 revealed by functional magnetic resonance imaging. *Nature* (in press).

330. E. A. DeYoe, J. Neitz, D. Miller, J. Wieser, Functional magnetic resonance imaging (FMRI) of visual cortex in human subjects using a unique video graphics stimulator, *in* "Proc., SMRM, 12th Annual Meeting, New York, 1993," p. 1394.

331. R. L. DeLaPaz, J. Hirsch, N. Relkin, J. Victor, L. Bartoshuk, R. Norgren, T. Prichard, Human gustatory cortex localization with functional MRI, *in* "Proc., SMR, 2nd Annual Meeting, San Francisco, 1994," p. 335.

332. S.-G. Kim, J. Ashe, K. Hendrich, J. M. Ellerman, H. Merkle, K. Ugurbil, A. P. Georgopoulos, Functional magnetic resonance imaging of motor cortex: hemispheric asymmetry and handedness. *Science* **261**, 615-616 (1993).

333. P. Jezzard, A. Karni, G. Meyer, M. Adams, A. Prinster, L. Ungerleider, R. Turner, Practice makes perfect: a functional MRI study of long term motor cortex plasticity, *in* "Proc., SMR, 2nd Annual Meeting, San Francisco, 1994," p. 330.

334. J. M. Ellerman, D. Flament, S.-G. Kim, H. Merkle, P. Andersen, T. Ebner, K. Ugurbil, Cerebellar activation due to error detection/correction in a visuo-motor learning task: a functional magnetic resonance imaging study, *in* "Proc., SMR, 2nd Annual Meeting, San Francisco, 1994," p. 331.

335. S. M. Rao, J. R. Binder, T. A. Hammeke, D. L. Harrington, K. Y. Haaland, J. A. Bobholz, J. A. Frost, B. M. Myklebust, R. D. Jacobson, P. A. Bandettini, J. S. Hyde, Functional magnetic resonance imaging correlates of cognitive motor learning: preliminary findings, *in* "Proc., SMR, 2nd Annual Meeting, San Francisco, 1994," p. 329.

336. G. McCarthy, A. M. Blamire, D. L. Rothman, R. Gruetter, R. G. Shulman, Echo-planar magnetic resonance imaging studies of frontal cortex activation during word generation in humans. *Proc. Natl. Acad. Sci. USA* **90**, 4952-4956 (1993).

337. R. M. Hinke, X. Hu, A. E. Stillman, S.-G. Kim, H. Merkle, R. Salmi, K. Ugurbil, Functional magnetic resonance imaging of brocs's area during internal speech. *Neuroreport* **4**, 675-678 (1993).

338. L. Rueckert, I. Appollonio, J. Grafman, P. Jezzard, R. J. Jr., D. LeBihan, R. Turner, Magnetic resonance imaging functional actiavtion of left frontal cortex during covert word production. *J. Neuroimaging* **4**, 67-70 (1994).

339. R. Menon, S. Ogawa, D. W. Tank, J. M. Ellermann, H. Merkle, Visual mental imagery by functional brain MRI, *in* "Proc., SMRM, 12th Annual Meeting, New York, 1993," p. 1381.

340. S. Ogawa, D. W. Tank, R. Menon, J. M. Ellermann, H. Merkle, K. Ugurbil, Functional brain MRI of cortical areas activated by visual mental imagery, *in* "Book of Abstracts, Soc. for Neuroscience 23'rd Annual Meeting, Washington D. C., 1993," p. 976.

341. S. M. Rao, J. R. Binder, P. A. Bandettini, T. A. Hammeke, F. Z. Yetkin, A. Jesmanowicz, L. M. Lisk, G. L. Morris, W. M. Mueller, L. D.Estkowski, E. C. Wong, V. M. Haughton, J. S. Hyde, Functional magnetic resonance imaging of complex human movements. *Neurology* **43**, 2311-2318 (1993).

342. J. M. Tyszka, S. T. Grafton, W. Chew, R. P. Woods, P. M. Colletti, Parceling of mesial frontal motor areas during movement using functional magnetic resonance imaging at 1.5 tesla. *Ann. Neurol.* **35**, 746-749 (1994).

343. J. R. Binder, S. M. Rao, T. A. Hammeke, F. Z. Yetkin, E. C. Wong, W. M. Mueller, G. L. Morris, J. S. Hyde, Functional magnetic resonance imaging (FMRI) of auditory semantic processing. *Neurology* **43 (Suppl. 2) [Abstr.]**, 189 (1993).

344. J. R. Binder, S. M. Rao, T. A. Hammeke, J. A. Frost, P. A. Bandettini, A. Jesmanowicz, J. S. Hyde, Lateralized human brain language systems demonstrated by task subtraction functional magnetic resonance imaging. *Arch. Neurol.* (in press).

345. J. D. Cohen, S. D. Forman, T. S. Braver, B. J. Casey, D. Servan-Schreiber, D. Noll, Activation of prefrontal cortex in a non-spatial working memory task with functional MRI. (submitted).

346. J. D. Cohen, S. D. Forman, B. J. Casey, D. C. Noll, Spiral - scan imaging of dorsolateral prefrontal cortex during a working memory task, *in* "Proc., SMRM, 12th Annual Meeting, New York, 1993," p. 1405.

347. A. M. Blamire, G. McCarthy, A. C. Nobre, A. Puce, F. Hyder, G. Bloch, E. Phelps, D. L. Rothman, P. Goldman-Rakie, R. G. Shulman, Funcitonal magnetic resonance imaging of human pre-frontal cortex during a spatial memory task, *in* "Proc., SMRM, 12th Annual Meeting, New York, 1993," p. 1413.

348. D. LeBihan, R. Turner, T. Zeffiro, C. A. Cuenod, P. Jezzard, V. Bonnerot, Activation of human primary visual cortex during visual recall: a magnetic resonance imaging study. *Proc. Natl. Acad. Sci. USA* **90**, 11802-11805 (1993).

349. P. Hedera, S. Lai, E. M. Haacke, A. J. Lerner, A. L. Hopkins, J. S. Lewin, R. P. Friedland, Abnormal connectivity of the visual pathways in human albinos demonstrated by susceptibility-sensitized MRI. *Neurology* **44**, 1921-1926 (1994).

350. Y. Cao, E. M. Vikingstad, P. R. Huttenlocher, V. L. Towle, D. N. Levin, Functional magnetic resonance studies of the reorganization of the human hand sensorimotor area after unilateral brain injury in the perinatal period. *PNAS* (in press).

351. P. F. Renshaw, D. A. Yurgelun-Todd, B. M. Cohen, Greater hemodynamic response to photic stimulation in schizophrenic patients: an echo planar MRI study. *Am. J. Psychiatry* **151**, 1493-1495 (1994).

352. G. D. Jackson, A. Connelley, J. H. Cross, I. Gordon, D. G. Gadian, Functional magnetic resonance imaging of focal seizures. *Neurology* **44**, 850-856 (1994).

353. F. Wenz, L. R. Schad, K. Baudendistel, F. flomer, J. Schroder, M. V. Knopp, Effects of neuroleptic drugs on signal intensity during motor cortex stimulation: functional MR-imaging performed with a standard 1.5 T clinical scanner, *in* "Proc., SMRM, 12th Annual Meeting, New York, 1993," p. 1419.

354. H. C. Breiter, K. K. Kwong, J. R. Baker, C. E. Stern, J. W. Belliveau, T. L. Davis, L. Baer, R. M. O'Sullivan, S. L. Rauch, C. R. Savage, M. S. Cohen, R. M. Weisskoff, T. J. Brady, M. A. Jenike, B. R. Rosen, Functional magnetic resonance imaging of symptom provocation in obsessive - compulsive disorder, *in* "Proc., SMRM, 12th Annual Meeting, New York, 1993," p. 58.

355. H. C. Breiter, S. L. Rauch, K. K. Kwong, J. R. Baker, R. M. Weisskoff, D. N. Kennedy, T. L. Davis, A. Jiang, M. S. Cohen, C. E. Stern, J. W. Belliveau, L. Baer, R. L. O'Sullivan, C. R. Savage, T. J. Brady, M. A. Jenike, B. R. Rosen, Functional magnetic resonance imaging of sumptom provocation in obsessive compulsive disorder. (submitted).

356. G. L. Morris, W. M. Mueller, F. Z. Yetkin, V. M. Haughton, T. A. Hammeke, S. Swanson, S. M. Rao, A. Jesmanowicz, L. D. Estkowski, P. A. Bandettini, E.C.Wong, J. S. Hyde, Functional magnetic resonance imaging in partial epilepsy. *Epilepsia* **35**, 1194-1198 (1994).

357. R. Turner, P. Jezzard, *in* "Functional neuroimaging. Technical foundations." (R. W. Thatcher, M. Hallett, T. Zeffiro, E. R. John, M. Huerta, Eds.), p.69-78, Academic Press, San Diego, 1994.

358. R. G. Schulman, A. M. Blamire, D. L. Rothman, G. McCarthy, Nuclear magnetic resonance imaging and spectroscopy of human brain function. *Proc. Natl. Acad. Sci. USA* **90**, 3127-3133 (1993).

359. J. W. Prichard, B. R. Rosen, Functional Study of the Brain by NMR. *Journal of Cerebral Blood Flow and Metabolism* **14**, 365-372 (1994).

360. M. E. Cohen, S. Y. Bookheimer, Localization of brain function using magnetic resonance imaging. *TINS* **17**, 1994 (1994).

361. W. W. Orrison, J. D. Lewine, J. A. Sanders, M. F. Hartshorne, "Functional Brain Imaging," Mosby-Year Book, Inc., St. Louis, 1995.

362. P. A. Bandettini, J. R. Binder, E. A. DeYoe, J. S. Hyde, *in* "Encyclopedia of Nuclear Magnetic Resonance Imaging" (D. M. Grant, R. K. Harris, Eds.), John Wiley and Sons, Chichester, in press.

363. P. A. Bandettini, J. R. Binder, E. A. DeYoe, S. M. Rao, A. Jesmanowicz, T. A. Hammeke, V. M. Haughton, E. C. Wong, J. S. Hyde, *in* "Diffusion and Perfusion Magnetic Resonance Imaging" (D. LeBihan, Ed.), pp. 351-362, Raven Press, New York, 1995.

364. K. K. Kwong, Functional magnetic resonance imaging with echo planar imaging. *Magn. Reson. Quart.* **11**, 1-20 (1995).

365. P. A. Bandettini, E. C. Wong, *in* "Echo - planar imaging" (F. Schmitt, M. Stheling, R. Turner, Eds.), Springer – Verlag, Berlin, in press.

366. E. C. Wong, A. Jesmanowicz, J. S. Hyde, Coil optimization for MRI by conjugate gradient descent. *Magn. Reson. Med* **21**, 39-48 (1991).

367. E. C. Wong, Shim insensitive phase correction for EPI using a two echo reference scan, *in* "Proc., SMRM, 11th Annual Meeting, Berlin, 1992," p. 4514.

368. A. Jesmanowicz, E. C. Wong, J. S. Hyde, Phase correction for EPI using internal reference lines, *in* "Proc., SMRM, 12th Annual Meeting, New York, 1993," p. 1239.

369. H. S. Wilf, "Mathematics for the physical sciences," Dover, New York, 1962.

370. H. Forster, Personal communication.

371. L. Stryer, "Biochemistry," W. H. Freeman and Company, New York, 1981.

372. J. R. Pappenheimer, Passage of molecules through capillary walls. *Physiol. Rev.* **33**, 387 (1953).

373. R. Mills, Self-diffusion in normal and heavy water in the range 1 - 45°. *J. Phys Chem* **77**, 685 - 688 (1975).

374. D. LeBihan, R. Turner, Intravoxel incoherent motion imaging using spin-echoes. *Magn. Reson. Med.* **19**, 221-227 (1991).

375. R. L. Grubb, M. E. Raichle, J. O. Eichling, M. M. Ter-Pogossian, The effects of changes in $PaCO_2$ on cerebral blood volume, blood flow, and vascular mean transit time. *Stroke* **5**, 630 - 639 (1974).

376. L. Ott, "An Introduction to Statistical Methods and Data Analysis," Duxbury Press, Boston, 1984.

377. A. Prinster, C. Pierpaoli, P. Jezzard, R. Turner, Simultanenous measurement of $\Delta R2$ and $\Delta R2^*$ in cat brain during hypoxia and hypercapnia, *in* "Proc., SMR, 2nd Annual Meeting, San Francisco, 1994," p. 439.

378. W. H. Press, S. A. Teukolsky, W. T. Vetterling, B. P. Flannery, "Numerical recipies in C. The art of scientific computing.," Cambridge University Press, New York, 1992.

379. R. W. Cox, A. Jesmanowicz, Personal communication.

380. J.-H. Gao, S. K. Holland, J. C. Gore, Nuclear magnetic resonance signal from flowing nuclei in rapid imaging using gradient ehoes. *Med. Phys.* **15**, 809 - 814 (1988).

381. R. J. Seitz, P. E. Roland, C. Bohm, T. Greitz, T. S. Stone-Elander, Motor learning in man: a positron emission tomographic study. *Neuroreport* **1**, 57-60 (1990).

382. M. P. Deiber, R. E. Passingham, J. C. Colebatch, K. J. Friston, R. S. Frackowiak, Cortical areas and the selection of movement: a study with positron emission tomography. *Brain Res* **84**, 393-402 (1991).

383. J. M. Orgogozo, B. Larson, Activation of the supplementary motor area during voluntary movement in man suggests it works as a supramotor area. *Science* **206**, 847-850 (1979).

384. P. E. Roland, E. Meyer, T. Shibaski, Y. L. Yumamoto, C. J.Thompson, Regional cerebral blood flow changes in cortex and basal ganglia during voluntary movements in normal human volunteers. *J. Neurophysiol* **48**, 467-478 (1982).

385. P. E. Roland, B. Larsen, N. A. Lassen, E. Skinhoj, Supplementary motor area and other cortical areas in organization of voluntary movements in man. *J. Neurophysiol* **43**, 118-136 (1980).

386. P. E. Roland, E. Skinhoj, N. A. Lassen, B. Larsen, Different cortical areas in man in organization of voluntary movements in extrapersonal space. *J. Neurophysiol* **43**, 137-150 (1980).